Semi-Physical Real-Time Models with State and Parameter Estimation for Diesel Engines

Vom Fachbereich
Elektrotechnik und Informationstechnik
der Technischen Universität Darmstadt
zur Erlangung des Grades eines Doktor-Ingenieurs (Dr.-Ing.)
genehmigte Dissertation

von

Alexander Weber

Referent:	Prof. Dr.-Ing. Dr. h.c. Rolf Isermann
Korreferent:	Prof. Dr. techn. Christian Beidl
Tag der Einreichung:	28. March 2023
Tag der Prüfung:	12. Juli 2023

D 17 · Darmstadt 2023

Semi-Physical Real-Time Models with State and Parameter Estimation for Diesel Engines

Genehmigte Dissertation von Alexander Weber
Darmstadt, Technische Universität Darmstadt
Tag der mündlichen Prüfung: 12. Juli 2023
Jahr der Veröffentlichung der Dissertation auf TUprints: 2023

D 17 · Darmstadt 2023

Bitte zitieren Sie dieses Dokument als:
URN: urn:nbn:de:tuda-tuprints-247585
URL: http://tuprints.ulb.tu-darmstadt.de/24758

Dieses Dokument wird bereitgestellt von tuprints,
E-Publishing-Service der TU Darmstadt
http://tuprints.ulb.tu-darmstadt.de
tuprints@ulb.tu-darmstadt.de

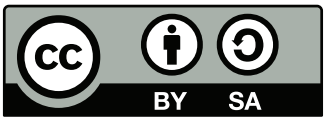

Die Veröffentlichung steht unter folgender Creative-Commons-Lizenz:
CC BY-SA 4.0 International
https://creativecommons.org/licenses/by-sa/4.0/deed.en/

Preface

Diese Dissertation ist das Ergebnis meiner Zeit als wissenschaftlicher Mitarbeiter am Institut für Automatisierungstechnik und Mechatronik (IAT) an der TU Darmstadt. Betreut wurde meine Forschungsarbeit von Prof. Dr.-Ing. Dr. h. c. Rolf Isermann, Leiter der Forschungsgruppe Regelungstechnik und Prozessautomatisierung (RTP). Des Weiteren wurde meine Arbeit dankenswerter Weise durch die Forschungsvereinigung Verbrennungskraftmaschinen (FVV) e.V. fachlich und finanziell unterstützt. Den Teilnehmern des Arbeitskreises sowie insbesondere Stefan Lindner danke ich für die vielen Diskussionen und Anregungen aus dem Blickwinkel der Automobilindustrie.

An erster Stelle möchte ich Prof. Dr.-Ing. Dr. h. c. Rolf Isermann dafür danken, dass er mir das Privileg des wissenschaftlichen Arbeitens und die Promotion ermöglicht hat. Durch seine hervorragende fachliche Förderung und die Möglichkeiten und Freiräume, die er mir während meiner Promotion gewährte, konnte ich mich sowohl fachlich als auch persönlich weiterentwickeln. Herrn Prof. Dr. techn. Christian Beidl, Leiter des Instituts für Verbrennungskraftmaschinen und Fahrzeugantriebe der TU Darmstadt, möchte ich für das Interesse an meiner Forschungsarbeit und die Übernahme des Korreferats herzlich bedanken.

Meine Zeit am IAT wird mir besonders durch die Kolleginnen und Kollegen, sowohl der Forschungsgruppe Regelungstechnik und Prozessautomatisierung (RTP), als auch des Fachgebiets Regelungstechnik und Mechatronik (RTM), positiv in Erinnerung bleiben. Auf Seiten des RTP möchte ich mich bei Simon und Florian für die Unterstützung bei der Einarbeitung in die Motorenwelt bedanken und bei Jakob und Philipp für den fachlichen Austausch zu Schätz- und Identifikationsmethoden. Den vielen wissenschaftlichen Mitarbeitern des RTM verdanke ich, dass für mich auch die zweite Hälfte meiner Zeit am IAT weiterhin viel Freude bereitet hat. Mein besonderer Dank gilt Ilse, Brigitte, Alfred und Corina für die Herzlichkeit, stetige Hilfsbereitschaft und die vielen guten Gespräche abseits der fachlichen Arbeit.

Abschließend möchte ich meiner Familie und meinen Freunden für die Unterstützung während dieser prägenden Zeit danken. Allen voran danke ich Pia für die Motivation und den unermüdlichen Rückhalt besonders in der finalen Phase des Zusammenschreibens. Ohne dich hätte ich diese Arbeit nicht zu Ende bringen können.

Bielefeld, September 2023
Alexander Weber

The paradox is that nowadays it is easier to complicate things,
while the simplification turns out to be challenging

Contents

List of Symbols

1. General letter symbols

a	parameters of differential or difference equations
b	parameters of differential or difference equations
c	spring constant, constant, concentration, stiffness
d	damping coefficient
e	equation error, control deviation $e = w - y$, number $e = 2.71828\ldots$
f	fault, frequency ($f = 1/T_p$, T_p period), function $f(\ldots)$
g	gravitational acceleration, function $g(\ldots)$, impulse response
i	integer, gear ratio, index, $\sqrt{-1}$ (imaginary unit)
j	integer, index
k	discrete number, discrete time $k = t/T_0 = 0, 1, 2, \ldots$ (T_0: sampling time)
l	index, length
m	mass, order number
n	rotational speed, order number, disturbance signal
p	pressure, index, controller parameter, probability density function, process parameter
q	controller parameter
r	rate, radius,
s	Laplace variable $s = \delta + i\omega$
t	continuous time
u	input signal change ΔU
v	velocity, specific volume, disturbance signal
w	speed, average gas velocity
x	space coordinate, state variable
y	output signal change ΔY, space coordinate, control variable change ΔY, signal
z	space coordinate, z-transform variable $z = \exp T_0 s$, operating point variable
$\hat{x}$	estimated or observed variable
$\tilde{x}$	estimation error
$\bar{x}$	average, steady-state value
x_0	initial state

A	area, constant parameter
B	magnetic flux density
C	capacitance
D	damping ratio, diameter
E	module of elasticity, energy, potential, bulk modulus
F	filter transfer function, force
G	weight, transfer function

H	magnetic field strength, height
I	electrical current, mechanical momentum, torsion, second moment of area
J	moment of inertia
K	constant, gain
L	inductance
M	torque
N	discrete number, windings number
P	power, probability
Q	heat (energy)
R	electrical resistance, gas constant
S	spectral density, sum, performance criterion
T	absolute temperature, time constant
T_0	sampling time
U	input variable, manipulated variable (control input), voltage
V	volume
X	space coordinate, air mass fraction
Y	output variable, space coordinate, control variable
Z	space coordinate, disturbance variable
$\mathbf{a}$	vector
$\mathbf{A}$	matrix
$\mathbf{A}^{\mathrm{T}}$	transposed matrix
$\mathbf{I}$	identity matrix
$\boldsymbol{\theta}$	parameter vector
$\mathbf{P}$	covariance matrix
$\mathbf{Q}$	covariance matrix of process noise
$\mathbf{R}$	covariance matrix of measurement noise
$\boldsymbol{\psi}$	data vector
$\boldsymbol{\theta}$	parameter vector
$\mathbf{u}$	input variable vector
$\mathbf{v}$	measurement noise variable vector
$\mathbf{w}$	weighting factor vector, process noise variable vector
$\mathbf{x}$	state variable vector
$\mathbf{y}$	output variable vector
$\mathbf{z}$	operating point variable vector
α	coefficient, angle
β	coefficient, angle
γ	specific weight, correcting factor
δ	decay factor, impulse function
ε	error, compression ratio
ϕ	validity function, activation function
φ	(crank shaft) angle

η	efficiency
ϑ	temperature
κ	isentropic coefficient
λ	air-fuel ratio, thermal conductivity, forgetting factor
μ	friction coefficient, permeability, membership function
ν	kinematic viscosity, index
π	number $\pi = 3.14159\ldots$
ψ	data vector
ρ	density
σ	complex crank angle frequency, step function, standard deviation
τ	time constant
θ	parameter
χ	mass fraction
ω	angular frequency, $\omega = 2\pi/T_\mathrm{p}$: T_p period
Δ	change, deviation
Π	product
Σ	sum

2. General mathematical abbreviations

$\exp(x)$	$= e^x$
$E\{\ldots\}$	expected value of a statistical variable
$\mathcal{L}\{\ldots\}$	Laplace transform
$\sum\{\ldots\}$	sum function
$\Pi\{\ldots\}$	product function
$\sigma(\ldots)$	step function
$\delta(\ldots)$	impulse function
max(...)	maximum function returning the maximum value
min(...)	minimum function returning the minimum value
$\dot{y}$	$\mathrm{d}y/\mathrm{d}t$ first derivative with respect to time t
$\ddot{y}$	$\mathrm{d}^2y/\mathrm{d}t^2$ second derivative with respect to time t
y'	$\mathrm{d}y/\mathrm{d}\varphi$ first derivative with respect to crank angle φ
y''	$\mathrm{d}y^2/\mathrm{d}\varphi^2$ second derivative with respect to crank angle φ
$y^{(j)}$	$\mathrm{d}^j y/\mathrm{d}x^j$ j-th derivative (higher order) with respect to an arbitrary variable x
$\partial y/\partial x$	partial derivative of variable y with respect to an arbitrary variable x
var[]	variance

3. Letter symbols for internal combustion engines

3.1 Geometry and time (DIN 1304, ISO 31)

A	area	m^2
a	acceleration	m/s^2
b	breadth	m
c	absolute velocity	m/s
d	diameter	m
D	characteristic diameter	m
f	frequency	Hz
g	acceleration of free fall, gravitational acceleration	m/s^2
h	height	m
l	length	m
n	rotational speed	1/s, rpm
r	radius	m
s	actuator position	m
u	peripheral velocity	m/s
V	volume	m^3
v	specific volume	m^3/kg
w	relative velocity	m/s
ω	angular velocity	rad/s

3.2 Mechanics (DIN 1304, ISO 31)

a	specific work	J/kg
m	mass	kg
$\dot{m}$	mass flow rate	kg/s
p	pressure	Pa
c_d	orifice discharge coefficient	1
E	energy	J
F	force	N
J	moment of inertia	kg m^2
L	angular momentum	kg m^2/s
M	torque	Nm
P	power	W
W	work	J
$\nu, \nu = \eta/\rho$	kinematic viscosity	m^2/s
η	dynamic viscosity	Pa s
η	efficiency	1
ρ	mass density	kg/m^3
Π	pressure ratio	1

3.3 Thermodynamics and heat transfer (DIN 1304, ISO 31)

c_p	specific heat capacity at constant pressure	J/(kg K)
c_v	specific heat capacity at constant volume	J/(kg K)
H	enthalpy	J/kg
h	specific enthalpy	J/kg
L	characteristic length	m
n	polytropic exponent	1
Nu	Nusselt number	1
Pr	Prandtl number	1
Q	heat energy	J
$\dot{Q}$	heat flow rate	W
q	specific heat	J/kg
R	universal/ideal gas constant (air: $R_{air} = 287.1$ J/(kg K))	J/(kg K)
Re	Reynolds number	1
S	entropy	J/K
s	specific entropy	J/(kg K)
T	thermodynamic temperature	K
U	internal energy	J
u	specific internal energy	J/kg
X	mass fraction	1
α	coefficient of heat transfer	W/(m^2 K)
κ	isentropic exponent	1

3.4 Engine specific symbols

α_{ped}	accelerator pedal position	%
b_f	fuel consumption	kg/h
b_{sfc}	effective specific fuel consumption	g/kWh
c_m	mean piston speed	m/s
c_{NOx}	nitrogen oxide concentration	g/m^3
c_{op}	opacity	%
c_{pa}	soot concentration	g/m^3
Δt_{pi}	timing of pilot injection	ms
$\Delta\varphi_{pi}$	crank angle of pilot injection (difference angle to main injection)	°CS
ε	compression ratio	1
h	valve lift	m
H_l	lower fuel heating value	J/kg
φ	crank angle	°CS
φ_{mi}	crank angle of main injection	°CS
φ_{pi}	crank angle of pilot injection	°CS
φ_{po}	crank angle of post injection	°CS
φ_{ign}	ignition angle	°CS

λ_{cr}	stroke/connecting rod ratio	m/m
λ	air-fuel ratio (excess air factor)	1
λ_a	air expenditure	1
λ_p	connecting rod ratio	1
l_{char}	characteristic (representative) length	m
l_{cs}	connection rod length	m
L_{st}	stoichiometric air requirement, $L_{st} \approx 14.5$ for diesel	kg/kg
m_{burn}	fuel mass involved in burn-out phase	mg
m_{diff}	fuel mass involved in diffusive combustion phase	mg
m_{gf}	vaporized, gaseous fuel mass	mg
m_f	injection fuel mass	mg/cyc
$\dot{m}_f$	injection fuel mass flow	kg/h
m_{mi}	main injection mass	mg/cyc
m_{pi}	pilot injection mass	mg/cyc
m_{pre}	fuel mass involved in premixed combustion phase	mg
$\dot{m}_{eng,in}$	gas flow into the engine	kg/h
$\dot{m}_{eng,out}$	gas flow out of the engine	kg/h
m_{air}	air mass per cycle	mg/cyc
M_{aux}	auxiliaries torque	Nm
M_{cyl}	torque of one cylinder	Nm
M_{eng}	crankshaft mean torque at flywheel	Nm
M_f	friction torque	Nm
M_g	gas force torque	Nm
M_i	indicated torque	Nm
M_l	load torque	Nm
M_m	dynamic masses torque	Nm
M_{tow}	towed torque, motoring torque	Nm
$\dot{m}_{air}$	air mass flow	kg/h
q_{inj}	injection quantity	mm^3/cyc
q_{mi}	main injection quantity	mm^3/cyc
q_{pi}	pilot injection quantity	mm^3/cyc
r_{cs}	crankshaft radius	m
s_p	piston stroke (position)	m
$r_{(hp/lp)egr}$	(high-pressure/low-pressure) exhaust gas recirculation ratio	1
V_c	clearance/compression volume per cylinder	m^3
V_d	displaced volume per cylinder	m^3
V_D	total displacement (all cylinders)	m^3
w_p	(crank angle resolved) piston velocity	m/s
X	air mass fraction	mg/mg
X_{cyl}	(global) air mass fraction of in-cylinder gas	mg/mg
X_{mix}	(local) air mass fraction in the mixture and reaction zone	mg/mg
z	number of cylinders	1

3.5 Combustion analysis

p_{cyl}	in-cylinder pressure	Pa/°CS
$\mathrm{d}p_{\mathrm{cyl}}/\mathrm{d}\varphi$	(in-cylinder) pressure gradient	Pa/°CS
p_{mi}	mean indicated pressure	Pa
p_{tow}	towed cylinder pressure (no injection)	Pa
p_{imep}	brake mean effective pressure	Pa
Q_{f}	released burning energy (german: freigesetzte Brennenergie / Brennverlauf)	J
$\mathrm{d}Q_{\mathrm{f}}/\mathrm{d}\varphi$	burn rate (german: Brennrate)	J/°CS
Q_{h}	heat release (german: Wärmefreisetzung / Heizverlauf)	J
$\mathrm{d}Q_{\mathrm{h}}/\mathrm{d}\varphi$	heat rate (german: Heizrate)	J/°CS
Q_{w}	wall heat transfer	J
φ_{Q5}	location of mass fraction burned 5%	°CS
φ_{Q50}	location of mass fraction burned 50% (CA50)	°CS
φ_{Q95}	location of mass fraction burned 95%	°CS

3.6 Subscripts for internal combustion engines

1	state variables in front of the compressor
3	state variables in front of the turbine (in the exhaust manifold)
4	state variables after the turbine
5	state variables after the DPF
2c	state variables after the compressor
2i	state variables in the intake manifold
2ic	state variables after the intercooler
a	ambient
af	air filter
afl	air flaps
air	(ambient) air
b	burned
bf	burned fuel
burn	burn-out phase of diesel combustion)
c	compressor
ca	crank angle
cam	camshaft
char	characteristic value
cr	connecting rod
cs	crankshaft
cd	combustion duration
cl	cooler
cr	common rail
cyl	cylinder

diff	diffusive combustion phase
dpf	Diesel particulate filter
ds	delivery start
ec	exhaust closes
eff	effective
eg	exhaust gas
egr	exhaust gas recirculation (EGR)
eng	engine
eoc	end of combustion
et	(injector) energizing time
eth	exhaust throttle valve
ev	exhaust valve
evc	exhaust valve closed
evo	exhaust valve open
f	fuel, friction
gas	gas flow
geo	geometrical
gf	gaseous (vaporized) fuel
h2o	coolant water
hfm	hot-film mass flow sensor
hpcl	high-pressure EGR cooler
hpegr	high pressure exhaust gas recirculation
hpp	high pressure pump
id	ignition delay / injection duration
ign	ignition
in	streaming in
int	intake
inj	injector
io	intake opens
ith	intake throttle
iv	intake valve
ivc	intake valve closed
ivo	intake valve open
lpcl	low-pressure EGR-cooler
lpegr	low-pressure exhaust gas recirculation
lpp	low-pressure pump (fuel pump)
meas	measured
mi	main injection
mix	mixing and reaction zone
mv	metering valve
oil	oil
out	streaming out
p	piston

pcv	pressure control valve
pi	pilot injection
pm	(soot) particle matter
pre	premixed combustion
r	rod
rail	rail system
red	reduced
sim	simulated
soc	start of combustion
soe	start of (injector) energizing
soi	start of injection
st	gas storage
t	turbine
tc	turbocharger
th	throttle, theoretical
u	unburned
v	volumetric, isochoric
vtg	variable geometry turbocharger
w	wall

3.7 General Abbreviations

BEV	Battery electric vehicles
CCU	Carbon capturing and utilization
DAC	Direct air capturing
DiCoRS	Digital Combustion Rate Shaping
EiL	Engine-in-the-Loop
ECU	Electronic Control Unit
EDC	Electronic Diesel Controller
FCEV	Fuel cell electric vehicles
FPGA	Field Programmable Gate Array
FVV	Forschungsvereinigung Verbrennungskraftmaschinen e.V.
HEV	Hybrid electric vehicles
HiL	Hardware-in-the-Loop
ICEV	Internal combustion engine vehicle
MiL	Model-in-the-Loop
PSH	Pumped-storage hydroelectric (power plants)
PHEV	Plug-in hybrid vehicles
PtL	Power-to-liquid (power plants)
RCP	Rapid Control Prototyping
SiL	Software-in-the-Loop
ViL	Vehicle-in-the-Loop
XiL	X-in-the-loop

3.8 Abbreviations for internal combustion

APC	Airpath controller
BSFC	Brake specific fuel consumption
CA50	Crank angle φ_{Q50} where 50 % of total fuel is burned (center of combustion)
CAN	Controller Area Network
CASEM	Crank-angle synchronous engine model
CC	Combustion controller
CI	Compression-ignition
CF	conformity factor
CRS	Common-rail systems
CS	Crankshaft angle
DOC	Diesel oxidation catalyst
DPF	Diesel particulate filter
EDC	Electronic Diesel Control
ECU	Electronic control unit
EGR	Exhaust gas recirculation
EGT	Exhaust gas treatment
ERM	Engine-related measure
HFM	Hot film measurement
HCCI	Homogenouos charge compression ignition
HP-EGR	High-pressure exhaust gas recirculation
IGS	Initial in-cylinder gas state
LTC	Low temperature combustion
LP-EGR	Low-pressure exhaust gas recirculation
MBCA	Model-Based Combustion Analysis
MVEM	Mean-value engine model
NEDC	New European Driving Cycle
OP	Operating point of the engine
PEMS	Portable emission measurement systems
PCCI	Partially premixed compression ignition
RDE	Real driving emissions
SI	Spark-ignition
SOC	start of combustion
VGT	Variable geometry turbocharger
WLTC	Worldwide harmonized Light vehicles test cycle
WLTP	Worldwide harmonized Light vehicles test procedure

3.9 Abbreviations for modeling, system identification and control theory

ACF	Auto correlation function
ANN	Artificial Neural Networks
CCF	Cross correlation function

CFD	Computational Fluid Dynamics
CKF	Cubature Kalman filter
EE	equation error
EKF	Extended Kalman filter
IMC	Internal model control
HHT	Hinging Hyperplane Tree
KF	Kalman filter
LS	Least Squares
LOLIMOT	Local Linear Model Tree
LOPOMOT	Local Polynomial Model Tree
MPC	Model predictive control
NN	Neural networks
OE	output error
RLS	Recursive Least Squares
RBF	Radial basis functions
SS	State-space representation
SPKF	Sigma-Point Kalman Filter
SVF	State variables filter
SRCKF	Square-root Cubature Kalman filter
SRUKF	Square-root Unscented Kalman filter
UKF	Unscented Kalman filter
UT	Unscented transformation

Kurzfassung

Steigende Anforderungen hinsichtlich der Reduzierung und Kraftstoffverbrauch (CO_2) und Schadstoffausstoß erfordern ein präzises elektronisches Motormanagement. Innermotorische Maßnahmen zur Erfüllung dieser Anforderungen sorgen für eine Zunahme an Variabilität und Systemkomplexität. Zur Bewältigung steigender Systemkomplexität hat sich die modellbasierte Entwicklungsmethodik bewährt. Dabei spielt die virtuelle Entwicklung mit Echtzeitmodellen eine immer wichtigere Rolle. Die entsprechenden Modelle können entweder theoretisch auf Grundlage bekannter physikalischer Gesetzmäßigkeiten hergeleitet werden (White-Box-Modelle) oder experimentell am Prüfstand durch mathematische Modellierung des gemessenen Eingangs- und Ausgangsverhaltens gewonnen werden (Black-Box-Modelle). Beide Modellierungsarten haben ihre Vor- und Nachteile.

In dieser Arbeit wird eine semi-physikalische Modellierungsmethodik vorgestellt, die die Vorteile von theoretischer und experimenteller Modellierung kombiniert und deren Nachteile umgeht. Die Grundidee ist es, geeignete, vereinfachte Gleichungsstrukturen zu finden und durch rekursive, echtzeitfähige Parameterschätzmethoden die unbekannten Parameter experimentell zu bestimmen. Daraus ergeben sich physikalisch interpretierbare Echtzeitmodelle, die in der Lage sind, ihre Parameter an den aktuellen Motorbetriebspunkt anzupassen und auf andere Motoren besser übertragbar sind. Die Modellierungsmethodik wird auf das Luftsystem und die Verbrennung eines Common-Rail-Dieselmotors mit variablem Turbolader sowie Hoch- und Niederdruck-Abgasrückführung angewandt. Der Schwerpunkt dieser Arbeit liegt auf der Herleitung entsprechender Modelle für die Verbrennung.

Es wird ein semi-physikalischer Modellansatz für die Modellierung der Dynamik von Brennraumprozessen entwickelt und mit Zustands- und Parameterschätzverfahren kombiniert. Der Modellansatz ermöglicht eine echtzeitfähige, kurbelwinkelaufgelöste Berechnung des Zylindergaszustands, der Gemischbildung sowie die Bestimmung der charakteristischen Verbrennungsanteile der Dieselverbrennung (vorgemischte, diffusive Verbrennung und Ausbrand). Die technische Umsetzung erfolgt nahe am Indiziersystem, womit eine kurbelwinkelaufgelöste Modelladaption anhand des gemessenen Brennraumdruckverlaufs ermöglicht wird. Die Modell-Identifikation erfolgt mithilfe von kombinierter Zustands- und Parameterschätzung im stationären Motorbetrieb. Die Modellparameter werden zyklusaufgelöst geschätzt und konvergieren innerhalb von 30-60 Arbeitszyklen zu einem konstanten Wert. Abschließend wird die Anwendung der Methode im Rahmen einer modellbasierten Verbrennungsanalyse aufgezeigt, sowie der Einsatz semi-physikalischer Modelle zur Echtzeit-Motorsimulation im Rahmen des Hardware-in-the-Loop Testens von Steuergeräten beschrieben.

Das Forschungsvorhaben (Projekt Nr. 1231) wurde von der Forschungsvereinigung Verbrennungskraftmaschinen (FVV) e.V. (Frankfurt am Main, Deutschland) finanziell und fachlich gefördert.

Abstract

Increasing requirements for the reduction of fuel consumption (CO_2) and emissions require a precise electronic management of combustion engines. Engine-related measures to meet these requirements lead to an increase in variability and system complexity. To cope with increasing system complexity, model-based development methodology has proven effective. In this context, virtual development with real-time models plays an increasingly important role. The corresponding models can either be derived theoretically on the basis of known physical laws (white-box models) or obtained experimentally on the test bench by mathematically modeling the measured input and output behavior (black-box models). Both types of modeling have their advantages and disadvantages.

A semi-physical modeling methodology is presented that combines the advantages of theoretical and experimental modeling and overcomes their disadvantages. The goal is to find suitable, simplified equation structures and to determine their unknown parameters experimentally by real-time capable, recursive parameter estimation methods. This leads to physically interpretable real-time models that are able to adapt their parameters according to the current engine operating behavior and thus offer good transferability to other engines. The semi-physical modeling methodology is applied to the air system and combustion of a common rail diesel engine with a variable exhaust gas turbocharger and high- and low-pressure exhaust gas recirculation. The focus lies on the derivation of semi-physical real-time model for the combustion and its underlying processes inside the cylinder.

A semi-physical model approach for modeling the dynamics of combustion chamber processes is developed and combined with state and parameter estimation methods. This model approach enables crank angle-resolved calculation of the in-cylinder gas states and the determination of the characteristic combustion components of diesel combustion (premixed, diffusive combustion and burn-out). The technical implementation is realized close to the pressure indication system of the engine test bench, enabling a crankshaft-resolved model adaptation based on measured in-cylinder pressure. Model identification is performed using combined state and parameter estimation in steady-state engine operation. Model parameters are estimated perpetually for each duty cycle and converge to a constant value within 30-60 engine duty cycles. Final estimation results are stored as functions of engine operating point using experimental modeling. In this way, semi-physical real-time models are created directly online during the measurement.

The treated method is considered as an extension of the functionality of conventional pressure indication systems. Furthermore, the derived semi-physical models are used for real-time engine simulation in the context of hardware-in-the-loop testing of ECUs.

The research project (Project No. 1231) was financially and advisory supported by the Research Association for Combustion Engines (FVV) e.V. (Frankfurt am Main, Germany).

1 Introduction

This work deals with methods for a systematic generation of *real-time capable and physics-oriented combustion engine models*, which can be applied in several phases of the engine development and the ECU calibration process. This chapter provides an introduction to this work and describes its motivation and scientific contribution in a social and technological context. At the beginning of this chapter, the current technological challenges in the field of engine development and control unit application are described. To cope with these challenges the model-based development methodology is presented as a solution approach. In particular, the advantages and possible applications that arise from the use of online-capable, physically-interpretable models in the different development phases are treated in more detail. In conclusion, the objectives and the scientific contributions of this work are formulated, and the thesis outline is presented in this first chapter.

On December 12, 2015, the so-called *Paris Agreement* was adopted at the *International Climate Conference* COP 21 in Paris, in the course of which 197 countries have committed themselves to transform the global economy in a climate-friendly way by reducing human made greenhouse gases[1] in order to limit global warming to below two degrees Celsius and, if possible, to below 1.5 degrees Celsius above pre-industrial levels. As consequence, the European Union and its member countries have ratified concrete national emission targets and measures to meet the *Paris Agreement*.

The implementation of the Paris Agreement in Germany will lead to massive technological and economic transformations in all energy sectors, from the energy industry, manufacturing industry, transport, buildings as well as in agriculture and waste management. In October 2019, the German Federal Government introduced the *Klimaschutzprogramm 2030* (engl.: Climate Protection Program 2030) with the main target to reduce the greenhouse gas emissions in all energy sectors by 55 % compared to 1990, see Fig. 1.1. In 2020, the national CO_2 emission reduction target of 40 percent lower than 1990 emissions was barely reached. While the CO_2 emissions of the sectors energy, industry, building, and agriculture have been steadily declining at about 10 to 15 % per decade, emissions levels in the transportation sector, responsible for about 17 to 20 % of total emissions, have remained nearly constant; although the specific fuel consumption of combustion engines has been significantly reduced through efficiency improvements over the past 30 years, see Fig. 1.2. In the case of passenger cars, efficiency gains were compensated by an increase in vehicle mass and engine output, while heavy trucks registered an efficiency increase of around 33 %.

[1] Primary (anthropogenic) greenhouse gases with the *Greenhouse Warming Potential* (GWP): Carbon dioxide (CO_2) with GWP$=1$, Methane (CH_4) with GWP≈ 30, and Nitrous oxide (N_2O) with GWP≈ 265

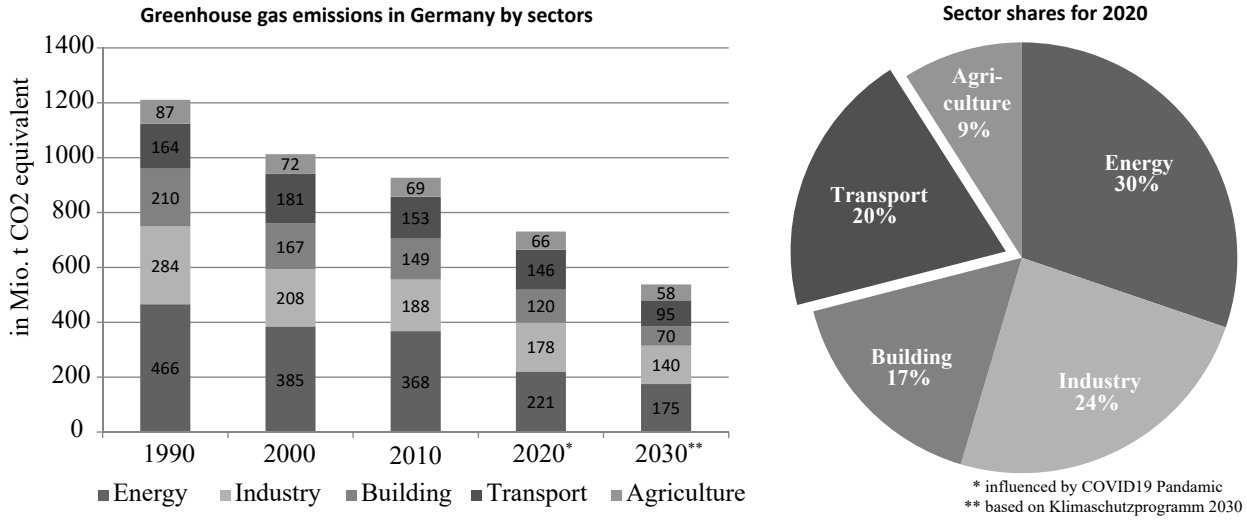

Figure 1.1: Total greenhouse gas emissions in Germany from 1990 to 2020 and target values for 2030 (Source: BMVI, Umweltbundesamt March 2021)

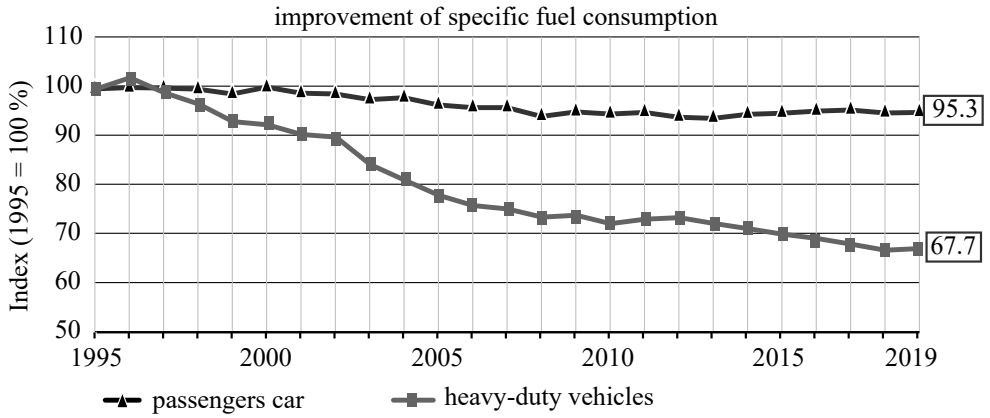

Figure 1.2: Development of specific fuel consumption of cars and trucks in Germany over the last 25 years relative to 1995

In the transportation sector, carbon dioxide (CO_2) is the primary greenhouse gas, which is released during the combustion of fossil fuels such as gasoline and diesel. By projecting the trend of the last few years, a significant reduction of the transportation volume is rather unlikely, see Fig. 1.3. Since the level of transport and mobility will likely further increase, the targets of the German Climate Protection Programm 2030 can only be achieved through *Decarbonization* or *Defossilization*. Behind these terms lie two targets that are being pursued worldwide. In the context of transportation, decarbonization aims to develop a CO_2-emission-free propulsion technology, while defossilization aims to develop non-fossil CO_2-neutral fuels, which can be produced with low cost on an industrial scale. For a realistic comparison of both solutions approaches, the total CO_2 balance from the extraction and provision of the propulsion energy to the conversion into kinetic energy (*Well-to-wheel*) must be taken into account. The energy efficiency of all sub-processes plays a role, as do the economic aspects, such as the installation of the necessary supply infrastructure.

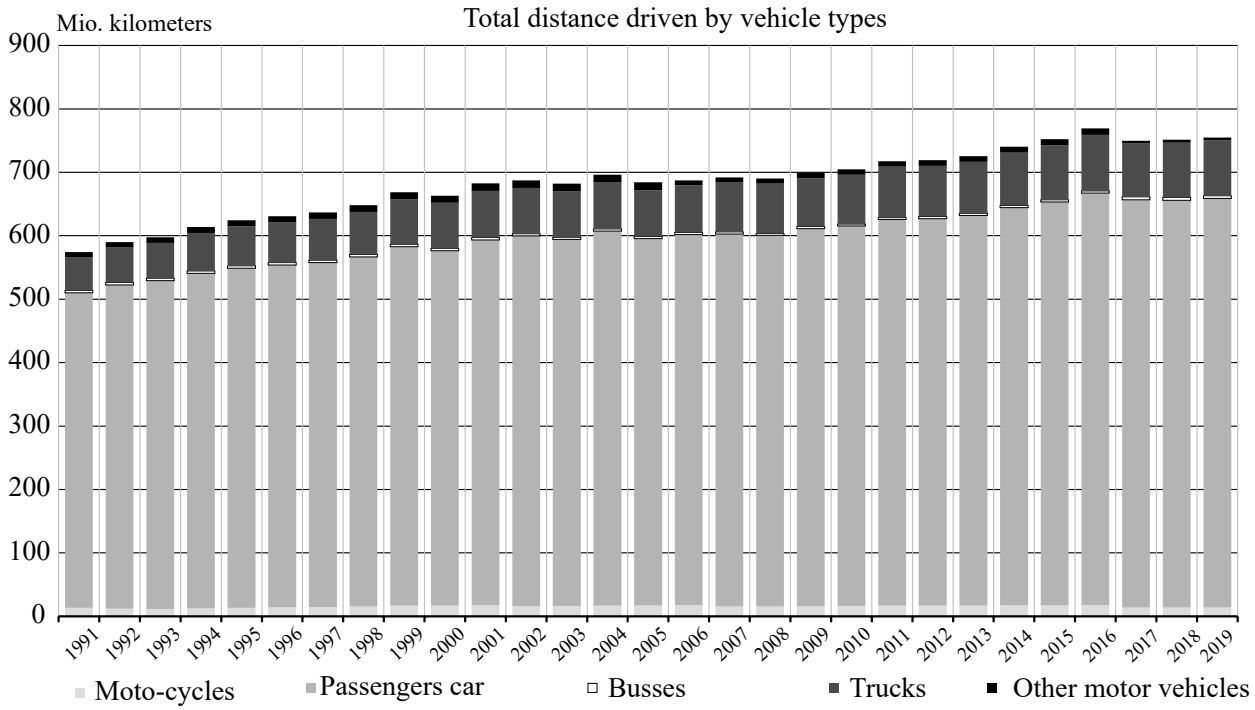

Figure 1.3: Total kilometers driven by different vehicle types in Germany (Source: German Federal Ministry of Transport and Digital Infrastructure (BMVI))

Decarbonization through electrification of the powertrain

Through electrification of the powertrain a reduction or even an avoidance of CO_2 emissions can be achieved. For *battery electric vehicles* (BEV), the combustion engine is replaced by an electric motor supplied with electrical energy from an onboard Lithium-ion battery pack. Compared with liquid fuels, vehicle batteries have a significantly lower gravimetric energy density, see Fig.1.4. A trade-off between the driving range and the vehicle mass and size of BEVs must be found. Consequently, with current battery technology the range of BEVs is usually limited to a maximum of 300 to 500 kilometers. *Hybrid electric vehicles* (HEV)[2] combine the benefits of both propulsion systems, however, require greater effort and higher costs for the development and coordination of both propulsion technologies and energy management. The electric drive systems allow driving in urban traffic without CO_2 emissions, while the combustion engine acts as range extender for longer distances on country roads or highways. In addition, the electric motor in generator mode can be used to charge the battery by using the braking energy. Alternatively, fuel cells powered by hydrogen can be used as range extender. In *fuel cell electric vehicles* (FCEV), the electrical energy for the electric motor is obtained by the oxidation of hydrogen in the fuel cell. The vehicle battery serves then only as a buffer storage and can therefore be dimensioned much smaller.

BEVs and FCEVs do not produce any local CO_2 or other pollutant emissions during operation. To improve the air in urban and metropolitan areas, most industrialized countries are subsidizing the transition to electric vehicles through purchase incentives and tax breaks. However, to achieve an

[2] including *Plug-in hybrid vehicles* (PHEV) whose batteries can be charged via a plug

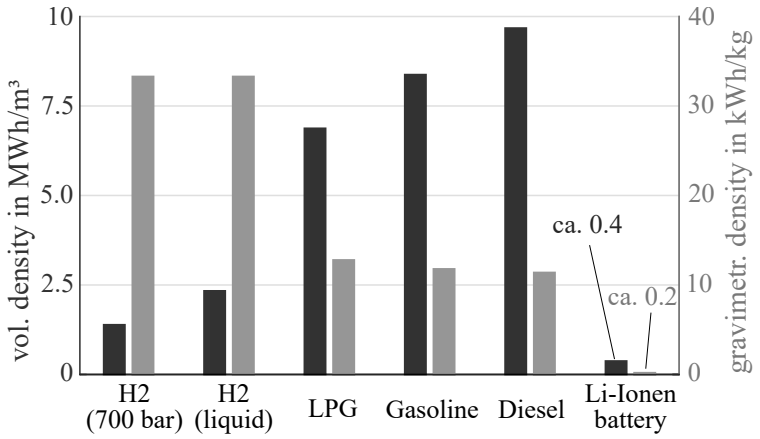

Figure 1.4: Comparison of energy densities of different energy source

actual CO2 reduction compared to conventional powertrain with combustion engines, the electrical energy for charging the vehicle battery, as well as for the production of hydrogen, must be provided from renewable energy sources, such as energy from wind, solar or hydro power, see Fig. 1.5. Wind and solar plants are not suitable for covering the base load of energy supply due to their volatility. Unfortunately, no scalable technological solution exists for storing large amounts of electrical energy. In order to realize load balancing with renewable energy sources, the share of renewable energies would have to be massively increased. In addition, a Europe-wide energy grid with intelligent, cross-border load control would be required. Pumped-storage hydroelectric (PSH) power plants can be used as buffer storages. In case of an excess of renewable energy, electric energy is stored in form of gravitational potential energy using electric pumps. In case of wind and sun lows, the potential energy is transformed back into electric energy using turbines. However, their capacity is rather limited. Further, an excess of renewable energy can be exploited for producing hydrogen (HGHH-Project 2022).

Compared to vehicle batteries, hydrogen has a much higher energy density, giving FCEVs similar ranges as vehicles with internal combustion engines, see Fig. 1.4. In both cases, only if the electrical energy for charging or hydrogen production comes from renewable sources, it is reasonable to classify BEV and FCEV as *zero-emission vehicles*, not including their manufacturing.

Since the generation of hydrogen by electrolysis is an additional process step with an energy efficiency of about 60 to 70 % (Töpler and Lehmann 2017), more renewable energy must be used compared to the direct charging of BEVs. Currently, in most industrialized and energy-dependent countries, both electrical energy and hydrogen are generated from fossil energy source or nuclear power plants. Electric power is often generated to a significant extent from coal and gas power plants. Hydrogen is currently mostly used in industrial applications, where it is almost exclusively produced from natural gas.[3] A transformation of the energy industry to renewables is the basis for the success of both, BEVs and FCEVs.

[3] over 90 % of hydrogen is produced from fossil fuels. Only 4 % is obtained from electricity via electrolysis Töpler and Lehmann (2017)

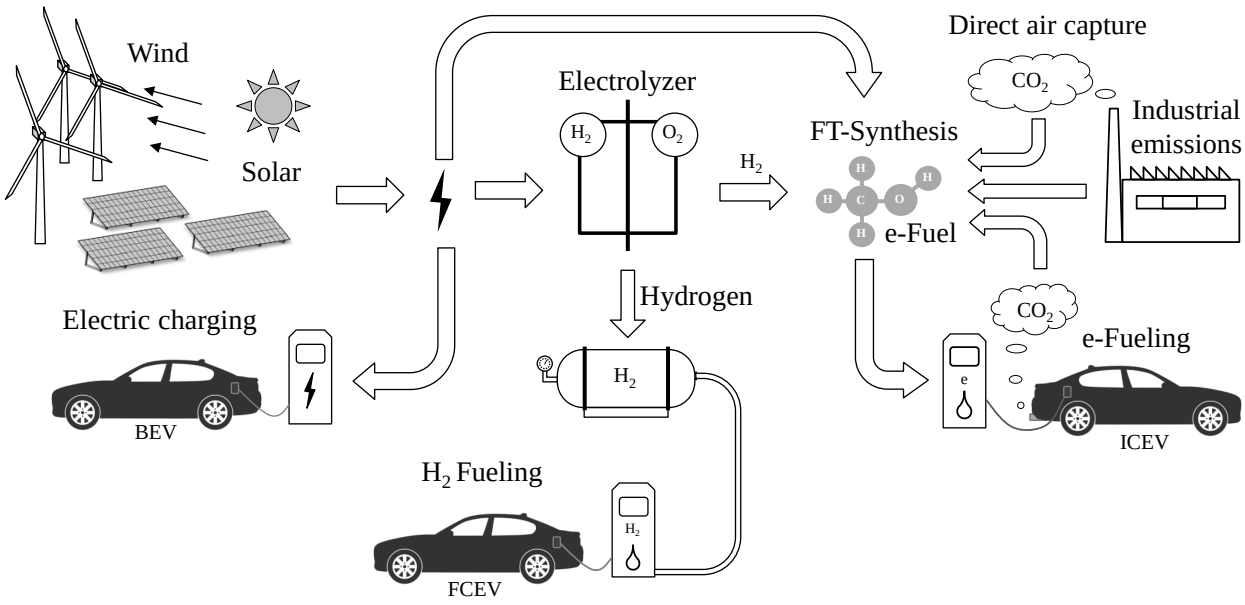

Figure 1.5: Illustration of the decarbonization and defossilization of transportation sector

In addition, the infrastructure for battery charging is not yet in place and will most likely have to be built up over a period of years. For concerning fuel cell vehicles (FCEV) as an alternative, a sufficiently dense network of hydrogen filling stations would be necessary. But due to its physical properties, transport and storage of hydrogen [4] is accompanied with additional energy losses that reduces the well-to-wheel balance of FCEVs. Furthermore, existing fuel station grid cannot be used for hydrogen fueling without additional modification. The success of electric vehicles therefore depends to a large extent on the development of the share of renewable energy and on the build-up of charging and hydrogen filling station infrastructure.

Defossilization through synthetic fuels

Defossilization aims to substitute fossil fuels as an energy source by *synthetic* or *alternative fuels*. Since synthetic fuels are chemical energy carrier, they are differentiated in terms of chemical composition and the source of the energy stored. Due to their advantageous chemical and physical properties, such as high energy density and low boiling temperature (transportability), hydrocarbons (C_nH_m) have proven to be a viable energy carrier in many application areas in the energy and transport sector, compare to Fig. 1.4. Due to their chemical proximity to fossil fuels, they are also suitable for blending with gasoline and diesel, which allows a smooth phase-out of fossil fuels, (Maus 2019). Investigations haven proven the suitability of using synthetic fuels (as blends or pure) in series production engines, see i.e. Münz et al. (2016) and Steinhaus et al. (2021).[5] Consequently, the existing propulsion technology and the infrastructure worldwide can continue to be used. The

[4] High Density Polyethylene (HDPE) pressure tanks are used for storage and transport, in which the hydrogen is compressed to 700 bar, representing the best trade-off between volumetric and gravimetric storage density (Töpler and Lehmann 2017)

[5] Besides, reduction in pollutant emissions and efficiency increases were obtained

production requires the chemical components, carbon and hydrogen, as well as renewable energy for generation. If the hydrocarbons are obtained from biomass, they are referred to as *regenerative fuels* or *biofuels*; if they are obtained with electrolysis and the admixture of carbon, they are referred to as *e-fuels*.

Biofuels, such as bioethanol and biodiesel, have been added to conventional fuels for many decades. In many countries and regions, there are different mandatory standards that regulate the proportion of biofuels in gasoline and diesel.[6] An increasing addition of biofuel or even a complete substitution by biofuels is generally considered to be very controversial due to many aspects, although biofuels have a significantly better carbon footprint than fossil fuels. A major issue against an increased use of biofuels is the competing use of land both for growing food to feed the world's population and for conserving natural carbon sinks such as rainforests and moorlands. For agricultural vehicles and tractors, the use of biofuels, which can be produced locally on agricultural premises, is seen advantageous from an economic and sustainability point of view.

A more sustainable alternative are *e-fuels*, obtained from renewable electric energy sources in so-called *Power-to-Liquid* (PtL) plants. E-fuels are long-chain hydrocarbons, such as e-methanol or OME with similar properties as fossil fuels, obtained from H_2 and CO_2 via Fischer-Tropsch synthesis (short: FT synthesis). The hydrogen is produced from renewable energy sources via electrolysis. Carbon dioxide can be obtained from three sources, either *direct air capture* (DAC), from combustion emissions of renewable/fossil fuels, or from the exhaust gases of industrial plants, such as cement factories, where process-related unavoidable CO2 emissions are generated. DAC is the most attractive option from an ecological point of view, as it is closest to the natural carbon cycle. However, from an economic point of view, DAC is the most inefficient option, since the atmospheric CO_2 must be concentrated from a maximum dilution at high energetic cost (Maus 2019). With the other two options, CO_2 can be extracted in much higher concentrations by capturing emissions at specific points (tailpipe or smokestack), stored and reused to produce e-fuels. [7] In this way, a circular economy for CO_2 can be implemented. Similarly, the success of e-fuels rises and falls with the availability of renewable energy. Since in most industrial countries, the share of renewable energies is not sufficiently high due to an overall high energy demand of all sectors, leading car manufacturers are investing in Power-to-Fuel plants in suitable regions (rich in wind or sun) to enable future automobiles running on internal combustion engines supplied by e-fuels, e.g. Power-to-Liquid project in Chile (Kluesener et al. 2022).

Considering the well-to-wheel energy efficiency, the advantages are on the side of the electrification of the drive (70% efficiency compared to 15% for e-fuels). However, when considering energy density, storage capability, transportability, and the cost of building an infrastructure, the advantages are on the side of e-fuels.

Most experts agree that *all these drive concepts* will be used in the next decade (drive technology mix) depending on the application area. Consequently, the existing development effort must be

[6] in Germany: B7 diesel with 7% biodiesel and E5/E10 Gasoline with 5/10% bioethanol

[7] Industrial processes generally denoted as carbon capture and utilization (CCU) or carbon capture and recycling (CCR)

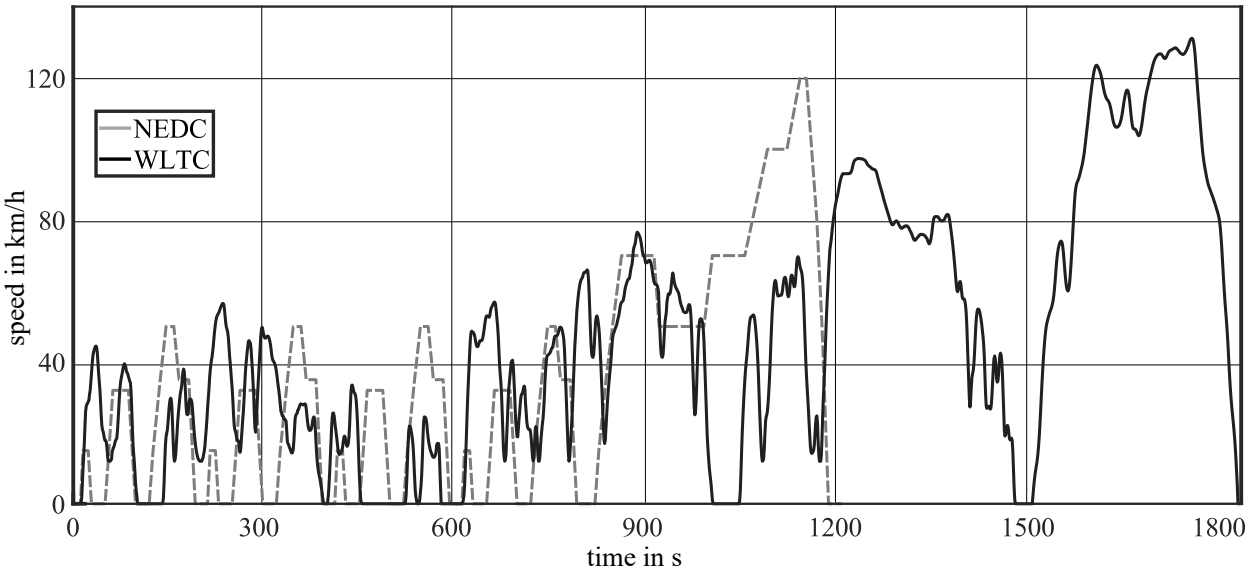

Figure 1.6: Comparison of the vehicle speed profiles of NEDC (EURO 1-6) and WLTC (WLTP) tests

shared. Nevertheless, the development tasks are becoming more and more complex and challenging due to increasing demands on the drive systems. Existing development methods must be further improved and simplified.

1.1 Current technological problems and challenges

Due to the discrepancy between the legally permitted pollutant vehicle emissions for test cycles and the emissions actually occurring in road traffic, vehicles powered by internal combustion engines and the test procedure for vehicle approval are the subject of social discourse.

Emission standards for vehicle approval

In September 2017 the EU introduced a new emissions legislation EURO 6c/6d-Temp for vehicle approval within the EURO 6 emissions standard, which has been in force since 2014. The EURO 6c emission standard introduced the *Worldwide harmonized Light vehicles test procedure* (WLTP) for determining exhaust emissions and fuel consumption of passenger cars and light commercial vehicles as a replacement for the until then effective *New European Driving Cycle* (NEDC). The introduction of the WLTP aims to ensure worldwide standardized and a more realistic consumption and emission values on the test bench. Within WLTP the *Worldwide harmonized Light Duty Test Cycle* (WLTC) is performed on a chassis dynamometer. Compared to the former NEDC - which is rather a synthetic driving cycle - the WLTC represents a more realistic driving cycle leading to a more dynamic speed and load profile during the driving test, compare Fig. 1.6.

With the introduction of EURO 6d-Temp the passing of the WLTC serves only as first step of the type approval. The car manufacturers are further obliged to ensure the compliance of EURO 6

emission limits under real driving conditions by performing additional driving tests on the road. The so-called *Real Driving Emissions* (RDE) are measured on the road using *portable emission measurement systems* (PEMS), which are connected to the exhaust pipe of the vehicle. The real driving emissions must not deviate too far from the emission limits of the laboratory test on the chassis dynamometer. The tolerated deviation from laboratory emission limits are defined by a conformity factor (CF), which takes the measurement tolerance of the PEMS in RDE tests into account. The conformity factor is reviewed annually and updated if necessary. Since 2020, the EURO 6d emission standard has been in force according to which the real driving emissions may only be increased by conformity factor of 1.43.

Increasing requirements and system complexity

The implementation of RDE leads to *increasing requirements* for the electronic engine control management. Compared to NEDC and WLTC, the emission-related ECU calibration must be performed for a significantly *larger engine operating range*, which increases the calibration effort enormously, see Fig. 1.7 a).

In order to meet RDE requirements both engine-related measures (ERM) and exhaust gas aftertreatment (EGT) has to be taken into account for optimization of fuel consumption and reduction of pollutant emissions. The optimal and coordinated *combination of ERM and EGT* is mandatory to fulfill the requirements under all possible driving situations and environmental conditions.

Future more stringent emission legislations require alternative powertrain concepts to be developed. For example, different configurations of exhaust gas aftertreatment systems (EGT), electrification of the powertrain train or the use of CO2-neutral, synthetic fuels in combustion engines must be developed and investigated under RDE aspects. This means that in addition to external real-world influences, such as environment conditions, traffic, etc., the variation and complexity of the powertrain configurations is also increasing, see Fig. 1.7 b).

Generally, most technical measures are often accompanied by introduction of additional variability that leads consequently to increasing complexity of ECU calibration process. Furthermore, all measures allow only a trade-off between emission and fuel consumption reduction, which has to be found by an engine operation point dependent optimization of all control variables. The task of optimizing is extremely complicated due to the complex nonlinear engine behavior, the different technological disciplines and many dependencies between the control variables. Therefore, more effective development methodologies are required to address these increasing requirements and system complexity of the vehicle under test.

Paradigm change in the development process

The introduction of RDE has led to a paradigm change in the engine development process – from driving cycle-based to maneuver-based development (Maschmeyer, Kluin, et al. 2015). In the past, the engine development process was focused on passing a predefined test cycle, which could be

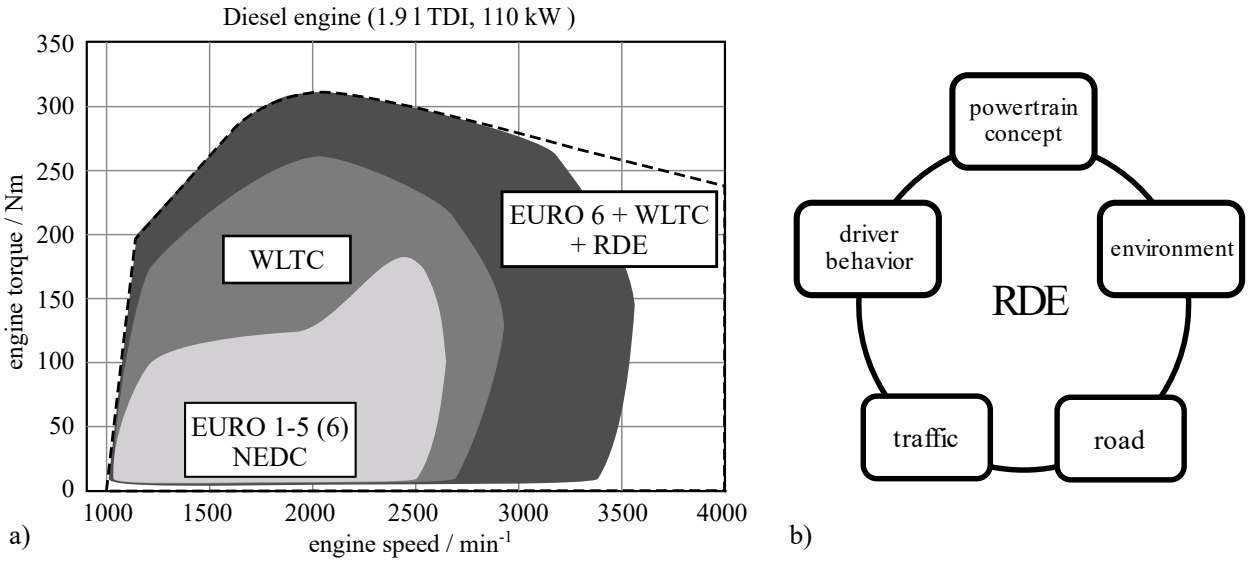

Figure 1.7: a) Comparison of the engine operating ranges of NEDC, WLTC and RDE (in accordance to T. Huber et al. (2014)) b) Illustration of the challenges of *Real Driving Emission* (RDE)

tested in an early development stage under laboratory conditions. Considering *RDE* a defined comparison basis for the development is omitted. The real driving tests and their analysis can only be *conducted in a prototype vehicle* under unknown and random test conditions for the first time. At this *late stage of development*, any real world problems that arise can only be resolved with great effort and costs. However, an evaluation of real driving emissions would be desirable in the early stage of the development process.

The *model-based development* has proven to be a reasonable development methodology for managing the increasing complexity of the engine control design and calibration, see e.g. Isermann (2014). To cope with the vast amount of possible test scenarios and powertrain configurations, a *virtual development environment* including simulation models of system components and considering any *real world influences* (driver behavior, traffic scenarios, weather, etc.) must be introduced in the powertrain development process (Maschmeyer, Beidl, et al. 2016). To address the RDE requirements, the existing model-based engine development process must be *extended by simulation models* of the external real world components, e.g. models of vehicle, driver, road and traffic. Additionally, environmental influences like the ambient temperature, pressure and humidity must be included as variables into the existing engine models.

1.2 Model-based engine control development and applications

The main objective of the model-based development methodology is to gain knowledge in order to be able making important design decision about the product specifications in the early development phase (*frontloading*). This helps to avoid high costs and effort caused by design errors in the early development phase and improves the efficiency in the overall development process.

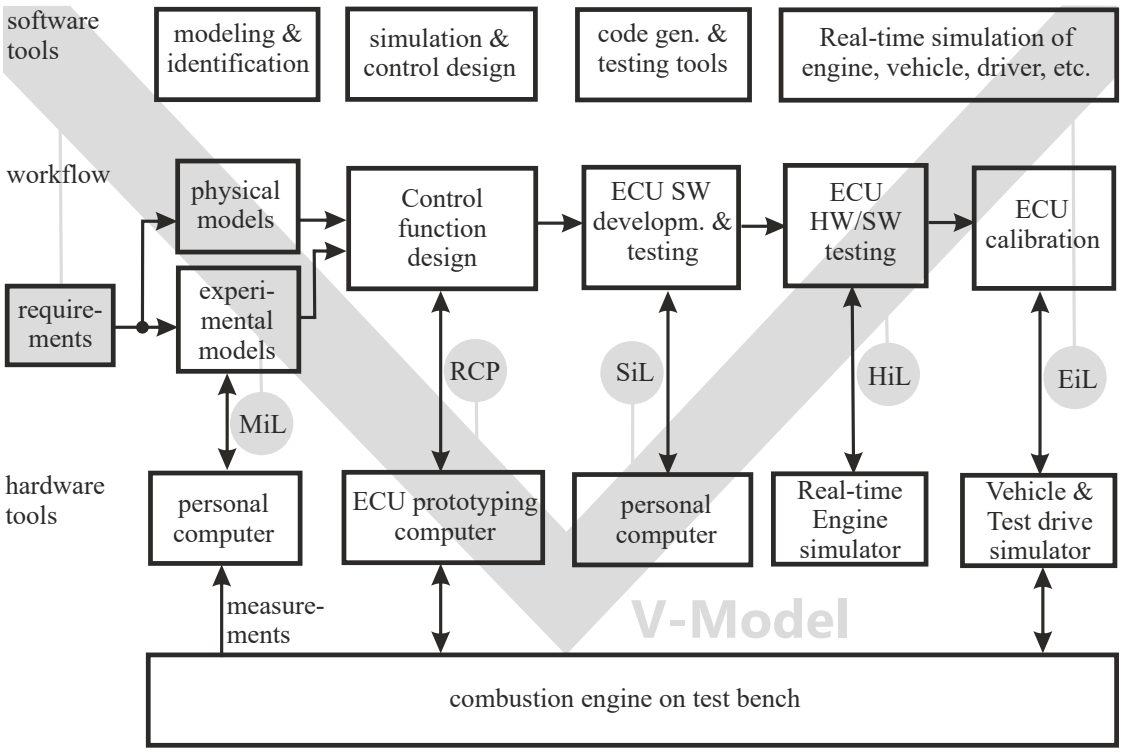

Figure 1.8: Workflow of model-based engine control function development with regard to RDE requirements; based on Isermann (2014)

The main task is to derive adequate simulation models of the system to be developed. This involves the derivation of a mathematical description of the properties and behavior of the considered technical system as well as its model parameters through the alignment to measurements, which is referred to *system identification* or *parameter identification*. Modeling involves also investigating the properties of the considered system in detail and acquiring knowledge of how the system works and behaves. From the perspective of the design and calibration engineers, gaining of knowledge through system modeling is very important but often an underestimated aspect in the development process.

Fig. 1.8 shows the workflow of a model-based ECU development process including the tasks, the use of software and hardware tools as well as the application of development and testing techniques at particular development stages.

1.2.1 Model-based development methodology

In the development and testing of mechatronic systems, the use of so-called *X-in-the-loop* techniques in combination with *Rapid Control Prototyping* (RCP) has been established. The *X* stands for a system component to be developed or tested, e.g. device or software code under test, which is embedded in a virtual simulation environment (in the loop). The virtual simulation environment contains behavioral models of the environment as well as realistic models of the interfaces to the system components. By embedding the system component to be tested in a simulation environment,

it can be designed and tested under repeatable and comparable conditions. It is further differentiated between open-loop and closed-loop applications. Open-loop means no interaction or feedback between the device under test and the simulation environment, while closed-loop applications aim to integrate the device under test within realistic environment leading to higher requirements for signal integrity and real-time capability of the simulation environment.

Depending on the object under test, it is differed between *Model-* (MiL), *Software-* (SiL) and *Hardware-in-the-loop* (HiL). MiL represents testing of simulation models and SiL the testing of production software of an ECU. In general, the testing of a real electronic control unit (ECU) within a simulated environment is referred to as HiL, see Fig. 1.8. Since an ECU excepts input and output signals during runtime in so-called *real-time*, the application of the HiL method requires ECUs to be embedded on signal-level in a *real-time simulation* environment. On the contrary, MiL and SiL application underlie no time-related requirements. Both can be carried out in real-time or ideally faster by development or testing engineers on dedicated simulation hardware, which can be an ordinary desktop PC.

For Rapid Control Prototyping, control functions can be developed and tested on high performance prototype hardware within a real-time environment at the engine test bench or even during test drives. The technical limitations of the ECU target hardware can be left aside and the focus can be put on control function development.

Hardware-in-the-Loop applications become more and more important due to the increasing ECU calibration and validation effort accompanied with the introduction of mandatory RDE tests. Engine and vehicle measurements can be carried out separately at the engine test bench or on the road and simulated afterwards at the HiL test bench to develop and validate the ECU functions. The parameters of the HiL simulation models can be varied as required in order to cover a wide range of test and fault cases at low cost. Besides cost reductions the ECU function can be developed and tested on the target hardware under real-time conditions within a *safe environment*, where critical test scenarios do not have any negative consequences for the test engineers or the test hardware.

The boundary between real components and simulated environment can be shifted if further system components are the focus of development and testing. In the context of engine development, methods such as *Engine-in-the-Loop* (EiL) and *Vehicle-in-the-Loop* (ViL) have been established. EiL test benches equipped with a prototype engine allow engine development and testing embedded in a virtual driving test environment involving the simulation of the traffic, the driver, the vehicle and the ambient conditions (e.g. inside an altitude and climate chamber).

With regard to RDE requirements, for the model-based engine development exist a high demand for *fast calculating or even real-time capable combustion and emission models* which enable *predicting* real driving emissions of various test drive scenarios and can be applied in the early stages of the development process as well as for the ECU development and calibration.

1.2.2 Model development and application

A model describes a reduced representation of the properties of a system on in terms of mathematical equations. The model equations are either theoretically derived with the use of physical laws or empirically expressed by general mathematical functions that approximate the behavior of the system. In addition to the derivation of model equations, modeling also requires the determination of unknown model parameters, which is also referred to as *model identification*. Unknown model parameters can either have physical meaning and thus be derived from the system properties or be free tuning parameters that must be determined in order to ensure that the model behavior approximates the real system behavior as closely as possible. The availability of information about the system to be modeled and measurement data also determine the choice of model used.

The simulation models used in the different stages of the development are usually purpose-oriented and reproduce only certain properties. In general, simulation models differ in their level of detail and their computational effort depending on their target application and the computation device (target hardware).

In the early stage of the development, detailed physical simulation models are used for the investigation of design studies or for the proof of concepts. Physical models contain the functional description $\mathbf{y} = f(\mathbf{x}, \mathbf{u}, \boldsymbol{\theta})$ between the physical input variables $\mathbf{u}$, the output variables $\mathbf{y}$ and state variables $\mathbf{x}$. The state variables are described based on basic physical equations including not exactly or partially known physical parameters $\boldsymbol{\theta}$. However, existing dependencies of the physical parameters on construction data or on the operation point variables $\mathbf{z}$ must be known. To adapt the physical model to the actual system behavior, an unknown functional description for these physical parameters (parameter models $\boldsymbol{\theta} = g(\mathbf{z}, \mathbf{w}, ...)$) using additional parameters $\mathbf{w}$ (weight factors) must be found and determined based on measurements. The structure and equations of the resulting physical model is often very complex and non-linearly coupled, so that solving a nonlinear optimization problem is required for the identification of the overall model.

Due to the significant increase in computational power over the past decades, powerful simulation tools as *Computational Fluid Dynamics* (CFD) simulation software have made their way into the engine development process. These models are based on first principle equations (white-box models) and aim to predict the gas flows, combustion process as well as the pollutant emissions on the basis of constructive design parameters only. Due to their high model complexity, along with high computational effort, detailed physical simulation models usually run only on personal or high performance computers in offices. Such detailed models are not suitable for real-time application or to be integrated in other development tasks, e.g. in the ECU development and calibration or in the simulation of RDE tests.

In recent decades, computing power and functional amount of electronic control units have increased, while the costs have decreased. This has enabled simulation models running on control units and allowing more complex model-based controller to be executed on the target hardware. However, this has led also to greater effort in the design and calibration of the controllers and an increasing demand for fast calculating or real-time capable simulation models that can be generated

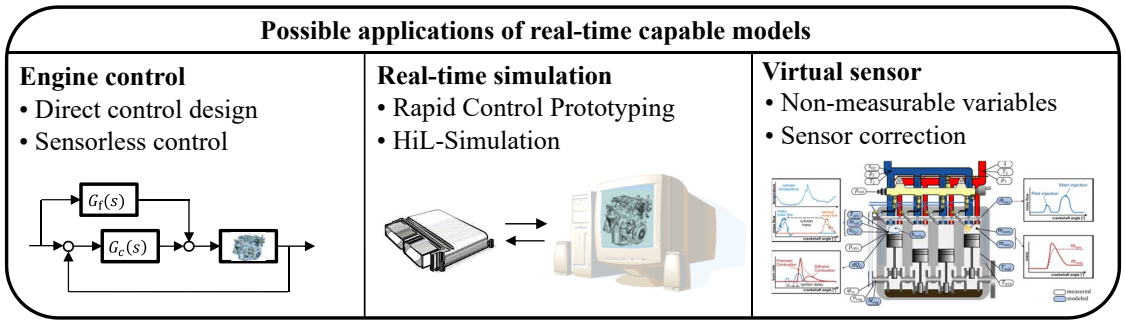

Figure 1.9: Possible application areas of real-time models

automatically. To further accelerate the development process, simulation models are used in all development tasks and stages. To meet this demand, *experimental* or *data-driven modeling methods* have been introduced into the model-based development process.

Generally, in *experimental* or *data-based modeling*, the input-output relationship is approximated using generalized mathematical description (*black-box models*) such as *lookup*-tables, polynomials, neural networks (NN), radial basis function (RBF), etc. Such methods are also referred to in connection with machine learning and artificial intelligence. The model generation is therefore carried out automated by using specially adapted parameter optimization and structure search algorithms, which are denoted as *model identification*, see Isermann and Münchhof (2011). Commercial modeling tools provide support in generating such models, e.g. by MathWorks or ETAS ASCMO. However, black-box models are only able to reproduce the measured input-output behavior. Thus, they generally *lack on extrapolation capability*. Data-based models cannot be generally transferred to other systems; therefore they are not suitable for investigating different system configurations and variants in development studies. The generalized model structure and parameters offer *little insight* into the underlying physical behavior. Moreover, the model accuracy depends very much on the quality of the available measurement data and its coverage of system's operation range (design of experiments).

The usability of *real-time capable models* offers additional fields of application, especially in case of real-time capable models, for the model-based development process. Fig. 1.9 shows an overview of the possible online application of real-time models. The range of applications varies from previously mentioned vehicle simulations in real driving situations at the EiL-test bench to virtual sensors of non-measurable information for process analysis, up to model-based control, in which real-time models are used for optimal control.

When designing ECU functions, real-time models are applied in two ways (Fig. 1.9, left). Firstly, they can be used as part of a control algorithm, e.g. model predictive control (MPC) or internal model control (IMC). In such cases, the models allow the prediction of the dynamic behavior. Secondly, real-time models are used to calculate non-measurable variables online and allow feedback control (sensorless control). In this way, expensive or difficult-to-implement sensors can be omitted without compromising control quality.

Besides in online applications, fast calculating models can also be used to accelerate offline simulation studies (SiL/MiL), e.g. to predict fuel consumption and emissions for different RDE test scenarios in significantly less time.

Real-time capable models can be used to determine *non-measurable variables* (*virtual sensors*) giving application engineers additional information and a better insight into system's behavior at the test bench. Wherever measuring technology reaches its limits, model-based estimation techniques can be applied for correcting sensor deficiencies such as noise, time delay, etc. Examples for combustion engines are the calculation of unmeasured mass flows through throttle and valves, or the correction of dynamically delayed exhaust gas temperatures and emissions at certain locations in the air path system of combustion engines.

The main advantage of physical modeling is its *physical interpretability* and *transferability* to other systems. In contrast, experimental modeling allows the approximation of any arbitrary system behavior by using automated identification methods, which are not suitable for online applications. Considering the features of both physical and experimental modeling, a gap reveals between these modeling methods. *Semi-physical modeling* approach (grey-box modeling) fills this gap and offers a compromise between *physical interpretability* and *model complexity*. By combining basic physical equations including physically interpretable parameters with experimental models for the more complex system behavior, the advantages of both modeling methods can be exploited and the disadvantages overcome. In semi-physical modeling, physical equations are assumed as given and only the functional descriptions for the physical model parameters are identified using experimental modeling. This leads to a lean overall model and a less sophisticated model identification problem, which qualifies semi-physical models for online application.

1.3 Objectives and scientific contribution

The objective of this work is to develop a systematic and efficient modeling methodology for generating *physically oriented real-time models* with good model accuracy and at an adequate level of effort. To achieve this goal, the principle of semi-physical modeling shall be used as well as online-capable methods for model identification. The modeling methodology is demonstrated using the example of a common-rail diesel engine with *dual exhaust gas recirculation* (EGR) and *exhaust gas turbocharger* with variable turbine geometry (VGT). Fig. 1.10 shows the structure as well as the inputs and outputs of such diesel engine by means of its signal flow scheme. The methodology is applied to all subsystems of the engine. The tools used to create this work are listed in Appx. A.4.

To this end, the greatest challenge in engine modeling has been the generation of accurate real-time combustion and emission models. There is no simple modeling approach which is able to describe sufficiently accurate the complex physical (transport phenomena) and chemical processes (reaction kinetics) involved in engine combustion. Due to the cyclic and engine speed dependent operation mode of combustion engines and the fact that the processes of injection, mixture formation, ignition, combustion and emission formation take place only within relatively short time scales,

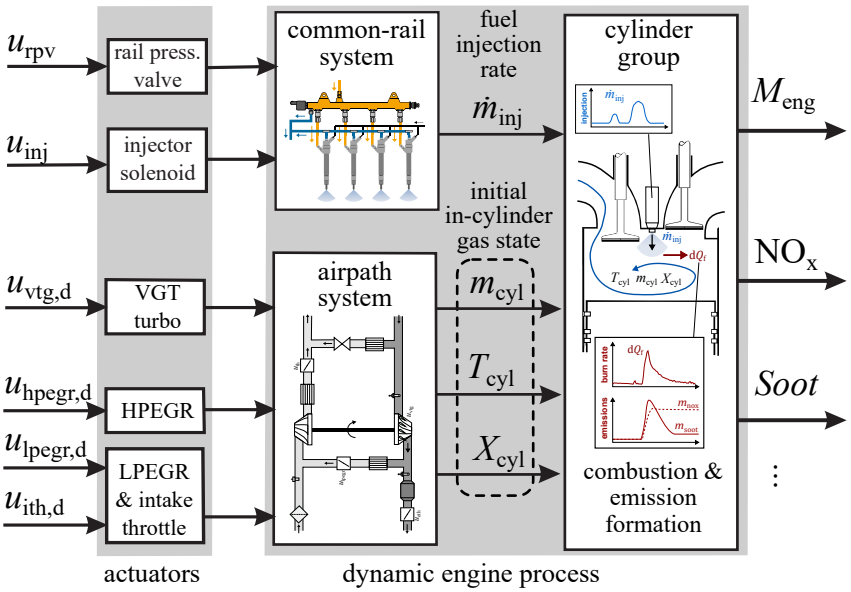

Figure 1.10: Signal flow scheme of a diesel engine with a common-rail injection system and an air path system including high pressure (HP-EGR) and low pressure exhaust gas recirculation (LP-EGR) and an exhaust gas turbocharger with variable turbine geometry

further complicates the modeling. For example, the rotation by one degree of crankshaft angle corresponds to $\approx 55\mu$s at an engine speed of about 3000 1/min. Thus, the calculation step size must be sufficiently small to model these processes in sufficient detail. At least a crankshaft angle resolution of 1° is required for modeling heat release during combustion.[8] Since the requirement of real-time capability is already very challenging with regard to the technical implementation, the computational effort and complexity of both model calculations and identification has to be kept as low as possible.

From the perspective of model identification, there are usually *no further in-cylinder measurements*, apart from the *in-cylinder gas pressure* and the *crankshaft angle position*, available at engine test bench, see Fig. 1.11. To enable model identification based on this information, *additional variables* must first be reconstructed by using physics-based models in combination with state estimation techniques. The application of online state and parameter estimation methods in the calculation of cycle-resolved combustion chamber processes represents an additional scientific contribution of this work.

The modeling methodology to be developed is to be elaborated and tested on an engine test bench. For the development of real-time models and prove of their real-time capability, the *engine test bench* is equipped with prototyping real-time hardware and development environment (RCP). For further details regarding the test engine and the overall test bench setup see Fig. A.1 in Appx. A.1.

In the context of HiL testing of ECUs, semi-physical real-time models can be used for *real-time simulation* of the engine and other subsystems (driver, driving maneuver, environmental, and powertrain simulation).

[8] Crank-angle resolved emission modeling requires a higher crank-angle resolution $<< 1°$

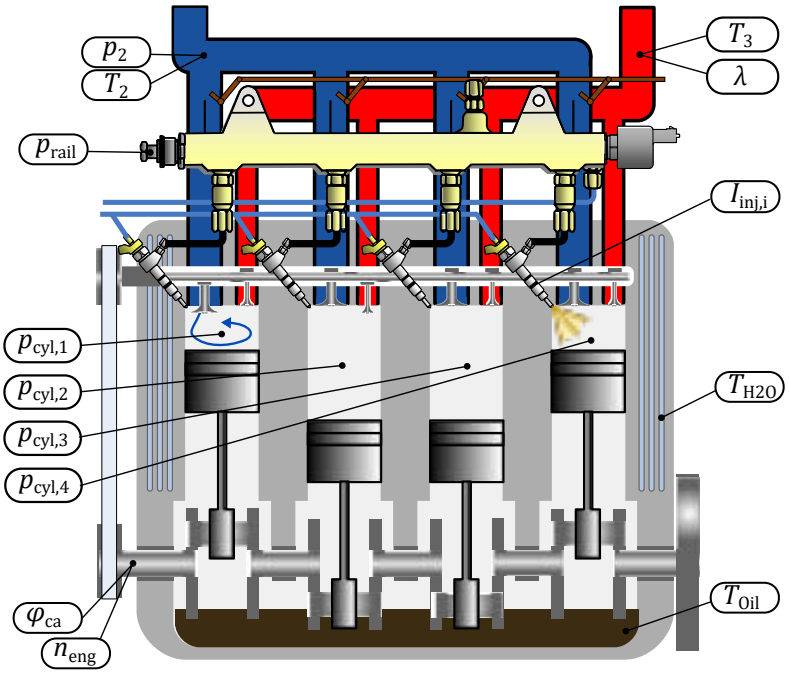

Figure 1.11: Cylinder group of the test engine (four cylinder common-rail diesel engine) with series sensors and additional in-cylinder pressure sensors

Furthermore, real-time models are also applicable in the design and adaptation of ECU functions. They can be *integrated into control functions* of a feedforward control to impose a certain dynamic behavior to a system or to serve as *virtual sensors* for the online determination of unmeasured system states. An example of an application, which is also treated in this work, is the *model-based combustion analysis* which serves as an extension to conventional pressure indication systems.

1.4 Thesis outline

After this introduction, the theoretical foundations of this thesis are briefly described in Ch. 2. The two types of modeling approaches, theoretical and experimental, are discussed, as well as some fundamental methods for model identification. Here, the focus is on online-capable identification methods. In this context, methods for combined state and parameter estimation using the Kalman filter are described. Based on these fundamentals, Sect. 2.4 concludes by proposing the semi-physical modeling approach with the incorporation of state and parameter estimation. The methodology presented in 2.4 is a main ingredient of this thesis.

The subsequent chapters 3 and 4 treat the application of the semi-physical modeling methodology to the two major subsystems of internal combustion engines, the air system and the cylinder group. In chapter 5 practical applications at the test bench are treated. On the one hand, this is the use of model-based state and parameter estimators to generate additional information about system variables that are not measurable or difficult to measure, and on the other hand, the use of real-time capable models in the context of hardware-in-the-loop simulation for efficient testing of ECUs.

2 Engine modeling and online-identification

The following chapter deals with the fundamentals of modeling and identification for online applications. Considered methods are discussed in the context of internal combustion engine modeling. First, the two main modeling approaches, theoretical and experimental modeling, are presented. Since modeling requires also the identification of model structure and parameters, methods for system identification are introduced. In this context, state and parameter estimation methods are presented using the system model to be identified in order to simplify and improve the identification process and to enable the estimation of unmeasurable system state variables. Subsequently, the *semi-physical modeling approach* is proposed which allows the derivation of lean, physically interpretable models meeting the requirements of real-time capability. The use of state and parameter estimation methods enable the generation of semi-physical models in online applications.

The desire to make certain prediction about the behavior of a system in the future based on system-immanent properties and observable data can be found in all situations of our life. Whether it is about tomorrow's weather, growth of population or economy, *system modeling* has proven be a valuable method for the prediction of future developments or for the support in decision making regarding the future.

From a technical and economic perspective, the efficiency and effort for model generation as well as the complexity and usability of the resulting model play an essential role. Thanks to technological development, the computational power of technical systems as well as the availability of data has increased dramatically. Nowadays, more and more data is collected in real time and can be processed directly with the help of the available computing power. Modeling methods that are suitable for online applications are of particular interest and therefore are the focus of this work.

There are basically two different ways how models can be generated. One way is to derive *physical, phenomenological or empirical equations* from fundamental theoretical considerations. The resulting *theoretical models* are then represented by a functional description between physical input variables u, state variables x, and parameters θ,

$$y = f(x, \theta), \tag{2.1}$$

where the parameters θ are either known or must be identified in order to match an observed physical behavior. Another way is to use *(data-driven) experimental* modeling tools to generate (automatically) a mathematical representation of the measured input-output behavior. To allow the approximation of any measured input-output data set, experimental models are generally based on a generic and adjustable mathematical formulation.

In both cases, the underlying mathematical descriptions have free equational and/or structural parameters that need to be adapted in such a way that the model behavior match given measurement data (*model identification*). In case of theoretically derived models, the model structure usually results from physical relations whereby the equation parameters must be identified by applying *parameter identification methods*. In experimental modeling, structure determining parameters can be identified either separately or simultaneously to the equation parameters. Thus, the model identification of experimental models is also denoted as *model training*.

2.1 Theoretical modeling of combustion engines

For the modeling of modern combustion engines and their technical components, corresponding model equations from different physical domains, e.g. mechanics, thermodynamics, chemical reaction kinetics and electricity, have to be set up and combined adequately (Isermann 2014).

First of all, system boundaries between physical domains and their subsystems are drawn and the interfaces between them are defined over which matter, energy and/or information flows are exchanged. By defining these cuts, the considered overall system is divided into subsystems such as sources, sinks, transformers, converters, and storages for energies, matters and information. The interfaces between these subsystems represent input and output variables such as mass and energy flows entering or leaving the subsystems. Storage elements are giving systems a kind of memory (internal state), which is described by state variables. Moreover, energy storages give a dynamic system behavior to a technical system.

The task of modeling consists of finding suitable mathematical equations for the relations between the internal state variables and the flow variables at the inputs and outputs of each subsystem (Konigorski 2017). In stating these equations one has to distinguish between *distributed parameter models* as one-/three-dimensional models and such with *lumped parameters* which are referred to as *zero/quasi-dimensional models* (Isermann 2007). Due to the computational demand of multi-dimensional models and with regard to the scope of this work, zero/quasi-dimensional models with lumped parameters lead to a lean model structure and therefore are better suited for the use in online applications. Following categories of basic equations exist for the theoretical modeling of processes with lumped parameters (Isermann 2014):

- balance equations (general storages, junction points)
- constitutive equations or physical state equations (sources, transformers, converters, special storages)
- phenomenological equations (sinks, dissipative elements).

The mathematical descriptions are usually differential equations and/or algebraic equations. Energy storages and flows are described by corresponding state and flow variables.

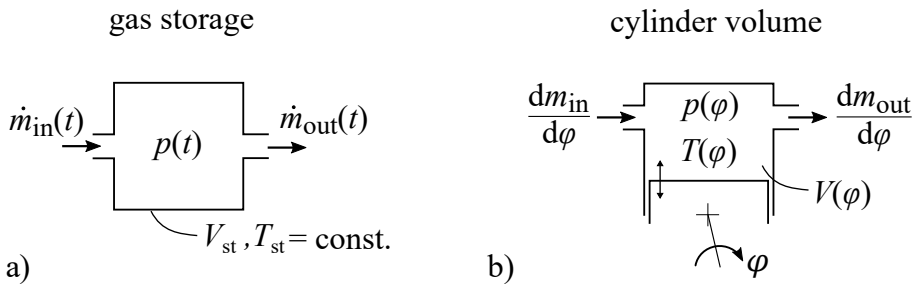

Figure 2.1: Examples for MVEM and CASEM: a) charging pressure model; b) in-cylinder gas pressure and temperature

2.1.1 Types of combustion engine models

In the context of modeling of combustion engines, the class of lumped parameter models can be further divided into *mean value engine models* (MVEM) and *crank angle synchronous engine models* (CASEM). Mean value engine models are generally formulated time-dependent $f(t)$ and are used in applications where the reciprocating operation of internal combustion engines can be neglected for the sake of simplicity. For example, in the field of ECU control function design, where it can be sufficient to model only the control-relevant engine dynamics by time-averaged state variables, e.g. mean engine torque or mean charge pressure/temperature in the engine's intake manifold. However, the influence of the engine speed must be considered by means of engine-speed dependent parameters, see e.g. Jung (2003), Ammann (2003), Eriksson (2007) or Guzzella and Onder (2010). An example of mean value engine model with lumped parameters is the gas storage model for the charging pressure in the intake manifold of combustion engines; see Fig. 2.1 a).

Crank angle synchronous models are formulated with respect to crankshaft angle φ. CASEMs are used for processes that rather depend on the current crankshaft position than on time t. This holds, for instance, for in-cylinder processes such as the in-cylinder gas pressure and temperature, see Fig. 2.1 b). Relevant state variables like cylinder volume, combustion pressure and temperature as well as the heat release during combustion are described as functions of the crankshaft angle $f(\varphi)$. For examples of zero/quasi-dimensional cylinder models see Constien (1991), Barba (2001), Torkzadeh (2003), Rether (2012), Zahn (2012) or Poetsch (2014).

However, the time dependency must also be taken into account through the relation between crank angle φ in °cs and time t in seconds by using the engine speed

$$\varphi(t) = \int \omega_{eng}(t)\mathrm{d}t \tag{2.2}$$

Under the assumption that the engine speed does not vary significantly during one engine operation cycle, the time-to-angle relation for infinitesimal small changes is given as

$$\mathrm{d}\varphi = \omega_{eng}\mathrm{d}t. \tag{2.3}$$

Time derivatives $\mathrm{d}x/\mathrm{d}t$ can also be transformed with respect to crank angle by using this relation

$$\frac{\mathrm{d}x}{\mathrm{d}\varphi} = \frac{1}{\omega_{eng}}\frac{\mathrm{d}x}{\mathrm{d}t}. \tag{2.4}$$

Eqs. (2.3) and (2.4) are applied to transform time-based equations into crank-angle based description. Furthermore, these relations are required to convert input and output variables in the transition between MVEMs and CASEMs.

2.1.2 Modeling of dynamic systems

The dynamic behavior of a technical system is usually described by differential equations in continuous-time domain or by difference equations in discrete-time domain.

Continuous-time dynamic processes

In general, a linear dynamic process with the order n and one input is described in mathematical terms by a differential equation with the following form:

$$\begin{aligned} y^{(n)}(t)+a_{n-1}(t)y^{(n-1)}(t) + ... + a_1\dot{y}(t) + a_0 y(t) \\ = b_m u^{(m)}(t) + b_{m-1}(t)u^{(m-1)}(t) + ... + b_1\dot{u}(t) + b_0 u(t), \end{aligned} \tag{2.5}$$

where $y^{(j)}(t) = \mathrm{d}^j y(t)/\mathrm{d}t^j$ represents the j-th derivative with respect to time t and a_i, b_i are the parameters of the differential equation determining the process dynamics. In system theory, linear differential equations are transformed into a frequency domain using the Laplace transformation (Föllinger 2013). The Laplace transformation of (2.5) leads to following transfer function $G(s)$ regarding the input signal $u(t)$ and output signal $y(t)$ with the complex frequency variable $s = j\omega$ in 1/s

$$G(s) = \frac{Y(s)}{U(s)} = \frac{b_0 + b_1 s + ... + b_{m-1}s^{m-1} + b_m s^m}{a_0 + a_1 s + ... + a_{n-1}s^{n-1} + a_n s^n} \tag{2.6}$$

Correspondingly, a crank angle synchronous function $f(\varphi)$ can be Laplace-transformed into crank angle frequency domain by using relation (2.4), see also Schmitt (1995). This leads to following transfer function with the complex crank angle frequency variable $\sigma = j\Omega$ in $1/^\circ\mathrm{cs}$

$$G(\sigma) = \frac{Y(\sigma)}{U(\sigma)} = \frac{b_0 + b_1\sigma + ... + b_{m-1}\sigma^{m-1} + b_m\sigma^m}{a_0 + a_1\sigma + ... + a_{n-1}\sigma^{n-1} + a_n\sigma^n}. \tag{2.7}$$

The crank angle frequency variable σ corresponds to the Laplace variable s in time frequency domain. Although, the model dynamics can be expressed both time-dependent or rotation angle-dependent, crank angle-dependent model description is advantageous with regard to modeling the dynamic processes in the cylinder chambers of the combustion engine. The time-dependent model description is more commonly used for modeling the dynamic behavior of the airpath.

Discrete-time dynamic processes

To realize the calculation of continuous-time differential equations on digital processors, differential equations as (2.5) are discretized by using a *difference quotient*

$$\left.\frac{\mathrm{d}y}{\mathrm{d}t}\right|_{t=k\cdot T_\mathrm{s}} \approx \lim_{T_\mathrm{s}\to 0} \frac{y(k\cdot T_\mathrm{s}) - y((k-1)\cdot T_\mathrm{s})}{T_\mathrm{s}}, \tag{2.8}$$

with a small sampling time T_s. The difference quotient (secant gradient) represents an approximation of the derivative (tangent gradient), becoming more precise, the smaller the sampling time is. For better readability, the notation y_k is used instead of $y(k \cdot T_\mathrm{s})$. Through successively substituting the difference quotient into the differential equation (2.5), the following *difference equation* is obtained

$$y_k + \hat{a}_{n-1} y_{k-1} + ... + \hat{a}_0 y_{k-n} = \hat{b}_m u_k + \hat{b}_{m-1} u_{k-1} + ... + \hat{b}_0 u_{k-m}. \tag{2.9}$$

Note that due to the substitution of the difference quotient, the physical parameters $\boldsymbol{\theta} = [a_i, b_j]^\mathrm{T}$ of the differential equation (2.5) differ from the model parameters $\mathbf{p} = [\hat{a}_i, \hat{b}_j]^\mathrm{T}$ of the difference equation (2.9). For larger sampling time, the *z-transformation* has to be applied (Isermann 1989).

Quasi-continuous-time dynamic processes

Determining the physical parameters $\boldsymbol{\theta}$ from identified model parameters $\mathbf{p}$ often requires solving nonlinear algebraic relations $\boldsymbol{\theta} = f^{-1}(\mathbf{p})$. In practice, to maintain a better interpretability of the model equations with physical parameters, the discretization is approximated by a *quasi-continuous formulation* instead of using difference quotients. Discrete difference variables Δy_k are introduced for the time derivatives of the differential equation by using the *explicit Euler method*

$$\left.\frac{\mathrm{d}y}{\mathrm{d}t}\right|_{t=k\cdot T_\mathrm{s}} \approx \Delta y_k = \frac{y_k - y_{k-1}}{T_\mathrm{s}}. \tag{2.10}$$

By substituting the derivatives in Eq. (2.5) according to (2.10), results the quasi-continuous-time formulation of a dynamic process as follows

$$\begin{aligned} \Delta^{(n)} y_k + a_{n-1} \Delta^{(n-1)} y_k + ... + a_1 \Delta y_k + a_0 y_k = \\ b_m \Delta^{(m)} u_k + b_{m-1} \Delta^{(m-1)} u_k + ... + b_1 \Delta u_k + b_0 u_k. \end{aligned} \tag{2.11}$$

If it can be assumed that the sampling time is sufficiently smaller than the dominating process dynamics, the quasi-continuous formulation can be used for the implementation on digital processors without losing the physical interpretability of equation parameters $\boldsymbol{\theta} = [a_i, b_j]^\mathrm{T}$. The transfer function of quasi-continuous-time dynamic process can then be derived the same way as for continuous-time differential equations, compare to Eqs. (2.6) or (4.48).

State space representation of dynamic processes

In control theory, an alternative form of representation is often chosen as mathematical description, especially for higher order dynamical systems, which was introduced by R. E. Kalman (Föllinger 2013). Thereby, the physically derived differential equations of a system are transformed into a more compact vector representation. Differential equations of higher order are transformed into an equation system of multiple first order differential equations. The equation variables are then classified into input u, output y, and state variables x and combined into a corresponding column vector, e.g. $\mathbf{x} = [x_1, x_2, ..., x_\mathrm{n}]^\mathrm{T}$. The resulting vector differential equation is known as the state space model of a system. A difference is made between linear and nonlinear state space models.

a) *Linear state space model*

For a linear dynamic system as Eq. (2.5), the (quasi-)continuous-time state space equations is given as

$$\begin{aligned} \dot{\mathbf{x}}(t) &= \mathbf{A}(t)\mathbf{x}(t) + \mathbf{B}(t)\mathbf{u}(t) \\ \mathbf{y}(t) &= \mathbf{C}(t)\mathbf{x}(t), \end{aligned} \tag{2.12}$$

with the *system matrix* $\mathbf{A}(t) \in \mathbb{R}^{(n\times n)}$, the *input matrix* $\mathbf{B}(t) \in \mathbb{R}^{(n\times p)}$ and the *output matrix* $\mathbf{C}(t) \in \mathbb{R}^{(q\times n)}$. The matrices contain the parametric relations between the inputs, states and outputs and determine the dynamic behavior of the system. The system matrix $\mathbf{A}(t)$ is also denoted as the dynamic matrix, since it describes the dynamic behavior of the system.

If the dynamic behavior is not time-varying, the matrices $\mathbf{A}(t)$, $\mathbf{B}(t)$ and $\mathbf{C}(t)$ become constant, which leads to the *linear time-invariant state space representation*

$$\begin{aligned} \dot{\mathbf{x}}(t) &= \mathbf{A}\mathbf{x}(t) + \mathbf{B}\mathbf{u}(t), \\ \mathbf{y}(t) &= \mathbf{C}\mathbf{x}(t). \end{aligned} \tag{2.13}$$

A discrete-time state space representation of (2.13) is given correspondingly as follows

$$\begin{aligned} \mathbf{x}_k &= \mathbf{A}_\mathrm{d}\mathbf{x}_{k-1} + \mathbf{B}_\mathrm{d}\mathbf{u}_{k-1}, \\ \mathbf{y}_k &= \mathbf{C}_\mathrm{d}\mathbf{x}_k. \end{aligned} \tag{2.14}$$

For time-varying systems the process, input and output matrices can change with each sampling step ($\mathbf{A}_\mathrm{d} = \mathbf{A}_k$, $\mathbf{B}_\mathrm{d} = \mathbf{B}_k$, $\mathbf{C}_\mathrm{d} = \mathbf{C}_k$).

b) *Nonlinear state space model*

The state space representation of a nonlinear, continuous-time dynamic system is written as

$$\begin{aligned} \dot{\mathbf{x}}(t) &= \mathbf{f}_\mathrm{c}\left(\mathbf{x}(t), \mathbf{u}(t), t\right), \\ \mathbf{y}(t) &= \mathbf{h}_\mathrm{c}\left(\mathbf{x}(t), t\right), \end{aligned} \tag{2.15}$$

with the *nonlinear process function* $\mathbf{f}_\mathrm{c}(\cdot) \in \mathbb{R}^{(n\times 1)}$ yielding the first order derivative of the *state vector* $\dot{\mathbf{x}}(t) \in \mathbb{R}^{(n\times 1)}$ and the *nonlinear output* or *observation function* $\mathbf{h}_\mathrm{c}(\cdot) \in \mathbb{R}^{(q\times 1)}$ yielding the *output vector* $\mathbf{y}(t) \in \mathbb{R}^{(q\times 1)}$. Both represent time-dependent matrix functions of the *input vector* $\mathbf{u}(t) \in \mathbb{R}^{(p\times 1)}$ and *state vector* $\mathbf{x}(t) \in \mathbb{R}^{(n\times 1)}$.

In order to obtain an approximation for the discrete-time state space representation of nonlinear continuous-time systems, the explicit Euler method with the sampling time T_s is used. The discrete approximation $\mathbf{f}_\mathrm{d}(\cdot)$ of the nonlinear continuous-time function $\mathbf{f}_\mathrm{c}(\cdot)$ yields to

$$\mathbf{x}_k \approx \mathbf{x}_{k-1} + T_\mathrm{s}\left[\mathbf{f}_\mathrm{c}(\mathbf{x}_{k-1}, \mathbf{u}_{k-1})\right] = \mathbf{f}_\mathrm{d}(\mathbf{x}_{k-1}, \mathbf{u}_{k-1}) \tag{2.16}$$

By discretization of both, process and observation functions of Eq. (2.15), results the discrete-time state space model for nonlinear dynamic system

$$\begin{aligned} \mathbf{x}_k &= \mathbf{f}_\mathrm{d}(\mathbf{x}_{k-1}, \mathbf{u}_{k-1}) \\ \mathbf{y}_k &= \mathbf{h}_\mathrm{d}(\mathbf{x}_k). \end{aligned} \tag{2.17}$$

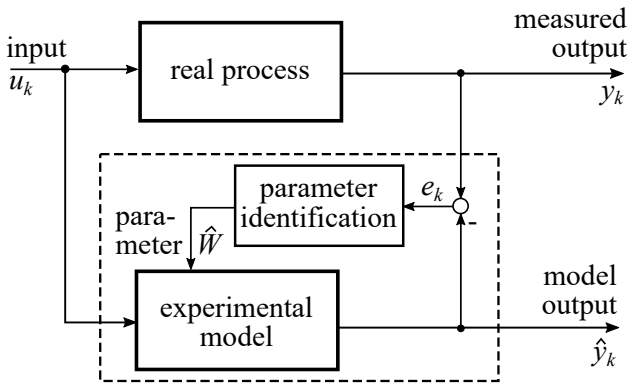

Figure 2.2: Scheme of experimental, data-based modeling

2.2 Experimental and data-based modeling

In technical systems where the physical behavior is not fully understood or theoretical modeling leads to large model complexity and computational effort with regard to its application, *experimental* or *data-based modeling* is applied to obtain a mathematical *black box model* without requiring detailed knowledge of the technical system's behavior, see Fig. 2.2.

Black box models are obtained systematically from the *measured input-output process behavior* by using specially developed identification methods; see Isermann and Münchhof (2011). Compared to theoretical models, black box models are able to match more precisely with the measured data. However, the model accuracy depends on the quality and comprehensiveness of the training data used to generate a black box model. That is why experimental modeling can lead to high measurement and calibration effort if the behavior is nonlinear.

Generally, in order to adapt to any system behavior, the mathematical formulation of black box models is chosen to be adjustable in both, the model structure and the model parameters. While the structure determines the general model characteristics and complexity, the parameters determine the specific behavior of the model (Nelles 2001). There are different types of black box models that differ in their mathematical description of the functional relation between inputs and outputs, i.e. whether it is (piece-wise) linear or non-linear. Another distinction is made between modeling stationary or dynamic process behavior.

In an increasingly complex world where a lot of data is collected, the demand for methods of data-driven modeling has increased and led to new impulses in the field of black box modeling research. This research area encompasses numerous modeling methods and applications, both in the technical environment as well as in everyday life, which are summarized under the terms *artificial intelligence* and *machine learning*. With regard to the scope of this work, the following overview is limited to *stationary black box models*, which are suitable for the use in online applications. More details regarding experimental models for linear and non-linear, as well as static and dynamic systems can be found e.g. in Sjöberg et al. (1995), Nelles (2001), Isermann and Münchhof (2011), and Sequenz (2013).

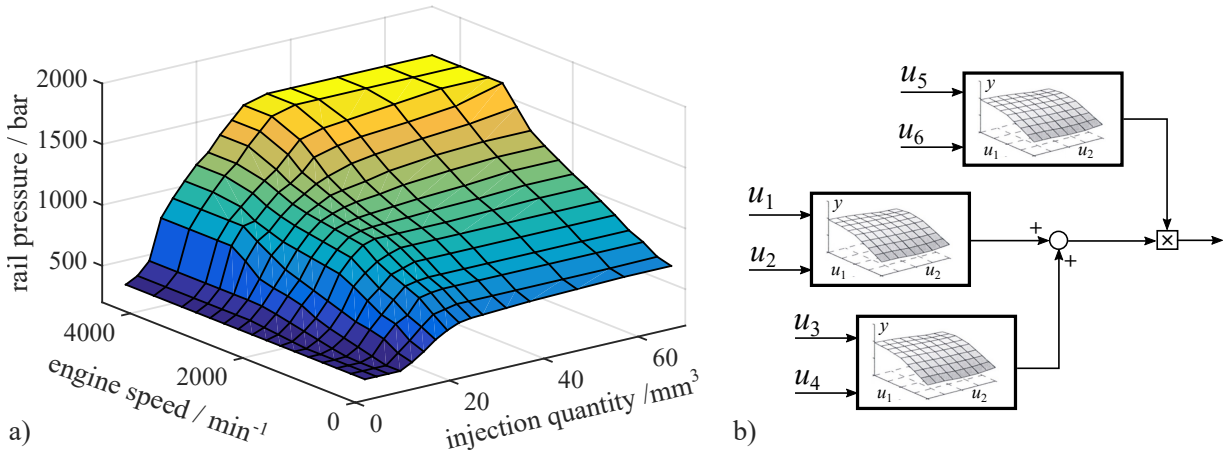

Figure 2.3: a) Example for a grid-based look-up table: Base-map for the desired rail pressure of a four-cylinder common-rail diesel engine; b) combination of several two-input maps

2.2.1 Grid-based look-up tables

In the ECU of automobiles, the most commonly used experimental models are grid-based look-up tables (maps), see an example in Fig. 2.3 a). Look-up table are particularly suitable for the modeling of lower dimensional stationary non-linear input-output-relations and applications where low computational effort and good interpretability is preferred. Since look-up tables are usually limited to two input variables, several two-dimensional look-up tables must be combined in order to represent higher dimensional relations (Sequenz 2013), see Fig. 2.3 b). In case of two inputs $\mathbf{u} = [u_1, u_2]^T$, the output is given as

$$y = g_{\text{map}}(\mathbf{u}), \tag{2.18}$$

whereas $y = f_{\text{map}}(\mathbf{u})$ represents a linear interpolation between the heights $w_{i,j}$ at the neighboring grid points $c_{i,j}$. Consequently, the model structure consists of the stored tables containing the heights $w_{i,j}$ and the corresponding grid points $c_{i,j}$. The grid points $c_{i,j}$ are usually defined equidistant over the input space.

The identification of lookup tables consists in determining the heights at the corresponding grid points. A fast calculation method for the online adaptation of grid-based look-up tables can be found in Vogt et al. (2004). In case of highly nonlinear relations $y = f_{\text{map}}(\mathbf{u})$, a sufficiently dense grid over the input space is required to reduce interpolation error and achieve high model accuracy.

2.2.2 Neuro-Fuzzy models

An alternative to look-up tables are *Neuro-Fuzzy models*. Neuro-fuzzy models combine the advantages of neural networks with the strengths of fuzzy systems, see for more details Nelles (1999), Isermann and Münchhof (2011), and Sequenz (2013). Their output results from a sum of L normalized activation functions $\Phi_i(\mathbf{u})$, also denoted as *validity function*, which are activated by the input $\mathbf{u} \in \mathbb{R}^{(p\times 1)}$, multiplied by a corresponding weighting factor w_i. A general formulation is

given by

$$y(\mathbf{u}) = \sum_{i=1}^{L} \Phi_i(\mathbf{u}) w_i. \tag{2.19}$$

The grid point height w_i is activated by an validity function $\Phi_i(\mathbf{u})$ in dependence of the current input variables $\mathbf{u} = \begin{bmatrix} u_1 & u_2 & \dots & u_p \end{bmatrix}$. Several activation functions $\Phi_i(\mathbf{u})$ are possible. The most commonly used activation function is the *Gaussian function* given as follows

$$\Phi_i(\mathbf{u}) = \exp\left[-\frac{1}{2} \left(\frac{(u_1 - c_{i,1})^2}{\sigma_{i,1}^2} + \frac{(u_2 - c_{i,2})^2}{\sigma_{i,2}^2} + \dots + \frac{(u_p - c_{i,p})^2}{\sigma_{i,p}^2} \right) \right]. \tag{2.20}$$

Such neuro-fuzzy models using Gaussian activation functions are denoted as extended normalized *Radial basis function* networks (RBF). In the simplest case, the centers $c_{i,j}$ are defined equidistant over the input space of each j-th input. The parameter $\sigma_{i,j}$ represents the standard deviation of the Gaussian functions and thus determines the overlap between the Gaussian functions. $\sigma_{i,j}$ can also be set equidistant or optimized in the framework of the model identification. However, it is advantageous to normalize the Gaussian activation functions through division by the sum of all Gaussian functions, leading to a normalized validity function

$$\begin{aligned} \hat{\Phi}_i(\mathbf{u}) &= \frac{\Phi_i(\mathbf{u})}{\sum_{i=1}^{L} \Phi_i(\mathbf{u})} = 1. \\ y(\mathbf{u}) &= \sum_{i=1}^{L} \hat{\Phi}_i(\mathbf{u}) w_i. \end{aligned} \tag{2.21}$$

The standard deviation parameters $\sigma_{i,j}$ determine then the smoothness of the transition between the Gaussian functions (*smoothness factors*). Due to the normalization only the Gaussian functions (*neurons*) next to the inputs u_i are active at the same time, thus, such models are termed as *local neuro-fuzzy model networks*, see Fig. 2.4. The weighting factors w_i can be seen as constant *local models* representing the height at the centers $c_{i,j}$ of the activation functions.

In general, arbitrary radial basis function can be used as activation functions. As an alternative to the Gaussian functions in Eq. (2.21), pyramidal activation functions are used. The pyramidal validity function is given in Sequenz (2013) as

$$\Phi_i(\mathbf{u}) = \frac{\prod_{j=1}^{p} \left(1 - \frac{\Delta u_j}{d_{i,j}}\right)}{\sum_{i=1}^{L} \left[\prod_{j=1}^{p} \left(1 - \frac{\Delta u_j}{d_{i,j}}\right) \right]}. \tag{2.22}$$

with the input distance

$$\Delta u_j = \max(\left| u_j - c_{0,i,j} \right|, 0), \tag{2.23}$$

where $c_{0,i,j}$ is the j-th dimension of the i-th model center and $d_{j,i}$ is the distance to next model center in the j-th dimension, see in Fig. 2.5 the illustrations of a one- and two-dimensional case.

Compared to other basis functions (i.e. Gaussian function), pyramidal functions have the advantage of having a piece-wise linear relation between the inputs, the weights and the output, allowing the

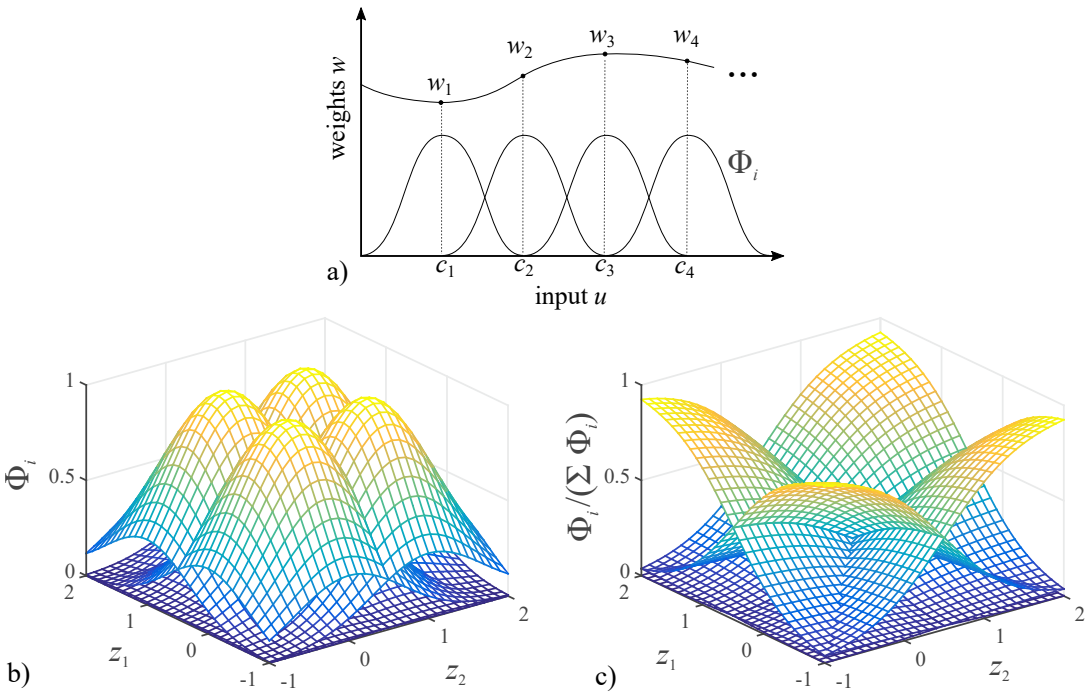

Figure 2.4: Local Neuro-Fuzzy model with *Gaussian radial basis functions*: a) One-dimensional, b) unnormalized and c) normalized two-dimensional representation

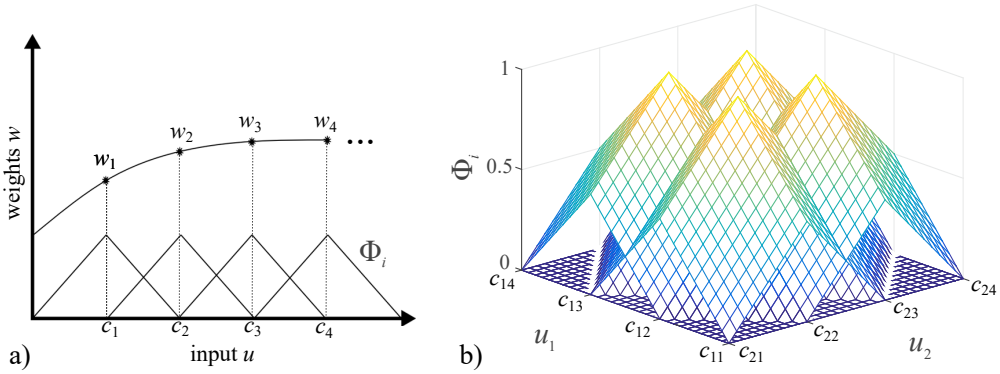

Figure 2.5: Local Neuro-Fuzzy model with *pyramidal radial basis function*: a) One-dimensional triangular and b) two-dimensional representation

application of fast recursive least-squares algorithm for the identification of the weights, see next Sect. 2.3. On the contrary, Gaussian activation functions are commonly used due to their properties of providing a smooth overlap between the local models and the ability of better approximation of nonlinear relationships.

The overall structure of such neuro-fuzzy model corresponds to a two-layer feedforward radial-basis function network, depicted in Fig. 2.6. The task in identification of (2.19) is then performed by determining the weighting factors w_i.

There are numerous other types of experimental models besides these two. They differ in the type of activation function (pyramidal, sigmoid, Gaussian, etc.), in the approach function for the

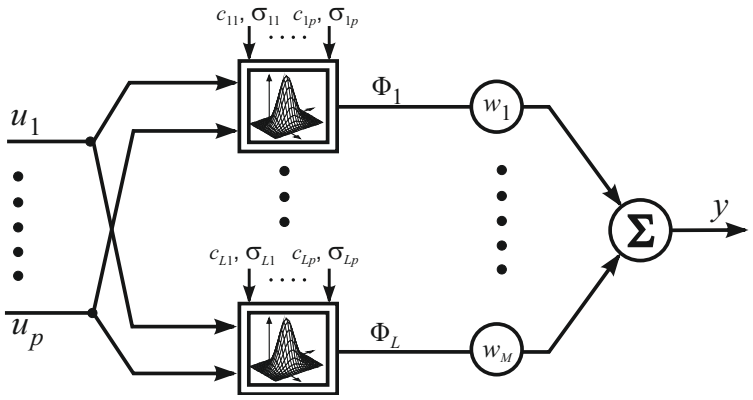

Figure 2.6: Structure of radial basis function (RBF) network (Isermann 2014)

local model (constant, linear, polynomial) and may also have modified properties with respect to structure search, see e.g. *local linear model tree* (LOLIMOT) presented in Nelles (2001), *hinging hyperplane tree* (HHT) in Töpfer (2002) or *local polynomial model tree* (LOPOMOT) in Sequenz (2013).

2.3 Online-identification methods

In the literature, the identification of parametric models is also referred to as *parameter identification* or *parameter estimation*. The following sections deal with system identification and estimation methods, which are particularly suitable for online application. The treated parameter estimation methods can be applied to both, theoretical and experimental models. An exception to this are state estimation methods, which are typically used to estimate non-measurable, physical system states. However, state estimation techniques can be applied for parameter estimation of nonlinear systems by including the parameters to be estimated into the state space vector. In this context, different state estimation algorithms and their benefits that evolve form the combination of both state and parameter estimation methods are presented.

2.3.1 Parameter estimation

The task of parameter estimation consists of the formulation and solving of an optimization problem regarding a parametric model error $e(t)$, see Fig. 2.2. An error $e(t)$ between the model output $\hat{y}(\hat{\theta}, t)$, as function of the parameters $\hat{\theta}$, and the measured reference output $y(t)$ must first be defined and incorporated into a cost function $V(\hat{\theta}, e(t))$. This cost function is minimized regarding the model error $e(t)$ by determining the optimal model parameter θ

$$\begin{aligned} e(t) &= y(t) - \hat{y}(\hat{\theta}, t) \\ \min_{\theta} & \; V(e(t)) \end{aligned} \tag{2.24}$$

There are many ways how this can be done. One way is to define the model error $e(t)$ as an output error (OE); another way is to define it as equation error (EE). While methods based on

OE representation require usually solving a nonlinear optimization problem, EE representations allow in some cases a *linear-in-the-parameters formulation* and therefore a direct calculation of the optimal parameters. The choice of solving algorithm and the resulting computational effort for solving the optimization problems depends significantly on the mathematical character of the parametric model and the chosen cost function.

For the choice of estimation method, a difference must be made between *linear* and *nonlinear parameter estimation*. While *linear-in-the-parameter estimation* allows lean and directly solvable formulations for the parameter (analytical solution), nonlinear parameter estimation requires usually numerical methods i.e. iterative optimization algorithms (Isermann and Münchhof 2011). The convergence depends on the complexity of optimization problem and many different other aspects, i.e. number of parameters to be estimated, starting value, etc. Since numerical methods often involve high computational effort, they are hardly qualified for real-time implementations.

When it comes to *real-time application*, further restrictions, i.e. fixed step size, convergence and duration of calculations, etc., have to be taken into account.

A further relevant aspect in real-time applications is the way how the real-time data is handled. One way is to handle the measurement data decoupled from the parameter estimation algorithm. For instance, the data is measured over a period of time, pre-processed and stored before it is used for parameter estimation (*batch processing*). In this case, solving the optimization problem in Eq. (2.24) involves considering the entire, up to that time recorded, measurement data at once. Such an approach leads to an increase in the complexity of the parameter optimization problem accompanied with high computational effort. Moreover, the estimates are not provided in real-time and are only available at the end of the measurement. Consequently, batch identification is more suitable for offline applications.

In online-application, *recursive methods* are used to reduce computational effort and provide an estimate after each sample step (Isermann and Münchhof 2011). A recursive formulation of the optimization problem in Eq. (2.24) is used, which allows an incremental update of the estimate using previous estimation result and incoming measurement data (*incremental processing*).

Least squares methods

The least squares method belongs to the regression methods and aims to minimize the quadratic error $e(k)^2$ between the output of a parametric equation $\hat{y} = f(\theta, u)$ and a data set $[u_1, ..., u_N; y_1, ...y_N]$ of N measurements. It can be applied on *linear parametric models* or nonlinear models, which are *linear-in-parameters*. The cost function $V(\theta)$ is defined as sum of squared errors which has to be minimized by adjusting the parameters θ

$$\min_{\theta} V(\theta) = \sum_{k=1}^{N} e(k)^2 = \sum_{k=1}^{N} [y(k) - \hat{y}(k)]^2 = \sum_{k=1}^{N} [y(k) - f(\theta, u(k))]^2 \tag{2.25}$$

For solving this optimization problem exist a non-recursive (LS) and a recursive (RLS) formulation of the least squares algorithm.

a) *Non-recursive least squares* (LS)

A vectorial notation is introduced for the mathematical description of the LS parameter estimation problem. Any linear or linear-in-parameter model, such as the discrete linear process in Eq. (2.9) or the experimental model in (2.19), can be formulated as a set of linear equations for N measurements,

$$\mathbf{y} = \boldsymbol{\Psi}\boldsymbol{\theta} + \mathbf{e}, \tag{2.26}$$

Considering the experimental model in (2.19), the *output vector* $\mathbf{y} \in \mathbb{R}^{(N\times 1)}$ and the *data matrix* $\boldsymbol{\Psi} \in \mathbb{R}^{(N\times L)}$ containing the relation to the input vector $\mathbf{u} \in \mathbb{R}^{(N\times p)}$ are given as

$$\mathbf{y} = \begin{bmatrix} y(1) \\ y(2) \\ \vdots \\ y(N) \end{bmatrix}, \quad \boldsymbol{\Psi} = \begin{bmatrix} \Phi_1(\mathbf{u}(1)) & \Phi_2(\mathbf{u}(1)) & \dots & \Phi_L(\mathbf{u}(1)) \\ \Phi_1(\mathbf{u}(2)) & \Phi_2(\mathbf{u}(2)) & \dots & \Phi_L(\mathbf{u}(2)) \\ \vdots & \vdots & \ddots & \vdots \\ \Phi_1(\mathbf{u}(N)) & \Phi_2(\mathbf{u}(N)) & \dots & \Phi_L(\mathbf{u}(N)) \end{bmatrix}, \tag{2.27}$$

with the unknown grid point heights w_i of each locally activated function $\Phi_i(\mathbf{u}(k))$ representing the parameters to be estimated ($N \geq L$)

$$\boldsymbol{\theta} = [w_1,\ w_2,\ \dots,\ w_L]^{\mathrm{T}} \tag{2.28}$$

and the measurement error $\mathbf{e} = \mathbf{y} - \boldsymbol{\Psi}\boldsymbol{\theta}$, $\mathbf{e} \in \mathbb{R}^{(N\times 1)}$. By minimizing the sum of squared measurement errors $V = \mathbf{e}^{\mathrm{T}}\mathbf{e}$ results the least squares solution for the parameter vector

$$\hat{\boldsymbol{\theta}} = \left(\boldsymbol{\Psi}^{\mathrm{T}}\boldsymbol{\Psi}\right)^{-1}\boldsymbol{\Psi}^{\mathrm{T}}\mathbf{y}. \tag{2.29}$$

Since this example, Eqs. (2.27)-(2.29), represents a *global parameter estimation problem*, where all parameters are determined at once by solving Eq. (2.29), one has to make sure that the inputs are well distributed across the input space, so that all locally activated functions $\Phi_i(\mathbf{u})$ are excited and the matrix product $(\boldsymbol{\Psi}^{\mathrm{T}}\boldsymbol{\Psi})$ has full rank. Otherwise, the inverse $(\boldsymbol{\Psi}^{\mathrm{T}}\boldsymbol{\Psi})^{-1}$ does not exist ($\det(\boldsymbol{\Psi}^{\mathrm{T}}\boldsymbol{\Psi}) \neq 0$). Since the computation of the inverse is complex and numerically ill-conditioned, in practice numerically more robust methods are used to solve (2.29), see for more details e.g. Björck (1996) and Golub and Van Loan (1996).

Since the model structure of experimental models, as (2.19), consists of several local models, it can be reasonable to apply the least square method only for the estimation of the parameters of simultaneously active local models. This leads to a *local parameter estimation problem*, where only the grid point heights w_i of the locally activated functions $\Phi_i(\mathbf{u}(k))$ have to be determined. For the two dimensional case $\mathbf{u} = [u_1, u_2]^{\mathrm{T}}$ with single output, each $k-$th measurement $(u_1(k), u_2(k), y(k))$ only affects a maximum of four local models y_i contributing to the global model output y

$$y(k) = \sum_{i=1}^{L=4} y_i(k) = \sum_{i=1}^{L=4} \Phi_i(\mathbf{u}(k))w_i \tag{2.30}$$

Assuming that all $N(\geq 4)$ measurements lie well distributed within the validity range of this four local models, leads to a significant reduction in the computational effort required for solving

Eq. (2.29) regarding one dimension ($L = 4$). Moreover, local parameter estimation method can be further combined, which is referred to as *global-local parameter estimation*, see e.g. Töpfer (2002) and Zimmerschied (2008). In online learning, only a finite number of local models are activated at the same time of each $k-$th measurement. Consequently, it is reasonable to assume a local parameter estimation in online learning.

a) *Recursive least squares* (RLS)

To achieve a further significant reduction of computational effort (regarding the dimension N) and make the least square method more suitable for online applications, the recursive formulation of the least squares approach can be used. The parameter estimate using non-recursive LS method for the sample step k is given as

$$\hat{\boldsymbol{\theta}}(k) = \mathbf{P}(k)\boldsymbol{\Psi}^{\mathrm{T}}(k)\mathbf{y}(k) \tag{2.31}$$

with the covariance matrix

$$\mathbf{P}(k) = \left(\boldsymbol{\Psi}^{\mathrm{T}}(k)\boldsymbol{\Psi}(k)\right)^{-1} \tag{2.32}$$

With the recursive formulation of the least squares method, as presented in Isermann and Münchhof (2011), the parameters $\hat{\boldsymbol{\theta}}_{k-1}$ from previous $(k-1)$-sample step are updated with each new measurement $\mathbf{y}_k$ by

$$\hat{\boldsymbol{\theta}}_k = \hat{\boldsymbol{\theta}}_{k-1} + \boldsymbol{\gamma}_k\left[\mathbf{y}_k - \hat{\mathbf{y}}_k\right] = \hat{\boldsymbol{\theta}}_{k-1} + \boldsymbol{\gamma}_k\left[\mathbf{y}_k - \boldsymbol{\Psi}_k^{\mathrm{T}}\hat{\boldsymbol{\theta}}_{k-1}\right], \tag{2.33}$$

whereas $\boldsymbol{\gamma}_k$ is the *correction factor* given as

$$\boldsymbol{\gamma}_k = \frac{1}{\alpha + \boldsymbol{\Psi}_k^{\mathrm{T}}\mathbf{P}_{k-1}\boldsymbol{\Psi}_k}\mathbf{P}_{k-1}\boldsymbol{\Psi}_k, \tag{2.34}$$

representing an *adaptation rate* or *learning rate*. The forgetting factor α allows an adaptation of estimates in case of time-varying process behavior. For a forgetting factor $\alpha < 1$ the current error e is weighted higher than the past errors, so that the parameters adapt in case of model error changes (*weighted recursive least squares* (WRLS)). A suitable choice of α requires a compromise between noise suppression ($\alpha = 1$) and adaptation to time-varying process behavior ($\alpha < 1$). In most applications $0.9 < \alpha < 0.995$ is chosen.

The covariance matrix $\mathbf{P}_{k-1}$ is also updated each calculation step using the data vector $\boldsymbol{\Psi}$ and the correction factor $\boldsymbol{\gamma}_k$ as follows

$$\mathbf{P}_k = \frac{1}{\alpha}\left(\mathbf{I} - \boldsymbol{\gamma}_k\boldsymbol{\Psi}_k^{\mathrm{T}}\right)\mathbf{P}_{k-1}. \tag{2.35}$$

The recursive least squares algorithm consists of these three equations above, however, the evaluation is performed in the sequence (2.34), (2.33), (2.35), see Ljung and Söderström (1983) and Goodwin and Sin (1984). For the start of calculation initial values for the parameters $\boldsymbol{\theta}_0$ as well as the covariance matrix $\mathbf{P}_0$ have to be defined.

Since the global estimation approach is accompanied with further disadvantages, e.g. numerical robustness, etc., see Nelles (1999), the local estimation approach based on RLS algorithm is chosen

for the online-identification of experimental models, see Sect. 2.4. More detailed information regarding a fast recursive least squares algorithms for look-up tables with simplifications for an accelerated computation is given in Vogt et al. (2004).

2.3.2 State estimation using Kalman filters

Whenever process states are partially unknown, measurements underlie sensor noise or falsifications, *state observers* or *state estimators* are used to generate an accurate estimate of these process states. The most applied representative of state estimators is the *Kalman filter* (KF) or its extension, the *Extended Kalman filter* (EKF), which can also be applied to nonlinear systems or for a combined state and parameter estimation. Both, KF and EKF are based on a *predictor-corrector principle*. The Kalman filter assumes that the state of a system or process is described probabilistically by a probability density distribution corresponding to a Gaussian normal distribution, which can be described by the mean and the covariance - i.e. up to the statistical moment of second order (Welch and Bishop 2006). For further details regarding state estimation by using Kalman filtering refer to i.e. Gelb et al. (1974), Maybeck (1979), Welch and Bishop (2006), and Grewal and Andrews (2008)

Linear state estimation using Kalman filter

In systems with approximately linear process dynamics, the *Discrete Kalman filter* is used for state estimation, introduced by Rudolf E. Kalman (Kalman 1960). A linear discrete-time state space representation as given in (2.14) is presumed

$$\begin{aligned} \mathbf{x}_k &= \mathbf{A}_k \mathbf{x}_{k-1} + \mathbf{B}_k \mathbf{u}_{k-1} + \mathbf{w}_k, \\ \mathbf{y}_k &= \mathbf{C}_k \mathbf{x}_k + \mathbf{v}_k, \end{aligned} \tag{2.36}$$

where $\mathbf{w}_k$ and $\mathbf{v}_k$ are additive random process variables representing uncorrelated white process and measurement noise with zero mean $\mathrm{E}\{\mathbf{w}_k \mathbf{v}_k^{\mathrm{T}}\} = \mathbf{0}$ and with the covariances $\mathbf{Q}_k = \mathrm{E}\{\mathbf{w}_k \mathbf{w}_k^{\mathrm{T}}\}$ and $\mathbf{R}_k = \mathrm{E}\{\mathbf{v}_k \mathbf{v}_k^{\mathrm{T}}\}$. In practice, the process noise $\mathbf{Q}_k$ and measurement noise covariances matrices $\mathbf{R}_k$ are assumed to be symmetric diagonal, where the diagonal elements are the error covariance of the corresponding process or measurement variables, respectively. Generally, the $\mathbf{Q}_k$, $\mathbf{R}_k$ can change with each time step k.

The Kalman filtering algorithm is divided into two alternating calculation steps, see Fig. 2.7. The a priori estimates of the state vector $\hat{\mathbf{x}}_k^-$ and the error covariance matrix $\mathbf{P}_k^- = \mathrm{E}\{\mathbf{e}_k^- \mathbf{e}_k^{-\mathrm{T}}\}$ with the a priori estimate error $\mathbf{e}_k^- = \mathbf{x}_k - \hat{\mathbf{x}}_k^-$ are calculated during the *prediction step* (time update). In the *correction step* (measurement update), the Kalman gain $\mathbf{K}_k$ is calculated by using the error covariance estimate $\mathbf{P}_k^-$ and the output matrix $\mathbf{C}$. The state estimate $\hat{\mathbf{x}}_k$ results then from the correction by using the Kalman gain $\mathbf{K}_k$. The Kalman gain $\mathbf{K}_k$ and the error between the measurement $\mathbf{y}_k$ and the predicted output $\hat{\mathbf{y}}_k = \mathbf{C}_k \hat{\mathbf{x}}_k^-$ are then used to correct the predicted state vector. Afterwards, the covariance matrix $\mathbf{P}_k$ has to be corrected with regard to the Kalman gain $\mathbf{K}_k$.

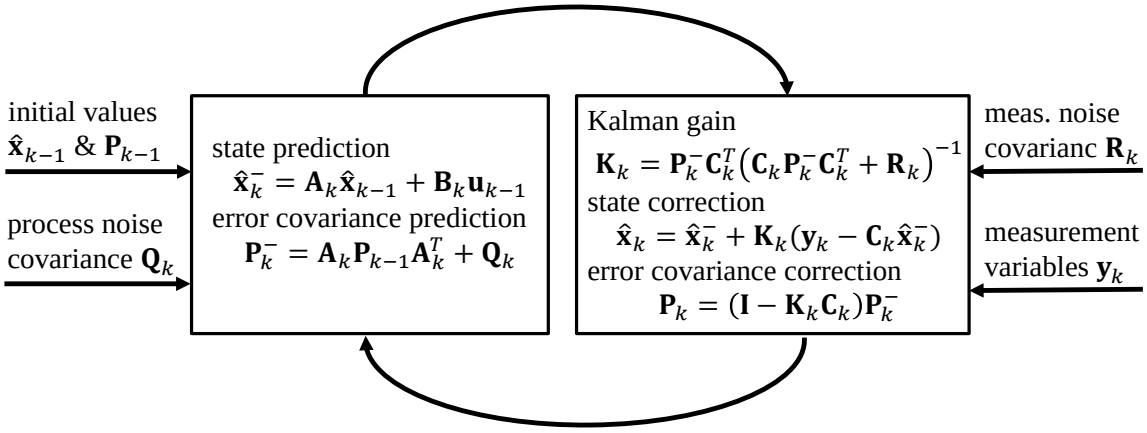

Figure 2.7: Predictor-corrector principle of *Kalman filter* (KF)

If both process and observation matrix are constant ($\mathbf{A}_k = \mathbf{A}$, $\mathbf{B}_k = \mathbf{B}$, $\mathbf{C}_k = \mathbf{C}$) and the modeled error covariances of process noise $\mathbf{Q}_k = \mathbf{Q}$ and measurement noise $\mathbf{R}_k = \mathbf{R}$ are assumed to be constant, the Kalman gain only needs to be calculated once. Then, the Kalman filter can be interpreted as *linear quadratic estimator*, which is optimal regarding the modeled process noise covariance $\mathbf{Q}$ and measurement noise covariance $\mathbf{R}$.

Tuning of filter parameters

Generally, the noise covariance matrices represent the filter parameters and are used for filter tuning.[1] The measurement noise covariance $\mathbf{R}$ is determined from the measured output $\mathbf{y}_k$ prior to filter operation. The process noise covariance is usually adjusted empirically and in relation to the measurement noise covariance $\mathbf{R}$.

If a simple model with poor accuracy is used, higher process noise covariance $\mathbf{Q}$ must be selected to incorporate a particular uncertainty into the process, so that the estimation relies more on the measurement variable $\mathbf{y}_k$. However, if the model accuracy is relatively high, smaller process error noise covariances should be selected in order to put more weight (trust) on the a priori state prediction (compare with $\hat{\mathbf{y}}_k = \mathbf{C}_k\hat{\mathbf{x}}_k^-$). This can be shown mathematically by inserting the equation for error covariance prediction into the equation for the calculation of Kalman gain.

$$\mathbf{K}_k = \frac{(\mathbf{A}\mathbf{P}_{k-1}\mathbf{A}^{\mathrm{T}} + \mathbf{Q}_{k-1})\mathbf{C}^{\mathrm{T}}}{\left(\mathbf{C}\mathbf{P}_{k-1}\mathbf{C}^{\mathrm{T}} + \mathbf{R}_k\right)}. \tag{2.37}$$

It can be seen that the relation between process noise covariance $\mathbf{Q}$ and measurement noise covariance $\mathbf{R}$ is decisive whether the estimation is rather based on the prediction from filter model or on the measurement, compare this to state correction in Fig. 2.7. Dynamic tuning of the relation between the diagonal elements of the covariance matrices allows filter adaptation to changing system conditions, i.e. for time-varying systems, changing sensor properties, etc. More details

[1] In the remainder of this work, the (entries of the) covariance matrices are referred to as filter parameters for the sake of simplicity.

regarding the tuning of noise parameters of the Kalman filter algorithm are presented in Sect. 2.3.4 in terms of *adaptive Kalman filters*.

Nonlinear state estimation

In most technical applications the system dynamics and observation are nonlinear and can change with time (time-varying behavior). The discrete state space representation of such nonlinear system is given in generalized form as

$$\begin{aligned} \mathbf{x}_k &= \mathbf{f}\left(\mathbf{x}_{k-1}, \mathbf{u}_{k-1}\right) + \mathbf{w}_k, \\ \mathbf{y}_k &= \mathbf{h}\left(\mathbf{x}_k\right) + \mathbf{v}_k, \end{aligned} \tag{2.38}$$

with the process noise $\mathbf{w}_k$ acting on the nonlinear process function $\mathbf{f}(\cdot)$ and the measurement noise $\mathbf{v}_k$ acting the nonlinear observation function $\mathbf{h}(\cdot)$ and affecting the output. For the properties of process and measurement noise processes apply the same assumptions as in the linear case.

In the literature, several nonlinear state estimation methods based on the concept of the Kalman filter exist. In order to apply the Kalman filter algorithm to nonlinear systems, the KF-algorithm is extended so that the statistical properties of the system state (mean and covariance) can be propagated through the nonlinear process and observation model.

a) *Extended Kalman filter* (EKF)

The most common and most simple extension is the *Extended Kalman filter*, which can be applied for nonlinear state estimation as well as for parameter estimation, see Fig. 2.8. Hereby, all nonlinear model functions are linearized each sampling step based on a first-order Taylor series, so that the Kalman filter algorithm can be applied. However, the underlying assumption that the nonlinear system behaves almost linearly within the sampling time interval must be valid.

The a priori prediction of the state $\hat{\mathbf{x}}_k^-$ is based on the nonlinear process model (2.38), whereas the prediction of the error covariance $\mathbf{P}_k^-$ requires first calculating the Jacobian matrix $\mathbf{F}_k$ of the nonlinear process function $\mathbf{f}(\cdot)$. The Jacobian matrix $\mathbf{F}_k$ consists of partial derivatives with respect to current state estimate $\hat{\mathbf{x}}_{k-1}$ from previous sampling step

$$\mathbf{F}_{k-1} = \left.\frac{\partial \mathbf{f}\left(\hat{\mathbf{x}}_{k-1}, \mathbf{u}_{k-1}\right)}{\partial \mathbf{x}}\right|_{\hat{\mathbf{x}}_{k-1}, \mathbf{u}_{k-1}} \tag{2.39}$$

The a priori estimate of the error covariance $\mathbf{P}_k^-$ is then determined based on this Jacobian matrix $\mathbf{F}_k$ of the process model, compare Fig. 2.8.

In the correction step, the Kalman gain $\mathbf{K}_k$ is calculated by using the error covariance estimate $\mathbf{P}_k^-$ and the Jacobian matrix $\mathbf{H}_k$ of the nonlinear observation function $\mathbf{h}(\cdot)$ The Jacobian matrix results analogously from partial derivation of $\mathbf{h}\left(\hat{\mathbf{x}}_k^-\right)$ with respect to $\hat{\mathbf{x}}_k^-$, see Fig. 2.8. The Kalman gain $\mathbf{K}_k$ and the error between the measurement $\mathbf{y}_k$ and the predicted output $\hat{\mathbf{y}}_k = \mathbf{h}\left(\hat{\mathbf{x}}_k^-\right)$ are then used to calculate the a posteriori state estimate $\hat{\mathbf{x}}_k$

$$\hat{\mathbf{x}}_k = \hat{\mathbf{x}}_k^- + \mathbf{K}_k\left(\mathbf{y}_k - \hat{\mathbf{y}}_k\right) = \hat{\mathbf{x}}_k^- + \mathbf{K}_k\left(\mathbf{y}_k - \mathbf{h}(\hat{\mathbf{x}}_k^-)\right), \tag{2.40}$$

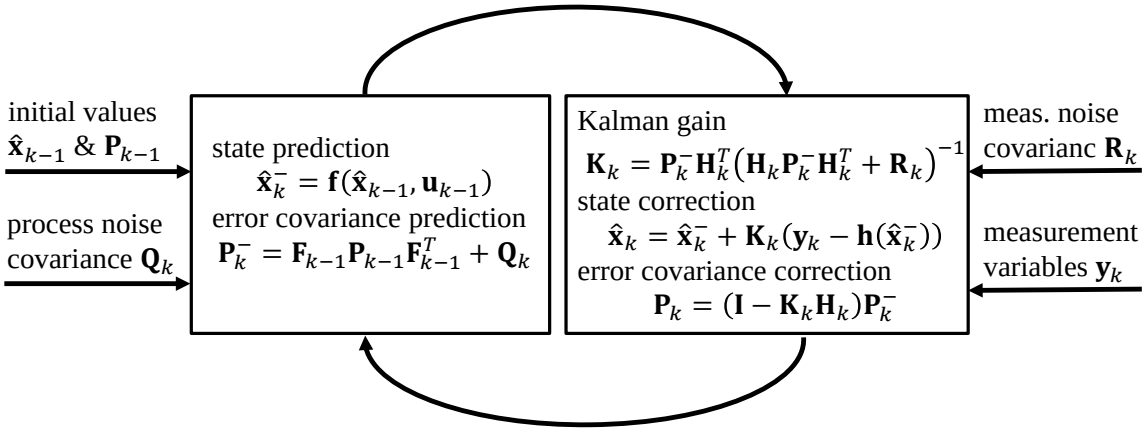

Figure 2.8: Predictor-corrector principle of *Extended Kalman filter* (EKF)

For a more detailed derivation and further information, see Welch and Bishop (2006), Grewal and Andrews (2008) or Isermann and Münchhof (2011).

For highly nonlinear system, the application of KF or EKF show some disadvantages with regard to robustness and implementation issues. Since the error covariances are determined analytically from the linearization of the nonlinear model, the statistical properties are only propagated through KF-algorithm by a first order approximation of the nonlinearity. This can lead to a highly unstable filter performance if the assumption of local linearity is violated (Julier and Uhlmann 1997, p. 2).

In many applications, the derivation of the Jacobian matrices can be difficult. For instance, if process functions $\mathbf{f}(\cdot)$ or observation functions $\mathbf{h}(\cdot)$ have discontinuities and the current point of linearization $(\mathbf{x}_{k-1}, \mathbf{u}_{k-1})$ lies on the discontinuity, then the Jacobian matrix may not exist, so that the covariance cannot be calculated. If the current point of linearization lies close to the discontinuity, the linearised estimates are not capable to account this discontinuous behavior (Julier and Uhlmann 1996, p. 9).

Further extensions or modifications of the Kalman filter algorithm exist, which are not only able to overcome these drawbacks of the EKF by addressing its approximation issues (Wan and Van der Merwe 2000) but also provide a derivative-less framework for new type of filters (Van der Merwe 2004). The class of such modified Kalman filters is summarized under the term *Sigma-Point Kalman filters*.

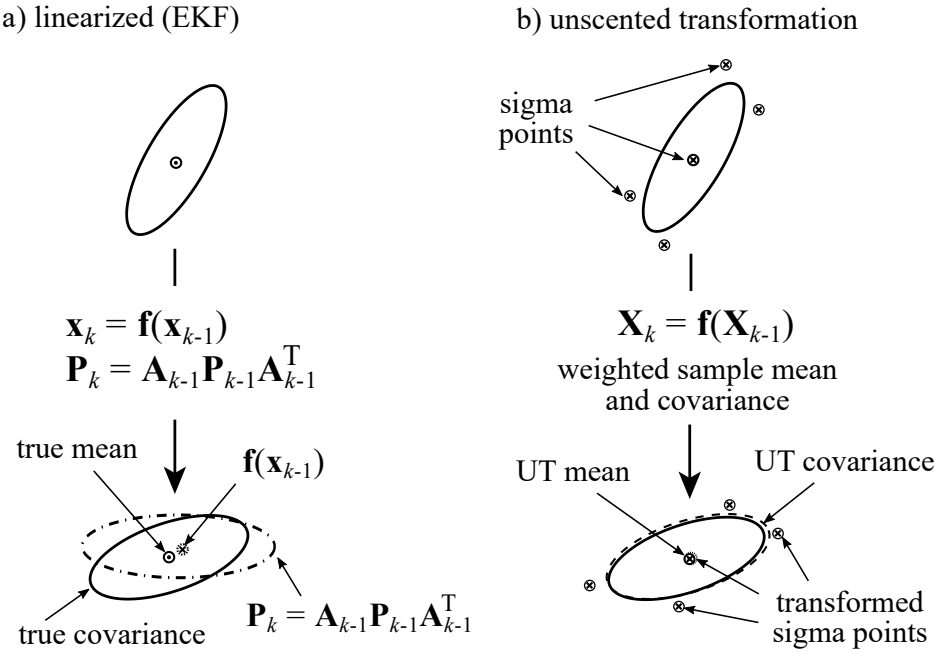

Figure 2.9: Example of the UT for mean and covariance propagation: comparison of a) first-order linearization (EKF) and b) unscented transformation (from Van der Merwe (2004))

b) *Sigma-Point Kalman filter* (SPKF)

The *Sigma-Point Kalman filter* (SPKF) is a recursive, nonlinear filtering algorithm developed in the Kalman filtering framework, which works with so-called *sigma-points* (SP)[2]. The sigma-points are deterministically chosen vector points in the state space with associated weighting factors representing the properties of a stochastic random variable (mean and covariance) in a particular way.

The first and most commonly known representative of SPKF is the *Unscented Kalman filter* (UKF). The UKF appeared first in Julier and Uhlmann (1997), although the idea and method was originally initiated two years before by Uhlmann (1995) as a new generalized approach for filtering dynamic systems with nonlinear processes and observation models. The fundamental component of the UKF is the *unscented transformation* (UT) which uses a set of appropriately chosen weighted *sigma-points* to parameterize the means and covariances of probability distributions (Julier and Uhlmann 1997). The idea is that it is mathematically easier to transform a probability distribution of a random variable through a nonlinear function by using a set of weighted vector points, instead of using an entire probability density function (Julier and Uhlmann 1996). Fig. 2.9 illustrates the idea and the procedure of the unscented transformation in comparison to the EKF.

While the EKF requires differentiable model equations and a sufficiently small calculation step size to guarantee a stable behavior, the *unscented transformation* allows a derivative-less propagation of the statistical properties of stochastic random variables through a nonlinear function and is therefore compatible with any arbitrary nonlinear process and observation model; even with non-

[2] also called *cubature points* by Arasaratnam and Haykin (2009); corresponding filters referred to as *Cubature Kalman filters* (CKF)

differentiable or discontinuous functions (Julier and Uhlmann 1996). Since the evaluation of Jacobians is not required, the implementation is also far easier compared to EKF. Furthermore, the prediction yields to more accurate mean and covariance estimates that those through linearization, see Fig. 2.9. In Julier and Uhlmann (1996), it is shown that the unscented algorithm is able to partially incorporate information from the higher order moments of approximation, leading to greater accuracy. Wan and Van der Merwe (2000) demonstrates the performance gain in applications including state, parameter and dual estimation, see Sect. 2.3.3.

The *unscented transformation* consists of the following steps:

1. Compute sigma-points $\mathbf{X}_{k-1}$
2. Assign weights w_i to each sigma-point
3. Transform the sigma-points through nonlinear function $\mathbf{X}_k^- = \mathbf{f}(\mathbf{X}_{k-1}, \mathbf{u}_{k-1})$
4. Compute the mean $\mathbf{x}_k^-$ and covariance $\mathbf{P}_k^-$ from weighted and transformed points via integration rule

There are several filter designs based on the UT-framework that differ in the number of evaluated sigma-points and the choice of the numerical integration rule for approximating the probability density of the random variables (B. Ritter 2020, p. 21). In Julier and Uhlmann (2002) UT-methods are examined for minimizing the number of sigma-points for real-time control, estimation and filtering applications. Van der Merwe and Wan (2001) have developed a square root formulation of the UT[3] which propagates the mean and square root of the covariance matrix, instead of the covariance matrix itself (Julier and Uhlmann 2004).

c) *Cubature Kalman filter* (CKF)

The *Cubature Kalman Filter* (CKF) is a nonlinear Bayesian filter introduced by Arasaratnam (2009), which uses an efficient, spherical-radial cubature integration rule which scales only $2n_x$ sigma-points equally and linearly with the state vector dimension n. Compared to other SPKF, the CKF is very easy to implement, well-suited for higher-order systems and supposed to be superior to the UKF with regard to robustness (Arasaratnam and Haykin 2009). However, it is noteworthy, that the CKF represents a special case of the UKF with a certain choice of filter parameters (B. Ritter 2020). Due to these advantageous properties in terms of implementation effort and robustness, the CKF and its square root version SR-CKF are considered in the remainder of this thesis. The notation used corresponds to B. Ritter (2020).

The initialization of the CKF starts with the initialization of the initial values for the state estimate (mean) $\mathbf{x}_0$ and the initial error covariance $\mathbf{P}_0$. The required $2n_x$ sigma-points are equally weighted and only depend on the system dimensionality n_x (number of system states)

$$w_\mathrm{p} = \sqrt{n_x} \qquad \text{and} \qquad w_\mathrm{m} = \frac{1}{2n_x} \tag{2.41}$$

[3] there are also numerically more robust square-root versions of UKF and CKF, denoted as SR-UKF and SR-CKF

The prediction step starts with the evaluation of the set of sigma-points $\boldsymbol{\mathcal{X}}_{k-1} \in \mathbb{R}^{(n_x \times 2n_x)}$ from the previous state estimate $\hat{\mathbf{x}}_{k-1}$ and the matrix square-roots of the previous error covariance matrix $\mathbf{P}_{k-1}$, which is determined by using the efficient and stable Cholesky decomposition $\mathbf{P} = \mathbf{C}\mathbf{C}^{\mathrm{T}}$ (Golub and Van Loan 1996)

$$\boldsymbol{\mathcal{X}}_{k-1} = \hat{\mathbf{X}}_{k-1} + w_{\mathrm{p}} \left[\sqrt{\mathbf{P}_{k-1}} \quad -\sqrt{\mathbf{P}_{k-1}} \right] = \hat{\mathbf{X}}_{k-1} + w_{\mathrm{p}} \left[\mathbf{C}_{k-1}^{\mathrm{T}} \quad -\mathbf{C}_{k-1}^{\mathrm{T}} \right] \tag{2.42}$$

where $\hat{\mathbf{X}}_{k-1} \in \mathbb{R}^{(n_x \times 2n_x)}$ is a matrix containing $2n_x$ column vectors of $\hat{\mathbf{x}}_{k-1}$. The prediction procedure is carried out as follows: Each sigma-point is transferred through the nonlinear process model $\mathbf{f}(\cdot)$, yielding a set of transformed samples

$$\boldsymbol{\mathcal{X}}_k^* = \mathbf{f}\left(\boldsymbol{\mathcal{X}}_{k-1}, \mathbf{u}_{k-1}\right). \tag{2.43}$$

The new predicted state estimate $\hat{\mathbf{x}}_k^-$ (mean) results from the weighted sum of transformed sigma-points $\boldsymbol{\mathcal{X}}_k^*$

$$\hat{\mathbf{x}}_k^- = w_{\mathrm{m}} \sum_{i=1}^{2n_x} \boldsymbol{\mathcal{X}}_k^*(:, i). \tag{2.44}$$

The prediction of error covariance is determined as

$$\mathbf{P}_k^- = w_{\mathrm{m}} \boldsymbol{\mathcal{X}}_k^* \left(\boldsymbol{\mathcal{X}}_k^*\right)^{\mathrm{T}} - \hat{\mathbf{x}}_k^- \left(\hat{\mathbf{x}}_k^-\right)^{\mathrm{T}} + \mathbf{Q}_{k-1}, \tag{2.45}$$

where $\mathbf{Q}_{k-1}$ is the process noise covariance. The prediction procedure is carried out only using standard vector and matrix operations, which means that the algorithm is suitable for any choice of process model.

The correction step starts with an update of the $2n_x$ sigma-points under the consideration of the new matrix square root of the predicted covariance matrix computed via Cholesky decomposition $\mathbf{P}_k^- = \mathbf{C}_k^- \mathbf{C}_k^{-\mathrm{T}}$

$$\boldsymbol{\mathcal{X}}_k^- = \hat{\mathbf{X}}_k^- + w_{\mathrm{p}} \left[\mathbf{C}_k^{-\mathrm{T}} \quad -\mathbf{C}_k^{-\mathrm{T}}, \right] \tag{2.46}$$

which are then transformed through the nonlinear observation model $\mathbf{h}(\cdot)$

$$\boldsymbol{\mathcal{Y}}_k^* = \mathbf{h}\left(\boldsymbol{\mathcal{X}}_k^-, \mathbf{u}_k\right), \tag{2.47}$$

in order to determine the predicted output

$$\hat{\mathbf{y}}_k = w_{\mathrm{m}} \sum_{i=1}^{2n_x} \boldsymbol{\mathcal{Y}}_k^*(:, i). \tag{2.48}$$

To compute the Kalman gain $\mathcal{K}_k$, first the cross covariance matrix $\mathbf{P}_k^{\mathrm{xy}}$

$$\mathbf{P}_k^{\mathrm{xy}} = w_{\mathrm{m}} \boldsymbol{\mathcal{X}}_k^* \left(\boldsymbol{\mathcal{Y}}_k^*\right)^{\mathrm{T}} - \hat{\mathbf{x}}_k^- \left(\hat{\mathbf{y}}_k\right)^{\mathrm{T}} \tag{2.49}$$

and the innovations covariance $\mathbf{P}_k^{\mathrm{yy}}$ considering measurement noise covariance matrix $\mathbf{R}_k$ must be determined by

$$\mathbf{P}_k^{\mathrm{yy}} = w_{\mathrm{m}} \boldsymbol{\mathcal{Y}}_k^* \left(\boldsymbol{\mathcal{Y}}_k^*\right)^{\mathrm{T}} - \hat{\mathbf{y}}_k \left(\hat{\mathbf{y}}_k\right)^{\mathrm{T}} + \mathbf{R}_k. \tag{2.50}$$

The Kalman gain $\mathcal{K}_k$ results then to

$$\mathcal{K}_k = \mathbf{P}_k^{\mathrm{xy}} \left(\mathbf{P}_k^{\mathrm{yy}}\right)^{-1}. \tag{2.51}$$

For the inverse of $\mathbf{P}_k^{\mathrm{yy}}$ to exist, the measurement noise covariance matrix $\mathbf{R}_k$ must be chosen appropriately (e.g. $\mathbf{R}_k \neq 0$). The corrected covariance matrix yields then to

$$\mathbf{P}_k = \mathbf{P}_k^{-} - \mathcal{K}_k \mathbf{P}_k^{\mathrm{yy}} \mathcal{K}_k^{\mathrm{T}}. \tag{2.52}$$

Finally, the corrected state estimate is computed from estimation error $\mathbf{e}_k = \mathbf{y}_k - \hat{\mathbf{y}}_k$

$$\hat{\mathbf{x}}_k = \hat{\mathbf{x}}_k^{-} + \mathcal{K}_k \left(\mathbf{y}_k - \hat{\mathbf{y}}_k\right). \tag{2.53}$$

The tuning of the CKF is done similarly to the EKF using the noise covariance matrices $\mathbf{Q}_{k-1}$ and $\mathbf{R}_k$. A numerically more robust, square-root version of the CKF is first presented in Arasaratnam and Haykin (2008). The *Square-Root Cubature Kalman filer* (SR-CKF) propagates the mean and the square roots of the covariance $\mathbf{S}_k = \sqrt{\mathbf{P}_k}$, instead of error covariances themselves. This leads to an improved numerical accuracy and guarantees symmetry and positive definiteness of the covariances, but at the expense of increased computational complexity (Arasaratnam 2009).

2.3.3 Combined state and parameter estimation

Since state estimation methods are usually based on a process model, the parameters $\boldsymbol{\theta}$ of the underlying process model must be known in advance and with sufficient accuracy, otherwise both state and covariance prediction would lead to great errors or even divergence. Another problem occurs in model identification if not enough process variables $\mathbf{x}$ are measured to determine all required model parameters $\boldsymbol{\theta}$. These process variables are often either not fully or only partially measurable which is defined by the model's output equation (2.38). For instance, if the derivative of variable is measurable but not its integral value, which is to be estimated, a *state variable filter*, providing appropriately filtered derivatives/integrals of signal, can be applied, see for more details Isermann and Münchhof (2011). However, in many applications the relations between the measured and unmeasured states have rather a physical and much more complex than temporal nature which requires the involvement of state estimation techniques in the model identification procedure.

If both, model parameters are unknown and systems state are not measureable, model identification requires a combination of state estimation and parameter estimation. There are two ways how a combined state and parameter estimation can be carried out:

- *Joint estimation*
- *Dual estimation*

In both cases, nonlinear state estimators such as the extended Kalman filter (EKF) or Sigma-point Kalman filter (SPKF) are applied.

Joint Estimation

The *joint estimation* represents a direct approach for estimating state variables and parameters simultaneously. This approach was introduced almost at the same time by Kopp and Orford (1963) and Cox (1964) in the context of adaptive control. The idea is to add the parameters to be estimated into the already existing state space representation, so that the state vector $\mathbf{x}_k$ and the parameter vector $\boldsymbol{\theta}_k$ are concatenated into one single *joint state vector* $\boldsymbol{\xi}_k = [\mathbf{x}_k \ \boldsymbol{\theta}_k]^{\mathrm{T}}$ and apply nonlinear state estimation algorithm (Ljung 1999; Isermann and Münchhof 2011).

For this reason, the parameters must be modeled as dynamic processes. In the simplest case, the parameters $\boldsymbol{\theta}$ of a time-invariant dynamic process are assumed to be constant. A general model approach for a constant parameter can be derived from the following differential equation

$$\frac{\mathrm{d}\theta}{\mathrm{d}t} = 0. \tag{2.54}$$

A discretization of this continuous parameter model (4.76) leads to a first order Markovian process, where the parameter $\boldsymbol{\theta}_k$ represents a random variable disturbed by a zero-mean, white noise $\mathbf{w}_{k-1}$ written as

$$\boldsymbol{\theta}_k = \boldsymbol{\theta}_{k-1} + \mathbf{w}_{k-1}. \tag{2.55}$$

The overall state space model for the joint estimation problem is then given as

$$\begin{aligned} \boldsymbol{\xi}_k &= \begin{bmatrix} \mathbf{x}_k \\ \boldsymbol{\theta}_k \end{bmatrix} = \begin{bmatrix} \mathbf{f}\left(\mathbf{x}_{k-1}, \mathbf{u}_k\right) \\ \mathbf{I} \cdot \boldsymbol{\theta}_{k-1} \end{bmatrix} + \begin{bmatrix} \mathbf{w}_{\mathrm{x},k} \\ \mathbf{w}_{\theta,k} \end{bmatrix}, \\ \mathbf{y}_k &= \mathbf{h}\left(\boldsymbol{\xi}_k\right) + \mathbf{v}_k, \end{aligned} \tag{2.56}$$

where $\mathbf{w}_{\mathrm{x},k}$ is the process state noise, $\mathbf{w}_{\theta,k}$ the parameter noise and $\mathbf{v}_k$ the measurement noise affecting the joint state vector or model output, respectively.

The filter tuning is done by choosing the corresponding covariance matrices $\mathbf{Q}_{x,k} = \mathrm{E}\{\mathbf{w}_{\mathrm{x},k}(\mathbf{w}_{\mathrm{x},k})^{\mathrm{T}}\}$, $\mathbf{Q}_{\theta,k} = \mathrm{E}\{\mathbf{w}_{\theta,k}(\mathbf{w}_{\theta,k})^{\mathrm{T}}\}$ and $\mathbf{R}_k = \mathrm{E}\{\mathbf{v}_k(\mathbf{v}_k)^{\mathrm{T}}\}$ within the Kalman filtering algorithm, see previous Sect. 2.3.2. The relation between the process covariance matrices $\mathbf{Q}_{x,k}$ and $\mathbf{Q}_{\theta,k}$ determines whether the Kalman filter algorithm relies more on the underlying process or parameter model. For instance, if the diagonal elements of the parameter covariance matrix $\mathbf{Q}_{\theta,k}$ are set to zero, the Kalman filter would only adjust the states $\mathbf{x}_k$ but not the parameters $\boldsymbol{\theta}$ during filtering. On the other hand, for the extreme case $\mathbf{Q}_{x,k} = 0$, the estimator relies fully on the state model and adjusts only the parameter estimates. So, an adaptation of the parameters can be controlled by manipulating the corresponding covariance matrix elements of $\mathbf{Q}_{\theta,k}$.

The initial values of the states $\mathbf{x}_0$ and parameters $\boldsymbol{\theta}_0$ as well as the corresponding initial error covariances $\mathbf{P}_0$ have to be selected wisely to avoid filter divergence. An advantage of joint estimation is the fact that the covariances of states and parameters can be set more easily relative to each other. Furthermore, since the mathematical relations between states and parameters are integrated in the filter model, joint estimation shows a more robust behavior against poorly chosen initial values. However, a disadvantage of the joint state formulations is that it leads to an increase of system order

and to a higher computational effort for the matrix computations within the filtering algorithm. Joint estimation is also applied in time-varying system to cope with changing parameters over time (Chui and Chen 2017).

Dual Estimation

In contrast to *joint estimation*, a *dual estimation* is carried out by using two separate estimators, one for the state estimation and another one for the estimation of parameters (Wan and Nelson 1997; Nelson 2000). The state estimator determines the state estimate $\hat{\mathbf{x}}_k$ based on the parameter estimates $\hat{\boldsymbol{\theta}}_k$, which are provided by a separate parameter estimator and the parameter estimator uses the state estimates $\hat{\mathbf{x}}_k$ provided by the state estimator. Consequently, the state estimates function as additional input of the parameter estimator and vice versa. Fig. 2.10 shows the difference between joint and dual estimation by means of their structure and signal flow.

In the *dual estimation* scheme, separate state space representations are used for the system states and the parameters. The *state estimation model* corresponds to Eq. (2.38), including the a priori parameter estimates $\hat{\boldsymbol{\theta}}_k^-$ as additional input

$$\begin{aligned} \hat{\mathbf{x}}_k &= \mathbf{f}\left(\hat{\mathbf{x}}_{k-1}, \hat{\boldsymbol{\theta}}_k^-, \mathbf{u}_{k-1}\right) + \mathbf{w}_{\mathbf{x},k}, \\ \hat{\mathbf{y}}_k &= \mathbf{h}\left(\hat{\mathbf{x}}_k, \hat{\boldsymbol{\theta}}_k^-\right) + \mathbf{v}_k. \end{aligned} \tag{2.57}$$

The general formulation of the *parameter model* $\mathbf{g}(\cdot)$ can be given correspondingly as function of the a priori state estimates $\hat{\mathbf{x}}_k^-$ and the parameter estimates $\hat{\boldsymbol{\theta}}_{k-1}$ and inputs $\mathbf{u}_{k-1}$

$$\begin{aligned} \hat{\boldsymbol{\theta}}_k &= \mathbf{g}\left(\hat{\boldsymbol{\theta}}_{k-1}, \hat{\mathbf{x}}_k^-\right) + \mathbf{w}_{\theta,k}, \\ \hat{\mathbf{y}}_k &= \mathbf{j}\left(\hat{\boldsymbol{\theta}}_k, \hat{\mathbf{x}}_{k-1}\right) + \mathbf{v}_k. \end{aligned} \tag{2.58}$$

The output function can be formulated as function of the a priori state estimates $\hat{\mathbf{x}}_k^-$ and the parameter estimates $\hat{\boldsymbol{\theta}}_k$. This can be any arbitrary linear or nonlinear model containing the paremeters to be identified, see i.e. Singhal and Wu (1989), Puskorius and Feldkamp (1991) and Wan, Van der Merwe, and Nelson (2000) for neural networks.

If the parameters are assumed to be constant and independent of the current system state, following parameter space model results for (2.58), see Wan, Van der Merwe, and Nelson (2000),

$$\begin{aligned} \boldsymbol{\theta}_k &= \boldsymbol{\theta}_{k-1} + \mathbf{w}_{\theta,k}, \\ \mathbf{y}_k &= \mathbf{j}\left(\boldsymbol{\theta}_k, \mathbf{x}_k\right) + \mathbf{v}_k, \end{aligned} \tag{2.59}$$

where the parameters $\boldsymbol{\theta}_k$ are modeled again as first order Markovian process as in Eq. (2.55), which corresponds to a stationary process excited by a zero-mean white noise $\mathbf{w}_{\theta,k}$. By modeling of the corresponding noise covariance matrix $\mathbf{Q}_{\theta,k}$ and the initial parameter-error covariance determines the performance of the parameter estimation.

The advantage of the *dual estimation scheme* is that modeling of process and measurement noise can be done separately, which leads to significant simplification of the filter tuning. Compared

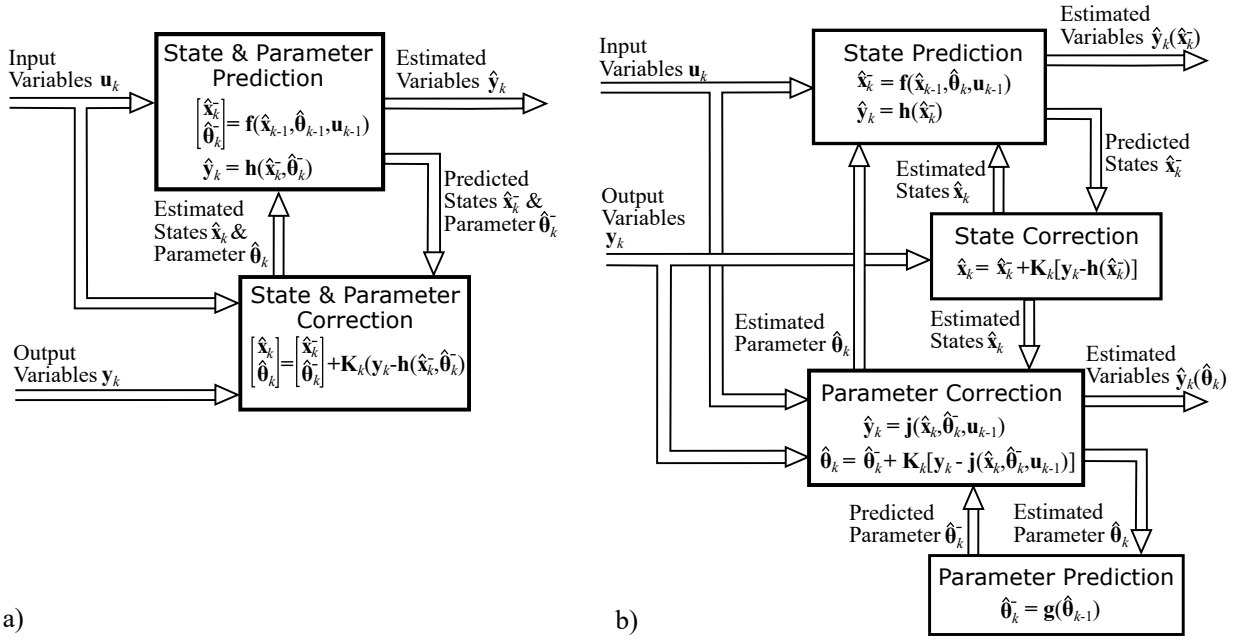

Figure 2.10: State and parameter estimation using Kalman filtering: a) Joint Estimation b) Dual Estimation

to joint estimation, the separation of one high order state space model into two lower order state space model reduces the computational effort. Additionally, switching off the estimation can be implemented much easier.

Furthermore, it allows a better handling between different model structures and approaches. In the scope of this work, it enables the possibility to use separate model types to combine physical models with experimental models, leading to semi-physical models. It is also a concept, which finds common usage in the field of machine learning; see i.e. Wan and Nelson (1997) or Nelson (2000), where the dual estimation scheme is applied on a broader class of nonlinear estimation problems.

2.3.4 Adaptive Kalman filters

Poor model accuracy, because of e.g. model simplifications or unconsidered time-varying behavior, can lead to divergence of the Kalman filter algorithm. Since the estimation models, which are incorporated within the Kalman filter algorithm, are only approximations of the real systems and the statistics of process and measurement noise are not certainly known, one has to ensure optimality and convergence of the estimation result by applying filter adaptation techniques (B. Ritter 2020). In general, there are two ways how filter adaptation can be implemented.

One approach is to adapt the model parameters $\boldsymbol{\theta}$ of the filter model $\mathbf{f}(\mathbf{x}, \boldsymbol{\theta}, \mathbf{u})$ in order to further reduce the deviation between the measurements of the real system and the predictions based on the filter model, see Fig. 2.10. This can be done by using a joint or dual estimation scheme, as

described in the previous Sect. 2.3.3. However, an appropriate filter tuning by means of adapting noise parameters still remains necessary to guarantee robust filtering.

A second approach deals with the adaptive design of the filter noise parameters. The usually pre-assumed constant filter noise covariances are adapted in order to meet with the real behavior. Moreover, an adaptation of the filter parameters also allows switch on and off of the estimation in particular situations. For example, in the case of pure parameter estimation, estimation algorithm can be activated only in certain situations, where it is known from empirical knowledge that the parameters may change. If the time-varying behavior of a parameter is known, but the estimation model does not cover this behavior, this time-varying behavior can be taken into account by adapting the filter noise parameters accordingly. This can be done by assuming a dynamic behavior for the filter noise parameters ($\dot{\mathbf{Q}}(t) \neq 0$).

In Wan, Van der Merwe, and Nelson (2000), a weight decay method is applied that reduces the covariances of the parameter noise variables $\mathbf{w}_{\theta,k}$ in order to switch off the adaptation over time. Bechtloff (2018) uses a first order low-pass element with other state variables as inputs for the modeling of the dynamic behavior of the filter noise parameters. However, a profound understanding of the dynamic system behavior is absolutely mandatory for successful implementation of this kind of approach.

If the process and measurement noise filter parameters are difficult to provide, a possible modification of the Kalman filtering algorithm is to concatenate the state variable $\mathbf{x}_k$ and the noise filter parameters $\mathbf{w}_k, \mathbf{v}_k$ together into a joint state

$$\tilde{\mathbf{x}}_k = \begin{bmatrix} \mathbf{x}_k \\ \mathbf{w}_k \\ \mathbf{v}_k \end{bmatrix} \tag{2.60}$$

This allows simultaneous estimation of both, state variables and corresponding noise parameters. The filter parameters are then optimized in accordance to the propagated estimation error. Since process and measurement noise are simultaneously estimated, only the initial values of the error covariance $\mathbf{P}_0$ have to be defined in advance for the filter tuning. A disadvantage of this method is the significant increase in system order.

Another possibility is to realize an adaptive Kalman filter is to use *adaptation rules* which are typically based on the filter innovation $\mathbf{e}_k = \mathbf{y}_k - \hat{\mathbf{y}}_k$, whereby different methods such as correlation method, Maximum-Likelihood estimation or a so called Master-Slave-Approach are applied to adapt the filter covariances within an UKF framework (Mehra 1970; Mehra 1972; Song, Qi, et al. 2006; Song, Jiang, et al. 2007). The Master-Slave approach uses a dual estimation scheme, where the filter states and filter noise parameters are estimated using two separate and parallel working Kalman filter. A comprehensive overview of filter adaptation rules is given in B. Ritter (2020).

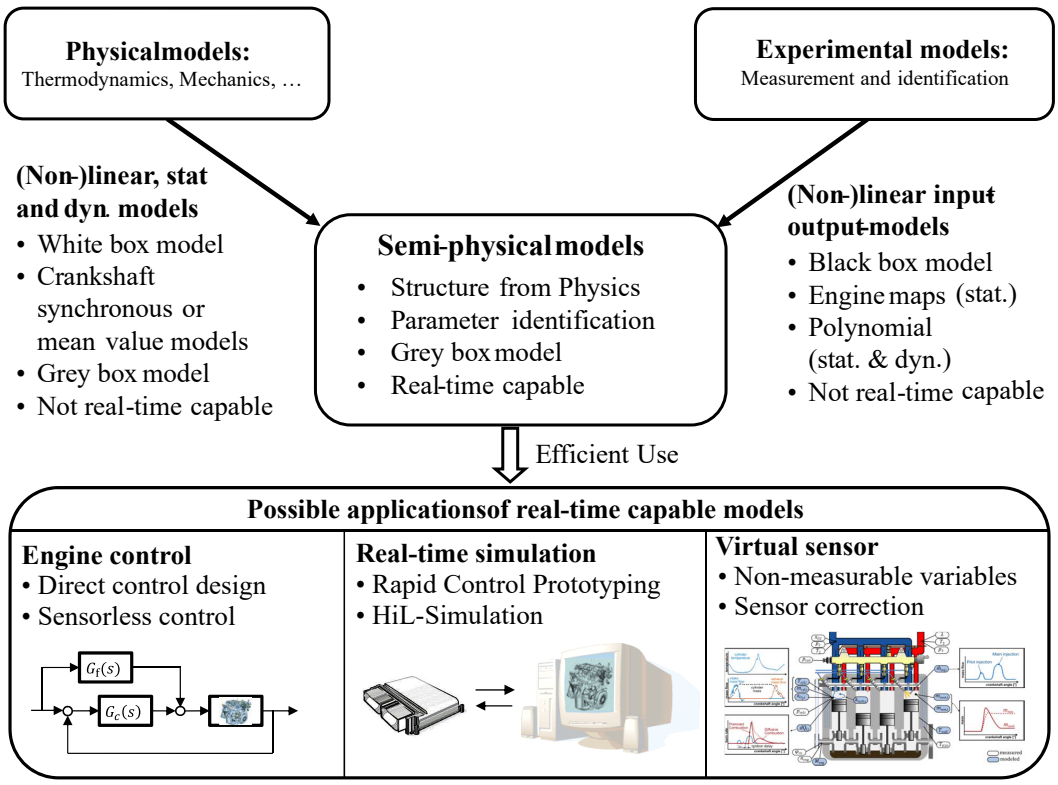

Figure 2.11: Concept of semi-physical modeling with online-parameter estimation

2.4 Semi-physical modeling with online-parameter estimation

Both, theoretical and experimental modeling have particular advantages and disadvantages, a combination of both has several benefits in the ECU calibration process. A *semi-physical modeling approach* is proposed, that combines the advantages of physical and experimental modeling and overcomes their disadvantages. Due to a lean model structure and adaptability, *semi-physical models* are particularly suitable for various real-time applications, see Fig. 2.11.

Since modeling is generally system-specific and purpose-oriented, there is no standard procedure for semi-physical modeling. However, some guidelines can be formulated, which can be derived considering the aspects of physical interpretability, real-time capability and model identification. The overall goal is always to generate a model that is as accurate as possible and that reproduces the real behavior of the system. The following sections give some recommendations how to proceed with the derivation of a semi-physical real-time model.

Basic idea of semi-physical modeling

By using fundamental but simple physical laws for modeling provides physical interpretability of model structure and their parameters, and ensures transferability of the resulting model to other systems. Only the essential and observable properties should be modeled; ideally on the basis of *linear-in-parameter equations* to allow the application of linear parameter estimation methods.

However, modeling of real world influences often leads to model equations, where the parameters are neither constant nor affect linearly the equation's output. In these cases, simplifications or mathematical approximations must be made in order to achieve a linear-in-parameter model description while maintaining a physically oriented model structure. In many cases, nonlinearity can be extracted and taken into account by modelling a variability in physical parameters $\boldsymbol{\theta}$

$$\begin{aligned} \dot{\mathbf{x}}(t) &= \mathbf{f}(\mathbf{x}(t), \mathbf{u}(t), \boldsymbol{\theta}), \\ \mathbf{y}(t) &= \mathbf{h}(\mathbf{x}(t), \boldsymbol{\theta}). \end{aligned} \tag{2.61}$$

To ensure model adjustment to real system behavior, the deviation between a simplified semi-physical model and the real system behavior is then addressed by modeling a variable parameter behavior $\boldsymbol{\theta} = \mathbf{g}(\cdot)$.

The variable physical parameters $\boldsymbol{\theta}$ must be determined for a wide operating range by applying parameter estimation techniques. Thereby, the parameter behavior must be investigated regarding their dependencies on other variables such as input variables $\mathbf{u}(t)$, system states $\mathbf{x}(t)$, operating point variables or any other arbitrary variables that stand in a relation to the physical parameter. The most relevant influence variables are summarized in the parameter model input vector $\mathbf{z}(t)$ (z-regressor).

Since the variable parameter behavior is usually very system-specific and consequently difficult to model physically or empirically, experimental modeling has proven to be particularly suitable for the task of mapping any parameter behavior as follows, see Sect. 2.2,

$$\boldsymbol{\theta}(t) = \mathbf{g}(\mathbf{w}, \mathbf{z}(t)), \tag{2.62}$$

where $\mathbf{w}$ represent the parameters (weighting factors) of the parameter model and $\mathbf{z}(t)$ includes all input variables, system state variables and operating point variables affecting the parameter behavior. Any available system knowledge regarding the dependencies between the parameters and other variables should be taken into account to simplify the experimental modeling, e.g. by suitable selection of $\mathbf{z}(t)$.

As mentioned in Sect. 2.2, there several different other types of experimental models, which have proven to have advantageous properties for the approximation of complex nonlinear processes. However, the essential dynamic system behavior should be represented by the physical model structure, so that its physical parameters no longer show a dynamic behavior and are constant for a given input $\mathbf{z}(t)$. As a consequence, simple experimental modeling approaches can be used, which do not involve additional iterative partitioning algorithms and allow the application of online parameter estimation techniques for model identification.

Bringing all parts together leads to a generalized formulation for a semi-physical model

$$\begin{aligned} \dot{\mathbf{x}}(t) &= \mathbf{f}(\mathbf{x}(t), \mathbf{u}(t), \boldsymbol{\theta}(t)), \\ \boldsymbol{\theta}(t) &= \mathbf{g}(\mathbf{w}, \mathbf{z}(t)), \end{aligned} \tag{2.63}$$

consisting of a physically oriented model $\mathbf{f}(\cdot)$ for the behavior of the system states $\mathbf{x}$ and an experimental parameter model $\mathbf{g}(\cdot)$ providing the physical parameters $\boldsymbol{\theta}$. The model output $\mathbf{y}$

represents only the available measurements

$$\mathbf{y}(t) = \mathbf{h}(\mathbf{x}(t)), \tag{2.64}$$

which are used for the identification of the overall model and the estimation of non-measurable system states. The concepts for combined estimation of state variables and parameters are presented in the previous Sect. 2.3.3. Model identification involves then the determination of the weighting factors $\mathbf{w}$ of the experimental parameter models. Estimated state variables $\hat{\mathbf{x}}(t)$ can further be used for online identification of the parameter models (training).

The concept for the generation of semi-physical real-time models comprises the following core elements:

(a) Derivation of lean physically oriented model structure based on fundamental physical equations with unknown physical parameters which are assumed to be constant for a specific operating point (Sect. 2.1)
(b) Application of online state and parameter estimation, where non-measurable state variables $\hat{\mathbf{x}}$ and unknown physical parameters $\hat{\boldsymbol{\theta}}$ are estimated (Sects. 2.3.2 to 2.3.4)
(c) Experimental modeling of unknown physical parameters in dependence of input $\mathbf{u}$, state $\hat{\mathbf{x}}$ and operating point variables $\mathbf{z}$ (Sect. 2.2) by applying online-capable parameter identification methods (Sect. 2.3.1)

These core elements and the resulting signal flow structure of semi-physical modeling with combined state and parameter estimation techniques are shown in Fig. 2.12. The equations of the semi-physical model are transferred into discrete-time representation.

(a) Derivation of semi-physical models for combustion engines

In Fig. 2.12 (a), the semi-physical model consists of a physical behavior model $\mathbf{f}(\cdot)$ and an experimental model $\mathbf{g}(\cdot)$ for the physical parameters $\boldsymbol{\theta}$. The physical model parameters $\boldsymbol{\theta}$ are modeled experimentally $\mathbf{g}(\mathbf{z}, \mathbf{u})$ as functions of engine operating point $\mathbf{z}$, e.g. engine speed and load, and/or of other influencing inputs $\mathbf{u}$, such as control variables or actuator positions.

The physical model parts of the semi-physical engine models differ in the particular *physical domains* used for modeling, e.g. fluid mechanics in airpath modeling, hydraulics in injection modeling or chemical kinetics in combustion modeling. The semi-physical modeling of the engine's subsystem (Fig. 1.10), the *airpath system* and the *cylinder group*, is treated separately in the following chapters 3 and 4.

In general, the physical parameters $\boldsymbol{\theta}$ can be either assumed to be constant or variable depending on the inputs $\mathbf{u}$, the system state $\mathbf{x}$, the operating point $\mathbf{z}$.[4] However, in practice, relevant influences

[4] Additionally, parameters can change slowly over time due to wear and tear. However, slow parameter changes are taken into account by rerunning parameter identification after a period of time, so that the influence of time t is then neglected.

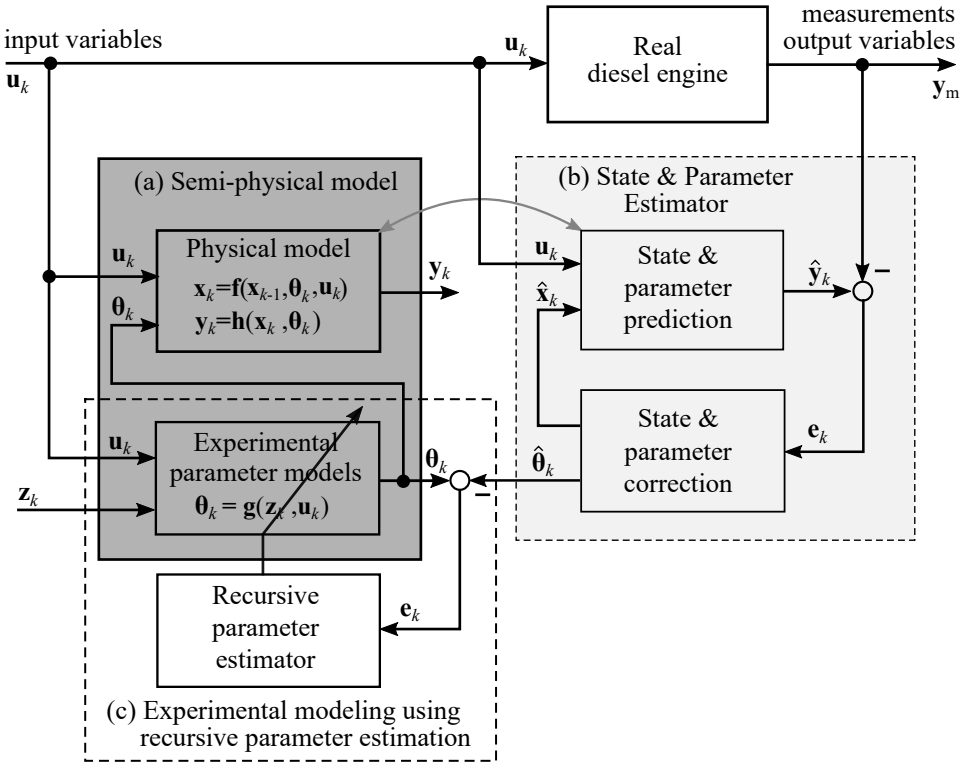

Figure 2.12: Scheme for semi-physical modeling with online state and parameter estimation: Physical model part of semi-physical model is also used for state and parameter estimation; estimated parameters of (b) serve as reference variables for the identification of (c) experimental parameter model

that affect model parameters are often known qualitatively, even though, the exact quantitative relation between the parameters and the influences is unknown.

A simple example of a semi-physical model is shown in Fig. 2.13. The engine mass flow can be modeled as a volumetric pump (Isermann 2014; Guzzella and Onder 2010). It approximates the engine mass flow $\dot{m}_{\text{eng}}$ through a theoretical pump mass flow $\dot{m}_{\text{th}}$ that is proportional to the engine speed n_{eng}, the displacement volume V_{d}, and the gas density $\rho = p/(RT)$. However, the real engine mass flow is reduced by real influences such as flow losses but can be taken into account by the volumetric efficiency η_{v}.

The volumetric efficiency η_{v} is typically a function of further variables such as intake pressure, engine speed or swirl flap position. It is commonly modeled experimentally by a look-up table that is identified during stationary measurements using the hot film sensor positioned in the intake pipe ($\dot{m}_{\text{eng,in}} \approx \dot{m}_{\text{hfm}}$, without EGR). Combining both, simple volumetric pump flow model and experimental model of volumetric efficiency, leads to a semi-physical engine mass flow model. In dynamic engine operation (or also with EGR), the hot film sensor measurements deviates from the real engine mass flow and thus cannot longer be used for experimental modeling of volumetric efficiency

$$\eta_{\text{v}} = \frac{\dot{m}_{\text{eng,in}}}{\dot{m}_{\text{th}}} = g(p_{\text{in}}, n_{\text{eng}}, \cdots) \approx \frac{\dot{m}_{\text{hfm}}}{\dot{m}_{\text{th}}}. \tag{2.65}$$

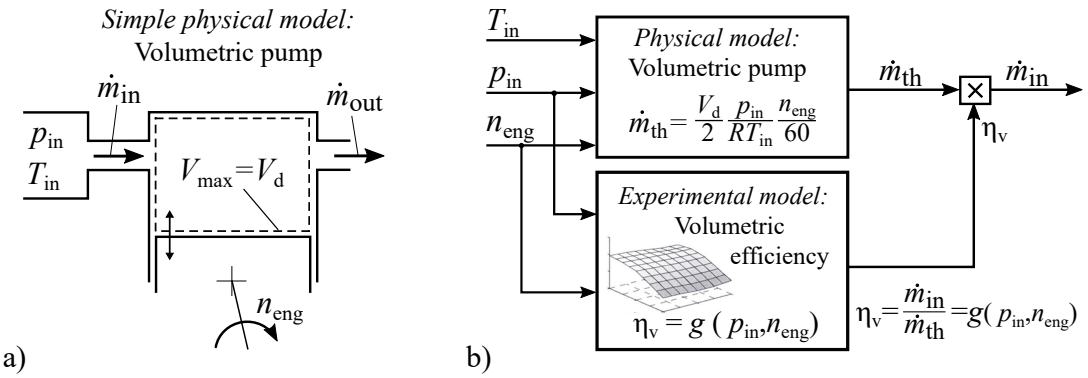

Figure 2.13: Example for semi-physical modeling of cylinder mass flow: a) Idealized cylinder mass flow modeled via volumetric pump and b) semi-physical modeling of the real cylinder mass flow with additional experimental model for the volumetric efficiency η_v

To identify this semi-physical engine mass flow model, a dual estimation problem must be solved, where the necessary reference variable $\dot{m}_{eng,in}$ must be determined first or in parallel in order to able to determine the look-up table parameters of the volumetric efficiency model, see Fig. 2.13 b). This represents a typical use case in modeling of technical systems where not enough measurements are available. By using combined state and parameter estimation methods, this dual estimation problem can be solved and thus the experimental model part of the semi-physical model can be identified.

(b) Application of state and parameter estimation

Fig. 2.14 shows the procedure for the generation of a semi-physical model using state and parameter estimation. A joint or dual estimation approach can be applied to estimate unknown system states $\hat{\mathbf{x}}_k$ and the physical parameters $\hat{\boldsymbol{\theta}}_k$ using the predictor-corrector principle of the Kalman filter algorithm, see Sect. 2.3.3. The state and parameter estimation is performed in steady-state engine operation.

In the prediction step, the physical model equations of the semi-physical model are used for model-based state and parameter prediction of both unmeasured state variables as well as unknown parameters. The parameters to be estimated $\hat{\boldsymbol{\theta}}_k$ are assumed to be constants during stationary engine operation. Within the state and parameter estimation $\hat{\boldsymbol{\theta}}_k$ are modeled according to Eq. (2.55) as first order Markovian processes. Using this parameter modeling approach ensures that the parameters converge to a constant value, see previous Sect. 2.3.3.

In the correction step, the a priori estimates are corrected on the basis of the available measurement variables $\mathbf{y}_m$ and the Kalman gain $\mathbf{K}_k$, calculated using the pre-defined filter parameters. How the filter parameters, represented by the noise covariance matrices $\mathbf{Q}_k$ and $\mathbf{R}_k$, are defined depends on the estimation problem and the underlying physical model used with the Kalman filter algorithm. However, $\mathbf{Q}_k$ and $\mathbf{R}_k$ are modeled in such a way that the parameter estimates are corrected more strongly than the estimated state variable. By doing so, the prediction model aligns with the real engine behavior by recursively correcting the estimated parameters. It is assumed that the real

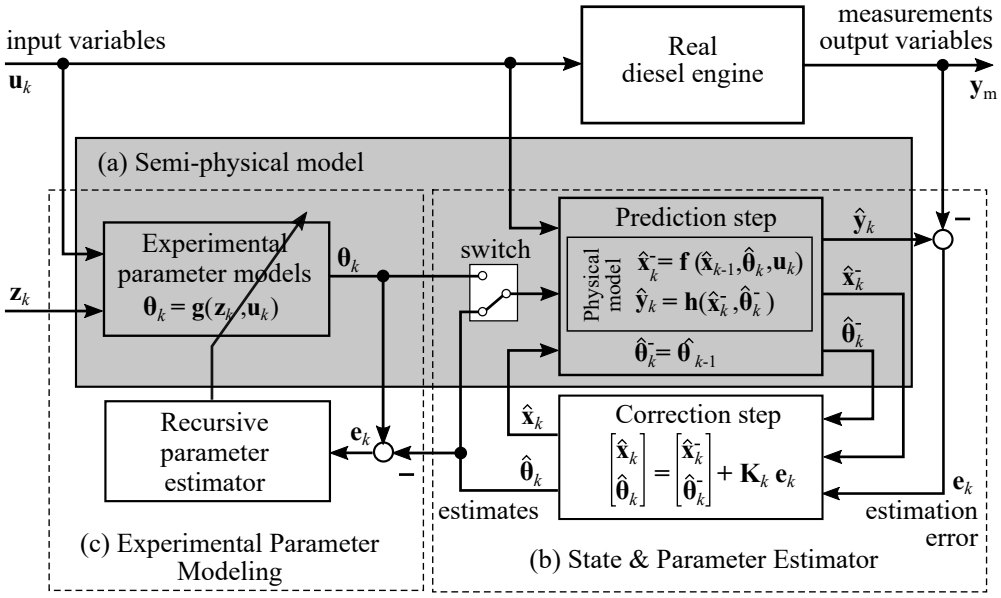

Figure 2.14: Procedure for generating semi-physical model (a) with state and parameter estimation (b): Prediction step results apriori estimates based on physical model equations, while in the correction step the prediction is corrected using the available measurement $\mathbf{y}_m$; (c) In parallel, the estimated parameters $\hat{\boldsymbol{\theta}}$ are modeled experimentally as a function of the operating point $\mathbf{z}$ and other input variables $\mathbf{u}$ (Kalman filter noise parameters $\mathbf{Q}_k$ (process noise covariance), $\mathbf{R}_k$ (measurement noise covariance) and initial values are not depicted

engine behavior in steady-state operation can be represented by the physical equations in the prediction model with a constant set of parameters.

Furthermore, manipulation of the filter parameters allows controlling the behavior of the Kalman filter algorithm during engine operation and to adjust the balance between prediction and correction according to the engine operation mode, see Sect. 2.3.4. For example, if the correction of the parameters is reduced via nulling of the associated filter parameters or due to convergence of parameters, the parameters become constant ($\hat{\boldsymbol{\theta}}_k = \hat{\boldsymbol{\theta}}_{k-1}$). Then, the output of the prediction step corresponds to the output of the semi-physical model for a given constant set of parameters.

In parallel, the estimated parameters $\hat{\boldsymbol{\theta}}$ are modeled experimentally as a function of current engine operating point $\mathbf{z}$ and other input variables $\mathbf{u}$, see Fig. 2.14 (c). After the parameter models are fully identified for the whole engine operation range, the correction step of the state and parameter estimation can be switched off completely. The parameters $\boldsymbol{\theta}_k$ are then provided by the identified experimental parameter models, which represents then a pure simulation of semi-physical models, emphasized by the greybox (a) in Fig. 2.14 (a) .

(c) Experimental modeling of estimated parameters

Using an experimental modeling approach, the variable behavior of a physical parameter θ is described mathematically by a radial-basis function according to Eq. (2.19) as sum of weighted

activation functions $\Phi_i(\mathbf{z})$

$$\theta(\mathbf{z}) = g(\mathbf{z}) = \sum_{i=1}^{L} \Phi_i(\mathbf{z}) w_i. = \theta(\mathbf{z}) = \mathbf{\Phi}(\mathbf{z})^{\mathrm{T}} \mathbf{w}, \tag{2.66}$$

where $\mathbf{w}^{\mathrm{T}} = [w_1, ..., w_L]$ is a column vector of the weight factors that need to be determined, and $\mathbf{\Phi}(\mathbf{z})$ includes all activation functions which are excited by the operating-point variables $\mathbf{z}$ acting as input. The number of the weights to be determined is given by the number p of input variables $\mathbf{z}^{\mathrm{T}} = [z_1, ..., z_p]$ and the required resolution and range of their input space. Online identification of the parameter models involves the determination of all weighting factors w_i along the entire input space of all considered influence variables $\mathbf{z}$. The estimated reference values $\hat{\boldsymbol{\theta}}_k$ for recursive identification of experimental parameter model $\mathbf{g}(\mathbf{z}_k, \mathbf{u}_k)$ are provided by the state and parameter estimator.

Fig. 2.16 a) shows the signal flow scheme of the online-identification of experimental parameter models. A pyramidal basis function is chosen as the activation function. Due to the piecewise linear relation it is well suited to be combined with the RLS algorithm (Fig. 2.5).

For each input variable $u_1, ..., u_p$, equidistant grid points $c_1, ..., c_L$ (centers of pyramidal basis functions) are defined across their input space. An initial matrix $\mathbf{W}$ containing the weight factors w (grid heights) is further defined according to input dimension p and the number of grid points of each input variable.

$$\mathbf{W} = \begin{bmatrix} w_{11} & \cdots & w_{1L} \\ \vdots & \ddots & \vdots \\ w_{L1} & \cdots & w_{LL} \end{bmatrix} \qquad \mathbf{P}_0 = \begin{bmatrix} p_{11} & \cdots & p_{1L} \\ \vdots & \ddots & \vdots \\ p_{L1} & \cdots & p_{LL} \end{bmatrix},$$

For each weighting factor w_i a corresponding diagonal element value $p_{0,i}$ of the initial error covariance $\mathbf{P}_0$ is assigned, which indicate the assumed estimation error at the start of the estimation process or represents the confidence of the weighting factor, respectively. The start of RLS-based identification is initiated by the initial error covariance matrix $\mathbf{P}_0$, whereas the value of each element of $\mathbf{P}_0$ determines the rate at which the corresponding weighting factors are adopted.

The parameter estimation problem of Eq. (2.66) can be significantly reduced if *only the currently excited activation functions* are considered. This leads to a local parameter estimation problem, where only the weighting factors of the currently active validity functions are estimated at the same time. This means, in case of two-dimensional input, only four weighting factors $[w_{\mathrm{i,j}}, w_{\mathrm{i+1,j}}, w_{\mathrm{i,j+1}}, w_{\mathrm{i+1,j+1}}]$ are estimated at the same time. Local parameter estimation for a two-dimension case is shown in Fig. 2.15. For multiple input case, the dimension of the estimation problem increases proportionally with the input dimension (dimension of $\mathbf{z}$). Presuming the estimation algorithm converges, the corresponding covariance $p_{0,i}$ of weighting factor w_i is minimized recursively. A decreasing error covariance indicates an increasing parameter confidence. The more the error covariance value is already minimized, the less the estimation algorithm adapts the corresponding weighting factors; until the error covariance can no further be minimized and parameter adaptation finally stops. This property offers a sort of training memory. A resetting of

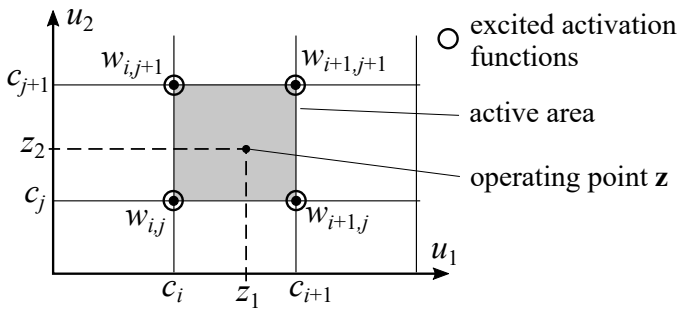

Figure 2.15: Local parameter estimation (weight factors w_{ij}) of an experimental model based on two-dimensional radial basis function with the input variables z_1 and z_2 defining the current operation point, compare Fig. 2.4 c) or Fig. 2.5 b); Only the circled (active) weight factors are estimated

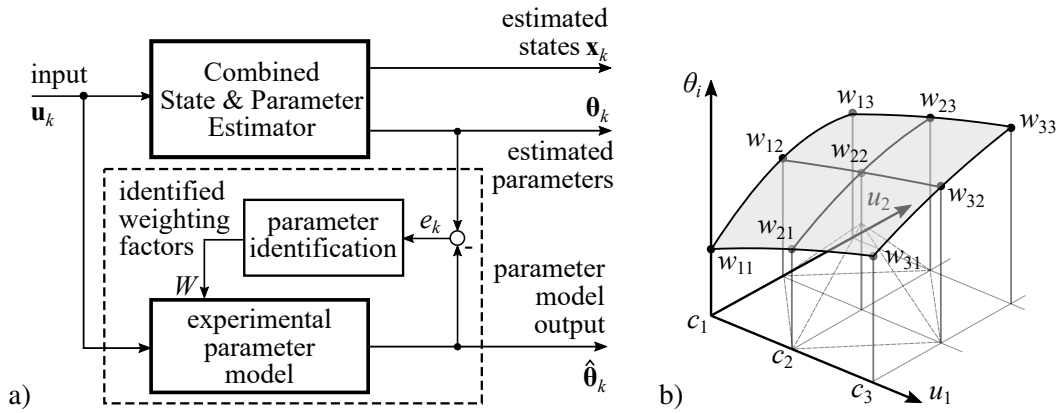

Figure 2.16: a) Structure and signal flow of online-identification of b) experimental parameter models of the estimated parameters using RLS algorithm, see also Sect. 2.3.1

the error covariance to the initial value leads to a rerun of the estimation, which allows changes in the parameter model, e.g. by wear and tear, to be accounted. Fig. 2.16 b) shows exemplarily a resulting experimental parameter model.

3 Semi-physical airpath modeling

A semi-physical airpath model of a diesel combustion engine with a variable exhaust gas turbocharger and both high- and low-pressure exhaust gas recirculation is derived, using the filling and emptying method with concentrated parameters. This includes modeling of the gas pipes and storages of the intake and exhaust system, the turbocharger, the exhaust gas recirculation, air filter and coolers as well as the actuators such as throttles and valves. The airpath state variables are modeled physically, whereas the unknown physical parameters are represented by experimental parameter models. By using recursive state and parameter estimation methods, gas state variables that are not measured in series engines, and the unknown model parameters are estimated online during stationary engine operation. Due to the lean model structure of the resulting semi-physical airpath model and the application of online-capable estimation methods, this modeling methodology can be used for an efficient model generation at the engine test bench.

The dynamic behavior of internal combustion engines, e.g. torque generation, emission characteristics, is significantly determined by the gas dynamics of the airpath system. The airpath dynamics are characterized by the charging pressure, the gas temperature, and the fresh air fraction in the intake manifold. These intake gas states determine the air charge, gas temperature and fresh air content in the combustion chambers of the cylinder group and therefore have a significant influence on combustion efficiency, the formation of pollutant emissions and the acoustics/lifetime of a combustion engine.

The structure of four-cylinder diesel engine with a VGT-turbocharger and dual-EGR is shown in Fig. 3.1. Due to cost reasons, series diesel engines are only equipped with a few sensors, so that most of the state variables depicted in Fig. 3.1 are not measured and unknown during engine operation. For load control, only the fresh air mass flow via the HFM sensor $\dot{m}_{\mathrm{hfm}}$, and the charge pressure $p_{2\mathrm{i}}$ and temperature $T_{2\mathrm{i}}$ in the intake manifold are available to the ECU of conventional series production engines. The mass flow sensor provides within the air path control the information about the fresh air mass flow $\dot{m}_{\mathrm{air}}(t) = \dot{m}_{\mathrm{HFM}}(t)$ entering the combustion engine. For control of emissions and exhaust aftertreatment systems (DOC/DPF), the exhaust gas temperature T_4 and the air-fuel ratio λ_4 in the exhaust tract are also measured, see Scharpf (2011).

Modern diesel engines are equipped with an adjustable exhaust gas turbocharger (VGT), offering higher engine performance, and with a high-pressure exhaust gas recirculation (HP-EGR). EGR is an engine internal measure to reduce NOx emissions by lowering peak combustion temperatures through the admixture of recirculated exhaust gas (inert gas) to the cylinder gas in the combustion chamber. By adding an additional low-pressure EGR, as depicted in Fig. 3.1, this NOx reduction

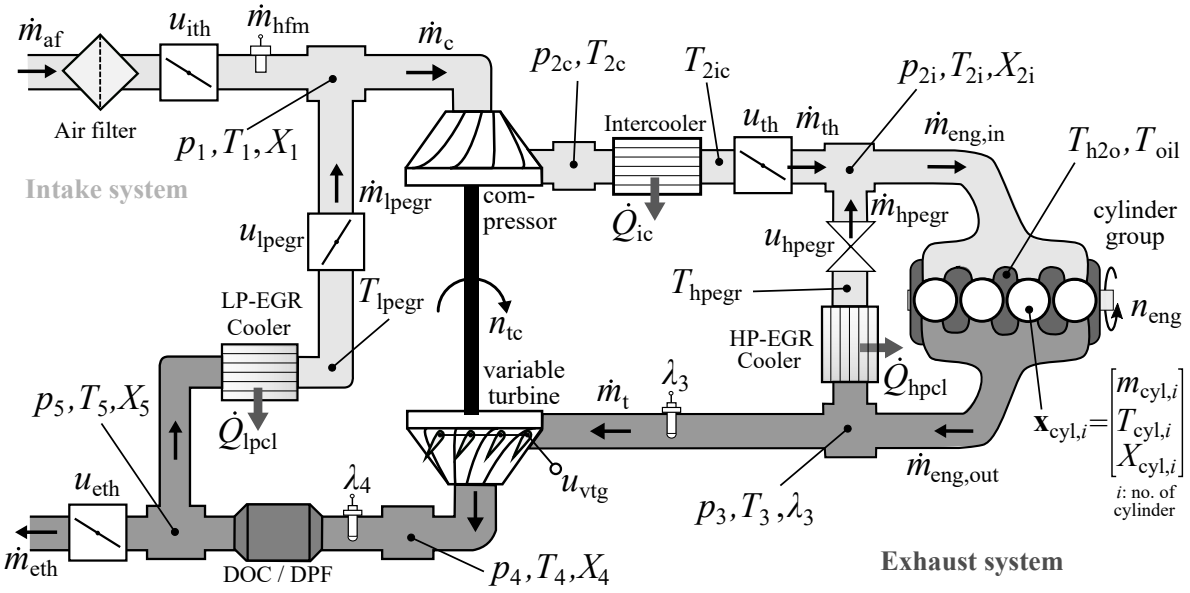

Figure 3.1: Structure of a four-cylinder diesel engine with high and low pressure exhaust gas recirculation and a turbocharger with variable turbine geometry (VGT)

measure can be extended to the higher load range without loss of performance, see Mrosek (2017) or Hadler et al. (2008). But these engine-related measures come with some drawbacks.

With the introduction of EGR, the amount of fresh air during combustion in the cylinder is no longer given explicitly by the HFM sensor. The *slower turbocharger dynamics*, due to the mechanical inertia of the turbocharger wheel, superimposes the *gas dynamics of the air system* and leads without countermeasures to a significant deterioration in engine response characteristics, especially during dynamic engine operation (turbo lag).

Model-based control structures have proven to be effective for optimal control of modern diesel engines. Model-based airpath controller are based on physical air and exhaust path models, which calculate the dynamic behavior of the air system with all relevant state variables and control them optimally with regard to the target variables (torque generation, emissions reduction, etc.) over a wide engine operating range.

For engine control, the most relevant airpath *control variables*[1] are the gas state $\mathbf{x}_{2i} = [p_{2i}, T_{2i}, X_{2i}]^T$ in the intake manifold. This gas state $\mathbf{x}_{2i}$ determines the *in-cylinder gas state* $\mathbf{x}_{cyl}$ provided to the combustion. Since the airpath dynamics is slower than the combustion dynamics for the reasons mentioned above, it dominates the dynamic behavior of the engine.[2] Intake pressure p_{2i} and temperature T_{2i} influence indirectly the in-cylinder gas mass m_{cyl} and temperature T_{cyl}, while the

[1] The EGR-rate $r_{egr} = \dot{m}_{egr}/\dot{m}_{air}$ is typically used instead of the air mass fraction X_{2i}

[2] Combustion process of the engine operating cycle represents a batch process that is cycle resolved and dependent on engine speed

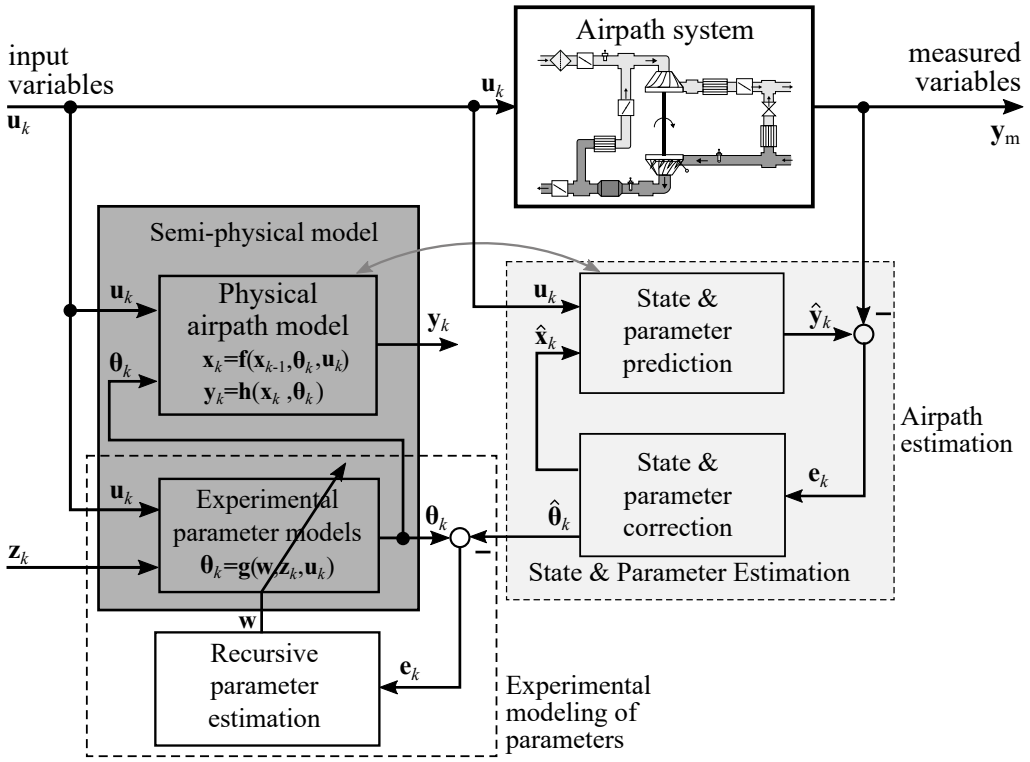

Figure 3.2: Structure and signal flow of semi-physical airpath model (emphasized in grey box) with airpath estimation (combined state and parameter estimation) and experimental modeling of parameters (dashed box), compare with Figs. 2.12 and 2.14

air mass fraction $X_{2\mathrm{i}}$ describes the mass fraction of fresh or unburned air in the gas mass flow $\dot{m}_{\mathrm{eng,in}}$ which enters the cylinder chambers and determines the air mass fraction inside the cylinder.[3]

The intake gas state $\mathbf{x}_{2\mathrm{i}}$ is controlled by the manipulation of the gas mass flows $\dot{m}$ through the airpath actuators (throttles, EGR-valves, etc.). The charging pressure $p_{2\mathrm{i}}$ is controlled via exhaust gas turbocharger with variable turbine geometry or waste gate valve. Charging temperature $T_{2\mathrm{i}}$ is cooled down in the intercooler but increases through admixture of hot exhaust gas $\dot{m}_{\mathrm{hpegr}}$ from HP-EGR. The air mass fraction $X_{2\mathrm{i}}$ is reduced at mixing points 1 and 2i in the intake system by admixing exhaust gas $\dot{m}_{\mathrm{lpegr}}$ and $\dot{m}_{\mathrm{hpegr}}$ ($X_{2\mathrm{i}} = 1$ for fresh air without EGR). Therefore, modeling of mass flows in the air and exhaust system is required for determining of the control variable $\mathbf{x}_{2\mathrm{i}}$.

Following Sects. 3.1 and 3.2 treats the *semi-physical modeling* of the intake and exhaust system and the turbocharger of the diesel engine depicted in Fig. 3.1. The underlying methodology of semi-physical modeling is described in the previous Sect. 2.4. The structure and signal flow of the semi-physical airpath model with *combined state and parameter estimation* is depicted in Fig. 3.2. In Sect. 3.3 follows the application of online estimation techniques for the determination of state variables and physical model parameter. The *combined state and parameter estimator* uses a physical airpath model to determine the unknown gas states $\hat{\mathbf{x}}$ in the air path and the physical parameters $\hat{\boldsymbol{\theta}}$ of the mass flow models of the airpath actuators (throttle, valves, compressors, and

[3] Due to residual gas remaining in the cylinder after exhaust phase, the resulting air mass fraction of cylinder gas after intake phase is lower than the air mass fraction of intake gas: $X_{\mathrm{cyl}} \leq X_{2\mathrm{i}}$

turbine). The estimated physical parameters $\hat{\boldsymbol{\theta}}$ are then used as a reference for online identification of its corresponding *experimental parameter models* $\boldsymbol{\theta} = \mathbf{g}(\mathbf{z}, \mathbf{u})$ that leads eventually to the identification of the overall semi-physical airpath model. Sect. 3.4 describes how the physical parameter are modeled by experimental models and identified online using recursive least squares algorithm.

3.1 Intake and exhaust system

In modeling of the air and exhaust gas path system of internal combustion engines, mean value models with lumped parameters based on the *filling and emptying* method have proven to be suitable for online-applications such as airpath control and diagnosis, (Merker, Schwarz, et al. 2006; Pischinger et al. 2009; Guzzella and Onder 2010; Isermann 2014).

The airpath system shown in Fig. 3.1 is represented by an alternating sequence of *gas storages* with ideal mixture and finite volumes (intake manifold, ducts, exhaust manifold), *flow restrictions* (throttles, valves, air filter) and *heat exchangers* (intercooler, EGR-cooler). These basic elements for mean-value modeling are depicted in Fig. 3.3. The modeling of the air and exhaust path aims to describe the gas states and flow variables at this components. The use of storage and flow variables allows physical modeling the dynamical behavior of the intake and exhaust system. Further examples for modeling of the airpath systems are given in Zahn (2012), Mrosek (2017), Zydek (2018).

The intake and exhaust manifold, as well as the air ducts between throttles and valves, are summarized in terms of their volume and represented by *gas storage elements*. Long air ducts and mixing points require a dedicated gas storage element, compare Fig. 3.1. To keep model complexity and stiffness reasonably low, small-volume ducts, such as the high-pressure exhaust gas recirculation, can be neglected (Guzzella and Onder 2010).

The representation of throttles, valves, air filters and cooler as *flow restrictions* allows modeling the pressure-gradient driven mass flows through these elements (pressure drop $p_{\text{out}}/p_{\text{in}} \leq 1$). Since the pressure drop along throttles, valves, and air filters and coolers is usually not very large, temperature changes are often neglected for the sake of simplicity, compare Fig. 3.3 b).

Heat exchanger models, as depicted in Fig. 3.3 c), are used to model temperatures changes of the mass flows in the intake and exhaust ducts. A lossless flow without pressure drop is often assumed ($p_{\text{out}} \approx p_{\text{in}}$), so that only the temperature changes. Since heat exchangers are usually placed upstream or downstream of a throttle or valve in the air system, the pressure drop can be taken into account in the flow restriction model, compare Fig. 3.1.

3.1.1 Gas storages with ideal mixture

The inputs of the storage elements are the mass flow rates of the inflowing $\dot{m}_{\text{in},i}$ ($i = 1, ..., p$) and outflowing gas mass $\dot{m}_{\text{out},j}$ ($j = 1, ..., q$), the inflow temperatures $T_{\text{in},i}$), and the inflow air mass

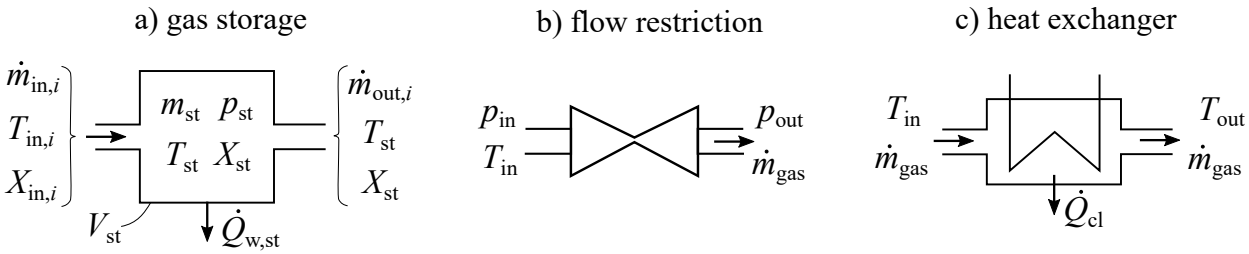

Figure 3.3: Gas flow representation with inputs, outputs and states of the basic elements of mean-value airpath modeling

fractions $X_{\mathrm{in},i} \in [0; 1]$. The temperature and air mass fraction of outflowing gas corresponds to the gas temperature and air mass fraction of the stored gas (ideal mixture). The actual model outputs are the gas states inside the gas storage defined by its mass m_{st}, gas pressure p_{st}, temperature T_{st} and air content X_{st}. These gas state variables are connected to each other via ideal gas law, see Appx. A.2.1.

The gas storage mass results from conservation law of mass

$$\frac{\mathrm{d}m_{\mathrm{st}}}{\mathrm{d}t} = \sum_{i=1}^{p} \dot{m}_{\mathrm{in},i} - \sum_{j=1}^{q} \dot{m}_{\mathrm{out},j} \tag{3.1}$$

Since the gas temperature changes are relatively slow compared to the gas pressure, the pressure change can be described in a good approximation based on the differential form of the ideal gas law ($\mathrm{d}T_{\mathrm{st}}/\mathrm{d}t \approx 0$)

$$\frac{\mathrm{d}p_{\mathrm{st}}}{\mathrm{d}t} = \frac{R_{\mathrm{air}} T_{\mathrm{st}}}{V_{\mathrm{st}}} \left[\sum_{i=1}^{p} \dot{m}_{\mathrm{in},i} - \sum_{j=1}^{q} \dot{m}_{\mathrm{out},j} \right], \tag{3.2}$$

with a constant storage volume V_{st} and the general gas constant for air R_{air}.

In general, the governing equation for the gas temperature T_{st} in the gas storage element is derived from the energy balance equation. However, the use of this balance equation, together with the equations (3.1) and (3.2), would lead to a coupled differential equation system. To avoid that, some reasonable assumptions and simplifications can be applied.

For large gas storage volumes ($\dot{m}_{\mathrm{in},i}/m_{\mathrm{st}} << 1$) with ideal mixture, a good approximation of the gas temperature T_{st} is given by the following differential equation

$$\frac{\mathrm{d}T_{\mathrm{st}}}{\mathrm{d}t} \approx \frac{1}{m_{\mathrm{st}}} \left[\sum_{i=1}^{p} (T_{\mathrm{in},i} - T_{\mathrm{st}})\, \dot{m}_{\mathrm{in},i} + \frac{1}{c_{\mathrm{v}}} \dot{Q}_{\mathrm{w,st}} \right]. \tag{3.3}$$

This differential equation represent a first order lag element with a time constant depending on the ratio $\dot{m}_{\mathrm{in},i}/m_{\mathrm{st}}$. In steady state operation the dynamic behavior of the storage temperature T_{st} converges towards the temperatures $T_{\mathrm{in},i}$ of the entering mass flows proportional to the corresponding mass flow rates.

The heat flow $\dot{Q}_{\mathrm{w,st}}$ represent the wall heat losses between the walls of storage gas and its environment. The wall heat transfer is described by Newton's law (Pflaum and Mollenhauer 1977)

$$\dot{Q}_{\mathrm{w,st}} = k_{\mathrm{w,st}} A_{\mathrm{w,st}} \left(T_{\mathrm{st}} - T_{\mathrm{a}}\right), \tag{3.4}$$

with the storage wall surface $A_{\mathrm{w,st}}$, the heat transfer coefficient $k_{\mathrm{w,st}}$ and the ambient temperature T_{a}. For the sake of simplicity, modeling the heat storage of walls and the wall temperature is not considered.

For the storage elements of the intake systems, the transported heat through the storage is much larger than the heat flow to the walls, so that the wall heat losses can be neglected $\dot{Q}_{\mathrm{w,st}} \approx 0$ (Isermann 2014). However, for storage elements of the exhaust system, where the temperature gradients are high and the heat losses are significant ($\dot{Q}_{\mathrm{w,st}} \neq 0$), the wall heat losses must either considered in Eq. (3.3), or if a cooler element, such as EGR-cooler, is included in the storage volume, the heat losses can be accounted to the cooling capacity of the cooler. The separate calculation of the wall heat losses becomes then obsolete.

Considering airpath systems with exhaust gas recirculation requires modeling of the air content at the particular mixing points of intake and exhaust system. For the characterization of the air content, the air mass fraction is defined as further state variable of a storage element

$$X_{\mathrm{st}} = \frac{m_{\mathrm{st,air}}}{m_{\mathrm{st}}} \tag{3.5}$$

It represent the ratio air mass and total gas mass inside the storage element. Since an ideal mixture is assumed in the gas storage, the air mass fraction X_{st} changes only due to deviating air mass fraction $X_{\mathrm{in},i}$ of inflowing mass flows. The differential equation is given as

$$\frac{\mathrm{d}X_{\mathrm{st}}}{\mathrm{d}t} = \frac{1}{m_{\mathrm{st}}(t)} \left[\sum_{i=0}^{p} (X_{\mathrm{in},i} - X_{\mathrm{st}}) \dot{m}_{\mathrm{in},i}(t) \right] \tag{3.6}$$

A more detailed derivation of the basic equations describing gas storages with ideal mixture can be found in Appx. A.2.6.

3.1.2 Flow restrictions

In the intake and exhaust system, throttles, valves, air filters and air coolers can be characterized as flow restrictions (with reduced flow area) causing a pressure drop $\Delta p = p_{\mathrm{in}} - p_{\mathrm{out}}$ in flow direction, see Fig. 3.3 b). The inputs of the flow restriction elements are the upstream p_{in} and downstream pressure p_{out} as well as the upstream temperature T_{in} for determining the upstream gas density ρ. The output of flow restrictions element is the mass flow rate $\dot{m}$, which is generally described by

$$\dot{m}(t) = \rho(t) A(t) w(\Delta p(t)). \tag{3.7}$$

The flow velocity w in m/s is driven by the pressure gradient Δp along the flow restriction $w(t) = f(\Delta p)$.

In components such as filters or coolers, the cross-sectional area is constant $A(t) = A_{\text{th}}$ and is determined theoretically from construction parameters of the components. However, the theoretical cross-sectional area of throttles and valve actuators $A(t) = A_{\text{th}}(u(t))$ is manipulated during engine operation by a manipulating variable $u(t)$ of the airpath controller, controlling the air flow or recirculated exhaust gas flow into the combustion chambers.

For real flows the real effective cross-sectional area differs from the theoretically determined cross-sectional area. This is taken into account by introducing a *flow coefficient* or *discharge coefficient* describing the relation between the actual, effective flow area A_{eff} and the geometrical flow area A_{th},

$$c_{\text{d}} = \frac{A_{\text{eff}}}{A_{\text{th}}} = f(A_{\text{th}}, \rho, w). \tag{3.8}$$

The flow losses depend generally on the cross sectional area of the flow restriction, the gas density ρ and the flow velocity w. To describe real flows in the airpath system and to be able to determine gas states based on them, the flow coefficient $c_{\text{d}} = f(\cdot)$ of each flow restriction must be modeled experimentally and identified based on mass flow measurements.

Generally, in modeling the flow restrictions, a distinction is made between *compressible* and *incompressible fluids*. The mass flow for incompressible (liquid) fluids is derived from *Bernoulli's equation* and can be written as

$$\dot{m}(t) = A_{\text{eff}}\sqrt{2\rho(p_{\text{out}} - p_{\text{in}})} = c_{\text{d}} A_{\text{th}}\sqrt{\frac{2p_{\text{in}}}{R\,T}(p_{\text{out}} - p_{\text{in}})} \tag{3.9}$$

For flow resistances such as in air filters and coolers, which have only small flow area constriction and thus small pressure drops, it is acceptable to use Bernoulli's equation for incompressible fluids (Isermann 2014). Considering compressible fluids, a steady isenthalpic flow through an orifice is assumed, which is given as (J. B. Heywood 1988)

$$\dot{m}(t) = A_{\text{eff}}\frac{p_{\text{in}}}{\sqrt{R_{\text{air}}T_{\text{in}}}}\Psi\left(\Pi\right) = c_{\text{d}} A_{\text{th}}\frac{p_{\text{in}}}{\sqrt{R_{\text{air}}T_{\text{in}}}}\Psi\left(\frac{p_{\text{out}}}{p_{\text{in}}}\right), \tag{3.10}$$

with the outflow function $\Psi(\Pi)$ considering two cases regarding the pressure ratio $\Pi = p_{\text{out}}/p_{\text{in}}$

$$\Psi\left(\Pi\right) = \begin{cases} \sqrt{\kappa\left(\frac{2}{\kappa+1}\right)^{\frac{\kappa+1}{\kappa-1}}}, & p_{\text{out}} < p_{\text{in}}\left(\frac{2}{\kappa+1}\right)^{\frac{\kappa}{\kappa-1}} \\ \Pi^{\frac{1}{\kappa}}\sqrt{\frac{2\kappa}{\kappa-1}\left(1 - \Pi^{\frac{\kappa-1}{\kappa}}\right)}, & p_{\text{out}} \geq p_{\text{in}}\left(\frac{2}{\kappa+1}\right)^{\frac{\kappa}{\kappa-1}}. \end{cases} \tag{3.11}$$

The outflow function $\Psi(\Pi)$ describes the flow velocity as a function of the pressure ratio Π along the valve opening. The term $p_{\text{in}}/\sqrt{R \cdot T_{\text{in}}}$ considers the gas density. The flow velocity of an one-dimensional, isentropic and stationary flow is

$$w_{\text{is}} = \sqrt{2\frac{\kappa}{\kappa-1}RT_{\text{in}}\left[1 - (\Pi)^{\frac{\kappa-1}{\kappa}}\right]} \tag{3.12}$$

For pressure ratios $\Pi \geq \left(\frac{2}{\kappa+1}\right)^{\frac{\kappa}{\kappa-1}} = \Pi_{\text{crit}}$ the critical gas velocity is reached (choked or critical flow). The critical pressure ratio Π_{crit} characterizes the case when the flow velocity cannot further increased by increasing the pressure ratio.

A simpler approximation of the outflow function is presented in Guzzella and Onder (2010):

$$\Psi(\Pi) = \begin{cases} \frac{1}{\sqrt{2}} & p_{\text{out}} < \frac{1}{2} p_{\text{in}} \\ \sqrt{\frac{2\Pi}{(1-\Pi)}} & p_{\text{out}} \geq \frac{1}{2} p_{\text{in}} \end{cases} \tag{3.13}$$

This equation (3.13) applies to many working gases with low temperature and an isentropic coefficient $\kappa \approx 1.4$, as they occur in the intake and exhaust paths of the internal combustion engines. The advantage of this outflow equation lies in the simpler calculation. Despite the physical origin of both equations (3.10) and (3.13) are not very suitable for a computationally efficient implementation (complex derivation with respect to state variables p_{out}, p_{in}).

A more mathematical formulation of the outflow function is presented in Zahn (2012) in the context of modeling the turbine mass flow of turbocharger. The outflow function is approximated by an exponential function

$$\Psi(\Pi) = c_1 \left[1 - e^{-c_2(1-\Pi)}\right] \tag{3.14}$$

The parameter $c_1 = 1/\sqrt{2}$ represents maximum value for pressure ratios $\Pi \leq \Pi_{\text{crit}}$. Parameter c_2 allows to adjust the outflow function for the subcritical case ($c_2 = 9..11$).

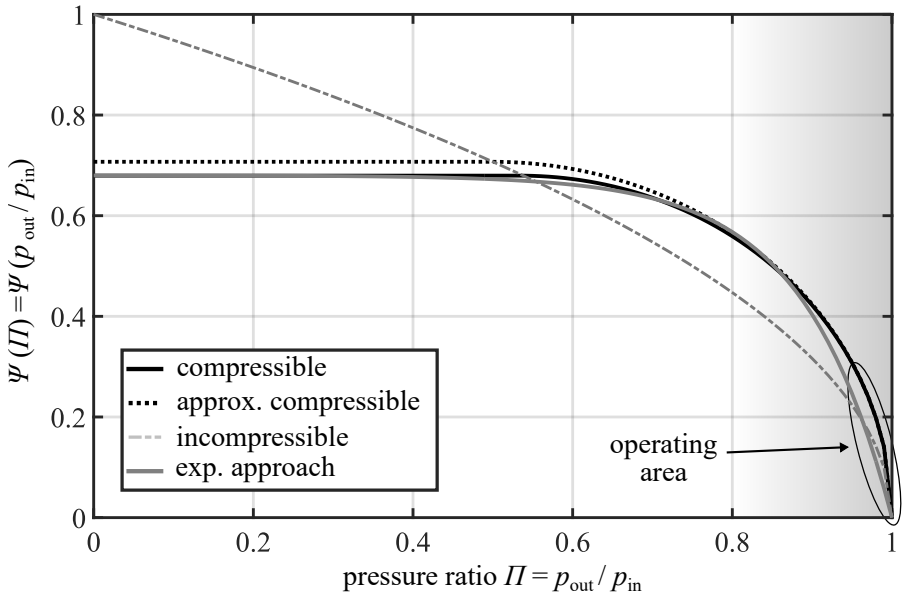

Figure 3.4: Comparison of the approaches for the outflow equation of flow restrictions

A comparison of these modeling approaches is shown in Fig. 3.4. Even though Eq. (3.14) is also nonlinear, this formulation has some advantages compared to the two physical equations (3.10) and (3.13). The gradient of (3.14) with respect to pressures can be easily formed, leading to a more compact expression for the derivative. On the contrary, Eqs. (3.10) and (3.13) have an infinite gradient in the region $p_{\text{in}} \approx p_{\text{out}}$. Their use in the calculation of the storage pressures and temperatures leads to a system that is non-Lipschitz and consequently difficult to integrate, especially for small pressure gradients, (Guzzella and Onder 2010). A disadvantage of Eq. (3.14) is the deviation in the region $p_{\text{out}}/p_{\text{in}} \approx 1$ compared to the physical approach (3.10), see Fig. 3.4.

However this deviation is acceptable considering the predominant advantages in the context of the scope of this work.

Given the advantages of exponential outflow function Eq. (3.14), it is used in the following to model the mass flows through throttles and valves, depicted in Fig. 3.1. The pressure drop in the air filter and the cooler elements can be modeled using Eq. (3.9). To keep model complexity and the number of parameters to be estimated low as possible, the pressure drop in air filter and cooler elements is accounted by a flow restriction element next to it, e.g. EGR-valve and cooler.

3.1.3 Heat exchanger

In internal combustion engines, several *heat exchangers* such as *radiators* or *oil and water coolers* are required to maintain an optimal and safe functioning of engine operation. The airpath system of a turbocharged engine with exhaust gas recirculation contains usually an *intercooler* after the compressor of the turbocharger and an *EGR-cooler* in order to increase combustion efficiency by reducing the charging temperature $T_{2\mathrm{i}}$. For an accurate modeling of the gas states in the intake and exhaust system, mathematical models of all heat exchangers are required, see Fig. 3.1.

Heat exchangers in the intake and exhaust system are generally modeled as stationary flow processes in an open thermodynamic system

$$\dot{m}_{\mathrm{gas}}\,(h_{\mathrm{in}} - h_{\mathrm{out}}) + \dot{Q}_{\mathrm{cl}} = U_{\mathrm{cl}} \tag{3.15}$$

with a heat transfer $\dot{Q}_{\mathrm{cl}}$ causing a change in specific enthalpy of the inflowing gas $\dot{m}_{\mathrm{gas}}$, compare Fig. 3.3 c). It is assumed that inflowing and outflowing mass flow are equal ($\dot{m}_{\mathrm{in}} = \dot{m}_{\mathrm{out}} = \dot{m}_{\mathrm{gas}}$). Depending on the direction of heat flow $\dot{Q}_{\mathrm{cl}}$, the outflow temperature T_{out} is lowered or raised compared to the temperature Tin.

The intercooler is an *air-to-air cross-flow heat exchanger*, whose coolant fluid is a flow of ambient air provided by the vehicle's airstream. The EGR cooler is a liquid *coolant-to-air tube bundle cooler*, where the engine coolant, provided by a cool pump, flows around the tubes in cross or counter flow (Isermann 2014). According to VDI-Wärmeatlas (2013), a heat exchanger is modeled based on a lumped parameter approach as a heat transfer between two fluids through a wall

$$\dot{Q}_{\mathrm{cl}} = k_{\mathrm{cl}}(\dot{V}_{\mathrm{gas}}, \dot{V}_{\mathrm{cl}})A_{\mathrm{cl}}\,(T_{\mathrm{in}} - T_{\mathrm{cl}}) \tag{3.16}$$

with averaged surface area A_{cl} and the overall heat coefficient k_{cl}, depending of the flow rate of the gas to be cooled $\dot{V}_{\mathrm{gas}}$ and the coolant flow rate $\dot{V}_{\mathrm{cl}}$, see for more details Appx. A.2.6 or Isermann (2014). Since liquid coolers are typically belt driven, it is assumed that the coolant flow $\dot{V}_{\mathrm{cl}}$ is proportional to the engine speed n_{eng}. In the case of the intercooler, the cooling air flow is determined by the vehicle speed.[4]

In order to consider the gas propagation time through the cooler element, cooler volume and the attached pipe section are summarized as a gas storage element with the volumes V_{cl}. The output

[4] At the engine test bench, the intercooler is operated at constant speed, hence a constant cooling flow is assumed

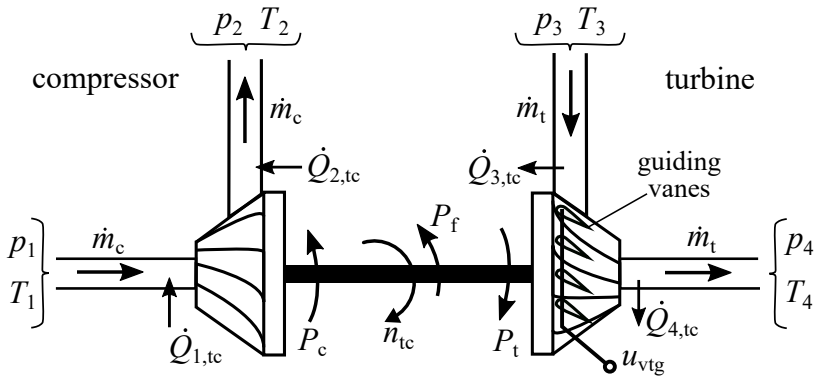

Figure 3.5: Scheme of a exhaust gas turbocharger with variable turbine geometry (VGT)

temperature of the heat exchanger can be derived from Eq. (3.15) as follows

$$\frac{\mathrm{d}T_{\mathrm{cl}}}{\mathrm{d}t} = \frac{1}{m_{\mathrm{cl}}}\left(\kappa(T_{\mathrm{cl,in}} - T_{\mathrm{cl}})\dot{m}_{\mathrm{gas}} + \frac{1}{c_{\mathrm{v}}}\dot{Q}_{\mathrm{ic}}\right) \tag{3.17}$$

This equation holds for all heat exchanger of Fig. 3.1. The pressure drop due to the flow resistance of the heat exchanger is neglected ($p_{\mathrm{out}} \approx p_{\mathrm{in}}$). Using ideal gas equation allows determining the gas storage mass $m_{\mathrm{cl}} = p_{\mathrm{in}} V_{\mathrm{cl}}/(R_{\mathrm{air}} T_{\mathrm{cl}})$. In the absence of heat dissipation ($\dot{Q}_i = 0$), the outlet temperature converges towards inlet temperature (first order lag element).

The overall heat coefficient of the intercooler k_{ic}, the HP-EGR-cooler k_{hpegrcl} and the LP-EGR cooler k_{lpegrcl} must be estimated via parameter estimation and modeled as function mass flows and engine speed by experimental modeling based on measurements or estimated variables. The corresponding heat transfer surfaces A_{cl} are assumed to be constant and can be included in the experimental parameter $k_i A_i = g_i(\dot{V}_{\mathrm{gas}}, \dot{V}_{\mathrm{cl}})$.

3.2 Turbocharger with VGT

The scheme of a exhaust gas turbocharger with variable turbine geometry is shown in Fig. 3.5. All relevant variables such the mass flows $\dot{m}$, the gas states (p, T) upstream and downstream, as well as the power quantities P and heat flows $\dot{Q}$ on both compressor and turbine are depicted. In VGT-Turbochargers, the inflow angle of the exhaust gas and the cross-sectional flow area can be varied through variable guiding vanes at turbine's inlet. The angle of the guiding vanes is continuously adjustable via pneumatic actuator or servomotor u_{vgt}.

An exhaust gas driven turbocharger converts the energy of the exhaust gas enthalpy flow $\dot{H}_3 = \dot{m}_{\mathrm{t}} h_3$ into mechanical power P_{t} via *expansion* of the exhaust gas (p_3, T_3) at the turbine impeller of the turbocharger. As a result of the expansion, the pressure and temperature of the gas at the turbine outlet (p_4, T_4) drops to a lower level. This mechanical turbine power P_{t} is used to drive the turbocharger shaft and the compressor impeller. The compressor impeller, driven by the shaft speed n_{tc}, sucks in the air at the intake (p_1, T_1) and compresses it to a higher pressure and temperature

level (p_2, T_2), so that the also boost pressure at the engine intake manifold is increased. This mechanical power is reduced by the friction loss P_f and the wall heat losses.

The turbine of the considered turbocharger is equipped with variable turbine geometry. The variable turbine vans allow changing the cross-sectional areas and the flow velocity through the turbine and thus changing the exhaust gas back pressure (Isermann 2014).

Overview on modeling of turbochargers

According to Zahn (2012) three different modeling approaches are suitable for the real-time simulation of turbochargers:

- Map-based thermodynamic model approach
- Artificial neural network (ANN) models
- One-dimensional fluid dynamic model approach

In map-based thermodynamic modeling, the global thermodynamic state changes in turbomachinery are considered as an irreversibly adiabatic compression or expansion process. The mathematical modeling is based on the comparison of turbocharger maps, provided by the manufacturer, with the equation for an isentropic state process (Zahn 2012). The standardized characteristic maps are determined on special test benches and therefore only describe the stationary behavior under specific environmental conditions, see i.e. Mayer and Krämer (2011). To make use of them, the input variables of the maps must be corrected or referenced by using fluid mechanical laws, independent of changing environmental conditions, see e.g. Sigloch (2008), Sidorow (2014), and Isermann (2014).

Model approaches based on artificial neural networks (ANN) are also frequently used. These can be generated automatically from measurement data without much previous knowledge using generic modeling software tools such as *LOLIMOT*, see i.e. Ayoubi (1996), Sinsel (2000), and Schaffnit (2002). The choice and the quality of the measurement data is of particular importance. However, since ANNs do not offer physical interpretability, lack of extrapolation capability and a high measurement effort, they are not considered in the following.

One-dimensional fluid dynamic turbocharger models are based on Euler's equation for turbomachinery, considering the change of the angular momentum of the gas flows, the continuity equation and the energy balance equation (Isermann 2014). Zahn (2012) proposed a semi-physical turbo charger model on a fluid dynamic model approach, which provides good model accuracy at moderate measurement and parameterization effort. The diabatic behavior of the turbocharger as well as the friction losses is physically modeled. Based on the experimental model approach according to Moraal and Kolmanovsky (1999), the compressor pressure ratio is described with the use of polynomial functions.

In contrast to the use of maps from manufacturer specifications, this also allows the turbocharger behavior to be described in engine-specific ranges, e.g. at low turbocharger speeds and in towing operation. On the other hand, the use of fluid mechanical models requires higher implementation

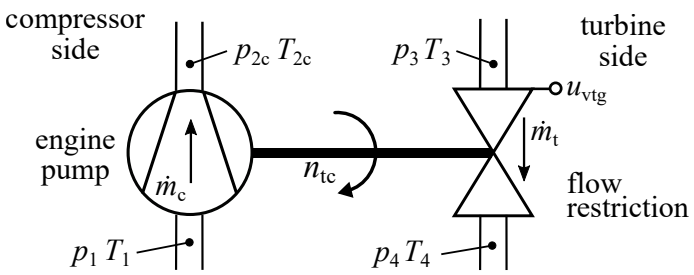

Figure 3.6: Scheme of the simplified mass flow model of an exhaust gas VGT-turbocharger: Compressor is idealized as an engine pump and the turbine as a variable flow restriction

effort and computational power. Additionally, due to the high modeling depth, the identification of model parameters requires the application of numerical optimization, which makes this modeling approach not suitable for the combination with online parameter identification methods.

Conclusion

With regard to the objective of this work, the fluid dynamic modeling approach according to Zahn (2012) is the most promising and is therefore adopted in the following. In order to qualify this semi-physical turbocharger model for real-time application and to reduce the number of parameters to be identified, simplifications are made on the modeling of the compressor and turbine performances.

In the following, the power P_t,P_c, and the mass flows $\dot{m}_t$, $\dot{m}_c$ of the turbine and the compressor, as well as the losses and heat transfers are described in more detail. To integrate the turbocharger model into the overall air path model, the outlet temperature at the compressor T_c and turbine outlet T_t are required.

Only the final model equations and the applied simplifications are described. For the detailed derivation of the turbocharger model equations, please refer to Zahn (2012), Isermann (2014) or Mrosek (2017).

3.2.1 Turbocharger mass flows

An essential quantity for describing the turbocharger is the mass flows at the compressor $\dot{m}_c$and the turbine impeller $\dot{m}_t$. Unlike the other air path actuators, such as throttles and valves (flow resistors), compressor and turbine mass flows are significantly influenced by the turbocharger speed n_{tc}. On the compressor side, the turbocharger speed n_{tc} increases the pressure difference between upstream and downstream pressure, while a higher speed n_{tc} reduces the pressure difference on the turbine side.

Compressor mass flow

The compressor mass flow is a function of turbocharger speed n_{tc} and the ratio between upstream and downstream pressure $\Pi_{\mathrm{c}} = p_{2\mathrm{c}}/p_1$, which can be determined from compressor map provided by the turbocharger manufacturer. However, these maps do not allow to derive an unique relation between pressure ratio and compressor mass flow (Zahn 2012; Mrosek 2017). To overcome this issue, following the approach is proposed by Moraal and Kolmanovsky (1999).

First, the pressure ratio Π_{c} over the compressor impeller is modeled as stationary compressor map

$$\Pi_{\mathrm{c}} = \frac{p_{2\mathrm{c}}^*}{p_1} = f_{\mathrm{exp}}(\dot{m}_{\mathrm{c}}, n_{\mathrm{tc}}) \tag{3.18}$$

where $p_{2\mathrm{c}}^*$ is the upstream pressure introduced as an intermediate state and $f_{\mathrm{exp}}(\dot{m}_{\mathrm{c}}, n_{\mathrm{tc}})$ is the compressor map modeled mathematically as an experimental model, e.g. polynomial function or ANN. The dynamic behavior of the compressor mass model is then modeled using a one-dimensional momentum equation by Moraal and Kolmanovsky (1999) given as

$$\frac{\mathrm{d}\dot{m}_{\mathrm{c}}(t)}{\mathrm{d}t} = \frac{A}{l}(p_{2\mathrm{c}}^* - p_{2\mathrm{c}}). \tag{3.19}$$

This approach, proposed by Greitzer (1976), represents a simplified modeling of the pressure increase in the compressor by a thin *actuator disc* and a pipe duct section with cross-sectional area A and duct length l. Instead of describing the mass flow dynamics using the geometrical parameters of a pipe duct model, the physical relationship between the change of mass flow rate $\mathrm{d}\dot{m}_{\mathrm{c}}(t)/\mathrm{d}t$ and the pressure difference $\Delta p_{\mathrm{c}} = (p_{2\mathrm{c}}^* - p_{2\mathrm{c}})$

$$\frac{\mathrm{d}\dot{m}_{\mathrm{c}}(t)}{\mathrm{d}t} \propto \frac{\mathrm{d}p_{\mathrm{c}}(t)}{\mathrm{d}t} \approx \frac{\Delta p_{\mathrm{c}}}{\Delta t_{\mathrm{c}}} = \frac{(p_{2\mathrm{c}}^* - p_{2\mathrm{c}})}{\Delta t_{\mathrm{c}}}, \tag{3.20}$$

is described using the derivative of the so-called *engine pump rate* $\dot{m}_{\mathrm{p}}(t)$, see Fig.3.6,

$$\frac{\mathrm{d}\dot{m}_{\mathrm{c}}(t)}{\mathrm{d}t} = \frac{\mathrm{d}}{\mathrm{d}t}\left[\dot{m}_{\mathrm{p}}(t)\right] = \frac{\mathrm{d}}{\mathrm{d}t}\left[\eta_{\mathrm{vol}}\frac{n_{\mathrm{tc}}V_{\mathrm{cp}}}{RT_1}p_1\right], \tag{3.21}$$

with the pump volume V_{cp} of the compressor and the volumetric efficiency η_{vol}, which will not be considered further in the following. Using Eq. (3.21) allows relevant influences, such as gas temperature T_1 and turbocharger speed n_{tc}, to be taken into account when modeling the mass flow dynamics. Combining the pump rate (3.21) with the relation (3.20) leads to the following equation for the compressor mass flow

$$\begin{aligned}\frac{\mathrm{d}\dot{m}_{\mathrm{c}}(t)}{\mathrm{d}t} &= \frac{n_{\mathrm{tc}}V_{\mathrm{cp}}}{RT_1}\frac{(p_{2\mathrm{c}}^* - p_{2\mathrm{c}})}{\Delta t_{\mathrm{c}}} \\ &= \frac{n_{\mathrm{tc}}V_{\mathrm{cp}}}{RT_1}\frac{[p_1\Pi_{\mathrm{c}}(\dot{m}_{\mathrm{c}}, n_{\mathrm{tc}}) - p_{2\mathrm{c}}]}{\Delta t_{\mathrm{c}}}.\end{aligned} \tag{3.22}$$

The compressor mass flow model is divided in an experimental model (3.18) for the stationary pressure ratio over the compressor wheel and a physically motivated model (3.22) for the inherent dynamics of the mass flow $\dot{m}_{\mathrm{c}}$.

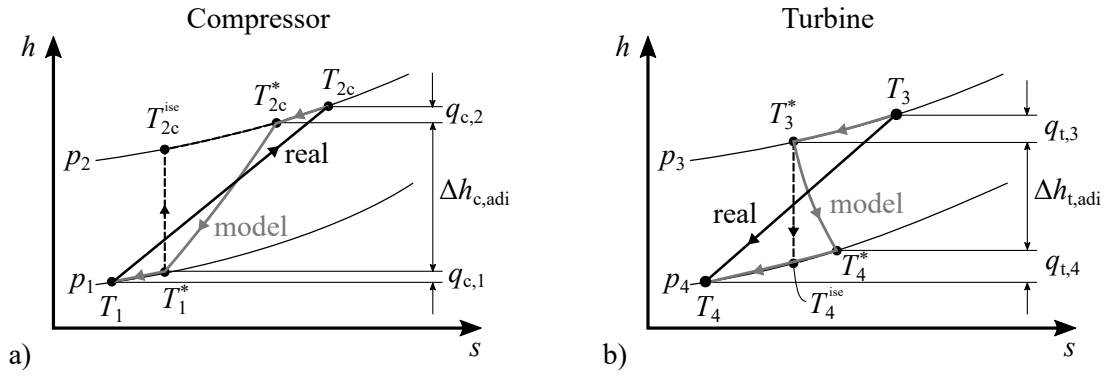

Figure 3.7: Schematic h-s-diagram of the diabatic compression and expansion processes of a) compressor and b) turbine; comparison of real process and modeled process

Turbine mass flow

In the literature it is common practice to model the turbine mass flow as a flow restriction (adiabatic throttle), see Fig.3.6. The turbine mass flow is then modeled by using the outflow equation of a throttle (Zahn 2012). For the sake of simplicity, the exponential-function-type approximation of the outflow function (3.14) is used, which yields to

$$\begin{aligned} \dot{m}_t(t) &= c_{\mathrm{d,t}}(n_{\mathrm{tc}}, u_{\mathrm{vgt}}) \frac{p_3}{\sqrt{RT_3}} \Psi_{\mathrm{t}}\left(\Pi_t\right), \\ &= c_{\mathrm{d,t}}(n_{\mathrm{tc}}, u_{\mathrm{vgt}}) \frac{p_3}{\sqrt{RT_3}} c_1 \left(1 - e^{-c_2(\Pi_t - 1)}\right), \end{aligned} \tag{3.23}$$

where $c_{\mathrm{d,t}}$ is the discharge coefficient, $\Pi_t = p_3/p_4$ is the turbine pressure ratio, and c_1 and c_2 are constant outflow function parameter, as described in Sect. 3.1.2. The discharge coefficient $c_{\mathrm{d,t}}(n_{\mathrm{tc}}, u_{\mathrm{vgt}})$ represents a parameter of the turbine mass flow model (3.23) and is modeled experimentally as function of the turbine vanes position u_{vgt} and the turbocharger speed n_{tc}. The effective cross sectional area is included in the parameter model $c_{\mathrm{d,t}}(n_{\mathrm{tc}}, u_{\mathrm{vgt}})$.

3.2.2 Turbocharger power

The irreversible diabatic processes at the compressor and the turbine impeller of the turbocharger are schematically depicted in a *h-s-diagram* in Fig. 3.7. Both, compression process and expansion process are characterized by an adiabatic enthalpy change Δh_{adi} and heat transfers q upstream and downstream of the corresponding impeller. Generally, the compressor or turbine power is a function of mass flow rate $\dot{m}$ and specific inner work a

$$P = \dot{m}a = \dot{m}\left(q_{\mathrm{in}} + \Delta h_{\mathrm{adi}} + q_{\mathrm{out}}\right) \tag{3.24}$$

The modeling of compressor and turbine power differs primarily in the modeling of the specific internal work and the adiabatic enthalpy change, respectively.

Compressor power

The diabatic compression process $1 \rightarrow 2$ is depicted in Fig. 3.7 a). This process can be modeled by an irreversible adiabatic enthalpy change $\Delta h_{\mathrm{c,adi}}$ and additional upstream and downstream heat transfers $q_{\mathrm{c},1}$ and $q_{\mathrm{c},2}$.

$$P_{\mathrm{c}} = \dot{m}_{\mathrm{c}} a_{\mathrm{c}} = \dot{m}_{\mathrm{c}} \left(q_{\mathrm{c},1} + \Delta h_{\mathrm{c,adi}} + q_{\mathrm{c},2} \right) \tag{3.25}$$

The adiabatic enthalpy change corresponds to the specific work of the compressor impeller. According to Isermann (2014), the mechanical *compressor power* is given by *Euler equation*

$$P_{\mathrm{c}} = \dot{m}_{\mathrm{c}} \Delta h_{\mathrm{c,adi}} = \dot{m}_{\mathrm{c}} (u_{\mathrm{c}2} c_{\mathrm{c}2,\mathrm{u}} - u_{\mathrm{c}1} c_{\mathrm{c}1,\mathrm{u}}), \tag{3.26}$$

with the inlet $u_{\mathrm{c}1}$ and the outlet $u_{\mathrm{c}2}$ tangential blade velocities of the compressor impeller and the corresponding absolute gas velocities $c_{\mathrm{c}1,\mathrm{u}}$ (inlet) and $c_{\mathrm{c}2,\mathrm{u}}$ (outlet). Assuming a swirl free inflow ($c_{\mathrm{c}1,\mathrm{u}} = 0$), (3.26) further simplifies to

$$P_{\mathrm{c}} = \dot{m}_{\mathrm{c}} u_{\mathrm{c}2} c_{\mathrm{c}2,\mathrm{u}} = \dot{m}_{\mathrm{c}} a_{\mathrm{c}}. \tag{3.27}$$

The term $u_{\mathrm{c}2} c_{\mathrm{c}2,\mathrm{u}}$ represents the specific inner work a_{c} including internal losses like friction, shock and gap loss. The compressor power depends then on the downstream gas flow velocity $c_{\mathrm{c}2,\mathrm{u}}$ and the blade velocity $u_{\mathrm{c}2} = \pi d_c n_{\mathrm{tc}}$, which is proportional to the turbocharger speed n_{tc} and the outer diameter of the compressor impeller d_{c}.

The peripheral component $c_{\mathrm{c}2,\mathrm{u}}$ of the absolute flow velocity at the compressor impeller outlet is derived from compressor velocity triangles including turbine specific parameters, such as the impeller outlet width $b_{\mathrm{c}2}$, the blade angle $\beta_{\mathrm{c}2,\mathrm{b}}$, and the so-called slip factor μ.[5] Taking into account these turbine-specific parameters and constants, the compressor power is given as follows (Mrosek 2017)

$$P_{\mathrm{c}}(t) = \dot{m}_{\mathrm{c}} a_{\mathrm{c}} = \mu \dot{m}_{\mathrm{c}} \left[(\pi d_{\mathrm{c}2} n_{\mathrm{tc}})^2 + \frac{\dot{m}_{\mathrm{c}} n_{\mathrm{tc}}}{\rho_{2\mathrm{c}}} \frac{\cot \beta_{\mathrm{c}2,\mathrm{b}}}{b_{\mathrm{c}2}} \right], \tag{3.28}$$

see Zahn (2012) and Isermann (2014) for more details. Considering the bracket term in Eq. (3.28), it can be concluded that the compressor work a_{c} (reduced by μ) is composed of a purely speed-dependent component and a second component that takes into account the actual flow velocity. As a semi-physical equation approach, the following equation is assumed for compressor power

$$P_{\mathrm{c}}(t) = \dot{m}_{\mathrm{c}} a_{\mathrm{c}} = \dot{m}_{\mathrm{c}} \left[k_{\mathrm{c}} \frac{n_{\mathrm{tc}} \dot{m}_{\mathrm{c}}}{\rho_{2\mathrm{c}}} \right] = k_{\mathrm{c}} \frac{n_{\mathrm{tc}} \dot{m}_{\mathrm{c}}^2}{\rho_{2\mathrm{c}}} \tag{3.29}$$

with the compressor work parameter k_{c} modeled by an *experimental model*

$$k_{\mathrm{c}} = g_{\mathrm{c}} \left(\dot{m}_{\mathrm{c}}, n_{\mathrm{tc}} \right). \tag{3.30}$$

as function of compressor mass flow and turbocharger speed. Combing Eqs. (3.29) and (3.30), the compressor power model consists of a *physical equation component* and an operating point-dependent *parameter model* $k_{\mathrm{c}} = g_{\mathrm{c}} \left(\dot{m}_{\mathrm{c}}, n_{\mathrm{tc}} \right)$, which is incorporated linearly into the equation for the compressor work.

[5] The slip factor μ depends on the impeller geometry and is often used to describe power losses expressed as the deviation between the actual flow angle and the theoretical blade angle of $c_{\mathrm{c}2,\mathrm{u}}$ (Sigloch 2008)

Turbine power

The *turbine power* is a function of turbine mass flow rate $\dot{m}_\mathrm{t}$ and the diabatic change of enthalpy $\Delta h_\mathrm{t,adi}$ caused by the expansion $3 \rightarrow 4$ of the exhaust gas at the turbine impeller, see Fig. 3.7 b). This diabatic process can be described as the result of an adiabatic irreversible compression process $\Delta h_\mathrm{t,adi}$ and the transfer of specific heats upstream $q_\mathrm{t,3}$ and downstream $q_\mathrm{t,4}$ of the turbine impeller, see also Fig. 3.5,

$$P_\mathrm{t}(t) = \dot{m}_t \Delta h_\mathrm{t,dia} = \dot{m}_t \left(q_\mathrm{t,3} + \Delta h_\mathrm{t,adi} + q_\mathrm{t,4}\right) \tag{3.31}$$

The irreversible adiabatic enthalpy change $\Delta h_\mathrm{t,adi}$ acts as fluid dynamic work on the turbine impeller. In contrast to the model approach of Zahn (2012), heat dissipation at the inlet $q_\mathrm{t,3}$ and the outlet $q_\mathrm{t,4}$ of the turbine are summarized into one heat transfer

$$q_\mathrm{t} = \frac{\dot{Q}_\mathrm{t}}{\dot{m}_\mathrm{t}} = q_\mathrm{t,3} + q_\mathrm{t,4}. \tag{3.32}$$

The change of adiabatic expansion work $\Delta h_\mathrm{t,adi}$ at the turbine is derived from Euler's equation. After applying of some simplification regarding the design of the turbine impeller and insertion of the different components of the turbine blade velocity and the gas velocity, the turbine power is given as (Isermann 2014)

$$P_\mathrm{t}(t) = -\dot{m}_t^2 \frac{n_\mathrm{tc}}{\rho_\mathrm{t}} \frac{\cot(\alpha_\mathrm{t})}{b_\mathrm{t}}, = -k_\mathrm{t} \dot{m}_t^2 \frac{n_\mathrm{tc}}{\rho_\mathrm{t}}, \tag{3.33}$$

with the gas density ρ_t which is approximated by the inlet gas density $\rho_3 = p_3/\sqrt{RT_3}$ and the turbine blade width b_t at the rotor inlet. It is assumed that the absolute gas flow angle relates to the angle α_t of the guiding vanes, which is determined by the VGT-actuator position $u_\mathrm{vgt} = f(\alpha_\mathrm{t})$. The flow angle dependent term and the turbine blade width are summarized in an introduced turbine power parameter k_t

$$k_\mathrm{t} = \frac{\cot(\alpha_\mathrm{t})}{b_\mathrm{t}} = g_t(u_\mathrm{vgt}). \tag{3.34}$$

which must be estimated based on available airpath measurements and then modeled by an experimental model approach. In example, Mrosek and Isermann (2010) propose a simple third order polynomial for $g_t(u_\mathrm{vgt})$.

The turbine power model (3.33) divides into a *physical model part*, which brings the physical variables $\dot{m}_t$, n_tc and ρ_t into a relation, and a *turbine geometry specific model part* (3.34), which is modeled *experimentally* as function of the VGT-actuator position u_vgt.

3.2.3 Shaft dynamics

The dynamics of the turbocharger is essentially determined by the inertia of the turbocharger shaft. The dynamic behavior of the turbocharger can be described using the turbocharger speed n_tc in 1/s, which results from torque balance in a power-related representation

$$\frac{\mathrm{d}n_\mathrm{tc}}{\mathrm{d}t} = \left(\frac{1}{2\pi}\right)^2 \frac{P_\mathrm{t} - P_\mathrm{c} - P_\mathrm{f}}{J_\mathrm{tc} n_\mathrm{tc}}. \tag{3.35}$$

The moment of inertia is determined experimentally from turbocharger speed measurements in dynamic engine operation on the test bench. The identified inertia is $J_{\mathrm{tc}} = 1.475 \cdot 10^{-5}$ kg m^2. The friction loss is expressed as viscous friction

$$P_{\mathrm{f}}(t) = M_{\mathrm{f}}(t)\omega_{\mathrm{tc}}(t) = k_{\mathrm{f}}\omega_{\mathrm{tc}}^2(t) = k_{\mathrm{f}}(2\pi n_{\mathrm{tc}})^2 \tag{3.36}$$

This simple quadratic approach with only one parameter to be determined provides a sufficient model accuracy up to higher turbocharger speeds, where the frictional power deviates marginally from a more detailed model (Zahn 2012).

3.2.4 Heat transfer

At the compressor impeller, the temperature rises not only as a result of the compression, but also through indirect heat transfer from the turbocharger housing. On the turbine side, a substantial amount of heat is also dissipated from the hot exhaust gas to the environment and the turbocharger housing during the expansion process, see Fig. 3.5. For a complete modeling of the airpath states, these heat flows must be considered by the turbocharger model in order to reproduce the output temperatures of the compressor and turbine, see Fig. 3.7.

Since the underlying heat transfer processes in the turbocharger are extremely complex and cannot be determined using conventional engine test bench sensors, this work relies on a simple stationary heat transfer model approach based on Newton's law, see Appx. A.2.1 *Heat transfer*. For more a detailed model approach that considers also heat transfer dynamics, see i.e. Zahn (2012). The approach presented here focuses only the heat dissipation of the exhaust gas on the turbine side $3 \rightarrow 4$ and the heat absorption of the intake gas on the compressor side $1 \rightarrow 2\mathrm{c}$.

In general, the heat transfer $\dot{Q}_{\mathrm{t}}$ from the exhaust gas (p_3, T_3) to the turbocharger housing is composed of a convective component, a component due to thermal radiation, and a component due to thermal conduction. Some of the exhaust gas heat is also transferred to the compressor mass flow via the turbocharger housing. However, a detailed modeling and balancing of these heat energy flows is omitted. Instead, it is simply assumed that the heat transfers $\dot{Q}_{\mathrm{t}}$ and $\dot{Q}_{\mathrm{c}}$ are mainly driven by the highest temperature gradient.

On the turbine side, the largest temperature difference lies between the exhaust gas and the environment (engine temperature)

$$\dot{Q}_{\mathrm{t}} = \alpha_{\mathrm{t}} A_{\mathrm{t}} \left(T_3 - T_{\mathrm{eng}}\right) = k_{\alpha \mathrm{t}} \left(T_3 - T_{\mathrm{eng}}\right) \tag{3.37}$$

On the compressor side, the exhaust gas heat is conducted via the turbocharger housing to the compressor flow $T_3 \rightarrow T_1$

$$\dot{Q}_{\mathrm{c}} = \alpha_{\mathrm{c}} A_{\mathrm{c}} \left(T_1 - T_3\right) = k_{\alpha \mathrm{c}} \left(T_1 - T_3\right) \tag{3.38}$$

For simplification, the unknown model parameters heat transfer coefficient α_i and heat transfer surface A_i are combined into a single parameter $k_{\alpha i}$.

The outlet temperatures of the turbine T_t is determined from Eq. (3.31) with the specific adiabatic expansion work $\Delta h_{t,adi} = P_t/\dot{m}_t$ and the summarized heat transfers (3.32) as follows

$$T_t = T_3 - \frac{P_t + \dot{Q}_t}{\dot{m}_t c_p} = T_3 - \frac{P_t + k_{\alpha t}(T_3 - T_{eng})}{\dot{m}_t c_p}, \tag{3.39}$$

with the isobaric heat capacity $c_p = 1005$ J/(kg K) of fresh air at the ambient conditions $T_a = 20°C$ and $p_a = 1.013$ bar. Analogously, the compressor outlet temperature T_c is obtained from Eq. (3.25) with the specific adiabatic work $\Delta h_{c,adi} = P_c/\dot{m}_c$ as follows

$$T_c = T_1 + \frac{P_c - \dot{Q}_c}{\dot{m}_c c_p} = T_1 + \frac{P_c - k_{\alpha c}(T_1 - T_3)}{\dot{m}_c c_p}. \tag{3.40}$$

The upstream and downstream heat transfers at the compressor impeller are summarized to $q_{c,1} + q_{c,2} = \dot{Q}_c/\dot{m}_c$, compare Fig. 3.5

3.3 Airpath estimation

In the following, the procedure for estimating the states and unknown parameter of the semi-physical airpath model, including the intake and exhaust system and the turbocharger, is referred to as *airpath estimation*. For the combined state and parameter estimation, the Cubature Kalman filter (CKF) algorithm is used, which has advantages in case of non-linear or discontinuous systems due to its derivative-free propagation of stochastic properties (means and covariances), see Sect. 2.3.2. The storage of the operating point dependent behavior of the estimated parameter is then referred to as experimental parameter modeling, see Sect.3.4. Airpath estimation comprises the model-based determination of unknown state variables and parameter models of the semi-physical airpath model based on the sensor information available during measurements at the engine test bed. The scheme of airpath estimation is shown in Fig. 3.2. As shown there, airpath estimation uses a joint state and parameter estimation approach (Sect. 2.3.3).

The state estimation is used to determine non-measured states $\mathbf{x}$, such as pressures and temperatures. The parallel estimation of the physical model parameters $\boldsymbol{\theta}$ allows the adaptation of the underlying estimation model $\mathbf{f}(\mathbf{x}, \boldsymbol{\theta}, \mathbf{u})$ to the real, measured system behavior $\mathbf{u} \rightarrow \mathbf{y}_m$. Since the physical parameters $\boldsymbol{\theta}$ can change depending on input $\mathbf{u}$ and operating point variables $\mathbf{z}$, this parameter behavior is modeled by an experimental modeling approach $\mathbf{g}(\mathbf{w}, \mathbf{z}, \mathbf{u})$, compare to Fig. 3.2.

The structure of the airpath model, including its modeled elements, such as air ducts/storages, actuators, cooler elements as well as compressor and turbine of the turbocharger, is shown in Fig. 3.1. As described in the previous Sects. 3.1 and 3.2, the state variables of these elements and their relations to each other are modeled using *simple physical equations*. Unknown engine-specific parameters and complex nonlinear characteristics are described by *experimental parameter models*. The variability in the parameters allows a model adaptation to the real behavior.

Available measurements

Available measurements in series engine are the pressure $p_{2\mathrm{i}}$ and temperature $T_{2\mathrm{i}}$ in the intake manifold, the fresh air mass flow rate $\dot{m}_{\mathrm{hfm}}$ using hot film mass sensor, the air-fuel ratio λ_4 and temperature T_4 downstream of the turbine. Engine speed n_{eng} and the oil/water temperature (T_{oil}, T_{h2o}) of the engine are also measured.

$$\mathbf{y}_{\mathrm{m,series}} = \begin{bmatrix} n_{\mathrm{eng}} & \dot{m}_{\mathrm{hfm}} & p_{2\mathrm{i}} & T_{2\mathrm{i}} & \lambda_4 & T_4 & T_{\mathrm{oil}} & T_{\mathrm{h2o}} \end{bmatrix}^{\mathrm{T}}.$$

The cylinder mass flows are unknown. The cylinder filling is typically determined using experimental models for the volumetric efficiency (lookup-tables) determined from stationary measurements (J. B. Heywood 1988), see also example in 2.4. In this work, the cylinder mass flows are provided by the cylinder group model, see Ch. 4.

These measurements are typically subject to sensor errors such as noise, drift and dynamic delays.[6] With the lambda probes it is only possible to measures the air-fuel ratio $\lambda_{3/4}$ in the exhaust path, so that the emission-relevant air mass fraction $X_{1/2\mathrm{i}}$ in the intake system remains unknown in transient engine operation, see Fig. 3.1.

At the engine test bed, additional pressure and temperature sensors in the intake path (p_1, T_1), ($p_{2\mathrm{c}}, T_{2\mathrm{c}}, T_{2\mathrm{ic}}$), in the exhaust path ($p_3, T_3$), ($p_4, T_4$), and in the EGR path ($T_{\mathrm{hpegr}}, T_{\mathrm{lpegr}}$) are used to simplify the airpath estimation. For modeling and identification of the coolers in the airpath, the outlet gas temperatures $T_{\mathrm{cl,out}}$ of the coolers must be measured using additional thermocouples. The air mass fractions X_1 and $X_{2\mathrm{i}}$ in the mixing points of the intake system are determined based on modeled mass flows.

To identify the parameters of the airpath actuator models (throttles, EGR valves), the turbocharger model and the cooler models, the corresponding upstream and downstream gas pressure and temperatures must be measured at the engine test bed. Furthermore, the turbocharger speed n_{tc} Eq. (3.35) and the turbocharger powers (Sect. 3.2.2) couple the mass flows and gas states on the turbine and the compressor side. Consequently, to identify this coupling as well as the dynamic behavior of the turbocharger, the turbocharger speed n_{tc} must be measured.

State estimation

The gas state variables are summarized into one gas state vector

$$\mathbf{x}_i = \begin{bmatrix} p_i & T_i & X_i \end{bmatrix}^{\mathrm{T}}.$$

The state variables $\mathbf{x}_i$ are determined by the state estimator in the prediction step based on the airpath model and dynamically corrected in the correction step using the corresponding measured signal values. Based on the state estimates $\hat{\mathbf{x}}_i$, the mass flow rates through the throttles, valves and

[6] Temperature sensor have a dynamic delay in the range of 1-2 seconds

the turbocharger impellers are calculated. For the sake of more compact notation, the mass flow variables of the air path model are summarized in the vector $\mathbf{M}_{\mathrm{ap}}$

$$\mathbf{M}_{\mathrm{ap}} = \begin{bmatrix} \dot{m}_{\mathrm{ith}} & \dot{m}_{\mathrm{c}} & \dot{m}_{\mathrm{th}} & \dot{m}_{\mathrm{t}} & \dot{m}_{\mathrm{eth}} & \dot{m}_{\mathrm{hpegr}} & \dot{m}_{\mathrm{lpegr}} \end{bmatrix}^{\mathrm{T}}. \tag{3.41}$$

These mass flows are dependent on the corresponding actuator input variables

$$\mathbf{u}_{\mathrm{ap}} = \begin{bmatrix} u_{\mathrm{ith}} & u_{\mathrm{th}} & u_{\mathrm{vgt}} & u_{\mathrm{eth}} & u_{\mathrm{hpegr}} & u_{\mathrm{lpegr}} \end{bmatrix}^{\mathrm{T}}, \tag{3.42}$$

whereby, compressor and turbine mass flows $\dot{m}_{\mathrm{c}}$ and $\dot{m}_{\mathrm{t}}$ are additionally dependent on turbocharger speed n_{tc}.

Parameter estimation

The parameter estimator determines the parameters $\boldsymbol{\theta}_{\mathrm{f}}$ (discharge coefficients, turbocharger power coefficient) of the flow variables

$$\boldsymbol{\theta}_{\mathrm{f}} = \begin{bmatrix} c_{\mathrm{ith}} & c_{\mathrm{c}} & k_{\mathrm{c}} & c_{\mathrm{th}} & c_{\mathrm{t}} & k_{\mathrm{t}} & c_{\mathrm{hpegr}} & c_{\mathrm{lpegr}} \end{bmatrix}^{\mathrm{T}} \tag{3.43}$$

based on the measured gas state variables $\mathbf{x}_i$ (measured reference variables). The parameters of the heat dissipations at the cooler elements $\dot{Q}_{\mathrm{ic}}$, $\dot{Q}_{\mathrm{hpcl}}$, $\dot{Q}_{\mathrm{lpcl}}$ and the heat transfers at the compressor and the turbine of turbocharger $\dot{Q}_{\mathrm{c}}$, $\dot{Q}_{\mathrm{t}}$ are estimated based on the corresponding upstream and downstream gas temperatures T_i. These parameters are summarized into the parameter vector

$$\boldsymbol{\theta}_{\mathrm{q}} = \begin{bmatrix} k_{\mathrm{ic}} & k_{\mathrm{hpcl}} & k_{\mathrm{lpcl}} & k_{\alpha\mathrm{c}} & k_{\alpha\mathrm{t}} \end{bmatrix}^{\mathrm{T}} \tag{3.44}$$

If a particular set of parameters $\boldsymbol{\theta}$ can be found that does not change during steady-state engine operation, it is legitimate to assume that these parameters may be dependent on the operating point, but must be constant for an engine operating point $(\mathbf{z}, \mathbf{u})$.[7] Then, for the model parameters follows

$$\begin{aligned} \boldsymbol{\theta} &= \mathbf{g}(\mathbf{z}, \mathbf{u}) \\ \Leftrightarrow \frac{\mathrm{d}\boldsymbol{\theta}}{\mathrm{d}t} &= \frac{\mathrm{d}}{\mathrm{d}t}\mathbf{g}(\mathbf{z}, \mathbf{u}) = 0. \end{aligned} \tag{3.45}$$

To keep input dimension of this experimental parameter model (3.45) low as possible, additional knowledge about the physical relation between $\boldsymbol{\theta}$ and the input variables $(\mathbf{z}, \mathbf{u})$ must be exploited.

In Sect. 3.4, the airpath model parameters $\boldsymbol{\theta}_{\mathrm{M}}$ and $\boldsymbol{\theta}_{\mathrm{Q}}$ are *modeled experimentally* as functions of their input variables $\mathbf{u}_{\mathrm{ap}}$ and other influencing variables $\boldsymbol{\theta}_{\mathrm{M}} = \mathbf{g}(\mathbf{u}_{\mathrm{ap}}, \cdots)$.

3.3.1 State and parameter estimation model

The estimation model for the intake and exhaust system can be divided into a low-pressure and a high-pressure subsystem separated from each other by the turbocharger stage, see Fig. 3.8. Compare

[7] operating point variable vector $\mathbf{z}$ includes the engine load and speed

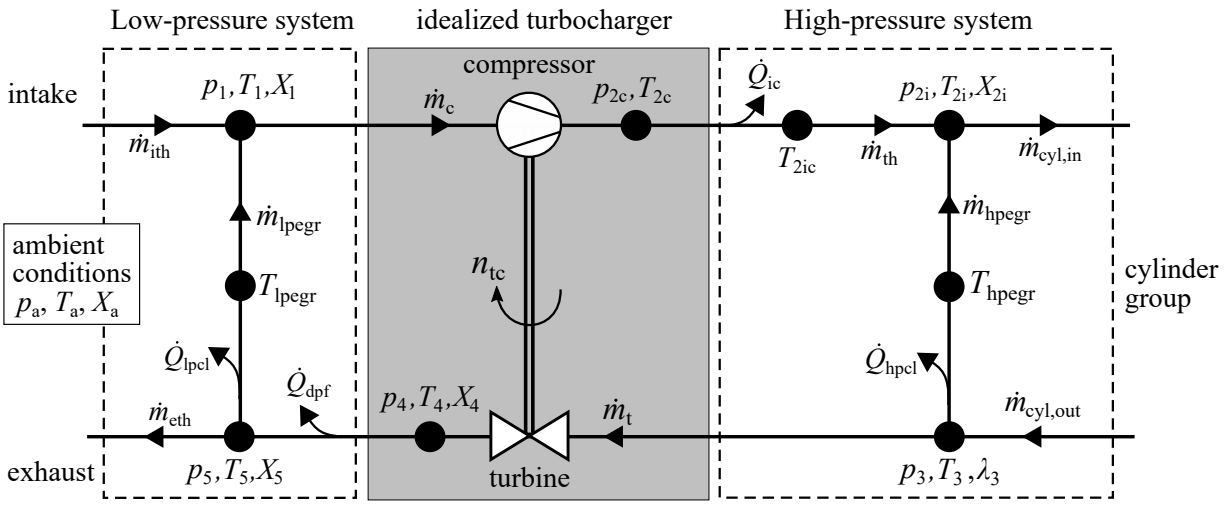

Figure 3.8: Simplified scheme of the airpath estimation model with the low-pressure subsystem before the turbocharger stage and the high-pressure subsystem after. VGT-Turbocharger is modeled by idealized elements (compressor as pump and turbine as flow restriction), compare with Fig. 3.1

to scheme in Fig. 3.1, some simplification are made in order to reduce model complexity of the state estimation model.

The high-pressure and the low-pressure subsystem are structured in the same way. The intake and exhaust gas ducts are represented by sequence of gas storages, which are connected via the exhaust gas recirculation. Due to these similarities, both estimation models are also derived in a similar way. In the intake path of low-pressure subsystem, simplification can be achieved by considering the flow resistance of the air filter in the model of the intake throttle.

In the high-pressure subsystem, the heat dissipation $\dot{Q}_{ic}$ of the intercooler is taken into account in addition to the heat dissipation $\dot{Q}_{hpegr}$ at the EGR cooler. The pressure drop in the intercooler and in both EGR-coolers is neglected. In the exhaust path, modeling of the flow resistance and heat dissipation of the DPF/DOC is neglected and taken into account by the nearby elements (exhaust throttle, LP-EGR cooler), see Fig. 3.1. To further simplify the model, the gas reservoirs 4 and 5 can be combined into one.

The estimation model for the turbocharger differs only in the fact that the intake path (compressor) and the exhaust path (turbine) are mechanically coupled via the turbocharger shaft instead of being connected via the EGR path, compare Fig. 3.1.

Generally, the airpath estimation can be split into these three subsystems depicted in Fig. 3.8, in order to reduce model complexity as well as to simplify the tuning of the state and parameter estimators. The mass flow variables represent then the model interfaces between these subsystems. The scheme of the airpath estimation for the high-pressure subsystem is shown exemplary in Fig. 3.9.

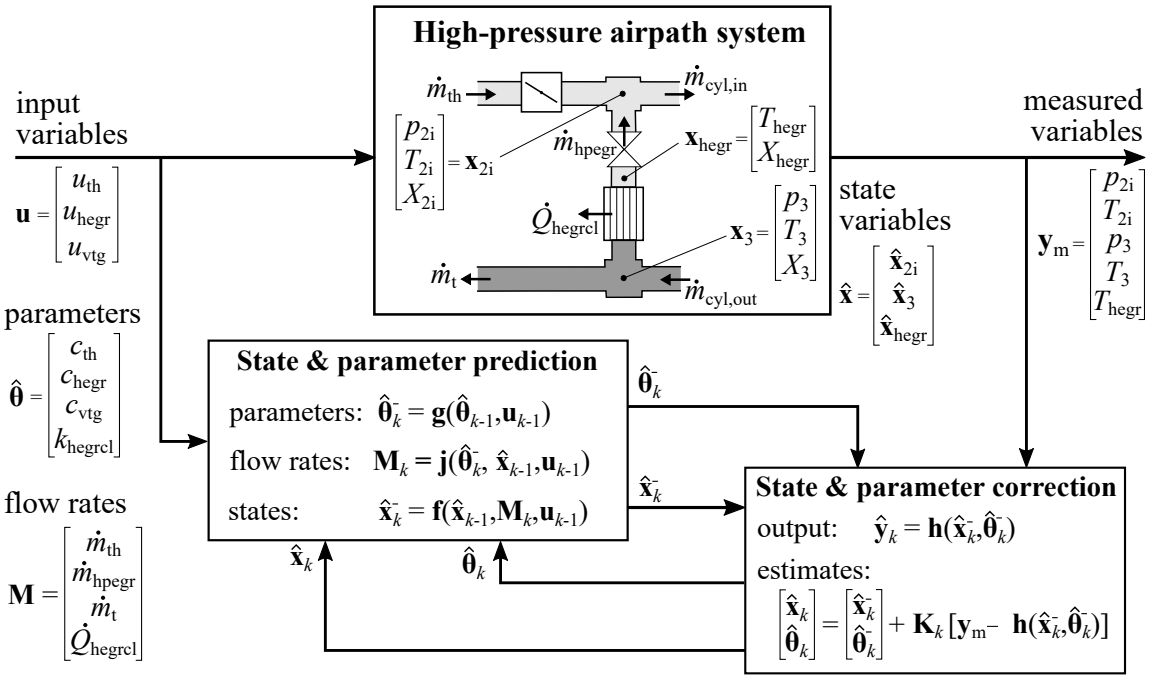

Figure 3.9: Scheme of high-pressure airpath estimation

Another advantage of this split is the fact that it allows different air path topologies to be modeled. For example, the high-pressure subsystem alone corresponds to the air system of a non-turbocharged suction engine. By omitting the low-pressure subsystem, the result is the air system of a turbocharged engine with a simple EGR.

Regardless of which subsystem of the air path is modeled, the equations of the estimation model can be distinguished into *state equations* for the gas states $\mathbf{x}_i$ in the storages and cooler volumes, *flow equations* for the mass $\dot{m}_i$ and heat flows $\dot{Q}_i$, and *estimation models for the physical parameters* θ_i. Note that the physical parameters in the estimation are modeled in a simplified way as constants without dependencies on other variables.

For application within state and parameter estimation, the equations must be transformed into the time-discrete representation using explicit Euler method; see also Sect. 2.3.3. Time derivatives are approximated by discrete difference variables as given in Eq. (2.10).

Gas state equations

The state equations for the gas state $\mathbf{x}_{st}$ in a gas storage of the airpath (subscript st =1, ..., 5) are given in discrete-time formulation as follows[8] (see Sect. 3.1.1):
Gas pressure

$$p_{st}(k) = p_{st}(k-1) + \frac{T_s R_{air} T_{st}(k-1)}{V_{st}} \left[\sum_{i=1}^{p} \Delta m_{in,i}(k-1) - \sum_{j=1}^{q} \Delta m_{out,j}(k-1) \right], \quad (3.46)$$

[8]The notation x_k, x_{k-1} is a more compact notation for $x(k)$, $x(k-1)$, see Sect. 2.1.2

Gas temperature with $\Delta Q_{\mathrm{w,st}} \approx 0$

$$T_{\mathrm{st}}(k) = T_{\mathrm{st}}(k-1) + \frac{T_{\mathrm{s}}}{m_{\mathrm{st}}(k-1)} \cdot \left[\sum_{i=1}^{p} \left[T_{\mathrm{in},i}(k-1) - T_{\mathrm{st}}(k-1) \right] \Delta m_{\mathrm{in},i}(k-1) \right], \quad (3.47)$$

Air mass fraction

$$X_{\mathrm{st}}(k) = X_{\mathrm{st}}(k-1) + \frac{T_{\mathrm{s}}}{m_{\mathrm{st}}(k-1)} \left[\sum_{i=0}^{p} \left[X_{\mathrm{in},i}(k-1) - X_{\mathrm{st}}(k-1) \right] \Delta m_{\mathrm{in},i}(k-1) \right]. \quad (3.48)$$

Equations (3.46) to (3.48) apply to all gas storages 1 to 5 in the air system (Fig. 3.8). The constant storage volumes V_{st} must be approximated from engine parameters or identified experimentally. Storage masses are determined using ideal gas law $m_{\mathrm{st}} = (p_{\mathrm{st}} V_{\mathrm{st}})/(R_{\mathrm{air}} T_{\mathrm{st}})$.

The temperature reduction caused by heat dissipation in the coolers is described by discretization of Eq. (3.17)

$$\begin{aligned} T_{\mathrm{cl}}(k) = T_{\mathrm{cl}}(k-1) + \frac{T_{\mathrm{s}}}{m_{\mathrm{cl}}(k-1)} \\ \cdot \left[\sum_{i=0}^{p} \left[T_{\mathrm{in},i}(k-1) - T_{\mathrm{cl}}(k-1) \right] \Delta m_{\mathrm{in},i}(k-1) + \frac{\Delta Q_{\mathrm{cl}}(k-1)}{c_{\mathrm{v}}} \right], \end{aligned} \quad (3.49)$$

whereas T_{cl} is the cooler outlet gas temperature, m_{cl} is the gas mass inside the cooler, and ΔQ_{cl} is the flow rate of heat dissipation. The flow resistance of coolers is neglected ($p_{\mathrm{cl,out}} \approx p_{\mathrm{cl,in}}$). The time delays of the air mass fractions due to the gas propagation times through the coolers are also modeled using Eq. (3.48).

The state equations for the gas states $\mathbf{x}_i$ of each i-th storage and cooler element are merged into one discrete-time state space representation as shown exemplary in Fig. 3.9.

$$\mathbf{x}_k = \begin{bmatrix} \mathbf{x}_1(k) \\ \vdots \\ \mathbf{x}_5(k) \end{bmatrix} = \mathbf{f}\left(\mathbf{x}_{k-1}, \boldsymbol{\theta}_k, \mathbf{u}_{k-1}\right) \quad (3.50)$$

The dimension of the state estimation model is given by the number of considered gas storages and cooler elements. If a turbocharger is considered, the turbocharger speed n_{tc} must be introduced as additional state variable. Its state equation is given by Eq. (3.35).

Flow equations

The mass flows through the throttles and EGR valves are described using the flow equation for compressible fluids (3.10)

$$\Delta m_i(k) = c_i\left(u_i, \cdots\right) \frac{p_{\mathrm{in}}(k)}{\sqrt{R_{\mathrm{air}} T_{\mathrm{in}}(k)}} \Psi\left(\frac{p_{\mathrm{out}}(k)}{p_{\mathrm{in}}(k)}\right). \quad (3.51)$$

The parameter c_i takes into account the actuator position characteristics $f(u_i)$, the cross-sectional area A_{th} and the discharge coefficient c_{d}. The exponential-function-type outflow function (3.14) is used for $\Psi(\cdot)$ since it allows an easier formulation of the derivative with respect to pressure ratio.

The cooling powers of airpath coolers are described by Eq. (3.16) as follows

$$\Delta Q_{\text{cl}}(k) = k_{\text{cl}}\left(\Delta m_i, n_{\text{eng}}\right) A_{\text{cl}}\left(T_{\text{h2o}} - T_{\text{cl}}(k)\right), \tag{3.52}$$

where the heat transfer coefficient k_{cl} depend on the mass flows rate of the gas to be cooled and the engine coolant flow rate, which is assumed to be proportional to engine speed n_{eng}.[9]

The mass and power flows of the turbocharger are calculated using the equations in Sects. 3.2.1 and 3.2.2. The compressor mass flow $\Delta m_{\text{c}}(k)$ is obtained using discretization of Eq. (3.22) and the turbine mass flow $\Delta m_{\text{t}}(k)$ is obtained using Eq. (3.23). Discretization of Eq. (3.33) and (3.25) yields to the turbocharger power flows $P_{\text{c}}(k)$ and $P_{\text{t}}(k)$.

The equations of the flow variables can be summarized into a discrete-time nonlinear state space representation, as exemplarily shown in Fig. 3.9 for the high-pressure subsystem.

$$\mathbf{M}_k = \begin{bmatrix} \Delta m_{\text{ith}}(k) \\ \vdots \\ \Delta Q_{\text{legr}}(k) \end{bmatrix} = \mathbf{j}\left(\boldsymbol{\theta}_{k-1}, \mathbf{x}_{k-1}, \mathbf{u}_{k-1}\right) \tag{3.53}$$

The flow variables represent intermediate quantities which are calculated based on the input variables and the estimates of state variables and parameters.

Parameter estimation models

Within the combined state and parameter estimation scheme, the physical parameters to be estimated $\boldsymbol{\theta}$, defined in Eqs. (3.43) and (3.44), are modeled as constants by simple Markovian first order processes (stochastic random variable). Through discretization of Eq. (3.45) results following time-discrete parameter model for each i-th parameter of $\boldsymbol{\theta}$

$$\boldsymbol{\theta}_i(k) = \boldsymbol{\theta}_i(k-1) + \mathbf{w}_i(k-1) \tag{3.54}$$

whereas the variable $\mathbf{w}_i$ represents the stochastic random parameter noise, acting on the constant parameter $\boldsymbol{\theta}_i$. By modelling this parameter noise variable, the adaptation of the parameter during state and parameter estimation is controlled. For $\mathbf{w}_i \neq 0$ the i-th parameter is adapted, while for $\mathbf{w} = 0$ the parameter is kept constant. The parameter noise variables are considered within the covariance matrices $\mathbf{Q}$ in the Kalman filter algorithm, see Sect. 2.3.2.

3.3.2 Joint gas state and estimation

Due to the large number of airpath states and parameters, it is reasonable to split the airpath estimator into the subsystems as shown in Fig. 3.8. This leads to three separate combined state and

[9] The coolant pump is typically connected by a V-belt to the crankshaft and driven by engine speed

parameter estimators, one for the low-pressure subsystem, one for the turbocharger stage and one estimator for the high-pressure subsystem. This partitioning significantly reduces the dimension of each of the three estimators. For example, the high-pressure subsystem estimator in Fig. 3.8 has 8 states and 4 parameters to be estimated.

For combined state and parameter estimation, a Sigma-point Kalman filter approach is chosen (CKF), see Sect. 2.3.3. Furthermore, a decision must be made between a joint or a dual estimation approach. In the following, simulation results for the joint estimation approach are shown. The equations for the state variables and parameters are derived from previous section. In addition, all equations are normalized regarding the states and parameters to be estimated in order to achieve a better filtering robustness and to facilitate the filter tuning by bringing all state variables and parameter in the value range of [0; 1].

By merging all time-discrete state and parameter equations together into one state space representation, a linear state space model of n-th order results for each estimator. The estimation model for each subsystem is given in state space representation as follows $(n = n_x + n_\theta)$[10]

$$\begin{aligned} \begin{bmatrix} \mathbf{x}(k) \\ \boldsymbol{\theta}(k) \end{bmatrix} &= \begin{bmatrix} \mathbf{f}\big(\mathbf{x}(k-1), \boldsymbol{\theta}(k-1), \mathbf{u}(k-1)\big) \\ \mathbf{I} \cdot \boldsymbol{\theta}(k-1) \end{bmatrix} + \begin{bmatrix} \mathbf{w}_\mathrm{x}(k) \\ \mathbf{w}_\theta(k) \end{bmatrix}, \\ \mathbf{y}(k) &= \mathbf{h}\big(\mathbf{x}(k)\big) + \mathbf{v}(k), \end{aligned} \tag{3.55}$$

with state variables $\mathbf{x}_\mathrm{hp} = [p_{2\mathrm{i}}, T_{2\mathrm{i}}, \cdots]^\mathrm{T}$ and parameters $\boldsymbol{\theta}_\mathrm{hp} = \big[c_\mathrm{th}, c_\mathrm{hegr}, \cdots\big]^\mathrm{T}$. The output vector $\mathbf{y}$ corresponds to the measured gas pressures $p_{i,\mathrm{m}}$ and temperatures $T_{i,\mathrm{m}}$ in the air path in order to formulate the estimation error

$$\mathbf{e}(k) = \mathbf{y}_\mathrm{m}(k) - \hat{\mathbf{y}}(k) = \mathbf{y}_\mathrm{m}(k) - \begin{bmatrix} \hat{p}_{2\mathrm{i}} \\ \hat{T}_{2\mathrm{i}}(k) \\ \hat{p}_3(k) \\ \hat{T}_3(k) \\ \hat{T}_{2\mathrm{ic}}(k) \\ \hat{T}_\mathrm{hegr}(k) \end{bmatrix}. \tag{3.56}$$

Using this estimation error equation (3.56), both the mass flows through the throttle valve $\dot{m}_\mathrm{th}$ and the HP-EGR valve $\dot{m}_\mathrm{hegr}$ and the heat removal $\dot{Q}_\mathrm{icl}$, $\dot{Q}_\mathrm{hpcl}$ of the coolers in the high-pressure subsystem are determined and their physical parameters c_th, c_hegr, k_icl, k_hpcl are estimated.

The joint estimator for the low-pressure subsystem is structured analogously. The joint estimator for the turbocharger stage differs insofar as the measured turbocharger speed n_tc is additionally used to estimate the turbocharger variables such as the turbocharger mass flows $\dot{m}_\mathrm{c}$, $\dot{m}_\mathrm{t}$ and powers P_c, P_t.

The estimation of turbocharger parameters is based on the gas state changes $(p_1, T_1) \rightarrow (p_{2\mathrm{c}}, T_{2\mathrm{c}})$ and $(p_3, T_3) \rightarrow (p_4, T_4)$, while the power quantities are estimated based on the momentum equation (3.35) and the measured turbocharger speed n_tc. Eqs. (3.39) and (3.40) for the turbocharger outlet

[10] It is also possible to use one estimation model for the estimation of the overall airpath system

temperatures T_c and T_t allow the estimation the turbocharger heat flows $\dot{Q}_c$, $\dot{Q}_t$ and heat transfer coefficients $k_{\alpha c}$, $k_{\alpha t}$.

Figures 3.10 and 3.11 show simulation results of the joint airpath estimators for two different engine operation scenarios. A detailed airpath simulation model, presented in Mrosek (2017), is used to generate the simulation data. The parallel simulations of the detailed airpath model and the airpath estimators are performed in a crank angle resolved sampling raster with the crank angle resolution of 18° CS. For visualization reasons, the simulated courses were converted into the time base.

In both scenarios, the airpath system is in the same initial state at the beginning of the simulation($q_{inj} = 15\text{mm}^2$, $n_{eng} = 1560$ 1/min). The airpath estimators are activated after about $t = 0.1$ s. In the first case, in Fig. 3.10, a manipulation of the HP-EGR valve u_{hegr} (step input) is performed at $t = 5.5$ s. In the second simulation scenario in Fig. 3.11, the VGT turbocharger u_{vgt} is adjusted at the same time $t = 5.8$ s.

The initial values for the estimates for the state variables $\mathbf{x}_0$ are chosen to be either equal to the ambient condition or set to a reasonable value. The diagonal elements of the initial error covariances $\mathbf{P}_0$, corresponding to the state variables $\mathbf{x}_i$, are calculated by using the square of the initial error $\mathbf{e}_x = (\mathbf{x}_0 - \mathbf{x}_{ref})^2$. The diagonal elements in $\mathbf{P}_0$ which represent the initial error covariances of the parameter to be estimated $\boldsymbol{\theta}$ are defined as a percentage of the initial parameter value $\mathbf{e}_\theta = (A \cdot \boldsymbol{\theta}_\mathbf{0})^2$ with $0 < A < 0.5$.

In the upper plots, the input variables of the air path actuators u_{th}, u_{hegr} and u_{vtg} and a comparison between the courses of estimated state variables and simulated reference courses is shown. The behavior of the airpath estimators is adjusted by modeling the values of the diagonal elements of the process noise covariance matrices $\mathbf{Q}$ and the measurement noise covariance matrices $\mathbf{R}$ (see Sect. 2.3.2),

$$\mathbf{Q} = \begin{bmatrix} \mathbf{Q}_x & 0 \\ 0 & \mathbf{Q}_\theta \end{bmatrix} = \begin{bmatrix} \mathrm{E}\{\mathbf{w}_x(\mathbf{w}_x)^\mathrm{T}\} & 0 \\ 0 & \mathrm{E}\{\mathbf{w}_\theta(\mathbf{w}_\theta)^\mathrm{T}\} \end{bmatrix} \quad \text{and} \quad \mathbf{R}_y = \mathrm{E}\{\mathbf{v}(\mathbf{v})^\mathrm{T}\}.$$

It can be seen that the estimated gas pressures and temperatures converge towards the reference courses after only a few milliseconds. This is achieved by assuming low values for the measurement noise covariances $\mathbf{R}_y$ of the reference pressures and temperatures, so that the Kalman filter algorithm relies strongly on their courses. Choosing higher values for the diagonal elements of the parameter noise covariance matrix $\mathbf{Q}_\theta$ leads to an adaptation of the parameters to be estimated and eventually to an overall adaption of the estimation model $\mathbf{f}(\mathbf{x}, \boldsymbol{\theta}, \mathbf{u})$ to match the behavior of the reference model.

The lower plots in Figs. 3.10 and 3.11 show the courses of the estimated mass flows and their associated estimated parameters. The estimated mass flow rates are compared with the simulated courses generated from the detailed airpath model (Mrosek 2017). The estimated mass flows correspond to the reference flows. Only during the transition phase after adjustment of the HP-EGR valve or the VTG the estimated mass flows deviate temporarily from the reference values. The mass flow through the HP-EGR valve converges more slowly towards the its corresponding reference

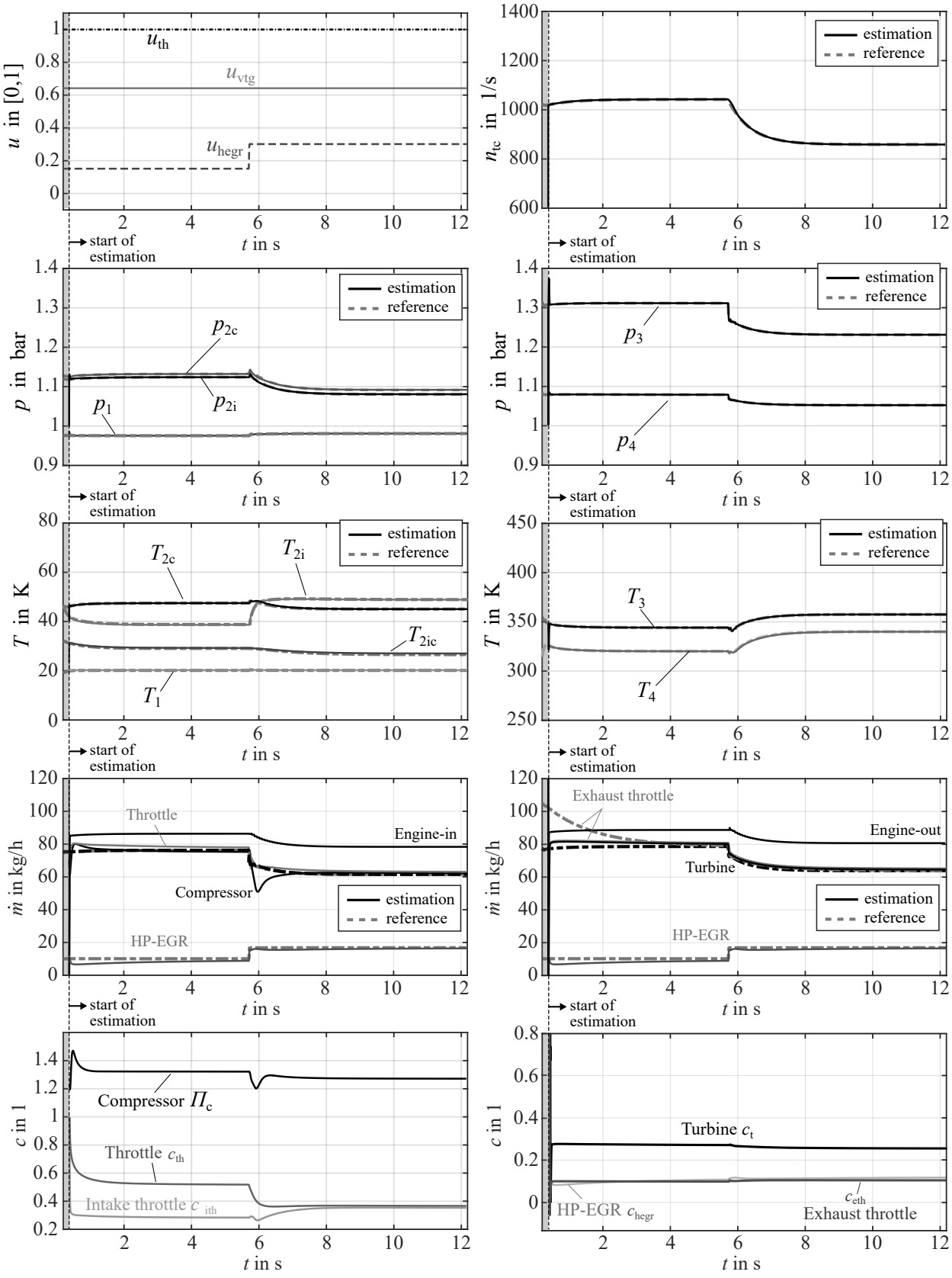

Figure 3.10: Simulation results of joint airpath state and parameter estimation for a manipulation of HP-EGR ($q_{\mathrm{inj}} = 15\mathrm{mm}^2$, $n_{\mathrm{eng}} = 1560$ 1/min)

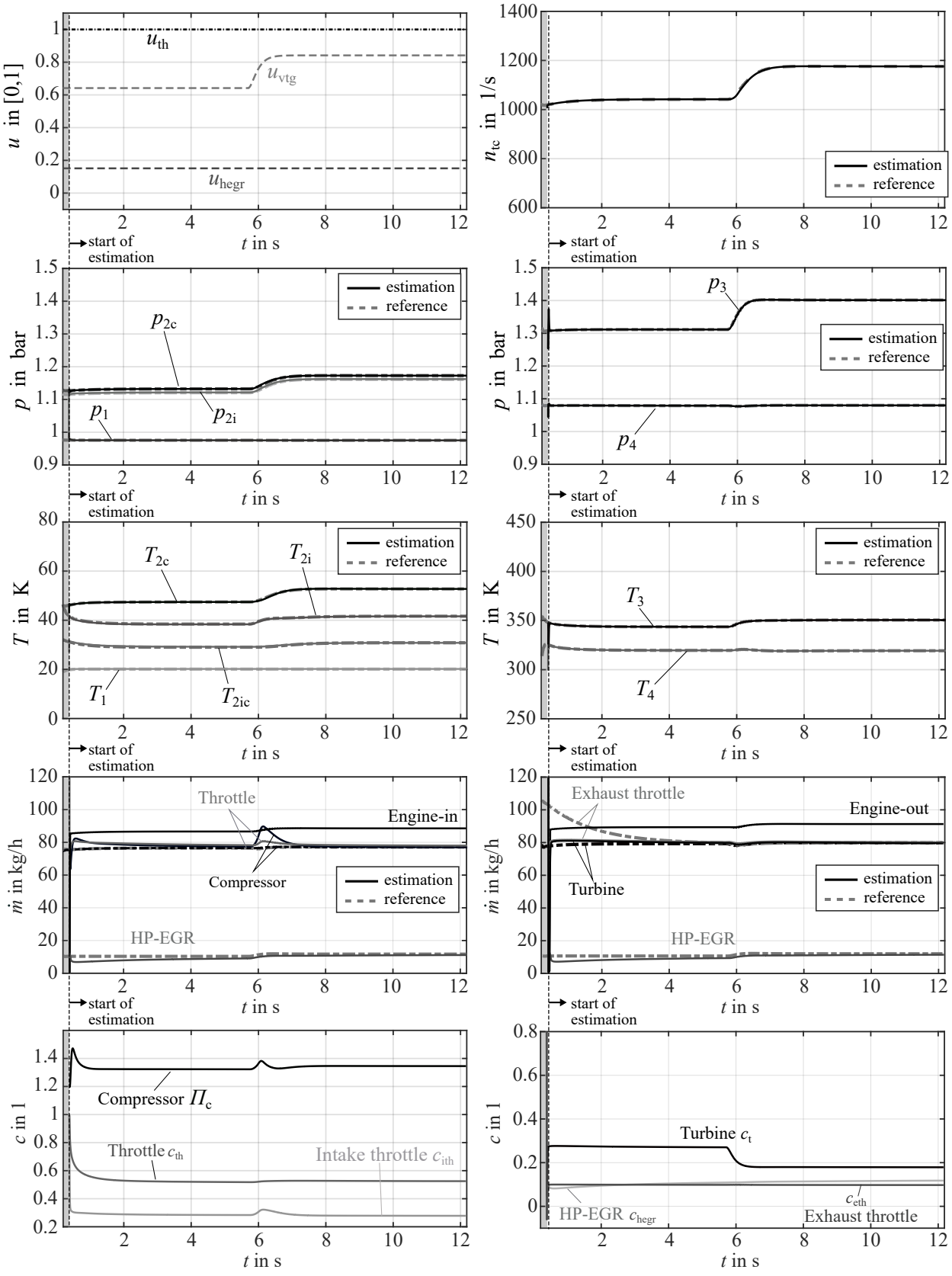

Figure 3.11: Simulation results of joint airpath state and parameter estimation for a manipulation of VTG-Turbocharger ($q_{\mathrm{inj}} = 15\mathrm{mm}^2$, $n_{\mathrm{eng}} = 1560$ 1/min)

value since the magnitudes of mass flow $\dot{m}_{\text{hegr}}$ and excitation u_{hegr} are lower compared to the other airpath actuators.

The bottom plots show the courses of the estimated parameters. It can be seen that the parameters change during excitation, but settle to a constant value during a stationary phase after a short period of time. It can be seen that the change in parameters correlates with other state variables. As soon as the engine operation state changes, the estimated parameters are adapted by the estimator as well in order to match the model variables with the reference variables. However, during steady state operation, both state variables and estimated parameters are in a steady state condition. The steady state condition of the parameters during these stationary engine operation phases can be used for the experimental modeling of the parameters as functions of influencing state variables.

3.4 Experimental parameter modeling

In the previous section, physical airpath parameters $\hat{\boldsymbol{\theta}}$, defined in Eqs. (3.43) and (3.44) are determined during engine operation using combined state and parameter estimators (Figs. 3.10 and 3.11). Further comparison with stationary engine measurement haven shown that the estimated parameters, such as the flow coefficients c_{th}, c_{hegr}, etc., adapt according to the input variables and engine operating point (engine speed, injection quantity).

For the identification of the overall semi-physical airpath model, the engine operating point-dependent behavior of the parameters $\boldsymbol{\theta} = \mathbf{g}(\mathbf{z}, \mathbf{u})$ must be mapped by experimental models. For this purpose, the airpath estimation is applied to 51 steady-state engine measurement points; see also Fig. 5.3 b). Resulting estimated parameters are used as reference values for modeling the parameter behavior. The procedure for measuring the steady-state engine operating points is described in Sect. 5.1.2.

The parameter behavior is modeled based on the approach (2.19) given in Sect. 2.4

$$\hat{\theta}(\mathbf{z}) = \boldsymbol{\Phi}(\mathbf{z})^{\mathrm{T}}\mathbf{W} = g(\mathbf{z}) = \sum_{i=1}^{L} \Phi_i(\mathbf{z}) w_i. \tag{3.57}$$

The experimental modeling is carried out by identifying the weights $\mathbf{W}$ during the steady-state operating phases in which the physical parameters $\hat{\boldsymbol{\theta}}$ have settled to a constant value. Here, the physical parameters serve as reference values $\hat{\theta}$ for identifying the weighting factor $\mathbf{W}$, see also Fig. 2.16 in Sect. 2.4. For a simple identification and online application of (3.57), pyramidal activation functions are used as basis function $\Phi_i(\mathbf{z})w_i$ of the experimental parameter model, according to the neural net models discussed in Sect. 2.2. The identification of the weighting factors of (3.57) is performed using the recursive least squares method described in Sect. 2.3.1. To keep the computational effort low, a local identification approach is applied.

The relevant influence variables that correlate with the variable parameter behavior represent the input vector $\mathbf{z}$. Both measured engine operating states and model states, which as a prerequisite must be constant in steady-state operation are well suited for the identification of $\mathbf{W}$.

The most important input variables for the parameters $\boldsymbol{\theta}_\mathrm{f}$ of the mass flow models are the actuator position $\mathbf{u}_\mathrm{ap}$ and the engine speed n_eng. The compressor pressure ratio Π_c is modeled by a two-dimensional compressor characteristic curve as a function of the estimated compressor mass flow $\dot{m}_\mathrm{c}$ and the turbocharger speed n_tc. For the experimental modeling of the turbocharger parameters k_c, k_t, the estimated mass flows $\dot{m}_\mathrm{c}$, $\dot{m}_\mathrm{t}$ and the estimated turbocharger speed n_tc are particularly suitable as input variables. The parameters k_icl, k_hpcl and k_lpcl of the air cooler elements of the airpath systems can be modeled as functions of the air mass flow $\dot{m}_i$ through the particular air cooler and the engine speed n_eng as a measure for the coolant flow.

All these experimental parameter models are obtained by simulation of the airpath estimators in parallel to the RLS-identification algorithm for the parameter models. Recorded steady-state measurements from the engine test bench are used as reference for the airpath estimator (offline data replay). However, this method can also be applied online during stationary measurements. The start of parameter model identification via RLS is achieved by setting a non-zero initial error covariance matrix $\mathbf{P}_0$, those entries p_i correspond to the weighting factors w_i of the matrix $\mathbf{W}$ and their initial error at a specific location in the input dimension $(z_1, z_2, ...)$; see Sect 2.4 for more details.

In Fig. 3.12, the two-dimensional experimental models for the discharge coefficients of the actuator mass flow models are shown. The engine speed n_eng, which determines the gas velocities through the intake and exhaust system, and the control variables u_i of the actuators represent the main influencing variables and therefore are used consequently as input variables for these parameter models.

Since there is a strong relation between turbocharger speed n_tc and compressor mass flow $\dot{m}_\mathrm{c}$, there is also a strong physical relation to the compression pressure ratio $\Pi_\mathrm{c}(p_{2\mathrm{c}}/p_1)$, which is described by a curve in Fig. 3.13. The identified parameter models of the power variables P_c, P_t and the heat transfers $\dot{Q}_\mathrm{c}$, $\dot{Q}_\mathrm{t}$ on the compressor and turbine side are shown in Fig. 3.14.

The identification results for parameter models of the heat dissipation of the intercooler and HP-EGR cooler are depicted in Fig. 3.15. These parameters are experimentally modeled as functions of the engine speed and the mass flow rate through the cooler element.

Since airpath estimator includes the semi-physical model in the prediction step, after disabling correction step of the Kalman filter algorithm and feeding the parameter from the identified experimental parameter models into the prediction model, the sought semi-physical airpath model results; compare Fig. 3.2 with Fig. 2.14.

3.5 Summary

A semi-physical real-time model of the intake and exhaust system of the internal combustion engine is derived using the well-known filling and emptying method by connecting basic elements of the air system (gas storages, flow resistors and heat exchanger). The unknown parameters,

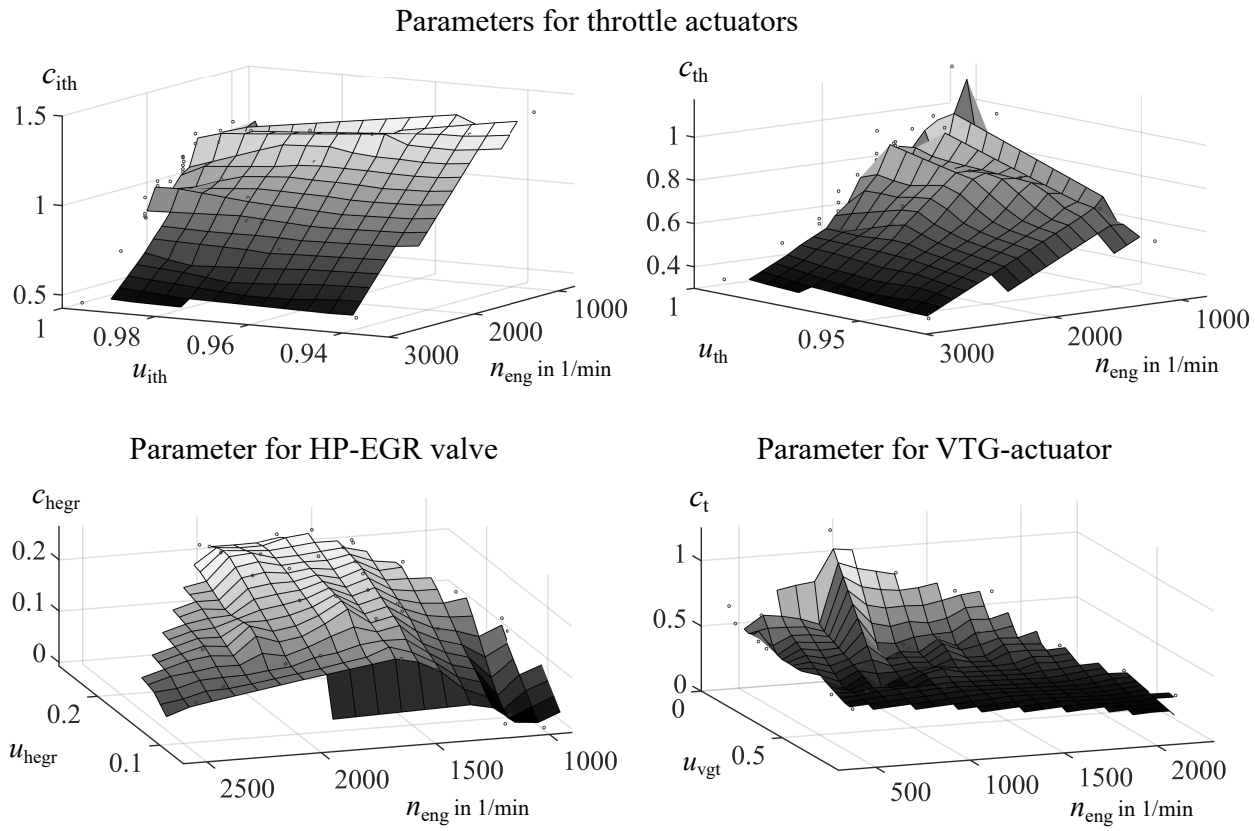

Figure 3.12: Identification results (interpolated) for parameter models of the flow coefficients c_i of the airpath actuators (mass flow models) in dependence of their input variables $u_i \in [0; 1]$ and the engine speed n_{eng} based on measured stationary engine operation points (circles), see Fig. 5.3

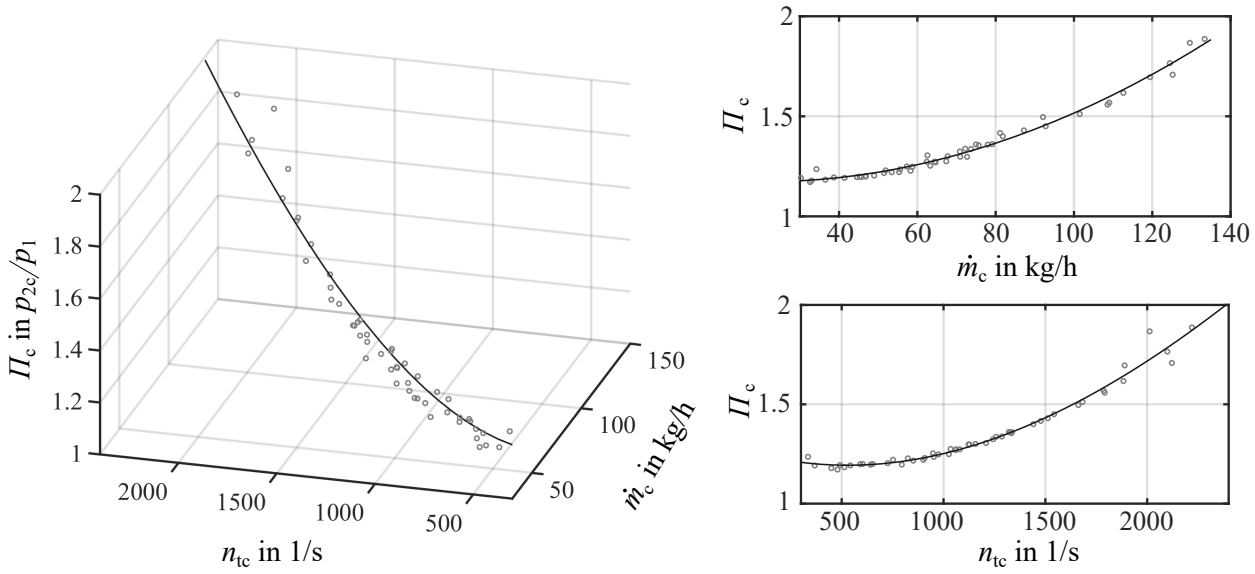

Figure 3.13: Identification results (interpolated) for the compressor parameters based on stationary measurements: pressure ratio curve is approximated by a two-dimensional curve $\Pi_{\mathrm{c}} = f(n_{\mathrm{tc}}, \dot{m}_{\mathrm{c}})$ based on measured stationary engine operation points (circles), see Fig. 5.3)

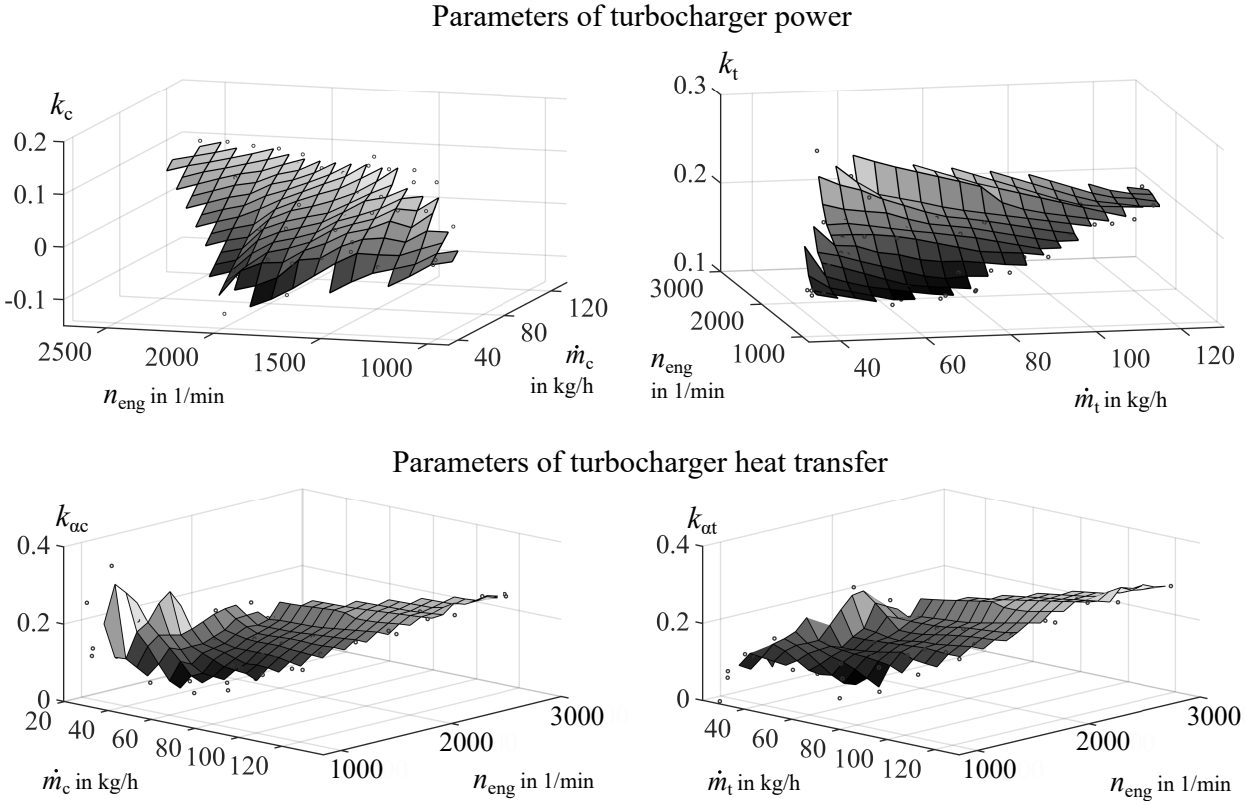

Figure 3.14: Identification results (interpolated) for the turbocharger parameter models $k_{c/t} = f(\dot{m}_{c/t}, n_{eng})$ of the heat transfer coefficients $k_{\alpha c/t} = f(\dot{m}_{c/t}, n_{end})$ as functions of associated mass flow rates and the engine speed based on stationary measurements based on measured stationary engine operation points (circles), see Fig. 5.3)

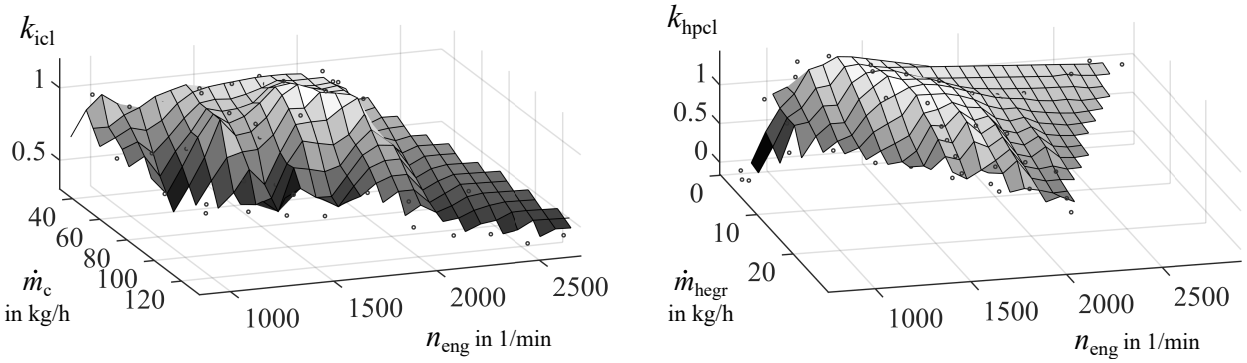

Figure 3.15: Identification results (interpolated) for the heat transfer coefficients $k_{icl/hpcl} = f(\dot{m}_{c/hpegr}, n_{eng})$ of the intercooler and high-pressure EGR-cooler as functions of associated mass flow rate and the engine speed based on measured stationary engine operation points (circles), see Fig. 5.3)

such as actuator discharge coefficients (including actuator characteristics) and heat exchanger heat transfer coefficients, can be modeled as functions of actuator actuation and operating point variables, such as engine speed and actuator position, by mathematical parameter models. However, a basic prerequisite for the identification of the parameter models is the existence of the measured or at least estimated gas states upstream and downstream of the actuators and air coolers.

A more challenging task in airpath modeling is the semi-physical modeling of the turbocharger. Starting from a fluid-dynamic modeling approach, a semi-physical turbocharger model is derived by model simplifications. The complex and geometry-specific behavior of the turbocharger is accounted by variable parameters. The resulting turbocharger equations can then be used in the prediction step of the combined state and parameter estimation. The estimated parameters are then experimentally modeled as functions of operating point variables such as engine speed or mass flow rate.

The semi-physical turbocharger model presented in this work allows a precise modeling of the steady-state turbocharger behavior. In order to be able to model the dynamic turbocharger behavior more accurately, the modeling and estimation approach described here must be extended by the estimation of the parameter of the mechanical friction losses and the parameter for the compressor surge dynamics.

Due to the lower system dynamics and the modularity of the airpath, the modeling methodology presented here is well applicable. A simple separation can be made between the physical model part, which contains the equations for the states, such as pressures, temperatures or turbocharger speed, and the non-physical model part consisting of parameter models, which are modeled experimentally as functions of engine operating point variables. Since the gas dynamics are essentially determined by the engine speed, the engine speed is also the most important input variable of the parameter models.

In general, the semi-physical modeling methodology can be applied to any air system of an internal combustion engine. The overall airpath state and parameter estimation problem can be divided into several joint estimators with lower system orders leading to a reduction of complexity and computation effort.

4 Semi-physical cylinder modeling

This chapter deals with semi-physical modeling of the in-cylinder processes inside an internal combustion engine. The focus lies on modeling the characteristics of diesel combustion that are important in the context of ECU development. This includes the thermodynamic gas state, the air mixture composition of the gas in the combustion chamber, as well as the combustion process including air-fuel-mixture formation, ignition and release of burning energy. First, the processes and states to be modeled, as well as their interdependencies, are analyzed. The available measurement technology is also considered, which limits the possibilities and depth of modeling.

The modeling and calculation of the combustion chamber processes is carried out in the crank angle domain, resulting in crank angle-synchronous models. The resulting semi-physical models are accomplished by online state and parameter estimation algorithms that enable the models to be generated online during the measurement. All applied identification and estimation methods exclusively use the measured in-cylinder gas pressure and the angular position as input variables for the determination of the non-measurable combustion chamber states and all necessary model parameters of the semi-physical models.

Internal combustion engines can be operated with many different combustion processes depending on the fuel type and the design of the internal combustion engine. First of all, a distinction is made between *compression-ignition* (CI) and *spark-ignition* (SI) engines. The SI-engines operate with gasoline as fuel, while CI-engines can run on either diesel or gasoline. However, CI-gasoline engines are rather a subject of research, while series CI-engines are usually diesel engines.

The combustion characteristics and control of SI- and CI-engines differs significantly. Fig: 4.1 shows cylinder pressure curves of CI- and SI-engines for comparison. While in SI-Engines the ignition event can be controlled by activation of the spark plug (ignition angle φ_{ign} in°CS before TDC), the compression-ignition combustion starts inside active areas of the air-fuel mixture (reaction zones) caused by the increase of temperature and pressure during compression. Therefore, the compression-ignition can only be controlled indirectly through the injection timing and rate (start of injection SOI: injection angle φ_{soi} in ° before TDC), and the thermodynamic gas state and composition of the cylinder gas (the temperature and reactivity of the in-cylinder gas).[1] Controlling via injection allows a fast cycle-to-cycle control, while the in-cylinder gas state is controlled via an airpath controller. For a control-oriented combustion modeling, both influences of injection rate and in-cylinder gas state must be taken into account.

[1] combustion engines with variable compression ratio are still subject of research

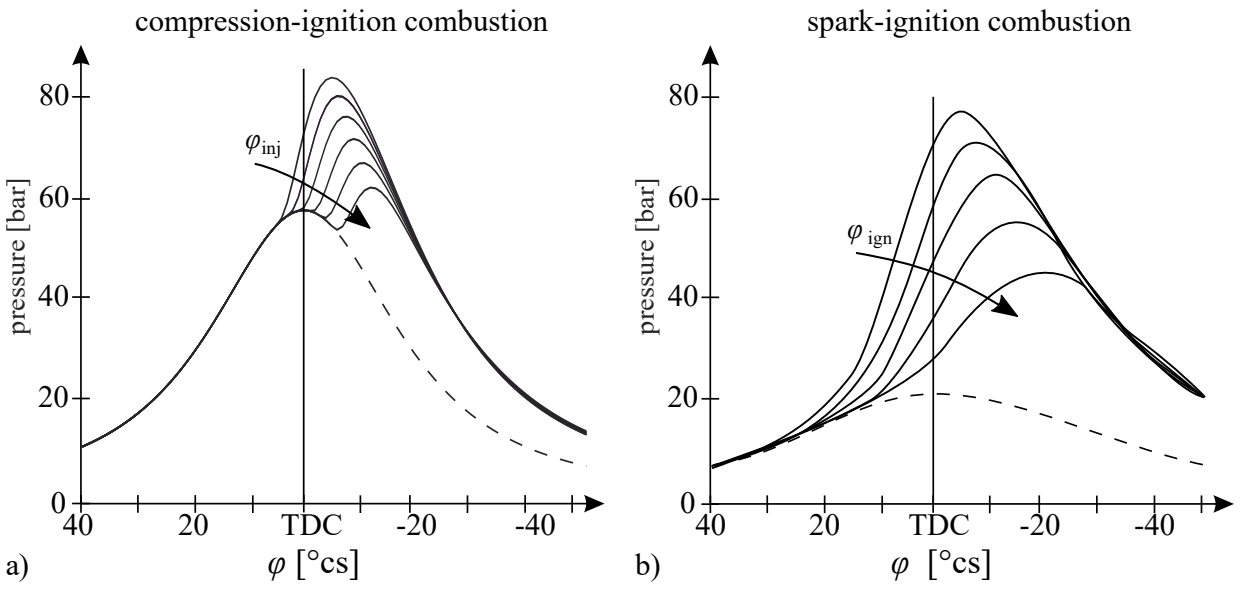

Figure 4.1: Cylinder pressure curve of a) compression-ignition diesel engines with varying start of injection angle φ_{inj} and b) spark-ignition gasoline engine with varying ignition angle φ_{ign} (Merker, Schwarz, et al. 2006). Dashed line indicates drag pressure curve during non-firing operation

Since modeling is generally purpose-oriented and the level of detail depends on the target application, model requirements must be defined accordingly. In this work, modeling is considered from the perspective of a control and application engineer. The beneficial aspect of this view is that the possibilities to influence a system as well as the limitation in terms of the available measurements are taken into account naturally. The consideration of both aspects leads to the modeling of only the essential characteristic system properties. These are properties that can be observed on the basis of existing measurements and manipulated with the help of control variables.

This chapter describes the derivation of a semi-physical real-time model for the relevant cylinder variables, such as the in-cylinder gas states and the rate of combustion. The basic idea of the semi-phyical modeling approach is described in Sect. 2.4. As a prerequisite for this chapter, an overview of the observable physical variables and processes inside the combustion chamber is given in Fig. 4.3 in Sect. 4.1.

In Sect. 4.2, the cylinder gas states and cylinder mass flows are described based on first principle laws from thermodynamics and fluid mechanics. A semi-physical wall heat transfer model is derived in Sect. 4.3 by mathematical simplification of existing wall heat transfer models.

For combustion modeling, a system-theoretical modeling approach is presented in Sect. 4.4, which is derived from the study of existing empirical and phenomenological combustion models. Since this work focuses on modeling of the diesel combustion in CI-engines, this new modeling approach describes the characteristics of inhomogeneous diesel engine combustion. The described approach allows the reproduction of the combustion process of modern diesel engines, which is characterized by the presence of a *premixed, quasi-homogeneous combustion* component and an *inhomogeneous*

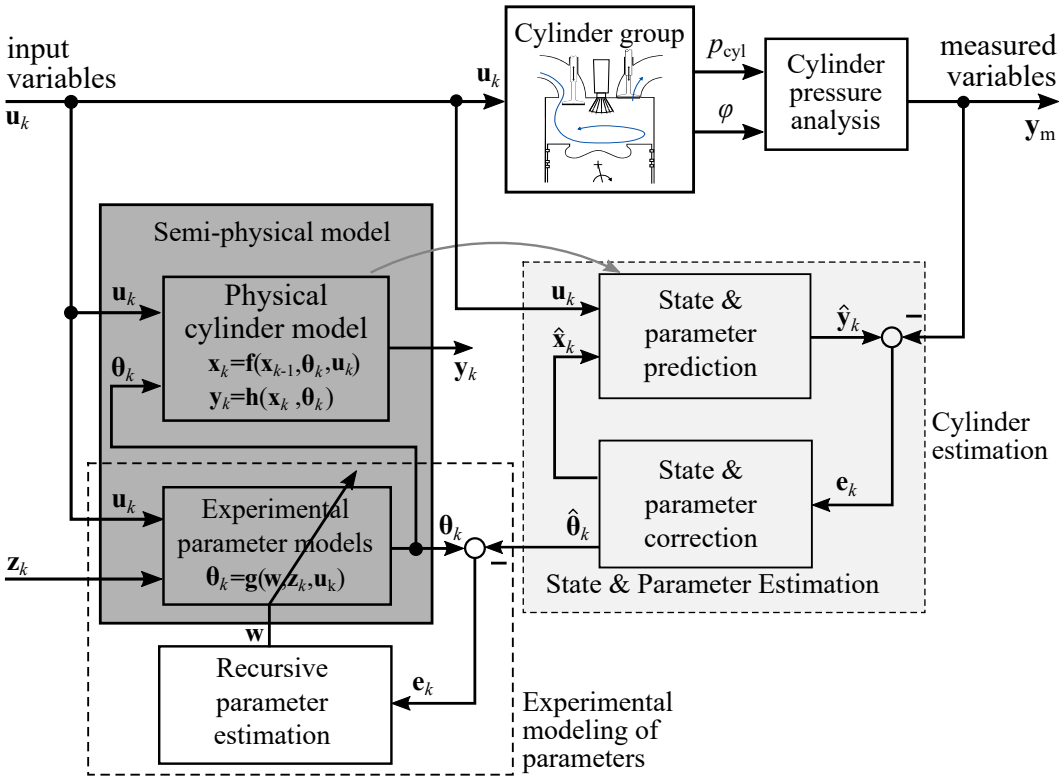

Figure 4.2: Structure and signal flow of semi-physical cylinder modeling with combined state and parameter estimation (cylinder estimation): The semi-physical model consists of a physical cylinder model with the state variables $\mathbf{x}$ and experimental models for the physical parameters $\boldsymbol{\theta}$ (emphasized with grey box), see Sect. 2.4

diffusive combustion in the boundary zones of the injection jet. Thus, this approach can in principle also be used to describe homogeneous combustion in gasoline engines. Moreover, due to its lean mathematical description, it is well suited for real-time application and combination with online parameter estimation methods.

The physical model equations are then used for combined state and parameter estimation (briefly denoted as *cylinder estimation*) to determine both, unknown cylinder state variables $\hat{\mathbf{x}}$ as well as physical model parameters $\hat{\boldsymbol{\theta}}$. Due to the partly non-linear model equations, a sigma-point Kalman filter is used (Sect. 2.3.2). The *cylinder estimation* is mainly based on the measured in-cylinder pressure p_{cyl}, the crankshaft angle φ and the airpath variables as external input variables. Since the quality of the cylinder estimation strongly depends on the quality of the pressure sensor signals and these sensors are typically subject to offset errors and sensor noise, methods for noise reduction and offset correction are taken into account.

The application of the derived semi-physical models for the cylinder estimation is described in Sect. 4.5. The scheme of the cylinder estimation is illustrated in Fig. 4.2. Two possible approaches for deriving a semi-physical cylinder model are treated in Sect. 4.5.1 and Sect. 4.5.2 in more detail.

For the identification of the overall semi-physical cylinder model, the estimated physical parameters $\hat{\boldsymbol{\theta}}$ are mathematically described by experimental models. Sect. 4.6 describes how the physical

parameters $\hat{\boldsymbol{\theta}}$ are modeled by experimental models $\boldsymbol{\theta} = \mathbf{g}(\mathbf{z}, \mathbf{u})$ and identified online using recursive least squares algorithm. This corresponds to the storage of the estimated parameters in an experimental model.

Since most series production engines are not equipped with in-cylinder pressure sensors, the resulting semi-physical cylinder model can also be used without an installed in-cylinder pressure sensor after online identification of the parameter models.[2]

4.1 Fundamentals on cylinder modeling

For the application of real-time models in control functions of the engine control, in real-time simulation or as virtual sensors, as mentioned in Sect. 1.2.2, the main target variables of the engine development process are engine torque M_{eng}, fuel efficiency b_{sfc}, engine pollutant emissions c_{NOx}, c_{pa}, etc. as well as other EGT-related variables such as the engine-out temperature $T_{\text{eng,out}}$, see Fig. 1.10. The investigation and optimization of these target variables requires modeling of the relevant in-cylinder variables such as the in-cylinder pressure, the combustion rate as well as the thermodynamic gas state and gas composition inside the combustion chamber.

With regard to the scope of this work, 0D-modeling approaches with lumped parameters have proven to be suitable for real-time applications, see 2.1. The combustion chamber is then interpreted as *one-zone*, whereby mass flows $\mathrm{d}m_i$, enthalpy flows $\mathrm{d}H_i$ and heat flows $\mathrm{d}Q_i$ can enter and exit across the zone boundaries, see Fig. 4.3 a). The circled variables in Fig. 4.3 a) are the only measured variables. All other variables must be calculated based on these measured variables and/or engine design parameters.

The cylinder gas is assumed to be homogenously distributed inside the zone, so that the same pressure and gas composition prevails in the whole combustion chamber. This allows the *thermodynamic gas state* of the in-cylinder gas to be modeled by means of a lumped parameter approach. In the following, the in-cylinder gas state is defined by following state vector $\mathbf{x}_{\text{cyl}}$

$$\mathbf{x}_{\text{cyl}}(\varphi) = \begin{bmatrix} p_{\text{cyl}}(\varphi) & V_{\text{cyl}}(\varphi) & m_{\text{cyl}}(\varphi) & T_{\text{cyl}}(\varphi) & X_{\text{cyl}}(\varphi) \end{bmatrix}^{\mathrm{T}}, \tag{4.1}$$

The thermodynamic gas state variables are related to each other by the ideal gas law[3], see Appx. A.2.1 for more details. Since pressure, temperature, mass and volume are connected via ideal gas law, three of these four gas state variables are enough to fully describe the thermodynamic gas state. The variable X_{cyl} represents the air mass fraction of in-cylinder gas

$$X_{\text{cyl}}(\varphi) = \frac{m_{\text{cyl,air}}(\varphi)}{m_{\text{cyl}}(\varphi)} = \frac{m_{\text{cyl,air}}(\varphi)}{m_{\text{cyl,air}}(\varphi) + m_{\text{f}} + m_{\text{cyl,egr}}(\varphi) + m_{\text{cyl,rg}}(\varphi)}. \tag{4.2}$$

[2] Exceptions are a few series engines with cylinder pressure-based combustion control, as for example VW 2.0l TDI (Hadler et al. 2008)

[3] Although, ideal gas law holds only for $p < 5$ bar (VDI-Wärmeatlas 2013), real gas behavior is neglected. However, real gas formulations, e.g. Soave-Redlich-Kwong, differ about maximal 2 to 4 % for pressures about 60 to 80 bar (Isermann 2014)

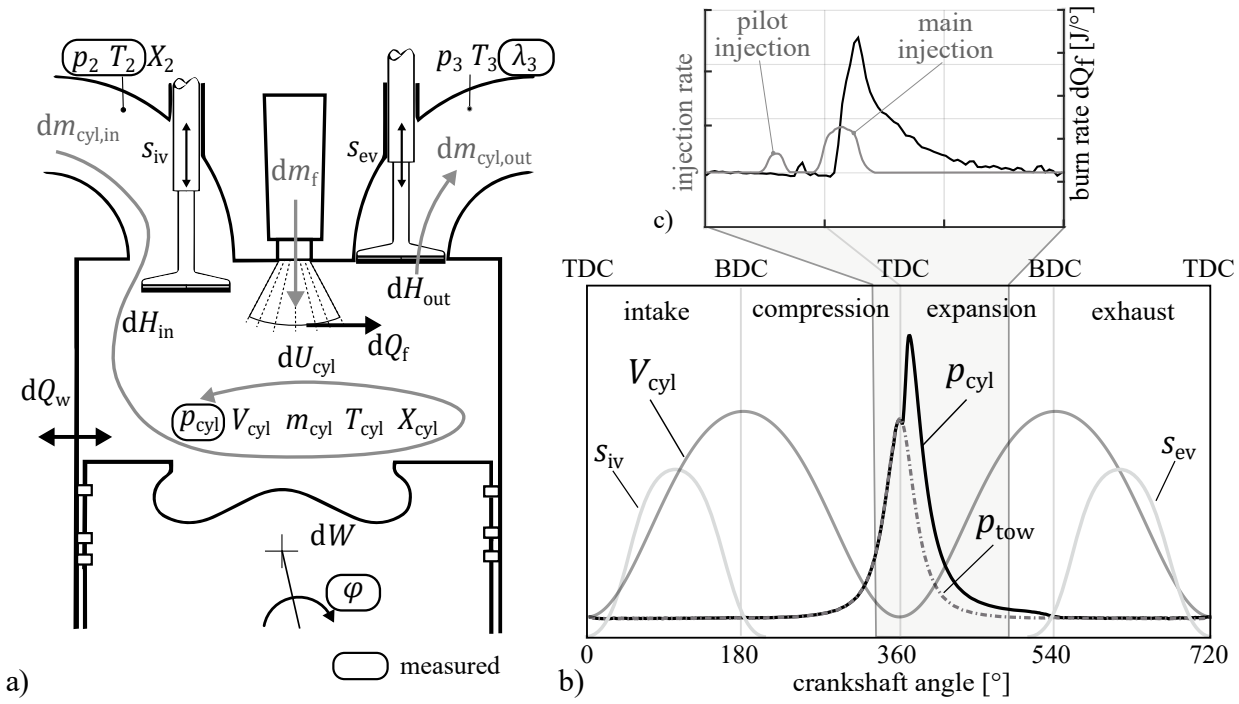

Figure 4.3: a) Schematic illustration of the combustion chamber of a diesel engine and the relevant internal engine states (one zone model); circled variables are measured b) courses of cylinder volume V_{cyl} and cylinder pressure p_{cyl} compared to drag pressure p_{tow} (towed operation); c) courses of injection rate dm_{inj} and burn rate dQ_f

It describes the relation between the mass of fresh air $m_{cyl,air}$ available for combustion and the total gas mass, which includes also the fuel mass m_f, burnt air from external exhaust gas recirculation m_{egr} or residual gas $m_{cyl,rg}$ remaining in the combustion chamber. A more common characteristic value for the combustion is the air-fuel ratio (AFR) λ. The AFR is a combustion parameter measured at the tailpipe that describes whether combustion took place in a lean or fuel-rich air-fuel mixture. However, for modeling the combustion process the air mass fraction X_{cyl} is more suitable, since it describes the actual air masses in the combustion chamber before combustion.

Fig. 4.3 b) depicts the working cycle of a four-stroke diesel engine by means of courses of the in-cylinder gas pressure $p_{cyl}(\varphi)$, the volume $V_{cyl}(\varphi)$ and the valve lifts of intake $s_{iv}(\varphi)$ and exhaust valve $s_{ev}(\varphi)$. Due to the piston movement, the cylinder volume $V(\varphi)$ and its change $dV(\varphi)/d\varphi$ are functions of the crankshaft angle. The equations for determining the crank angle resolved cylinder volume $V(\varphi)$ and the valve strokes $s_{iv}(\varphi)$ and $s_{ev}(\varphi)$ are given in Sect. A.2.5. Even though the valve timing as well as the valve curve are usually engine specific, they can be approximated using the engine design parameters.

The *gas exchange process*, also denoted as *low pressure phase*, where mass and energy flows entering (intake phase) and exiting (exhaust phase) the combustion chamber via intake and exhaust valve can be interpreted as an instationary process with open system boundaries. During the *high-pressure phase* (compression and expansion phase), the one-zone model can be interpreted as a closed thermodynamic system (blow-by neglected). In firing engine operation, the heat release

during combustion $\mathrm{d}Q_\mathrm{f}$ causes a pressure increase around the top dead center (TDC), which builds-up the engine torque, see Fig. 4.3 b); also compare to towed engine operation.

The combustion is characterized by means of a burn rate curve $\mathrm{d}Q_\mathrm{f}(\varphi)$, which is shown exemplarily in Fig. 4.3 c). During the combustion process (*expansion*), injected fuel mass is converted to burning energy Q_f. The release of burning energy is described total burn rate $\mathrm{d}Q_\mathrm{f}/\mathrm{d}\varphi$. Since combustion energy is added, Q_f is accounted with a positive sign. Depending on the current temperature gradient between gas temperature T_cyl and wall temperature T_w, the heat transfer rate $\mathrm{d}Q_\mathrm{w}/\mathrm{d}\varphi$ is either positive or negative. For instance, in a warmed-up internal combustion engine, there is usually a heat transfer from the hot inner cylinder walls to the cooler gas inflowing through the intake valves. Compression and combustion cause the gas temperature to exceed the cylinder wall temperature, so that the heat flow reverses and heat losses occur. Both heat release through combustion and heat transfer between cylinder gas and wall are subject to complex physical processes. Detailed modeling of these processes is not reasonable for real-time applications. Therefore, only zero- or quasi-dimensional modeling approaches are considered. The wall heat transfer model is treated in Sect. 4.3 and combustion modeling in Sect. 4.4.

The combustion process can be understood as a *batch process* where the reaction kinetics are essentially determined by the fuel injection rate $\dot{m}_\mathrm{inj}$ and the in-cylinder gas state $\mathbf{x}_\mathrm{cyl}$ prior to the start of injection φ_soi, which is denoted as *initial in-cylinder gas state* (IGS). As shown in Fig. 4.4 by the course of the in-cylinder pressure p_cyl over two working cycles, the *initial cylinder gas state* $\mathbf{x}_\mathrm{igs} = \mathbf{x}_\mathrm{cyl}(\varphi = \varphi_\mathrm{igs})$ is defined as the in-cylinder gas state after the intake valve closes and during compression prior to the start of injection φ_soi (SOI). [4]

The engine speed n_eng, intake pressure p_2i and temperature T_2i as well as the air mass fraction X_2i, which are either provided by measurements or determined from the air path model, treated in Chap. 3, represent the inputs of the cylinder model. The exhaust gas pressure p_3 and the air-fuel ratio $\lambda_{3/4}$ in the exhaust manifold are only used for model calibration. Engine speed n_eng affects all time-related processes inside the combustion, i.e. chemical reactions. For the crank angle synchronous calculation, time-related processes must be transformed into crank angle domain by using the engine speed in relation in Eq. (2.4).

4.2 Cylinder gas state modeling

Advanced combustion control strategies aim to optimize dynamic engine behavior and emissions. Especially during transient engine operation occur emission peaks, due to incomplete and non-optimal combustion process and contribute significantly to the total engine emissions in test cycles as well as under real driving conditions. Therefore, working cycle resolved information of the in-cylinder gas state are required in order to adopt injection parameters cycle-by-cycle according to the actual gas state and composition inside the combustion chamber. This requires cycle-resolved

[4] Since the SOI depends on engine operation point and the injection strategy, the crank angle of the initial in-cylinder gas state has to be chosen with regard to the earliest SOI, e.g. $\varphi_\mathrm{igs} = 320°\mathrm{cs} < \varphi_\mathrm{soi}$

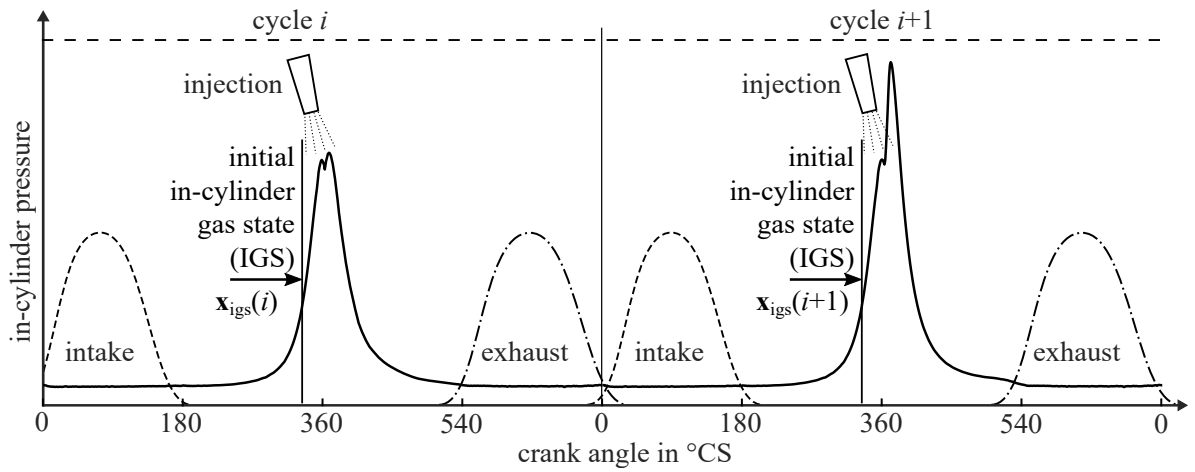

Figure 4.4: Cycle-resolved behavior of the initial cylinder gas state (IGS) $\mathbf{x}_{igs}$ during transient engine operation and optimal adjustment of the injection according to the current IGS

modeling of the processes in the cylinder based on the measurement of the in-cylinder pressure p_{cyl}, which provides insight into the transient intake and exhaust flow processes.

Several approaches exist for determining the cylinder charge and cylinder gas temperature at intake valve close (IVC), based on the measured cylinder gas pressure, see e.g. N. Müller (2003), Klein (2009), and Kocher et al. (2011). Zydek et al. (2016) describes a mean value modeling approach for the initial in-cylinder gas state based on a semi-physical model approach for the intake process. Thereby, the overall intake process is modeled as an polytropic state change from gas state in the intake manifold (p_{2i},T_{2i}) towards the in-cylinder gas state (m_{cyl}, T_{cyl}) prior to combustion (end of compression phase). The calibration of the model parameters is carried out by using the measurements of in-cylinder pressure during the compression stroke. Consequently, this semi-physical model provides the in-cylinder gas mass and temperature cycle-by-cycle. Since the intake mass flow is only modeled based on mean values of the intake gas pressure p_{2i} and temperature T_{2i} and only the cylinder pressure in the region before combustion is used, this model is not able to provide the real, pulsating mass flow through the intake valves.

In Gordon et al. (2018), a crank angle resolved and real-time capable gas exchange model is presented in the context of *Homogeneous Charge Compression Ignition* (HCCI)[5] control. This model is derived from governing physical equations and implemented for the application on a FPGA-based real-time systems allowing a crank angle resolved calculation of in-cylinder pressure and intake and exhaust valve mass flows. Since this model approach is physical based, it requires no parameterization of look-up tables. A more detailed physically based 0D Simulink model and a commercial GT-Power® model are used for offline model validation. However, Gordon et al. (2018) does not describe the procedure for determining the physical parameters.

[5] lean low-temperature combustion method (LTC) for part-load engine operation, in which a homogeneous mixture burns at temperatures below the NOx formation temperature (< 2000 K), achieved by a high EGR rate and earlier injection

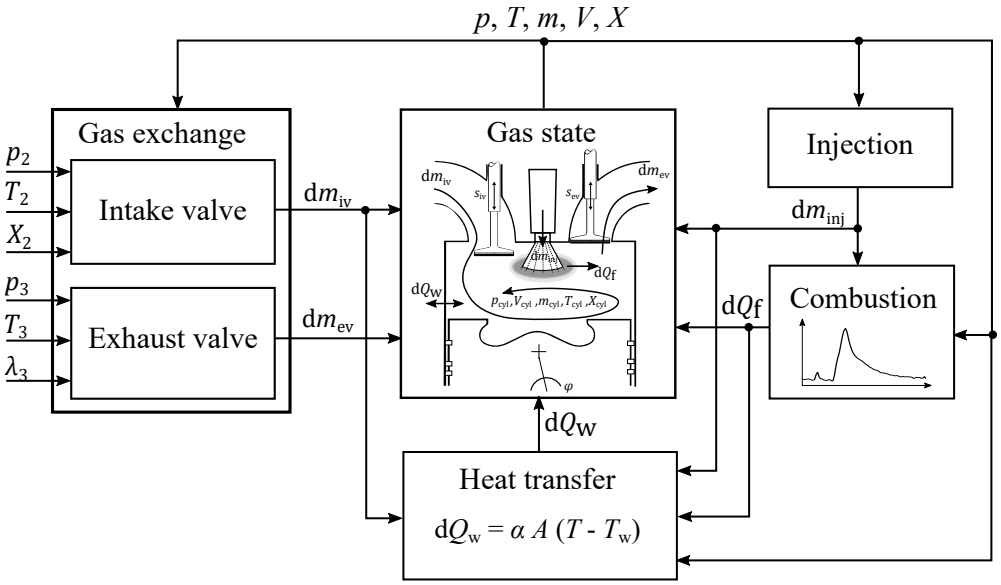

Figure 4.5: Signal flow diagram of semi-physical cylinder gas state model

In the following, a *semi-physical modeling approach* for the gas state in the cylinder is presented. The signal flow diagram and model structure of the cylinder model is shown in Fig. 4.5. The cylinder model consists of the *cylinder gas state model*, the *cylinder mass flow model*, and the *wall heat transfer model*. A *semi-physical fuel injection model* is used to describe the crank angle resolved injection rate during combustion. The derivation of this injection model is given in Appx. A.3. The diesel combustion process is described by a new *semi-physical combustion modeling approach*, which is treated in Sect. 4.4. All semi-physical models are based on basic physical equations for their state variables combined with experimental models for their parameters.

4.2.1 In-cylinder gas state

The in-cylinder gas state $\mathbf{x}_{\text{cyl}}$ given in Eq. (4.1) is fully described by the state variables: cylinder gas pressure p_{cyl}, cylinder gas volume V_{cyl}, cylinder gas mass m_{cyl}, cylinder gas temperature T_{cyl}, and air mass fraction X_{air}. The first four states describe the thermodynamic gas state, while the air mass fraction is additionally introduced to account for EGR and residual gas fraction in the combustion chamber. Since the cylinder volume V_{cyl} is given as a function of crankshaft angle (piston displacement), one of the four thermodynamic states can be calculated by using the ideal gas equation, so that in the following, only governing equations for three gas states need to be derived.

The change of in-cylinder gas temperature $\mathrm{d}T_{\text{cyl}}/\mathrm{d}\varphi$ is determined by using the first law of thermodynamics (A.32) with $R = R_{\text{air}} = 287.4$ J/(kg K)

$$\frac{\mathrm{d}T_{\text{cyl}}}{\mathrm{d}\varphi} = \frac{1}{m_{\text{cyl}} c_{\text{v}}(T_{\text{cyl}})} \left[-p_{\text{cyl}} \frac{\mathrm{d}V_{\text{cyl}}}{\mathrm{d}\varphi} + (h_{\text{in}} - u_{\text{cyl}}) \frac{\mathrm{d}m_{\text{in}}}{\mathrm{d}\varphi} - R T_{\text{cyl}} \frac{\mathrm{d}m_{\text{out}}}{\mathrm{d}\varphi} + \frac{\mathrm{d}Q_{\text{h}}}{\mathrm{d}\varphi} \right] \tag{4.3}$$

The change of cylinder gas mass $\mathrm{d}m_{\mathrm{cyl}}/\mathrm{d}\varphi$ can be determined from mass balance[6]

$$\frac{\mathrm{d}m_{\mathrm{cyl}}}{\mathrm{d}\varphi} = \frac{\mathrm{d}m_{\mathrm{in}}}{\mathrm{d}\varphi} + \frac{\mathrm{d}m_{\mathrm{out}}}{\mathrm{d}\varphi} + \frac{\mathrm{d}m_{\mathrm{f}}}{\mathrm{d}\varphi}. \tag{4.4}$$

The differential form of the ideal gas law (A.18) is formulated with respect to the crankshaft angle φ, using the relation between time and engine speed in Eq. (2.4) (assuming $R \approx$ const. for $\lambda > 1$, which is valid for diesel combustion engines)

$$p(\varphi)\frac{\mathrm{d}V(\varphi)}{\mathrm{d}\varphi} + V(\varphi)\frac{\mathrm{d}p(\varphi)}{\mathrm{d}\varphi} = R\,T(\varphi)\frac{\mathrm{d}m(\varphi)}{\mathrm{d}\varphi} + m(\varphi)\,R\frac{\mathrm{d}T(\varphi)}{\mathrm{d}\varphi}. \tag{4.5}$$

Rewriting (4.5) with regard to $\mathrm{d}p_{\mathrm{cyl}}/\mathrm{d}\varphi$ results the partial differential equation for the change of pressure

$$\frac{\mathrm{d}p_{\mathrm{cyl}}}{\mathrm{d}\varphi} = -\frac{1}{V_{\mathrm{cyl}}}\left[p_{\mathrm{cyl}}\frac{\mathrm{d}V_{\mathrm{cyl}}}{\mathrm{d}\varphi} - m_{\mathrm{cyl}}R\frac{\mathrm{d}T_{\mathrm{cyl}}}{\mathrm{d}\varphi} - RT_{\mathrm{cyl}}\frac{\mathrm{d}m_{\mathrm{cyl}}}{\mathrm{d}\varphi}\right] \tag{4.6}$$

The mass balance equation (4.4) and Eq. (4.3) are used to eliminate mass change $\mathrm{d}m_{\mathrm{cyl}}/\mathrm{d}\varphi$ and temperature change $\mathrm{d}T_{\mathrm{cyl}}/\mathrm{d}\varphi$ in Eq. (4.6).

$$\begin{aligned}\frac{\mathrm{d}p_{\mathrm{cyl}}}{\mathrm{d}\varphi} = &-\frac{1}{V_{\mathrm{cyl}}}\Bigg[p_{\mathrm{cyl}}\frac{\mathrm{d}V_{\mathrm{cyl}}}{\mathrm{d}\varphi} \\ &- \frac{R}{c_{\mathrm{v}}(T_{\mathrm{cyl}})}\left(-p_{\mathrm{cyl}}\frac{\mathrm{d}V_{\mathrm{cyl}}}{\mathrm{d}\varphi} + (h_{\mathrm{in}} - u_{\mathrm{cyl}})\frac{\mathrm{d}m_{\mathrm{in}}}{\mathrm{d}\varphi} - RT_{\mathrm{cyl}}\frac{\mathrm{d}m_{\mathrm{out}}}{\mathrm{d}\varphi} + \frac{\mathrm{d}Q_{\mathrm{h}}}{\mathrm{d}\varphi}\right) \\ &- RT_{\mathrm{cyl}}\left(\frac{\mathrm{d}m_{\mathrm{in}}}{\mathrm{d}\varphi} - \frac{\mathrm{d}m_{\mathrm{out}}}{\mathrm{d}\varphi}\right)\Bigg]\end{aligned} \tag{4.7}$$

With the introduction of the isentropic coefficient $\kappa = c_{\mathrm{p}}/c_{\mathrm{v}}$ and the neglect of temperature dependency of heat capacities c_{v} and c_{p} results after some rearranging following equation for the pressure change

$$\frac{\mathrm{d}p_{\mathrm{cyl}}}{\mathrm{d}\varphi} = -\frac{\kappa p_{\mathrm{cyl}}}{V_{\mathrm{cyl}}}\frac{\mathrm{d}V_{\mathrm{cyl}}}{\mathrm{d}\varphi} + \frac{\kappa R T_{\mathrm{in}}}{V_{\mathrm{cyl}}}\frac{\mathrm{d}m_{\mathrm{in}}}{\mathrm{d}\varphi} - \frac{\kappa R T_{\mathrm{cyl}}}{V_{\mathrm{cyl}}}\frac{\mathrm{d}m_{\mathrm{out}}}{\mathrm{d}\varphi} + \frac{\kappa - 1}{V_{\mathrm{cyl}}}\frac{\mathrm{d}Q_{\mathrm{h}}}{\mathrm{d}\varphi}. \tag{4.8}$$

As it can be seen by means of the four terms in Eq. (4.8), pressure change $\mathrm{d}p$ is influenced by the piston movement,

$$\mathrm{d}p_{\mathrm{cyl}}\Big|_{\mathrm{d}V} = -\kappa p_{\mathrm{cyl}}\frac{\mathrm{d}V_{\mathrm{cyl}}}{V_{\mathrm{cyl}}}, \tag{4.9}$$

the inflowing mass flow

$$\mathrm{d}p_{\mathrm{cyl}}\Big|_{\mathrm{inflow}} = \kappa R T_{\mathrm{in}}\frac{\mathrm{d}m_{\mathrm{in}}}{V_{\mathrm{cyl}}}, \tag{4.10}$$

and outflowing mass flow

$$\mathrm{d}p_{\mathrm{cyl}}\Big|_{\mathrm{outflow}} = \kappa R T_{\mathrm{cyl}}\frac{\mathrm{d}m_{\mathrm{out}}}{V_{\mathrm{cyl}}}. \tag{4.11}$$

and the heat exchange

$$\mathrm{d}p_{\mathrm{cyl}}\Big|_{\mathrm{d}Q} = p_{\mathrm{cyl}}\frac{\mathrm{d}T_{\mathrm{gw}}}{T_{\mathrm{cyl}}} = -p_{\mathrm{cyl}}\frac{\mathrm{d}Q_{\mathrm{h}} + \mathrm{d}Q_{\mathrm{w}}}{m_{\mathrm{cyl}}c_{\mathrm{v}}T_{\mathrm{cyl}}} \tag{4.12}$$

[6] Influence of injected fuel mass on temperature and pressure change can be neglected

between the cylinder gas and the walls of the combustion chamber (Urlaub 1995, p. 178). The first three terms describe an isentropic and adiabatic pressure change without heat exchange across the system boundaries $\mathrm{d}Q$. While the fourth term describes the heat release Q_h by combustion within the system boundaries and heat transfer Q_w across them.

The *thermodynamic in-cylinder gas state* is fully described by Eqs. (4.4) and (4.8). However, the last two equations are coupled with each other and consequently can only be determined iteratively. However, one can also omit the evaluation of the temperature equation (4.3), since a sufficient accuracy for the cylinder pressure curve is already obtained with Eq. (4.8). The temperature for the next computing step can be computed in good approximation with the help of the ideal gas equation based on the propagated in-cylinder mass and the volume (Urlaub 1995, p. 181)

$$T_\mathrm{cyl} = \frac{p_\mathrm{cyl} V_\mathrm{cyl}}{m_\mathrm{cyl} R} = \frac{p_\mathrm{cyl}}{\rho_\mathrm{cyl} R}, \tag{4.13}$$

whereby the influence of the gas composition on the gas constant R is neglected.

Since the availability of oxygen has a significant influence on the reaction kinetics of the combustion and emission formation process, the air mass fraction X_cyl of the cylinder gas represents an important input variable for the combustion and emission models. The air mass fraction X_cyl is determined by the air content of the intake mass flow, whereby the air content of the residual gas remaining inside the cylinders has to be considered. This can be described by following equation

$$\frac{\mathrm{d}X_\mathrm{cyl}}{\mathrm{d}\varphi} = \frac{1}{m_\mathrm{cyl}} \left[(X_\mathrm{2i} - X_\mathrm{cyl}) \frac{\mathrm{d}m_\mathrm{in}}{\mathrm{d}\varphi} - X_\mathrm{cyl} \frac{\mathrm{d}m_\mathrm{f}}{\mathrm{d}\varphi} - X_\mathrm{cyl} \frac{L_\mathrm{st}}{H_\mathrm{l}} \frac{\mathrm{d}Q_\mathrm{f}}{\mathrm{d}\varphi} \right]. \tag{4.14}$$

Assuming a *homogeneous mixture* inside the cylinder at all times (or at least during exhaust phase), outflowing mass flows have no influence on the air mass fraction X_cyl. Both injection and combustion reduce the proportion of air mass in the cylinder. The mass flows of intake and exhaust valves are determined in separate models as well as the wall heat transfer is treated separately in the following sections.

4.2.2 Cylinder mass flow

In general, gaseous mass flows through the cross sectional area of a valve or throttle are modeled by using the flow equation for compressible fluids introduced in Sect. 3.1.2 in the context of airpath modeling. The physical mass flow equations (3.7) to (3.14) are used to model the flow through the air path actuators (intake throttle and EGR valves). Compared to airpath throttles and valves, the cross-sectional area of the intake and exhaust valves is changing highly dynamic and cyclical during engine operation, so that a stationary flow process can no longer be assumed. The cylinder mass flow of intake and exhaust valves is highly instationary, builds up and declines abruptly during valve opening and closing, see Fig. 4.6.

The driving force for the intake valve mass flow is the pressure ratio between intake manifold pressure p_2i and cylinder pressure p_cyl during the intake process, while the pressure ratio between

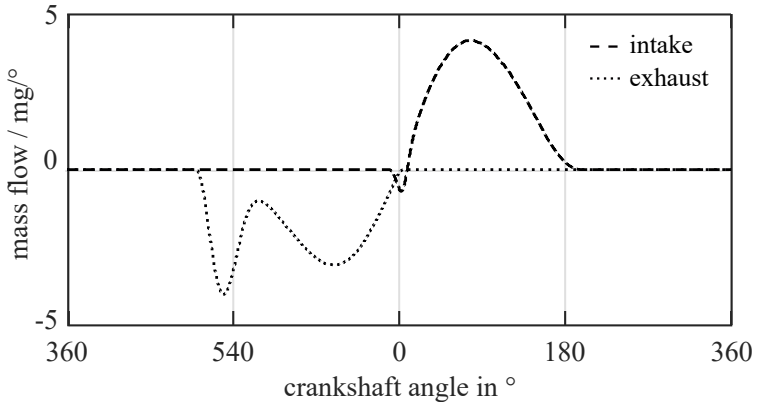

Figure 4.6: Course of cylinder mass flows through intake and exhaust valves during gas exchange phase, calculated with Eqs. (4.15) and (4.16)

p_{cyl} and exhaust manifold pressure p_3 determines the exhaust valve mass flow leaving the cylinder chambers during exhaust phase. Due to the piston movement, as well as in phases of valve overlap, a reversal of the pressure gradient can occur for a short time, so that theoretically a backflow could be observed.[7]

The pressure difference along the valves is however difficult to determine reliably, since both the cylinder pressure sensor as well as the pressure sensors at the intake (if available also at exhaust manifold) are corrupted by offset errors, sensor drift and signal noise. The installation location of the cylinder pressure sensors also plays an important role. Cylinder gas pressure is usually measured near the valve ports, so that the influence of flow during the gas exchange phase leads to an increase in sensor noise, which is clearly visible in the measured cylinder gas pressure, see Fig. 4.7. The pressure differences $\Psi_{\mathrm{in}} = p_{2\mathrm{i}}/p_{\mathrm{cyl}}$ and $\Psi_{\mathrm{out}} = p_{\mathrm{cyl}}/p_3$ lie in the range of the noise amplitude of the pressure sensors (50 to 200 mbar). Especially, the outflow function (3.10) is not suitable for pressure ratios around zero. For this reason, the simpler approach for the outflow function (3.14) is chosen to describe the valve mass flows. The valve mass flows through the intake valve are then given by

$$\begin{aligned}
\frac{\mathrm{d}m_{\mathrm{iv,f}}}{\mathrm{d}\varphi} &= c_{\mathrm{iv}} s_{\mathrm{iv}}(\varphi) A_{\mathrm{iv}} \sqrt{\frac{p_{2\mathrm{i}}\rho_{2\mathrm{i}}}{2}} \left[1 - e^{-10\left(1-\frac{p_{\mathrm{cyl}}}{p_{2\mathrm{i}}}\right)}\right], \text{ for } p_{2\mathrm{i}} \geq p_{\mathrm{cyl}} \\
\frac{\mathrm{d}m_{\mathrm{iv,b}}}{\mathrm{d}\varphi} &= c_{\mathrm{iv}} s_{\mathrm{iv}}(\varphi) A_{\mathrm{iv}} \sqrt{\frac{p_{\mathrm{cyl}}\rho_{\mathrm{cyl}}}{2}} \left[1 - e^{-10\left(1-\frac{p_{2\mathrm{i}}}{p_{\mathrm{cyl}}}\right)}\right], \text{ for } p_{\mathrm{cyl}} < p_{2\mathrm{i}}.
\end{aligned} \tag{4.15}$$

Analogously, the mass flow through the exhaust valve yields to

$$\begin{aligned}
\frac{\mathrm{d}m_{\mathrm{ev,f}}}{\mathrm{d}\varphi} &= c_{\mathrm{ev}} s_{\mathrm{ev}}(\varphi) A_{\mathrm{ev}} \sqrt{\frac{p_{\mathrm{cyl}}\rho_{\mathrm{cyl}}}{2}} \left[1 - e^{-10\left(1-\frac{p_3}{p_{\mathrm{cyl}}}\right)}\right], \text{ for } p_{\mathrm{cyl}} < p_3 \\
\frac{\mathrm{d}m_{\mathrm{ev,b}}}{\mathrm{d}\varphi} &= c_{\mathrm{ev}} s_{\mathrm{ev}}(\varphi) A_{\mathrm{ev}} \sqrt{\frac{p_3\rho_3}{2}} \left[1 - e^{-10\left(1-\frac{p_{\mathrm{cyl}}}{p_3}\right)}\right], \text{ for } p_3 \geq p_{\mathrm{cyl}}.
\end{aligned} \tag{4.16}$$

[7] In practice, however, this is difficult to prove on a series engine. One can probably rather assume that the flow build-up must have a certain low-pass behavior that the flow direction does not change abruptly, resulting in smoother course of mass inflow and outflow

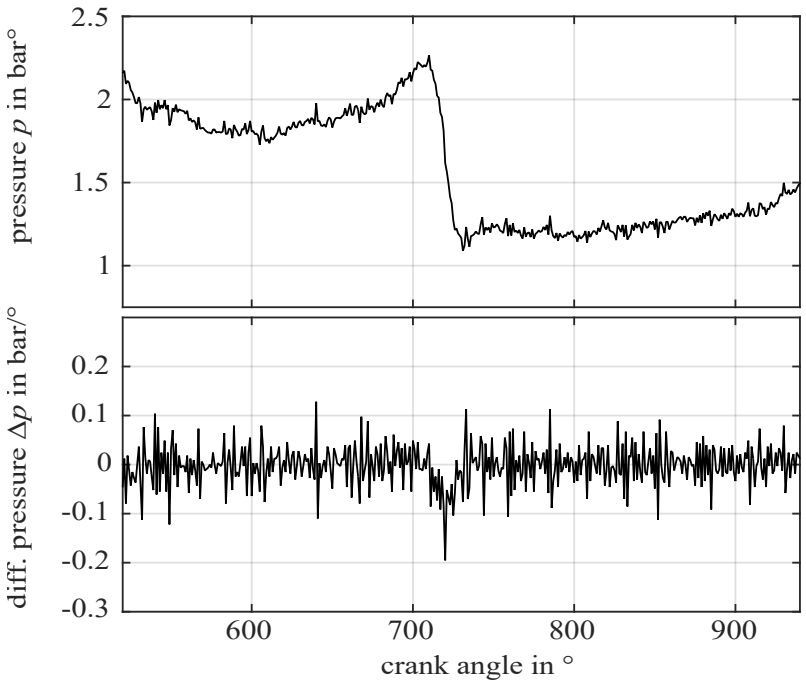

Figure 4.7: Course of measured cylinder pressure p_{cyl} and difference pressure $\Delta p_{\mathrm{cyl}}(k)/\varphi_{\mathrm{s}} = p\mathrm{cyl}(k) - p\mathrm{cyl}(k-1)$ with $\varphi_{\mathrm{s}} = 1°\mathrm{CS}$ during gas exchange phase

Generally, both flow directions (forwards and backwards) must be taken into account. However, comparisons of simulations and measurements on the test engine have shown that the flow direction at the exhaust valve is in outlet direction only.

The curves of the valve strokes $s_{\mathrm{iv}}(\varphi)$ and $s_{\mathrm{ev}}(\varphi)$ are normalized and described with respect to the crankshaft angle. While the parameters A_{iv} and A_{ev} represent the area of the corresponding valve discs and serve for dimensioning the theoretical cross-sectional flow area. Both, valve timing and valve diameter can usually be determined from engine data.

The intake and exhaust valve flow coefficients c_{iv} and c_{ev} are used for model fitting and must be determined experimentally. They also include factors to convert the output value of the mass flow equations to the desired physical unit. If necessary, a conversion factor from time-based representation to angle-based domain can be included additionally. The determination of the flow coefficients is described in Sect. 4.5.

The densities ρ_i in Eqs. (4.15) and (4.16) are determined from the particular upstream pressures and temperatures. For the intake valve equation the gas density in the intake manifold $\rho_{2\mathrm{i}}$ is used, which is determined from the charge pressure $p_{2\mathrm{i}}$ and the temperature $T_{2\mathrm{i}}$

$$\rho_{2\mathrm{i}}(\varphi) = \frac{p_{2\mathrm{i}}(\varphi)}{R_{\mathrm{air}} T_{2\mathrm{i}}(\varphi)}. \tag{4.17}$$

For the exhaust valve equation the current cylinder gas density $\rho_{\mathrm{cyl}}(\varphi)$ is used, which is determined from the estimated cylinder mass $m_{\mathrm{cyl}}(\varphi)$ and the cylinder volume $V_{\mathrm{cyl}}(\varphi)$

$$\rho_{\mathrm{cyl}}(\varphi) = \frac{m_{\mathrm{cyl}}(\varphi)}{V_{\mathrm{cyl}}(\varphi)}. \tag{4.18}$$

By using Eqs. (4.15) and (4.16), the cylinder mass flows during intake and exhaust processes have a characteristic shape, see Fig. 4.6. While the intake mass flow rate is mainly determined by the intake valve stroke, the exhaust mass flow rate is characterized by a superposition of an instantaneous flow rate driven by the pressure ratio between cylinder gas pressure p_{cyl} and the gas pressure at exhaust manifold p_3, see Fig. 4.7. When exhaust valve opens, the exhaust mass flow is dominated by pressure drop; despite the small cross-sectional flow at the beginning. In the further course, when the exhaust valve is fully open, the exhaust flow curve follows the shape of the valve stroke curve (J. B. Heywood 1988, p. 233).

For the calculation of the intake valve mass flow, only the intake pressure $p_{2\mathrm{i}}$ and temperature $T_{2\mathrm{i}}$ are required. Calculation of mass flows through the exhaust valve requires the exhaust gas pressure p_3 and if a backflow from exhaust manifold into the cylinder is taken into account also the exhaust gas temperature T_3. Since the pressure ratio determines the flow rate and direction, model accuracy depends significantly on the accuracy and quality of the pressure signals.

An alternative and simpler approach for modeling the cylinder mass flows is described in Weber (2019a) and Weber (2019b). This approach uses the upstream pressure instead of the pressure ratio, and the piston speed (change of in-cylinder volume displacement). The calculation of the intake valve and exhaust valve mass flow is carried out based on intake gas states ($p_{2\mathrm{i}}$, $T_{2\mathrm{i}}$) and in-cylinder gas states (p_{cyl}, T_{cyl}) only, without the need of pressure and temperature sensors (p_3, T_3) at the exhaust manifold. However, the characteristic shape of the cylinder mass flows, as shown in Fig. 4.6, can not be reproduced.

4.3 Cylinder wall heat transfer

Heat transfer between the cylinder gas and the inner cylinder walls in internal combustion engines occurs primarily by forced convection. The driving force for the heat transfer is thereby the turbulent charge motion inside the cylinder and the heat conductivity in the boundary layer caused by the temperature gradient between the cylinder gas temperature $T_{\mathrm{cyl}}(\varphi)$ and the temperature of cylinder wall surfaces T_{w}. Additionally, heat radiation is emitted by luminous soot particles during combustion. However, compared to the heat transfer from forced, turbulent convection, heat radiation takes only a minor role[8] due to the property of gases to be a selective radiator, which only transfer comparatively small amounts of heat (Pflaum and Mollenhauer 1977). However, the heat radiation component is often included in the coefficient of the heat transfer calculations (Merker, Schwarz, et al. 2006, p. 147).

The boundary layer, where temperature equalization process between the fluid and the wall takes place, is denoted as the temperature boundary layer. In the case of forced convection, there is additionally a flow boundary layer in which the gas velocity decreases up to the wall and disappears towards zero at the wall. The processes in the temperature and flow boundary layer determine the magnitude of heat transfer. In internal combustion engines, the cylinder gas flows are mainly

[8] even less in gasoline engines, since less luminous soot particles occur on a larger scale (Bargende 1991, p. 12 ff.)

turbulent, compressible as well as temporally and spatially nonstationary. Therefore, an analytical description of the boundary layers can not be found that is simple enough to be used for engine work cycle calculation (Bargende 1991, p. 13 ff.).

For online combustion analyses, *empirical calculation approaches* based on Newton's law are used to estimate the total heat transfer over a work cycle. These model approaches correspond to mean model approach with concentrated parameters. Pure-physics models (as an alternative to Newtonian approaches) are based on complex modeling approaches that have found little resonance in engine process computing. In addition, the *zero-/quasi-dimensional* description offers fast results at relatively low modeling and computational costs.

4.3.1 Heat transfer in combustion engines

In modeling cylinder wall heat transfer, the complex heat transfer processes are usually simplified into one overall heat transfer between cylinder gas and cylinder wall, described by using Newton's law. The stationary heat transfer between the in-cylinder gas and the surrounding cylinder surface is given by Newton's law

$$\frac{\mathrm{d}Q_\mathrm{w}}{\mathrm{d}\varphi} = \frac{1}{\omega_\mathrm{eng}} \alpha_\mathrm{w} A_\mathrm{w}(\varphi) \left(T_\mathrm{cyl}(\varphi) - T_\mathrm{w}\right), \tag{4.19}$$

with α_w in J/(m^2 K s) representing the heat transfer coefficient, the effective heat transfer surface $A_\mathrm{w}(\varphi)$ in m^2, and the conversion term $\mathrm{d}t/\mathrm{d}\varphi = 1/\omega_\mathrm{eng}$ in s/°cs. The heat transfer surface $A_\mathrm{w}(\varphi)$ changes during working cycle with respect to crankshaft angle φ. $A_\mathrm{w}(\varphi)$ can be calculated by using geometric relations and engine parameters; see e.g. Zahn (2012).

The temperature difference represents the driving force for the heat transfer. The mean cylinder gas temperature $T_\mathrm{cyl}(\varphi)$ changes during engine duty cycle, while the cyclic change of the mean wall temperature T_w is small compared to the change of gas temperature $T_\mathrm{cyl}(\varphi)$. Thus, T_w can be assumed to be constant during one combustion cycle ($T_\mathrm{w}(\varphi) \approx$ const.). Furthermore, dynamics of the wall temperature is slow due to the heat capacity of the engine bank.

The main challenge in modeling heat transfer is to find an adequate mathematical description for the heat transfer coefficient $\alpha_\mathrm{w}(\varphi)$ over the entire work cycle. Another challenge is to determine the mean wall temperature with regard to engine operation point $T_\mathrm{w} = f(n_\mathrm{eng}, ...)$.

Cylinder wall temperature

In general, the cylinder wall temperature T_w depends on the engine load, the engine speed and the current temperature condition of the engine (warm/cold). Experimental studies in Sargenti (2004) show that the cylinder wall temperature changes proportionally with the engine oil T_oil and coolant temperature T_h2o. The following modification of the Eq. (A.35) in Appx. A.2.3 is proposed, which better accounts for the behavior of modern engines ($\mathrm{C_{wt}}$ in in K/(Pa$\sqrt{\mathrm{m/60s}}$))

$$T_\mathrm{w} = T_\mathrm{h2o} + \frac{\mathrm{C_{wt}}}{10^5} p_\mathrm{2i} \sqrt{d_\mathrm{p} n_\mathrm{eng}}. \tag{4.20}$$

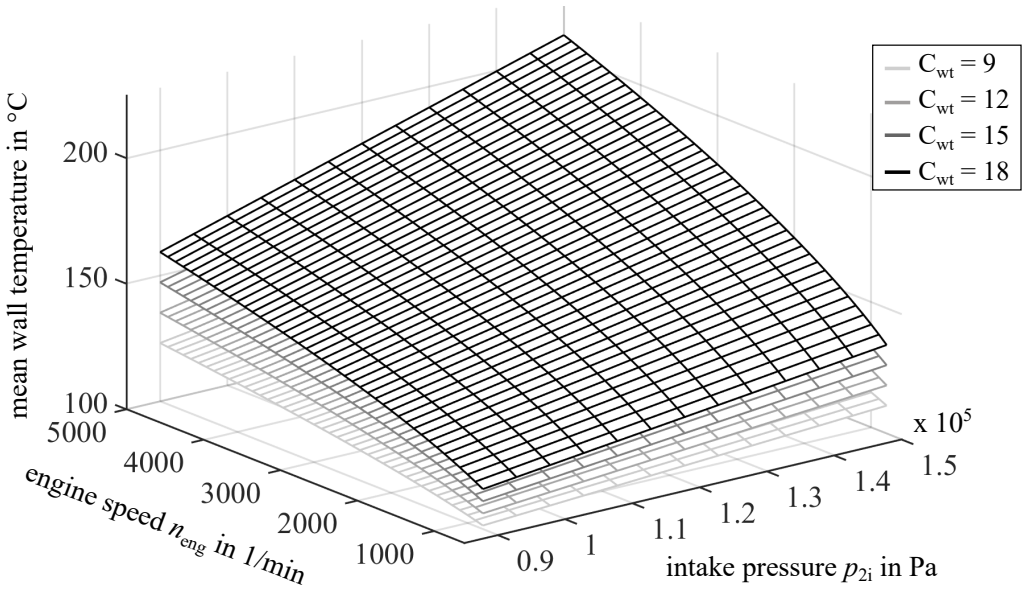

Figure 4.8: Curves of calculated wall temperature model Eq. (4.20) for different parameters C_{wt} in K/(Pa$\sqrt{\text{m/60s}}$)

with p_{2i} in Pa, d_p in m and n_{eng} in 1/min. The air excess factor (λ_{air}) is replaced by intake pressure p_{2i} in order to account engine load, since charging pressure represents a measure for cylinder filling. The engine coolant temperature T_{h2o} is used instead of a constant to address the thermal state of the engine. Model parameter C_{wt} serves for model adjustment, see Fig. 4.8.

Heat transfer coefficient

The developed approaches for the calculation of the heat transfer coefficient α_w can be divided into two categories: *Empirical approaches* such as that developed by Nusselt (1923), where a mathematical formula for the heat transfer coefficient is determined empirically from experiments, and approaches based on the *Similarity theory*, see Pflaum and Mollenhauer (1977, p. 41 ff.) for more details. However, only the latter can be applied to different combustion engines (Bargende 1991). The first and most commonly used approach for the heat transfer coefficient is the equation of Woschni (1970).[9]

Woschni's derivation of the heat transfer coefficient α is based on the similarity theory using the correlation of *dimensionless numbers* to describe the phenomena of the heat transfer. The global wall heat transfer coefficient α_w in J/(s m^{2}K) is given by Woschni (1970) as follows

$$\alpha_w = 130 \cdot d_p^{-0.2} \cdot p^{0.8} \cdot T^{-0.53} \cdot w^{0.8} \quad \text{(in SI units)}, \tag{4.21}$$

with the piston diameter d_p in m, in-cylinder gas pressure p in Pa and gas temperature T in K, and w in m/s. Woschni's approach for the local average velocity in the cylinder w describing the base turbulence level is composed of an engine speed-dependent term represented by the average piston

[9] it is also the first approach applied within a computer-aided calculation of the working cycle

speed $\overline{w}_\mathrm{p}$, see App. A.2.5, and a term considering the influence of the combustion using pressure difference $\Delta p_\mathrm{diff} = p - p_\mathrm{tow}$ during firing engine operation (Woschni 1970)

$$w = C_1 \overline{w}_\mathrm{p} + C_2 V_\mathrm{d} \frac{T_\mathrm{ivc}}{p_\mathrm{ivc} V_\mathrm{ivc}} (p - p_\mathrm{tow}) \quad \text{(in SI units)}. \tag{4.22}$$

Heat radiation and an increase of turbulence occur during combustion. Both are taken into account by the pressure difference p_diff between cylinder gas pressure p in firing operation mode and the gas pressure p_tow during towed engine operation. Material properties of in-cylinder gas are accounted by gas state at intake valve closed (IVC). Woschni proposes different constants C_1, C_2 for the gas exchange phase (low pressure phase) and the compression and expansion (high pressure phase).

Hohenberg (1980) proposed also an equation for the heat transfer coefficient, in which the variable cylinder volume $V(\varphi)$ in m^3 is considered as characteristic length instead of the piston diameter d_p.

$$\alpha_\mathrm{w} = 130 \cdot V^{-0.06} \cdot p^{0.8} \cdot T^{-0.4} \cdot (\overline{w}_\mathrm{p} + 1.4)^{0.8} \quad \text{(in SI units)}, \tag{4.23}$$

with cylinder volume V in m^3, p in Pa, T in K, and average piston speed $\overline{w}_\mathrm{p}$ in m/s. The improved approach of Bargende (1991) is originally developed for gasoline engines.[10] Similar to Hohenberg the variable cylinder volume is used as characteristic length to consider the specific engine geometry and crank angle dependence. Bargende proposed following equation for the heat transfer coefficient

$$\alpha_\mathrm{w} = C \cdot V^{-0.073} \cdot T_\mathrm{m}^{-0.477} \cdot p^{0.78} \cdot w^{0.78} \cdot \Delta \quad \text{(in SI units)}. \tag{4.24}$$

For the calculation of the temperature dependent material constants of the heat transfer coefficient, the mean temperature $T_\mathrm{m} = (T_\mathrm{cyl} + T_\mathrm{w})/2$ is used instead of the gas temperature. Compared to Woschni's approach, another combustion term Δ (dimensionless) is introduced that takes the temperature gradients in the burned and unburned zones into account and allows the consideration of turbulence increase during combustion. A further improvement is that the gas velocity - relevant for the heat transfer - is described by means of a global formulation of the k-ε turbulence model (El Tahry 1982). The calculation of turbulent kinetic energy k considers turbulence generation by the change of density and the squeezing flow through the piston movement. Turbulence generation by direct fuel injection was later considered in Barba (2001). The dissipation of turbulent kinetic energy is described by a dissipation rate ε. Required initial kinetic energy that considers the kinetic energy of intake gas flow, is formulated as function of averaged piston speed $\overline{w}_\mathrm{p}$, air excess ratio λ_air and engine design parameters (Bargende 1991). The *heat transfer relevant velocity* w in Eq. (4.24) is described by means of root mean square of the turbulent kinetic energy k in $\mathrm{m}^2/\mathrm{s}^2$ and the current piston speed $w_\mathrm{p}(\varphi)$ in m/s

$$w = \frac{1}{2} \sqrt{8k + w_\mathrm{p}(\varphi)^2}. \tag{4.25}$$

Further details on the turbulence model and on the determination of the mean gas velocity can be found in Bargende (1991).

Despite the complex processes involved in heat transfer, e.g. different engine types/geometries, locally varying temperature gradients, etc., Woschni's empirical zero-dimensional approach based

[10] Bargende's approach is later also applied to diesel engines in Barba (2001) and Kozuch (2004)

on similarity theory has proven to be successful in many engineering applications. With regard to the model enhancements described, it can be seen in which areas there is potential for improvement in the modeling. Examples for improvements are the consideration of the changing gas properties and more detailed modeling of the flow conditions.

Evaluation of existing model approaches

Although, the empirical formulations of Woschni, Hohenberg and Bargende are widely used for the calculation of heat transfer in combustion analyses, a disadvantage is that the recommended parameterization is no longer valid for modern, turbocharged combustion engines with direct injection and has to be adopted.

Own experimental investigations with the aid of online combustion analysis have shown that constants and parameters of the proposed heat transfer coefficient equations are not constant and must be adjusted for an accurate simulation of the heat transfer behavior over a wide engine operating range. It would be desirable if the parameter adaptation could also be done computer-aided and automatically. However, the mathematical formulation of these equations is not suitable for a combination with online capable parameter estimation techniques. Especially, the estimation of the exponents complicates the use of simple and online capable parameter estimation methods.

4.3.2 Heat transfer coefficient

The objective is to derive a simplified, physically motivated model of the heat transfer coefficient α based on the findings and modifications of previous approaches by Woschni, Hohenberg and Bargende. Instead of a generally valid formulation with constant model parameters, a simpler physically oriented formulation with operating point dependent parameters shall be found, where the parameters can be determined via an online estimation procedure.

An improvement of Woschni's Eq. (4.21) was achieved by Hohenberg (1980), and also later by Bargende (1991), through replacement of the piston diameter d_p by the variable cylinder volume V. However, due to the low exponents -0.06 or -0.073, the volume term has computationally only a marginal impact on the heat transfer coefficient; even for compression ratios of 18:1 like they are common in the diesel engine.

Furthermore, it is interesting to note that the product of the pressure term $p^{0.8}$ and the temperature term $T^{-0.477}$ is mathematically similar to the term $2p/\sqrt{RT}$ in the isenthalpic flow equation (3.10) for compressible fluids, see Sect. 3.1.2. For this simplified approximation of the product term, the physical unit can then be specified more simply as follows

$$p^{0.8}T^{-0.477} \approx \frac{2p}{\sqrt{RT}} \text{ in } \left[\frac{\mathrm{kg}}{\mathrm{m^2 s}}\right] \text{or} \left[\frac{\mathrm{J}}{\mathrm{m^3}} \cdot \frac{\mathrm{s}}{\mathrm{m}}\right]$$

However, the physical unit of the approximation does not correspond to the physical unit of the heat transfer coefficient being sought.

Approach for the heat transfer coefficient

The derivation of a model for the heat transfer coefficient can also be approached from the other side by raising the question, by which physical quantities the coefficient can be described to match its physical unit. In discussed empirical approaches, the mean gas pressure p and the mean gas velocity w are weighted with a relatively high exponent. Thus, both quantities must represent important variables influencing the heat transfer. Since the heat transfer is dominated by forced convection, further important quantity must be a gas velocity w describing the average charge motion inside the combustion chamber. Due to the negative exponent in the temperature term, it can be assumed that the gas temperature T must have an anti-proportional influence on the coefficient α. Both pressure p and gas velocity w, on the other hand, have a reinforcing effect on the heat exchange with the cylinder wall.

Starting from the physical unit of the heat transfer coefficient α in J/(m^{2}K), it can be described simply by the three relevant physical quantities pressure p, temperature T and velocity w as follows

$$\alpha \left[\frac{\mathrm{J}}{\mathrm{m^2 K\ s}}\right] = C \cdot p \left[\frac{\mathrm{N}}{\mathrm{m^2}}\right] \cdot \frac{1}{T[\mathrm{K}]} \cdot w \left[\frac{\mathrm{m}}{\mathrm{s}}\right] \tag{4.26}$$

with C as scaling parameter. Since Eq. (4.26) corresponds to a zero-dimensional modeling approach, the gas pressure homogeneously distributed and the mean gas temperature in the cylinder are used for p and T. These quantities are given either by measurements, as in the case of p, or stand in strong relationship with the other in-cylinder gas state connected via the ideal gas law (A.17). The term $C \cdot p/T$ describes the gas density in the cylinder, which serves to account the influence of material properties such as kinematic viscosity ν and thermal conductivity λ in a simplified way.

A quantitative comparison of discussed empirical approaches (4.21),(4.23), (4.24) and proposed approach (4.26) is depicted in Fig. 4.9. As it can be seen, the proposed approach (4.26) qualitatively maps the p-T dependencies. Quantitatively, the p/T-curve is even closer to the approach of Woschni and Bargende, which are almost coincident, than to the approach of Hohenberg, which outliers slightly due to different exponents.

Since both gas pressure p and gas temperature T are given, the degrees of freedom for model adaptation must be provided by the unknown gas velocity w.

Modeling in-cylinder charge motion

A model formulation is sought which depicts the average global flow conditions based on a zero- or quasi-dimensional representation. The global *k-ε turbulence model* is often used to describe the intensity of charge motion in the combustion chamber. Thereby, an average gas flow is then determined based on the superposition of a base flow due to the piston motion and a turbulent flow describing the fluctuation motion (J. B. Heywood 1988). As a measure for the fluctuation motion serves turbulent kinetic energy density k in m^2/s^2 representing the specific kinetic energy

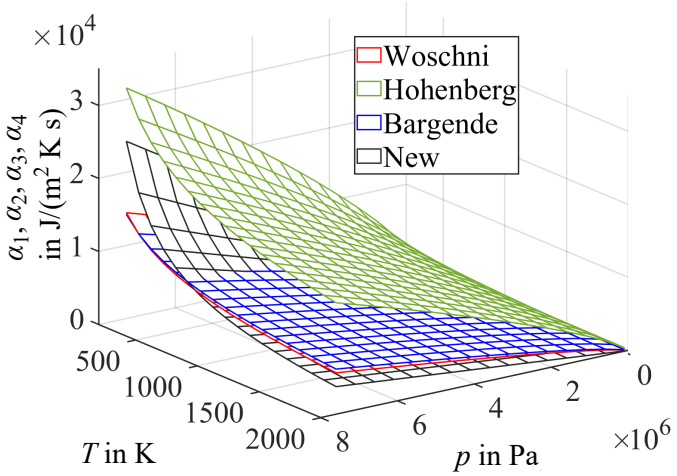

Figure 4.9: Comparison of output values of the terms $\alpha_1 = p^{0.8}T^{-0.53}$(Woschni), $\alpha_2 = p^{0.8}T^{-0.4}$ (Hohenberg), $\alpha_3 = p^{0.78}T^{-0.477}$ (Bargende), and $\alpha_4 = p/T$ with constants $C = 1$ (dimensionless) and velocity $w = 1$ m/s

of averaged turbulent fluctuations with regard to mass (Pischinger et al. 2009)

$$k = \frac{3}{2}w_t^2 \Rightarrow w_t = \sqrt{\frac{2}{3}k} \tag{4.27}$$

Both k and w_t can be used to describe turbulence intensity. However, since a gas velocity is sought for the calculation of the heat transfer coefficient, the idea is to model the turbulence velocity w_t in m/s directly, instead of taking the detour via the modeling of the turbulent kinetic energy density k. This leads to a simplification of both the mathematical description as well as the calculation of the coefficient.

In Bargende (1991), the change of turbulent kinetic energy density during compression and expansion phase is given as follows [11]

$$\frac{\mathrm{d}k}{\mathrm{d}t} = -\frac{2}{3}\frac{k}{V}\frac{\mathrm{d}V}{\mathrm{d}t} - c_{\mathrm{diss}}\frac{k^{3/2}}{l_{\mathrm{char}}} + c_{\mathrm{sq}}\frac{k_{\mathrm{sq}}^{3/2}}{l_{\mathrm{char}}}, \tag{4.28}$$

where the first term on the right-hand side is the change of kinetic energy through piston movement, the second term represents the dissipation rate with the dissipation constant c_{diss} and the characteristic length l_{char}, and the third term describes the generation of kinetic energy through squeeze flow with corresponding constant c_{sq}. The current volume of the combustion chamber is interpreted as a sphere. The characteristic length l_{char} is then given as the diameter of a sphere volume representing the cylinder volume

$$l_{\mathrm{char}} = \sqrt[3]{\frac{6}{\pi}V(\varphi)} \tag{4.29}$$

[11] This equation the for the change of turbulent kinetic energy density $\mathrm{d}k/\mathrm{d}t$ in $\mathrm{m}^2/\mathrm{s}^3$ was also used by many other authors, e.g. Poulos and J. Heywood (1983), J. B. Heywood (1988), Chmela, Orthaber, et al. (1998), and Barba (2001)

Compared to the kinetic energy caused by intake gas flow or fuel injection, the kinetic energy of squeeze flow k_{sq} can be neglected (Chmela, Orthaber, et al. 1998). By inserting the relation (4.27) in k on both sides of Eq. (4.28) and dividing through w_t results a differential equation for the turbulence velocity w_t

$$\frac{dw_t}{dt} = -\frac{w_t}{V}\frac{dV}{dt} - c_{diss}\frac{w_t^2}{l_{char}} \tag{4.30}$$

This equation describes the change of the mean gas velocity in the cylinder without the external influences of kinetic energy of intake gas flow, fuel injection and combustion turbulence. The gas flowing out during the exhaust process does not influence the charge motion and is therefore not considered. However, the pushing out of the gas by the piston in the exhaust phase is already taken into account by the first term in (4.34).

During the intake process, a charge motion is generated by the mass flow entering combustion chamber through the intake valve $dm_{iv,f}/dt$. Assuming quasi-stationary flow $dw_{iv,f}/dt \approx 0$, the charge motion indicated by intake process can be calculated as a function of the intake mass flow

$$\frac{dw_{int}}{dt} = \frac{1}{2}\frac{c_{int}}{l_{char}}w_{iv,f}^2 = \frac{1}{2}\frac{c_{int}}{l_{char}}\left(\frac{dm_{iv,f}/dt}{\rho_{2i}A_{iv,th}}\right)^2 \tag{4.31}$$

where ρ_{2i} is the density of intake gas and $A_{iv,th}$ is the theoretical cross-sectional flow area at fully open intake valve. Parameter c_{int} serves for model adjustment. The relation to the characteristic length l_{char} is intended to take the spatial dimension of current cylinder volume V during the intake process into account . In the compressed state at the beginning of the intake phase, the influence of the intake flow on the velocity of the charge motion is thus greater than at the end of the intake phase, where cylinder volume is at a maximum and the piston is at bottom dead center.

Analogously, an equation for the influence of injection and combustion can be formulated. The increase in charge motion due to injection yields to

$$\frac{dw_{inj}}{dt} = \frac{1}{2}\frac{c_{inj}}{l_{char}}w_{inj}^2 = \frac{1}{2}\frac{c_{inj}}{l_{char}}\left(\frac{dm_{inj}/dt}{\rho_f A_{inj,th}}\right)^2 \tag{4.32}$$

For the determination of injection velocity w_{inj}, a constant fuel density ρ_f and total cross-sectional flow area $A_{inj,th}$ of the injection nozzle is assumed. The increase in turbulence due to combustion can not be described that straightforward, since combustion does not exhibit an unidirectional flow velocity. However, by dividing with the lower heating value, a conversion rate can be determined that can be used in a similar way to describe the charge motion increase due to combustion

$$\frac{dw_{comb}}{dt} = \frac{1}{2}\frac{c_{comb}}{l_{char}}w_{comb}^2 = \frac{1}{2}\frac{c_{comb}}{l_{char}}\left(\frac{dQ_f/dt}{H_l\rho A_p}\right)^2 \tag{4.33}$$

The density of the cylinder gas ρ and the piston area A_p are used as reference quantities for determining the flow velocity.

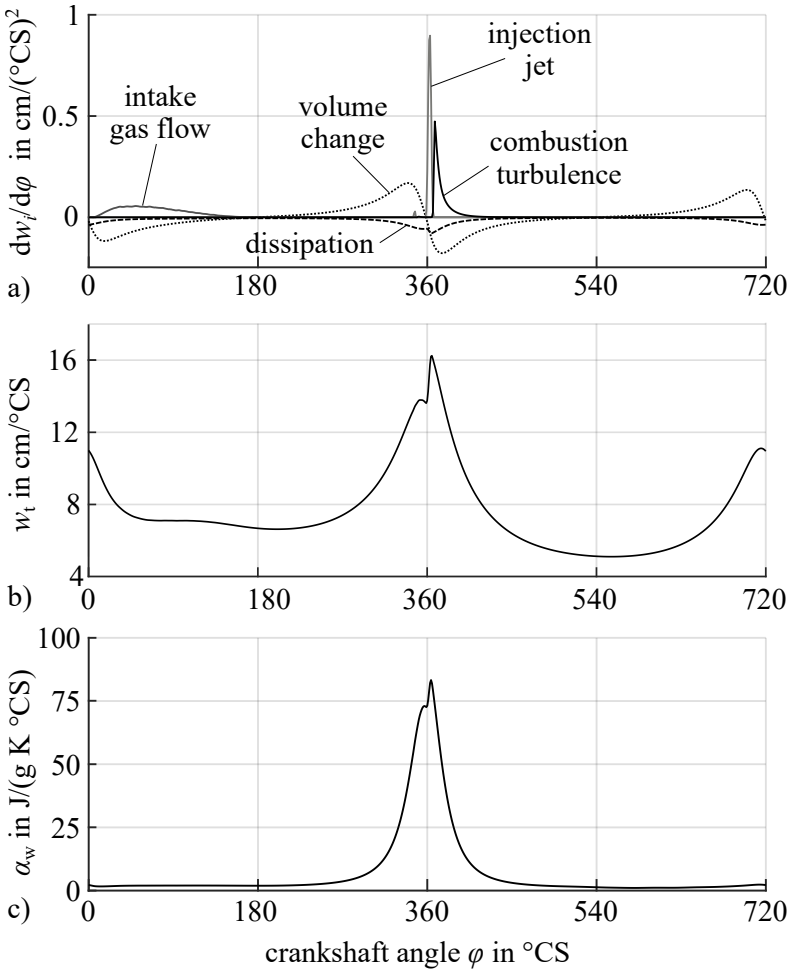

Figure 4.10: Simulation results of heat transfer model with new approach for heat transfer coefficient : Course of a) equation terms $\mathrm{d}w_i/\mathrm{d}\varphi$ of Eq. (4.34), b) average gas velocity w_t and c) heat transfer coefficient α_w Eq. (4.26) (operating point: $n_\mathrm{eng} = 1500$ 1/min, $q_\mathrm{inj} = 15\mathrm{mm}^3$)

The equation for the average gas velocity of the charge movement can be transformed into the crank angle domain with the aid of the rotational speed and the conversion rule (2.4)

$$\begin{aligned}\frac{\mathrm{d}w_\mathrm{t}}{\mathrm{d}\varphi} = &-\frac{1}{3}\frac{w_\mathrm{t}}{V}\frac{\mathrm{d}V}{\mathrm{d}\varphi} - c_\mathrm{diss}\frac{w_\mathrm{t}^2}{l_\mathrm{char}} \\ &+ \frac{1}{2}\frac{c_\mathrm{int}}{l_\mathrm{char}}\left(\frac{\mathrm{d}m_\mathrm{iv,f}/\mathrm{d}\varphi}{\rho_\mathrm{2i}A_\mathrm{iv,th}}\right)^2 + \frac{1}{2}\frac{c_\mathrm{inj}}{l_\mathrm{char}}\left(\frac{\mathrm{d}m_\mathrm{inj}/\mathrm{d}\varphi}{\rho_\mathrm{f}A_\mathrm{inj,th}}\right)^2 + \frac{1}{2}\frac{c_\mathrm{comb}}{l_\mathrm{char}}\left(\frac{\mathrm{d}Q_\mathrm{f}/\mathrm{d}\varphi}{H_\mathrm{l}\rho A_\mathrm{p}}\right)^2\end{aligned} \tag{4.34}$$

The parameters c_diss, c_int, c_inj and c_comb are determined within the cylinder state and parameter estimation based on the pressure. Furthermore, empirical relations between these parameters can also be defined in order to weight the individual influences among each other, which also simplifies the estimation problem. Fig. 4.10 shows simulation results of the Eqs. (4.30) to (4.34) and the resulting course of heat transfer coefficient α_w according to Eq. (4.26).

In Bargende (1991), the heat transfer relevant velocity w is determined from the root mean square of turbulent kinetic energy density k and the piston velocity w_p. However, if the charge motion

is described in the crank angle domain, the influence of the piston speed is eliminated by the conversion factor $\mathrm{d}t/\mathrm{d}\varphi = 1/\omega_{\mathrm{eng}}$ in s/°CS. This can be demonstrated easily by transforming the mean piston speed from time domain in m/s into the crank angle domain in m/°CS.

The wall heat transfer is now determined by Eqs. (4.19), (4.26) and (4.34). As shown in Fig. 4.10, the presented model approach provides the crank angle resolved course for the average gas velocity $w_{\mathrm{t}}(\varphi)$. Although, this quantity can not be verified by measurement, its determination is governed by physical principles, so that it can be used as a measure for the intensity of the charge motion inside the cylinder.

4.4 Combustion modeling

Meeting emission legislation requires modern diesel engines to be equipped with *emission-relevant internal measures* such as variable, high pressure common-rail injection systems allowing various injections patterns with up to eight injections within one working cycle, or dynamically controlled airpath systems supplying the combustion process with a desired in-cylinder gas charge, temperature and air content. *External measures* represent exhaust gas aftertreatment systems (EGT) such as Diesel oxidation catalyst (DOC), Diesel particle filter (DPF), or Selective catalytic reduction systems (SCR), which are applied to further reduce the raw emissions of soot particle, nitrogen oxides ($\mathrm{NO/NO_2}$), unburned hydrocarbons (HC) and carbon monoxides (CO). However, in order to guarantee an optimal operation of EGT systems (conditioning and regeneration), internal measures must be adopted accordingly, e.g. to increase the exhaust gas temperature by post-injection.

In this work, the focus lies on modeling of internal measures enabled by advanced airpath systems with turbocharger and exhaust gas recirculation (Chap. 3) and by the variability of high-pressure injection systems (Appx. A.3). To derive requirements for the combustion modeling, influences of injection and airpath on the combustion characteristics are analyzed in the following.

4.4.1 Analysis of combustion characteristics

The *cylinder pressure analysis* is used for combustion diagnostics to calculate the heat release rate $\mathrm{d}Q_{\mathrm{h}}/\mathrm{d}\varphi$ during combustion and to evaluate the characteristics of combustion based on characteristic values describing the course of in-cylinder pressure and heat release. Thereby, signals of in-cylinder gas pressure sensors, incremental encoder sensor and the phase sensor (for sensing the top dead center (TDC) of each cylinder) are used to depict the cylinder pressure curve with regard to crank angle for crankshaft angle position φ in °CS. By combining information of encoder signal and phase signal with engine design parameters, crank angle dependent curves such as cylinder volume $V(\varphi)$ and volume change $\mathrm{d}V(\varphi)/\mathrm{d}\varphi$ are reconstructed, see Appx. A.2.5. Fig. 4.11 shows the curves of cylinder pressure, heat rate and cumulative heating energy. Furthermore, the corresponding characteristic values are graphically depicted.

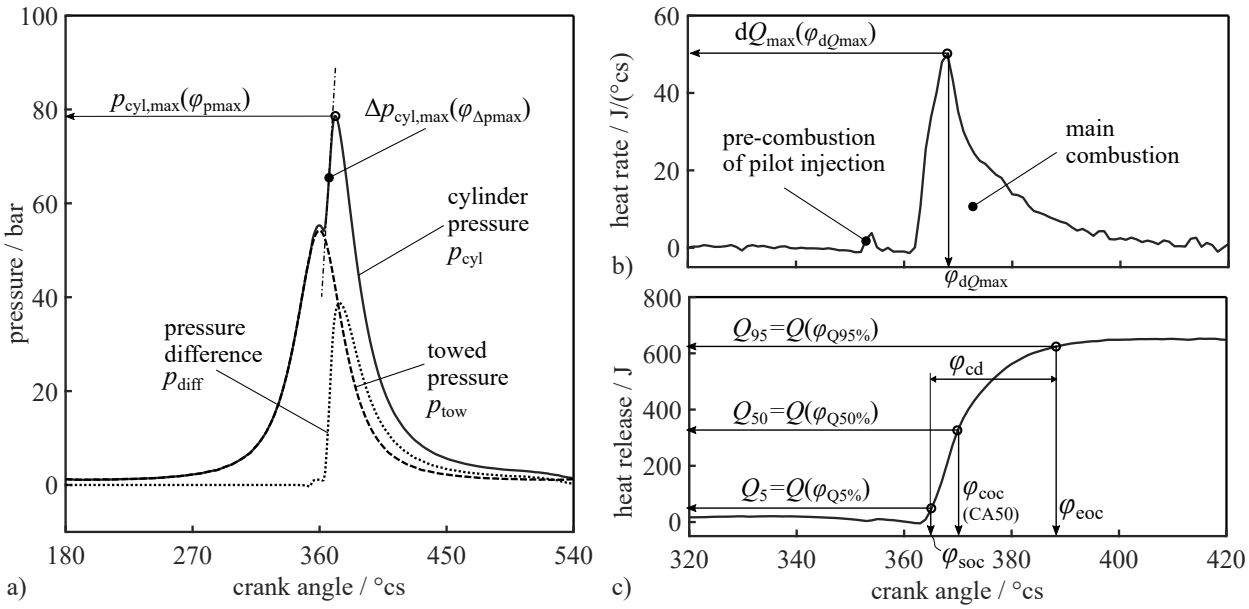

Figure 4.11: a) Cylinder pressure curve $p_{cyl}(\varphi)$ and pressure characteristics, b) heat rate $dQ_h(\varphi)$ and heat release curve $Q_h(\varphi)$ with combustion characteristics

Characteristic values of the pressure curve are the peak pressure p_{max} and corresponding angle at which the peak pressure occurs φ_{pmax}, as well as the peak value of the pressure gradient $dp_{max}/d\varphi$ at crank angle φ_{pmax}, see Fig. 4.11 a). These peak values are used for evaluation of engine noise and durability. In addition, the difference pressure $p_{diff}(\varphi)$ between fired operation and towed operation is often considered. Several methods for the reconstruction of tow pressure $p_{tow}(\varphi)$ can be found in the literature, see i.e. Leonhardt (1996) and N. Müller (2003). Another pressure-based characteristic value is the indicated mean effective pressure (IMEP), which represents a measure for engine load and allows the determination of indicated engine torque M_{ind}. The calculation of pressure and the heat rate characteristics are described in Appx. A.1.2.

The heat rate of combustion $dQ_h/d\varphi$, depicted in Fig. 4.11 b), is calculated from the relation between measured cylinder pressure $p_{cyl}(\varphi)$ and reconstructed cylinder volume $V_{cyl}(\varphi)$. There are basically two methods for calculating the rate of heat release (ROHR). One method is based on energy balance and the other on a comparison with an isotropic state change. Both methods are described in detail in Appx. A.1.2. Direct characteristic features of the combustion rate are the start of combustion φ_{soc} (or ignition angle φ_{ign}), the center of combustion φ_{coc}, and the end of combustion φ_{eoc} with respect to the TDC (at $\varphi_{tdc} = 360°$), shown in Fig. 4.11 c). Duration of combustion $\Delta\varphi_{cd}$ might also be of interest. The start angle of combustion is typically defined at the angle where the total heat release reaches 5% of total released heat ($\varphi_{soc} \approx \varphi_{Q5\%}$), while the end of combustion is defined at 95% of total heat release Q_h. The center of combustion φ_{coc} is often used as control variable in combustion control. It represents the crank angle where 50% of total heat energy is released ($\varphi_{coc} \approx \varphi_{Q50\%}$). In the literature, it is often referred to as CA50. In addition, the peak value of the combustion rate dQ_{max} is also of interest from the perspective of combustion noise and engine durability, see Fig.4.11 b). The total heat release value $Q_{95\%}$ is of interest in terms of fuel

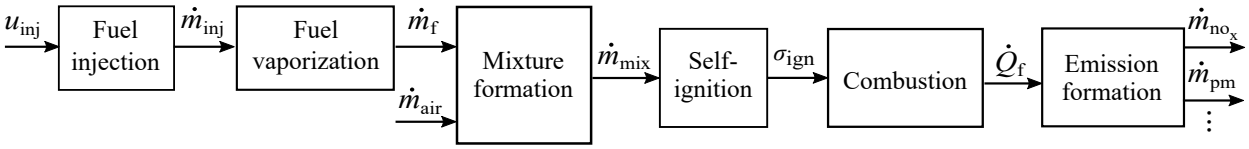

Figure 4.12: Overall diesel combustion process divided into sub-processes

efficiency. It can be set in relation to resulting torque or the fuel consumption of the combustion engine.

Thanks to the computational power of today's real-time processing systems, cylinder pressure analysis can also be performed online at the engine test bench. In this way, it is applied to optimize combustion and raw emissions in the framework of ECU calibration. In this context, cylinder pressure analysis is also referred to as *online combustion analysis*[12].

Characteristics of diesel combustion

Diesel combustion is characterized by a compression-ignition of an inhomogeneous air-fuel mixture inside the combustion. Due to this inhomogeneous and thus incomplete combustion, different pollutant emission such as nitrogen oxides, carbon oxides, soot particles and unburned hydrocarbons occur during combustion process.

The whole diesel combustion process can be divided into a series of sub-processes, see Fig. 4.12. Considering the combustion chamber globally, these sub-processes also run in parallel due to the inhomogeneities in the combustion chamber. Given the high complexity of diesel engine combustion, the complete representation and exact calculation of all processes and phenomena is still the subject of research. Consequently, only the basic aspects are briefly described below. More in-depth representations can be found in Stiesch (1999), Warnatz et al. (2007), Pischinger et al. (2009), Merker (2014), and Tschöke et al. (2018).

During the compression phase, fuel is injected into the hot and already compressed cylinder gas. Due to the high temperatures and high relative injection jet velocity, the liquid fuel breaks down into smaller and smaller droplets. While injection process is still ongoing, mixture zones of fuel droplets and air are forming at the border of the fuel jet by an admixture of surrounding cylinder gas. This process is denoted as *air entrainment*. The kinetic energy caused by injection jet further increases the turbulence inside the combustion chamber and supports the mixture formation. The temperature difference between hot cylinder air and fuel droplets in the mixture zones leads to a convective heat flow that heats up the fuel droplet until they finally evaporate. The mixing of hot air and fuel vapor, accompanied by an increase in heat and air-fuel ratio λ in the mixture zone, creates an ignitable mixture. Generally, the air-fuel mixture can be ignited in the range of $0.5 < \lambda < 1.5$ (Tschöke et al. 2018).

[12] With the term *online combustion analysis*, the focus lies more on the analysis of heat rate curve and the heat rate-based characteristics such as start of combustion, combustion center, etc.

The duration between the start of injection and ignition is referred to as the *ignition delay*. The ignition delay serves as a characteristic value (given in μs or in crank angle °CS) for describing the ignition process. It can be divided into physical and chemical components. The physical component comprises fuel jet propagation, evaporation and the mixture formation. The chemical component includes the chemical pre-reaction in the mixture up to *auto-ignition*.

The characteristic course of diesel combustion can be divided into *three combustion phases* that generally run consecutively, but also temporally overlap, see Fig. 4.13. At the beginning of auto-ignition, a *premixed combustion* begins in the highly reactive mixture zone formed during the ignition delay. *Premixed combustion* is characterized by higher burn rates causing steep pressure gradients at the beginning of combustion. Due to the low temperatures at the beginning of combustion but high turbulence rates, premixed combustion is primary kinetically controlled. The rate of chemical reactions determines the dynamics of premixed combustion and the duration of ignition delay determines the proportion of injected fuel that is chemically processed in the premixed combustion. The longer the ignition delay, the more fuel is premixed before combustion.

However, due to the large excess air that is usually present at the start of diesel combustion[13], high peak temperatures occur locally in the combustion chamber, leading to the formation of nitrogen oxides. This effect can be reduced by internal measures such as increasing the EGR rate (slowing down the reaction kinetics through lower oxygen availability) or by using one or more pilot injections[14] (oxygen reduction through pre-combustion).

After the premixed combustion of premixed fuel is completed and the injection process is still ongoing, follows the non-premixed *diffusive combustion*. Due to the high temperatures caused before by premixed combustion, the rate of the chemical reactions is significantly higher than the rate of the molecular transport processes (diffusion processes). Since the slower rate (dynamics) dominates the overall conversion rate, the rate of diffusive combustion is determined by the mixing rate of fuel and air (air entrainment). The mixing process is controlled by charge motion and turbulence, which is influenced by piston speed, injection pressure and further possible internal measures such as swirl flaps at the intake. Since the time constants of chemical reactions are generally smaller than the time constants of physical transport processes, diffusion combustion is generally slower than premixed combustion. Diffusive combustion takes place in the peripheral area of the injection jet, so in a heterogeneous mixture. The local air-fuel ratio λ there varies theoretically between $0 < \lambda < \infty$. In the fuel-rich mixture zones ($\lambda < 0.6...0.7$), the formation of soot occurs to a greater extent (soot formation).

After the end of injection and the collapse of the injection turbulence, the pressure and temperature at the flame front decreases, so that the chemical reactions rates are becoming slower than the mixing process. Total combustion rate is then again kinetic controlled. This last phase is denoted as *burnout*, in which the previously unburned fuel proportion in the combustion chamber is converted. In this phase, a post-oxidation of intermediate reactants takes place, during which the majority of

[13] Diesel combustion runs generally over-stoichiometric $\lambda >> 1$

[14] Pilot injections and pre-combustions raise cylinder gas temperature prior to main injection. This reduces ignition delay of main combustion and consequently it's premixed proportion

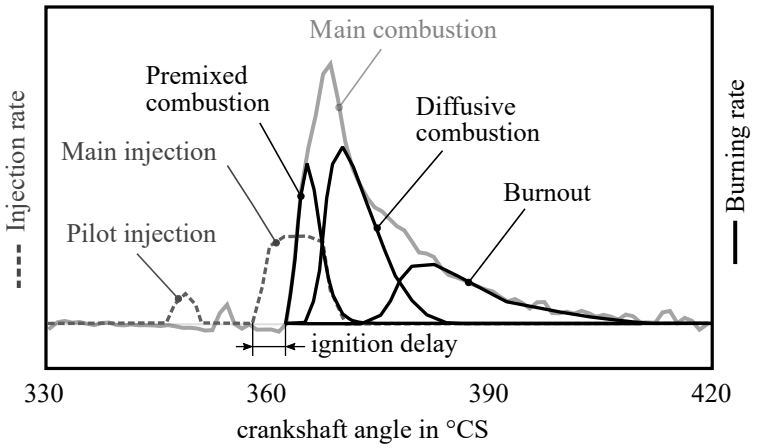

Figure 4.13: Simulation example of partially premixed diesel combustion composed of three individual combustion phase: Premixed combustion, Diffusive combustion and burn-out (compared to overall burn rate determined from in-cylinder pressure signal)

the soot particulate matter is oxidized (soot oxidation) (Hopp and Pfeiffer 1998). However, it is difficult to determine the transition between the decaying diffusive combustion and the kinetically slower burnout on the basis of the heat release curve, see Fig. 4.13. Despite its high significance for raw particulate emissions, modeling of burnout is therefore often neglected. The proportion of burnout is then included within the share of diffusive combustion.

The characteristics of the combustion affect the formation of pollutant emissions as well as the fuel efficiency. In general, a hot and fast combustion which is recognizable by a steep and high peak pressure leads to higher NO formation. A flatter and long combustion indicates a slower and rather mixing-controlled combustion which leads to less NO formation, but to higher soot particle emissions since mixing-controlled combustion takes place in an inhomogeneously mixed reaction zone. Consequently, there is a *trade-off between nitrogen oxide and soot emissions* and the course of the burn rate influences this trade-off. Further combustion processes, such as partially premixed or homogenous charge compression ignition (PCCI/HCCI), aim to find the optimum or overcome this trade-off and reduce the engine-out emissions.

Influences on combustion processes

The shape of combustion rate in Fig. 4.13 depends on engine speed and engine load and is influenced by control variables of the airpath and injection system. From the perspective of engine control, the load request M_{eng} must be fulfilled, while the engine speed n_{eng} is regarded as given. To optimize dynamic engine behavior, airpath and injection control must be optimized in terms of their interaction, see Fig. 1.10.

Engine load control via airpath system is achieved by controlling intake pressure $p_{2\mathrm{i}}$ and temperature $T_{2\mathrm{i}}$ in the intake manifold. Both define the density of intake gas entering the cylinder chambers and therefore relate to the resulting cylinder charge m_{cyl} after intake valve close. Control of the exhaust gas recirculation determines the air mass fraction X_{cyl} in the cylinder that influences the

emission formation during combustion. By controlling the cylinder charge and its air mass fraction, the initial in-cylinder gas state is provided under which combustion takes place. So, the initial in-cylinder gas state is in fact an input variable for the combustion process.

Load control on the part of the injection system is achieved by controlling the injection fuel quantity and the curve of injection rate, resulting from injection pressure (rail pressure) and injection timing. In modern common-rail diesel engines, fuel injection rate $\dot{m}_{\mathrm{inj}}$ can be manipulated almost independently of engine speed n_{eng} by adaptation of rail pressure p_{rail}, see Fig. A.6. Influence of rail pressure change can be seen for example in Fig. 4.15 by comparing a) and c). A rail pressure rise of 50% results in an increase of the injection rate, which in turn leads to an increase of the maximum burn rate. Furthermore, fuel injection quantity is split into multiple injections in order to optimize torque, specific fuel consumption and pollutant emissions. The partitioning of the injection quantity into several pre- and pilot-injections leads to a reduction of air content with every further injection. The pre-combustions have two effects on the main combustion: (1) With each pre-combustion, fresh air is removed from the combustion chamber, which slows down the rate of the main combustion due to lower availability of oxygen. (2) Pre-combustion raises the temperature in the combustion chamber, which increases the chemical reactivity of the combustion chamber gas. Theoretically, the injection angle φ_{inj} in °CS with regard to the top dead center and the injection duration $\Delta\varphi_{\mathrm{inj}}$ in μs or °CS must defined for each injection. But usually, multiple injections are defined relative to the injection angle φ_{mi} of the main injection. Manipulation of φ_{mi} allows shifting the start φ_{soc} or the center of combustion φ_{coc} (CA50) back and forth with respect to TDC. Thus, CA50 is controlled by manipulation of φ_{mi}. An early φ_{soc} before the TDC leads to an steep increase in burn rate due to gas density increase by compression. On contrary, a late φ_{soc} after the TDC tends to an deceleration of combustion rate due to already ongoing expansion phase.

Types of combustion rate curves

An increasing engine speed leads to flatter burn rate curve $\mathrm{d}Q_{\mathrm{f}}/\mathrm{d}\varphi$ with lower peak values with respect to the crank angle. The effect of increasing engine speed on burn rate is shown in Fig. 4.14 a) to c). With increasing engine load, the injection quantity must be increased accordingly, leading to a higher and longer burn rate curve. Fig. 4.15 shows the influence of injection rate variations. With regard to the combustion phases, a rough distinction can be made between three types of combustion processes. The first type, conventional diesel combustion is mainly dominated by diffusive combustion, shown in Fig. 4.14 a). This type of combustion generally occurs in engine operation areas with high loads and low to medium engine speeds. At high load operation, cylinder charge is usually increased due to higher intake pressure which eventually leads to higher in-cylinder gas pressures and temperatures prior to injection. The fuel is then injected into a hot gas mixture leading to fast ignition, so that combustion in mainly mixing-controlled, see Fig. 4.15a) and c). Due to the fact that the compression ignition starts quickly after start of injection, a premixed mixture zone can rarely build up. A pre-combustion can increase cylinder gas temperature in order to further reduce the ignition delay. Conventional diesel combustion offers the advantage of a simple load control, but also produces relatively high soot emissions (Pischinger et al. 2009).

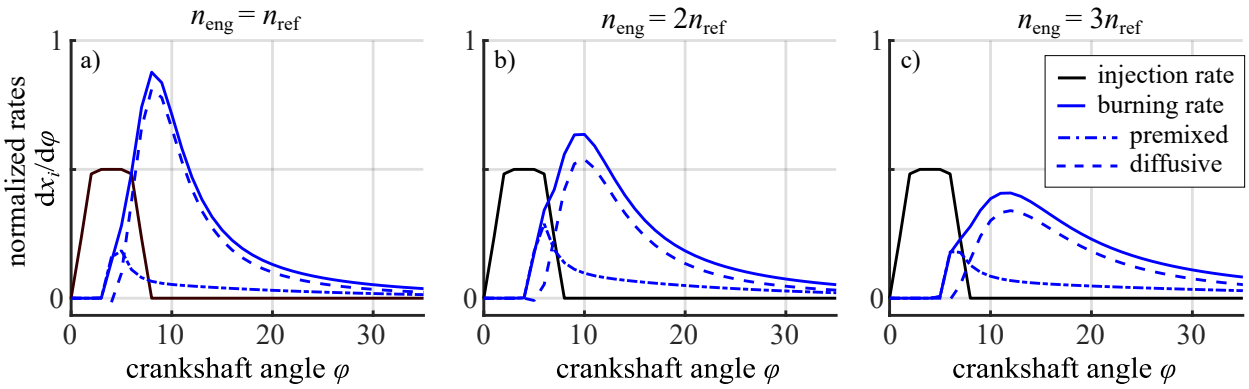

Figure 4.14: Simulation: Influence of increasing engine speed on diesel combustion process (increasing engine speed from left to right)

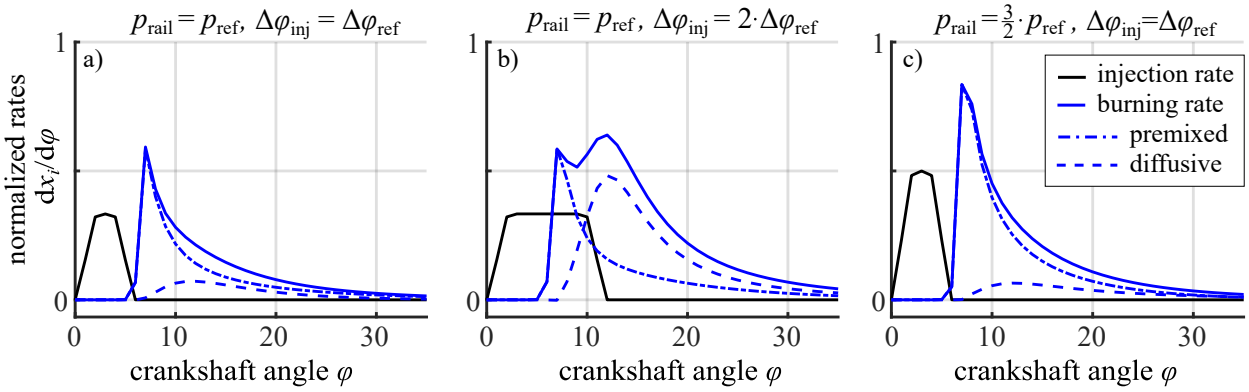

Figure 4.15: Simulations: Influence of injection duration and rate on diesel combustion process for constant engine speed: a) and c) mainly premixed combustion, b) partially premixed combustion

The second type of diesel combustion is a partially premixed combustion Compared to conventional diesel combustion, a partially premixed combustion is characterized by an increased proportion of premixed combustion. Two examples of partially premixed combustion are shown in Fig. 4.15 b) and slightly less prominent in Fig. 4.14 b). A partially premixed combustion occurs when longer ignition delays allow the build-up of a premixed reaction zone. This can be achieved by lowering reactivity or temperature of in-cylinder gas prior to ignition, for instance, by increasing EGR-proportion or smaller pre-combustion. Compared to Fig. 4.14 b), the share of premixed combustion phase in Fig. 4.15 b) is higher due to longer ignition delay. This results from lower engine speed and lower cylinder charge.

The third type represents a mainly premixed combustion with a steep rate increase and decrease as well as high burn rate peak value. This type of combustion occurs in lower engine load and speed where the ignition delay is relatively long, allowing enough time for premixing of the injected fuel. Consequently, the rate of a mainly premixed combustion process is dominated by reaction kinetics. Examples are depicted in Fig. 4.15 a) and more prominent in Fig. 4.15 c).

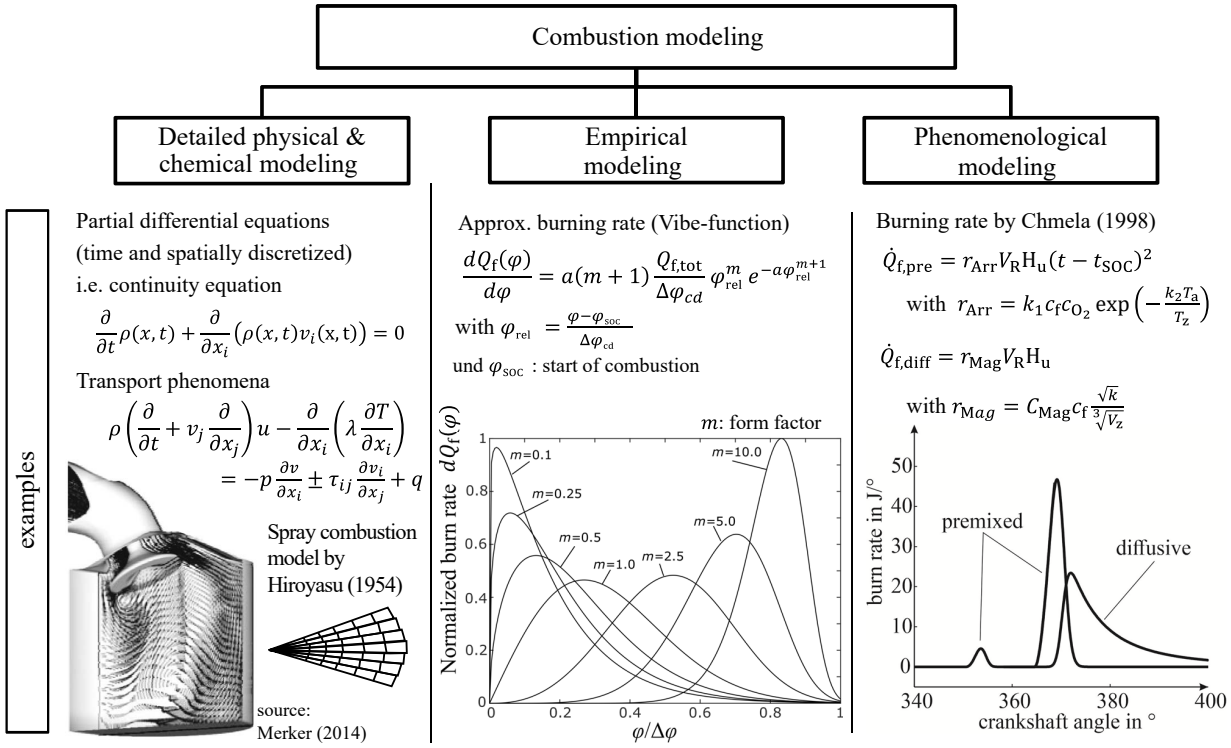

Figure 4.16: Overview: types of modeling the combustion of internal combustion engines

4.4.2 On modeling of combustion processes

The research field of modeling of internal combustion engines is interdisciplinary. It includes the disciplines of physics, chemistry, mathematics, numerics and data processing. Detailed reaction mechanisms include several hundred or even a thousand elementary reactions between more than a hundred different species (Stiesch 2003). Internal engine flows are always non-stationary, compressible, turbulent and reactive (Steiner 2004). Consequently, modeling and simulation of these physico-chemical processes in internal combustion engines is highly complex and therefore not considered with regard to the objective of this work. Fig. 4.16 provides an overview of the types of combustion modeling approaches with some examples. *Detailed physical and chemical modeling* is depicted in Fig. 4.16 for the sake of completeness. More details regarding detailed multidimensional spray and combustion models can be found i.e. in Hiroyasu, Kadota, et al. (1983), Stiesch (2003), Warnatz et al. (2007), and Merker (2014).

Empirical model and *phenomenological models* have already found application in the model-based development of ECU functions, e.g. Zahn (2012), Tschanz et al. (2012), and Elbert et al. (2016). In the following, these two combustion modeling approaches are explained using prominent examples. Based on their underlying properties, a *new semi-physical modeling approach* for the *partially premixed combustion* in diesel engines is derived that is suitable for use in real-time applications such as HIL and EIL, as well as for combination with online parameter and state estimation methods to enable effective model generation.

Empirical Modeling

It was the advent of the chain reaction theory that gave the impetus to the generation of mathematical expressions to describe the evolution of physico-chemical processes. The founder of this theory, Nikolai Nikolaevich Semenoff (or Semenov), who received a Noble Prize (1956) for its development. His monograph on chemical kinetics and reactivity of chain reactions became a standard book in kinetic chemistry (1934). In the simplest case of a gaseous substance undergoes an exothermic process in a space with a fixed volume. As a consequence of chain branching, the rate at which a quantity x of the substance reacts in time t can be expressed in terms of

$$\frac{\mathrm{d}x}{\mathrm{d}t} = Bx(P - x)$$

whereas B is a measure of the number of chain branching steps per active center, while P is the normalized pressure change associated with this event under the assumption that the reaction takes place in an enclosure of fixed volume. The solution results in a S-shaped curve.

$$x = \frac{P}{1 + e^{-BPt}}$$

Over the years, a number of functional relationships have been described in the combustion literature based on Semenov's findings. First study of the influence of combustion velocity on the work cycle of a diesel engines was done by Neumann (1934). In the following decades, empirical functions for the heat release in combustion engines with regard to time were introduced by Neumann (1936), Goncar (1954) and Vibe (1970).

$$x(t) = \left(3 - 2\frac{t}{t_\mathrm{d}}\right)\left(\frac{t}{t_\mathrm{d}}\right)^2 \qquad \text{(by Neumann)}$$

$$x(t) = 1 - \left(1 - \frac{t}{t_\mathrm{max}}\right)e^{-t/t_\mathrm{max}} \qquad \text{(by Goncar)}$$

$$x(t) = 1 - e^{-\int_0^t n\varsigma\,\mathrm{d}t} = 1 - e^{-f(t)} \qquad \text{(by Vibe)}$$

whereas $x(t) \in [0; 1]$ describes the progress of combustion. All these functions describe progress of combustion by an S-shaped curve. Considering only the fraction x of the initial substance ($1 - x = N/N_0$) that is involved in the reaction up to the time, following expression is obtained

$$x = 1 - e^{-\int_0^t n\varsigma\,\mathrm{d}t} = 1 - e^{-f(t)} \quad \text{with } f(t) = n\int_0^t \varsigma\,\mathrm{d}t$$

The proportionality factor n is a constant quantity with reasonable accuracy, since Vibe assumes that the effective acts of a chemical reaction mechanism are of one type and that these are also constant during the reaction. Because of the generality of this equation, it can also be applied to the combustion process in internal combustion engines. To solve it, one must additionally determine the integral that reflects the specific properties of the system. Vibe assumes a power function $\varsigma = at^m$ on the basis of the assumptions made concerning the course of the function and its properties. Inserting ς and integrating the equation yields the well-known expression for the combustion process

$$x = 1 - e^{-at^{m+1}} \quad \text{with } m > -1$$

where $x(t) = Q_{\mathrm{f}}(t)/Q_{\mathrm{f,max}}$ describes the fraction of the already converted fuel energy $Q_{\mathrm{f}}(t)$ with regard to the total burning energy release $Q_{\mathrm{f,tot}}$ bound chemically in the fuel

$$Q_{\mathrm{f}}(t) = Q_{\mathrm{f,tot}} \left(1 - e^{-at^{m+1}}\right) \tag{4.35}$$

This curve can also be formulated via the rotational speed as a function of the crank angle φ. For this purpose, the combustion duration $\Delta\varphi_{\mathrm{cd}}$ relative to start of combustion φ_{soc} must also be taken into account. For the proportionality factor one obtains $a = -6.908$

$$Q_{\mathrm{f}}(\varphi) = Q_{\mathrm{f,tot}} \left(1 - e^{-a\left(\frac{\varphi-\varphi_{\mathrm{soc}}}{\Delta\varphi_{\mathrm{cd}}}\right)^{m+1}}\right) \tag{4.36}$$

Derivative of (4.36) describes the burn rate with respect to crank angle φ

$$\frac{\mathrm{d}Q_{\mathrm{f}}(\varphi)}{\mathrm{d}\varphi} = \frac{Q_{\mathrm{f,tot}}}{\varphi_{\mathrm{cd}}} a(m+1) \left(\frac{\varphi - \varphi_{\mathrm{soc}}}{\Delta\varphi_{\mathrm{cd}}}\right)^{m} e^{-a\left(\frac{\varphi-\varphi_{\mathrm{soc}}}{\Delta\varphi_{\mathrm{cd}}}\right)^{m+1}} \tag{4.37}$$

In Vibe (1970), different measurement results of diesel engines running on gas oil are shown with form factor $-0.16 < m < 0.75$. For a diesel engine with compressor, form factor was varied around $m = 1.2$. Higher values for m are necessary if the maximum increase of burning rate is not at the start of combustion. On the contrary, for $m = 0$ results for Eq. (4.36) a first order lag element, which has the largest derivative at the beginning. This would correspond to Neumann's approach, where the combustion process is assumed to be a bimolecular reaction (Neumann 1936).

However, supercharged engines are the current standard technology in the passenger car sector. Vibe shows, however, that in addition to the fuel type, both the gas condition (in the form of the boost pressure) and the injection angle lead to different characteristic numbers. Although Vibe refers to the function ς as the density of active centers, it relates the combustion rate only to the combustion duration and not to the gas condition or the position of the combustion relative to top dead center.

For gasoline engines, the burn rate curve has a much stronger resemblance to an S-curve due to the flat increase of the start of combustion. To fit the Vibe function to gasoline engines, values $m > 2$ are used for the form factor in Vibe 1970. Vibe investigates the influence of different air fuel ratios λ. For $\lambda < 0.9$, combustion efficiency decreases, while the efficiency remains constant and the slope of the combustion function increases for $0.9 < \lambda < 1$. For $\lambda > 1$, however, the combustion duration then increases again with decreasing slope of the combustion function.

The Vibe function is more an empirical than a physically based model. It was designed for gasoline engines with external mixture formation and is not suitable for modeling the characteristic burn rate curve of partially premixed diesel combustion (Chmela, Orthaber, et al. 1998). For high m values, the decay of burn rate is too strong, which requires additional superimposed Vibe functions to describe several combustion phases, such as premixed combustion, diffusive combustion or burnout curve. Although, the concept of Double-Vibe function overcomes these limitations and it is not able to predict accurately the combustion phases of a diesel engine (Barba 2001). However, because of its simplicity, the Vibe function is often used in online applications for determining the rate of heat release, especially of gasoline engines.

Phenomenological combustion models

More promising and a compromise between simple empirical models and highly complex multi-dimensional models are phenomenological models. Some technical components such as converters or coolers, have the characteristics of sinks and losses where the internal processes run only in one direction and are not reversible without additional energy supply. These processes are characterized by irreversible equalization processes with increasing entropy caused by dissipation of mechanical or electrical energy, exchange of mass and heat or chemical reactions (Isermann 2014). They are described mathematically by *phenomenological equations*. Phenomenological models differ widely in their level of detail and the resulting computational effort (Merker 2014). Some examples of phenomenological equations that are also used in this work are flow resistances, heat transfer and chemical reactions.

A commonly used approach for modeling the burn rate is proposed in Chmela, Orthaber, et al. (1998), Chmela, Pirker, et al. (2007) and modified in Barba (2001). Zahn (2012) proved real-time capability of Chmela's combustion model as part of an engine simulation on a Hardware-in-the-Loop test bench. The technological merit of Chmela's approach is the fact, that the burn rate in diesel combustion engines is consisting of a chemically and a mixing controlled processes, which are described by two rate variables: turbulence controlled rate r_{Mag} and the kinetically controlled rate r_{Arr} based on *Arrhenius law*. These rates for modeling turbulent combustion were first introduced by Magnussen and Hjertager (1977).

In Chmela, Pirker, et al. (2007) and Barba (2001), the *Arrhenius law* is used for modeling the chemically controlled reaction rate of the premixed combustion. Arrhenius law describes the chemical reaction rate as a function of the reaction pressure p temperature T

$$r_{\mathrm{Arr}} = A p^n e^{-\frac{c_1 T_{\mathrm{a}}}{T}} = C_{\mathrm{Arr}} c_{\mathrm{F}} c_{\mathrm{O}} p^n e^{-\frac{c_1 T_{\mathrm{a}}}{T}}, \tag{4.38}$$

with mass concentration of fuel c_{F} and oxygen c_{O} and T_{a} representing the activation temperature. The burn rate of premixed combustion results from the product of reaction rate r_{Arr}, reaction volume V_{mix} and lower fuel heating value H_{l} (Chmela, Pirker, et al. 2007)

$$\dot{Q}_{\mathrm{f,pre}}(t) = C_{\mathrm{Arr}} m_{\mathrm{f,diff}} H_{\mathrm{l}} c_{\mathrm{F}} c_{\mathrm{O}} p^n e^{-\frac{c_1 T_{\mathrm{a}}}{T}} \tag{4.39}$$

The diffusive combustion is described by a mixing controlled reaction rate is given by Magnussen as follows

$$r_{\mathrm{Mag}} = C_{\mathrm{Mag}} c_{\mathrm{f}} \frac{\sqrt{k}}{l_{\mathrm{char}}}, \tag{4.40}$$

where k is the turbulent kinetic energy density and l_{char} the characteristic length, which is assumed to be the cubic root of the cylinder volume $l_{\mathrm{char}} = \sqrt[3]{V_{\mathrm{cyl}}}$. The local turbulence density is the driver for the mixing speed of the reactants. Turbulent kinetic energy density k is determined by a k-ε-turbulence model, which considers the turbulence generation and dissipation, see Sect. 4.3.2. The fuel concentration c_{f} represents the limiting concentration, controlling the rate diffusive combustion (Merker 2014). Burn rate of diffusive combustion is then given as

$$\dot{Q}_{\mathrm{f,diff}}(t) = C_{\mathrm{Mag}} m_{\mathrm{f,diff}} H_{\mathrm{l}} \frac{\sqrt{k}}{l_{\mathrm{char}}}. \tag{4.41}$$

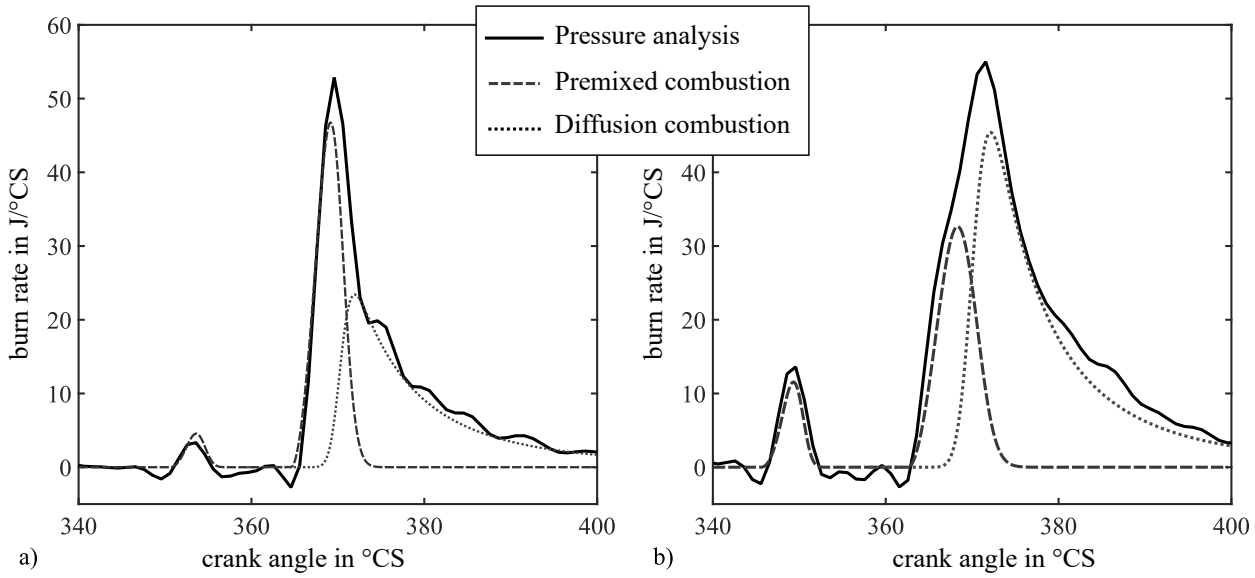

Figure 4.17: Simulation examples of premixed and diffusion combustion based on a phenomenological combustion model (Zahn 2012): a) $n_{\mathrm{eng}} = 1580$ 1/min, $m_{\mathrm{inj}} = 12.2$ mg and b) $n_{\mathrm{eng}} = 2020$ 1/min, $m_{\mathrm{inj}} = 19.3$ mg

It can be seen that the rate of diffusive combustion is determined by available fuel $m_{\mathrm{f,diff}}$ and the turbulence density k inside combustion chamber. Finally, the total combustion rate of the main combustion is obtained by summing the proportions of premixed combustion and diffusion combustion.

$$\dot{Q}_{\mathrm{f}}(t) = \dot{Q}_{\mathrm{f,pre}}(t) + \dot{Q}_{\mathrm{f,diff}}(t) \tag{4.42}$$

The division of the injected fuel into premixed and diffusive combustion is handled differently depending on the author, see for more details Chmela, Pirker, et al. (2007), Barba (2001), and Zahn (2012). Two simulation examples are shown in Fig. 4.17.

Additionally, a ignition delay model is required for describing the time delay between start of injection and ignition event. In Reinhardt (2008), several ignition delay models by Wolfer (1938), Sitkei (1964), Hiroyasu, Kadota, et al. (1983), and J. B. Heywood (1988) and Barba (2001) are investigated with regard to their ability to describe the ignition delay of modern diesel engines. All model approaches are based on a type of Arrhenius law equation proposed by Wolfer (1938), only with some modifications considering various influences i.e. pressure dependencies or local air-fuel-ratios. The parameters given in the corresponding literatures have been tested for a modern diesel engine. The best results were achieved by using the latest ignition delay model proposed by Barba (2001).

$$\tau = \tau_{\mathrm{phy}} + \tau_{\mathrm{chem}} = \tau_{\mathrm{phy}} + c_1 \left(\frac{p}{p_0}\right)^{c_2} \lambda_{\mathrm{zn}}^{c_3} \, \mathrm{e}^{\left(\frac{T_{\mathrm{a}}}{T}\right)} \tag{4.43}$$

Compared to the other approaches, Barba's ignition delay model considers local air-fuel ratio λ_{zn} by modeling a mixed zone. However, no overall parameter set can be given for multiple injections. Furthermore, the many parameters c_1, c_2, c_3 and T_{a} are acting nonlinearly in the Eq. (4.43) and thus can not be determined easily with simple estimation methods.

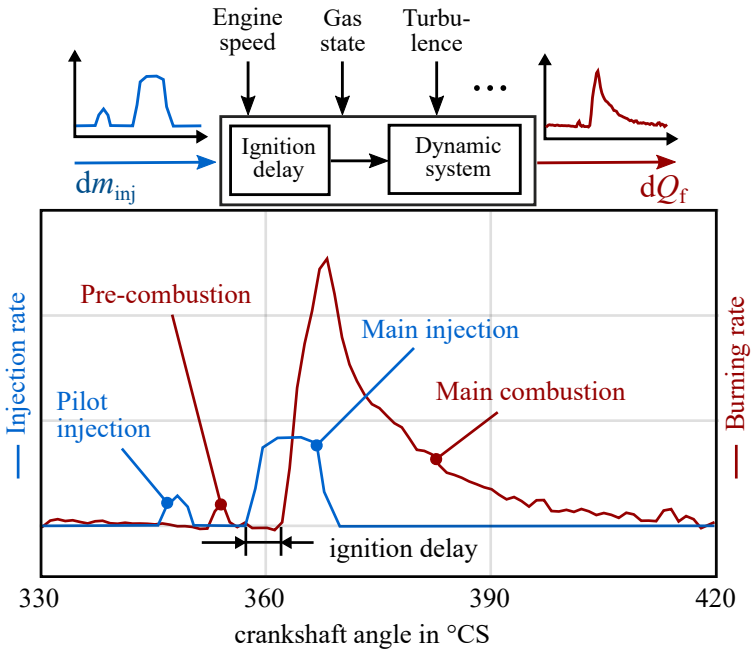

Figure 4.18: Inputs and outputs of diesel combustion engine with ignition delay represented by a dead time and the release of burning energy by a dynamic delay

An automated determination of parameters of presented phenomenological combustion models and their submodels is quite difficult due to the nonlinear model equations. Since the focus lies on the exact representation of underlying phenomena and less on a simple mathematical description, the determination of the model parameters is complicated. Iterative parameter optimization techniques have to be applied in order to estimate the parameters.

4.4.3 Semi-physical combustion model

In modeling diesel combustion, the correlation between the fuel injection $\dot{m}_{\mathrm{inj}}$ and the burn rate $\dot{Q}_{\mathrm{f}}$ resulting from combustion is of great interest. When examining the curves of injection rate $\mathrm{d}m_{\mathrm{inj}}/\mathrm{d}\varphi$ and burn rate $\mathrm{d}Q_{\mathrm{f}}/\mathrm{d}\varphi$ in the Fig. 4.18, it becomes apparent that the curve of the burn rate represents a dynamically delayed system response (output) of a dynamic process with the injection rate as the excitation (input). Consequently, the dynamics of burn energy release can be interpreted as dynamic process with input delay. The input-output behavior is illustrated by the signal flow diagram at the top of Fig. 4.18.

The main input variable is the injection rate $\mathrm{d}m_{\mathrm{inj}}/\mathrm{d}\varphi$ which must be derived from ECU's injection variables, see Appx. A.3 for modeling of common-rail injection. Additional input variables such as engine speed, gas pressure and temperature or turbulence intensity in the cylinder also influence the dynamics of the combustion and must be taken into account in the modeling of the dynamic process. Output variable is the crank angle resolved burn rate $\mathrm{d}Q_{\mathrm{f}}/\mathrm{d}\varphi$, composed of the burn rates of premixed combustion, diffusive combustion and burnout. Dead time between start of injection

(SOI) and the start of combustion (SOC) can be interpreted as input delay, which includes the processes of fuel injection and vaporization as well as the build-up of an ignitable air-fuel mixture.

Basic Idea of Semi-Physical Model Approach

The origin of the developed semi-physical model approach can be classified somewhere between Vibe's empirical approach and the phenomenological modeling approaches proposed by Barba (2001) or Chmela, Pirker, et al. (2007). The aim is to describe the release of burning energy in a mathematically simple way, while also incorporating the underlying phenomena such as mixture formation, spontaneous ignition and combustion components.

If comparing the Vibe function from Eq. (4.36) to the step response of a linear dynamic system with characteristic constant T in time domain, written as

$$x(t) = K\left(1 - e^{-t/T}\right), \tag{4.44}$$

some similarities are obvious. The proportionality factor K describes the height of the step excitation of the step response and corresponds to the parameter $Q_{\mathrm{f,tot}}$ in Eq. (4.36), representing the total amount of burning energy. Moreover, the exponents of Eqs. (4.36) and (4.44) correspond to each other in the following relation

$$t/T \sim a\varphi^{m+1} \tag{4.45}$$

If one sets the form factor m of the Vibe function equal to zero, the resulting Vibe function equals exactly an angle domain solution of step response of a first order differential equation with the *characteristic angle constant* τ [15]

$$Q_{\mathrm{f}}(\varphi) = Q_{\mathrm{f,tot}}\,(1 - e^{-a\varphi}) = H_{\mathrm{l}} m_{\mathrm{f}}\,(1 - e^{-a\varphi}) \sim x(\varphi) = K\left(1 - e^{-\varphi/\tau}\right). \tag{4.46}$$

The *angle constant* τ has then the dimension [°CS] and corresponds to the time constant in s. Consequently, the Vibe function can be interpreted as a step response of an first order lag element with a scalable angle reference $= \varphi^{m+1}$. Moreover, Eq. (4.45) shows also a correspondence between the parameter a and the characteristic angle constant $1/\tau$ of the step response. Adjusting of angle constant τ influences the rate at which the burn energy Q_{f} changes, but not the characteristic shape of its curve. However, the angular constant τ can be used to model a steeper or flatter release of burning energy. On the other hand, variation of m allows to adapt the shape of rate increase and decrease; compare Fig. 4.19 a). This effect can not be achieved by adjusting the angle constant τ. However, one could consider modeling of $Q_{\mathrm{f}}(\varphi)$ as a step response of a higher order dynamic process, see Fig. 4.19 b).

[15] Vibe's approach was originally developed for modeling the heat release in spark-ignition engines with external mixture formation. Since in spark-ignition engines all fuel can be assumed to be premixed at the event of spark-ignition, the assumption of an abrupt excitation of the combustion process by $K = H_{\mathrm{l}} m_{\mathrm{f}}$ is legitimate. Considering diesel engines with partially premixed of diffusive combustion, this assumption no longer holds. For this reason, Vibe-function is less suitable for modeling diesel combustion.

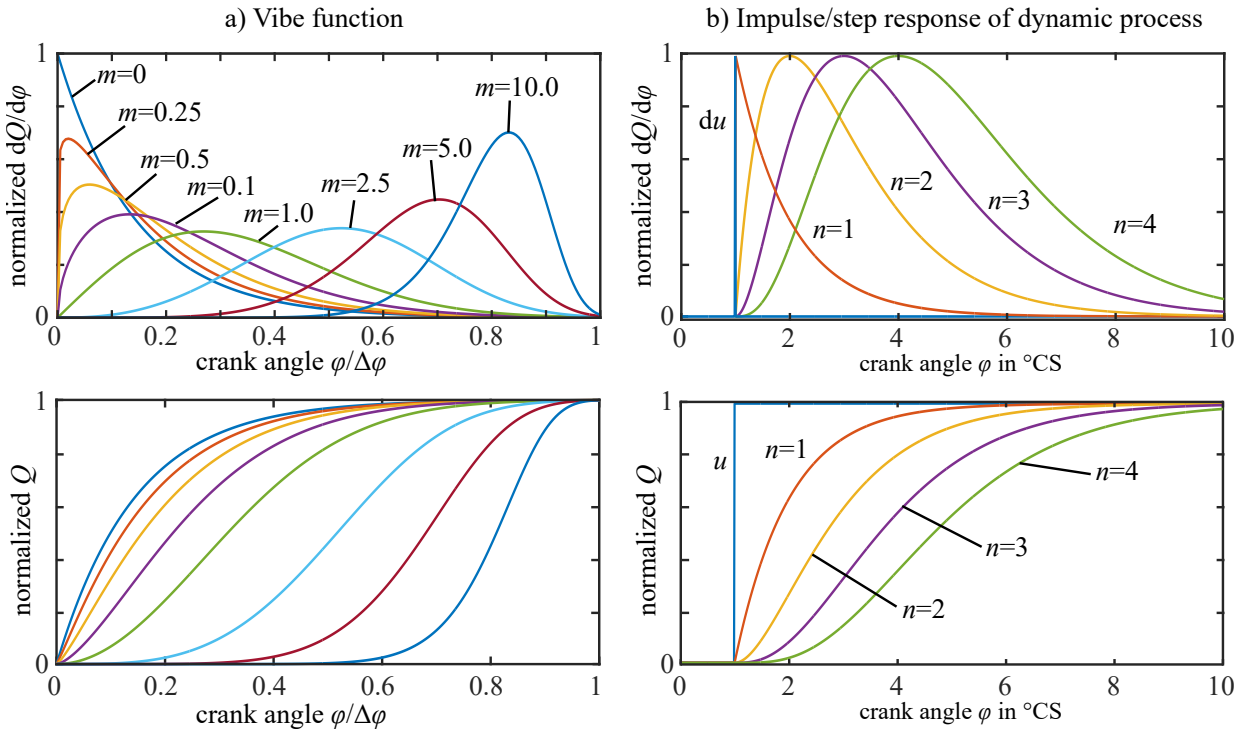

Figure 4.19: a) Course of Vibe function (normalized burn rate $\mathrm{d}Q_\mathrm{f}(\varphi)/\mathrm{d}\varphi$, burn release $Q_\mathrm{f}(\varphi)$ for different form factors m; b) normalized impulse response (top) and step response (bottom) of linear dynamic process $G(\sigma) = 1/(\sigma + 1)^n$ for different process order n

Combustion modeling by using linear dynamic processes

A system theoretical modeling approach would be to derive a transfer function from the basic physical equations of the system. In the case of combustion modeling, this would involve deriving and setting up the differential equations for the elementary chemical reactions as well as the algebraic relations (e.g. partial mass equilibrium). This would lead to a high-dimensional and nonlinear differential equation system that could not be calculated in any compact form. Especially the determination of the model parameters would not be possible without numerical parameter optimization methods.

An alternative modeling approach exploits the phenomena frequently observed in technical processes, where the dynamics of the overall process is essentially dominated only by a reduced number of processes. This is based on the fact that the time constants (eigenvalues) of the dynamical system differ significantly from each other and only the slower processes determine the dynamics of the overall process. One speaks then of quasi-stationarity, since the fast processes becomes quasi-stationary compared to the slow processes. The heat release during combustion represents a high-dimensional process, which is based on numerous physical and chemical subprocesses. Instead of modeling all underlying processes, the idea is to approximate the dynamics of heat release by a reduced-order dynamic process, which represents only the relevant and observable behavior.

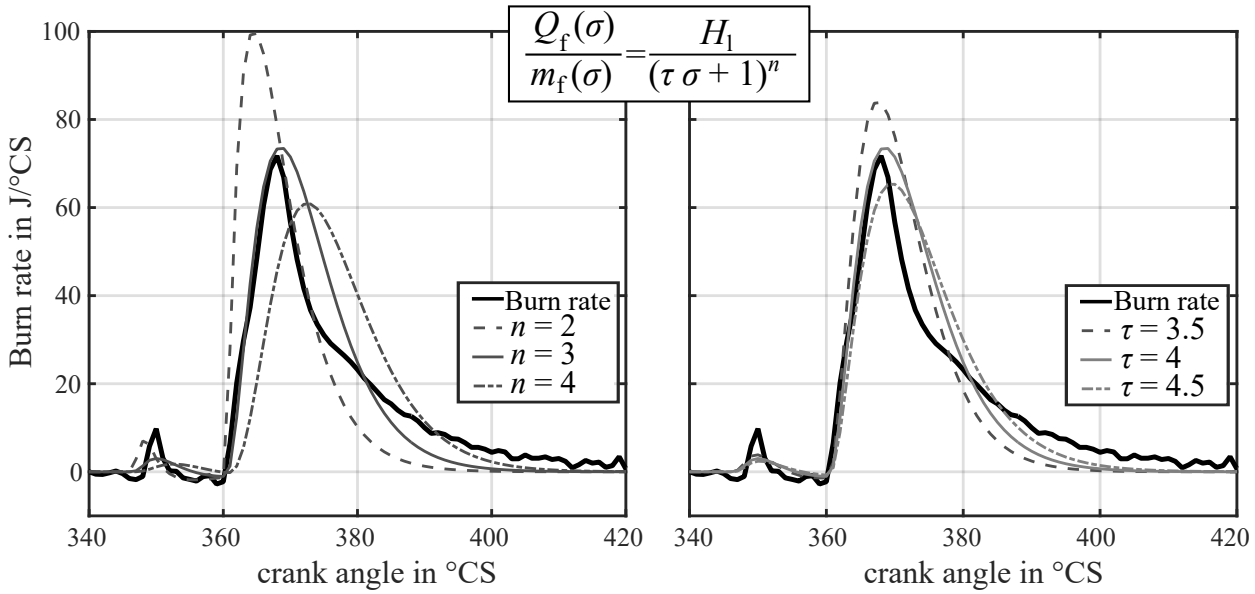

Figure 4.20: Approximation of burn rate of combustion using a transfer function a) variation of process order n; b) variation of angle constant τ (process order $n = 3$)

In Weber and Isermann (2017)[16], it has been shown that the dynamics of the combustion process can be simply approximated by high order linear differential equations, which generally can be written as

$$\begin{aligned} y^{(n)}(\varphi) + a_{n-1}y^{(n-1)}(\varphi) + \ldots + a_1 y'(\varphi) + a_0 y(\varphi) = \\ b_m u^{(m)}(\varphi) + b_{m-1}u^{(m-1)}(\varphi) + \ldots + b_1 u'(\varphi) + b_0 u(\varphi), \end{aligned} \tag{4.47}$$

where $y^{(j)} = d^j y(\varphi)/d\varphi^j$ represents the j-th order derivatives with respect to crankshaft angle φ. In general, the linear differential equation can be transformed via *Laplace transformation* into *crank angle frequency domain* (Föllinger 2013). This leads to following transfer function for release of total burning energy Q_f with the complex crank angle frequency variable σ in 1/°CS:

$$G_f(\sigma) = \frac{Q_f(\sigma)}{m_f(\sigma)} = \frac{b_0 + b_1\sigma + \ldots + b_m\sigma^m}{a_0 + a_1\sigma + \ldots + a_n\sigma^n}. \tag{4.48}$$

To approximate the course of burn energy release by the transfer function $G_f(\sigma)$, the input order m and output order n of the transfer function must be defined in advance. This is decisive choice since the process order of the transfer function determines not only the course of the transfer function output but also has consequences on the complexity of parameter identification (estimation of the parameter a_i and b_i or τ_i and β_i), see Fig. 4.19 b). Generally, a higher order transfer function has more degrees of freedom and allows a better approximation of a dynamic processes, especially in case of a slow and progressive increase of heat release at the beginning of combustion. For instance, a first order lag is not able to reproduce such slow and progressive increase, compare step response with $n = 1$ in Fig. 4.19 b).

[16]The approximation of heat rate curve, reconstructed from the pressure curve analysis, was performed online using a recursive least squares parameter estimator

Some assumptions can be applied in order to simplify the transfer function. First, the order n of the denominator can be chosen to be constant. Furthermore, the denominator polynomial is defined to have an n-multiple eigenvalue λ, assuming that the behavior of the considered process can be approximated by one dominant process dynamics only, which determines the course of the process, i.e. the slowest process dynamics. The denominator of Eq. (4.48) is assumed to have the order $m = 0$. This leaves the parameter b_0, which represents the stationary gain. If the injection quantity m_f is known, the numerator is to be set equal to one, assuming that the energy chemically bound in the fuel is almost completely converted. Then, b_0 is set to be equal to the lower caloric value of diesel fuel $H_\mathrm{l}(= Q_\mathrm{f}/m_\mathrm{f})$ and the transfer function for the release of burning energy Q_f becomes

$$G_\mathrm{f}(\sigma) = \frac{Q_\mathrm{f}(\sigma)}{m_\mathrm{f}(\sigma)} = \frac{H_\mathrm{l}}{(\tau\sigma + 1)^n} = \frac{H_\mathrm{l}}{\left(\frac{1}{r}\sigma + 1\right)^n}. \tag{4.49}$$

and for the burn rate $\mathrm{d}Q_\mathrm{f}/\mathrm{d}\varphi$ ($= Q'$ derivate of Q with respect to crank angle)

$$G'_\mathrm{f}(\sigma) = \frac{Q'_\mathrm{f}(\sigma)}{m'_\mathrm{f}(\sigma)} = \frac{H_\mathrm{l}\sigma}{(\tau\sigma + 1)^n} = \frac{H_\mathrm{l}\sigma}{\left(\frac{1}{r}\sigma + 1\right)^n}. \tag{4.50}$$

The whole process dynamics is then covered by only one parameter, which is interpretable as characteristic angle constant τ. This angle constant is a measure for the settling period of the step response of a dynamic process. Alternatively, for a better physical interpretability, the rate parameter r can be used ($r = 1/\tau$).

Fig. 4.20 shows exemplarily a comparison of the course of reconstructed burn rate $\mathrm{d}Q_\mathrm{f}/\mathrm{d}\varphi$ (from cylinder pressure analysis) and its approximation using the transfer function from Eq. (4.50). The derivative of the step response of $G_\mathrm{f}(\sigma)$ is shown. Some variations in system order n and in the characteristic constant τ are shown. It can be seen that both system order and angle constant have influence on the course of the transfer function output and allow an adaptation to the real course.

In the examples shown in Fig. 4.20, either the order n or the time constant τ describes the qualitative course of the burn rate. The advantage over the Vibe approach is given by the direct correlation between the injection rate and the combustion rate. It is possible to pre-set the order and to adapt the characteristic time constant to the reference course. Thereby only one parameter has to be determined. Additionally, the formulation as linear dynamic process offers great advantages. Several methods from the field of linear system theory can be used. With regard to the scope of this work, this mathematical formulation is suitable for the combination with parameter estimation methods in particular.

However, the courses of approximations in Fig 4.20 also indicate that it is not possible to approximate the characteristic diesel combustion consisting of pronounced premixed and diffusive combustion by only a single transfer function. Only in case of a highly premixed combustion or a conventional diesel combustion, it is sufficient to model burn rate by a single transfer function. For example, the combustion of small pilot-injection (*pre-combustion*) represents such a highly premixed combustion. Due to the long ignition delays of pilot-injection, it can be assumed that the injected fuel has enough time to be fully premixed at start of combustion, so that the combustion of a pilot-injection can be modeled by single transfer functions.

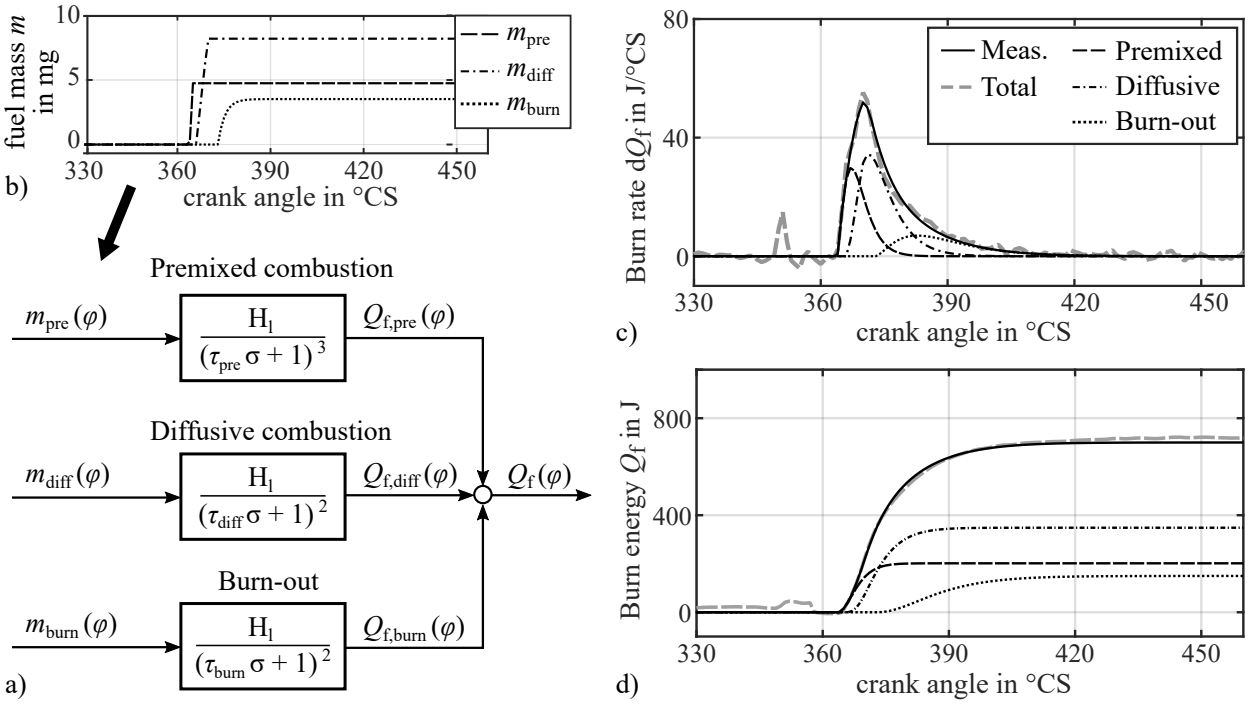

Figure 4.21: a) Scheme of diesel combustion model with three overlapping combustion phases $Q_{f,pre}$, $Q_{f,diff}$ and $Q_{f,burn}$, each modeled by a transfer function; b) Simulation of mixture formation model: Division of fuel injection into three fuel mass fractions acting as inputs of the three combustion phases; Simulation of c) total burn rate and d) total burn release of combustion model in comparison to real curves determined from cylinder pressure measurements

The characteristic main combustion in diesel engines consists of at least two (or three) combustion phases: premixed combustion, diffusive combustion (and burn-out). To achieve a better approximation, these combustion phases must be modeled by separate transfer functions, compare Fig. 4.21 a). However, a division into three combustion phases can not be reliably determined on the basis of heat rate curve only. The course of heat rate allows only a qualitative interpretation of the distribution. It also can be assumed that these combustion components are partly running parallel to each other and thus overlap in terms of time and magnitude. An accurate determination of these combustion shares is not possible without the introduction of additional models describing the underlying phenomena behind the occurrence of these combustion phase. Since the reasons for the occurrence of these different combustion phase lie in heterogeneous mixture formation. Consequently, a mixture formation model is required that provides a division of the injected fuel quantity into the fractions involved in each of the combustion phases, compare Fig. 4.21 b).

As a preview of the combustion model described later, Fig. 4.21 c) and d) shows simulations of the burn rate dQ_f and the burn energy release Q_f in comparison with the real curves obtained from cylinder pressure measurements. Burn rate and burning release are composed of the three overlapping combustion phases $Q_{f,pre}$, $Q_{f,diff}$ and $Q_{f,burn}$, each modeled by a transfer function, compare Fig. 4.21 a). The fuel mass fractions which represent the input of the three combustion phases are shown in Fig. 4.21 b). The underlying model equations are described in the following.

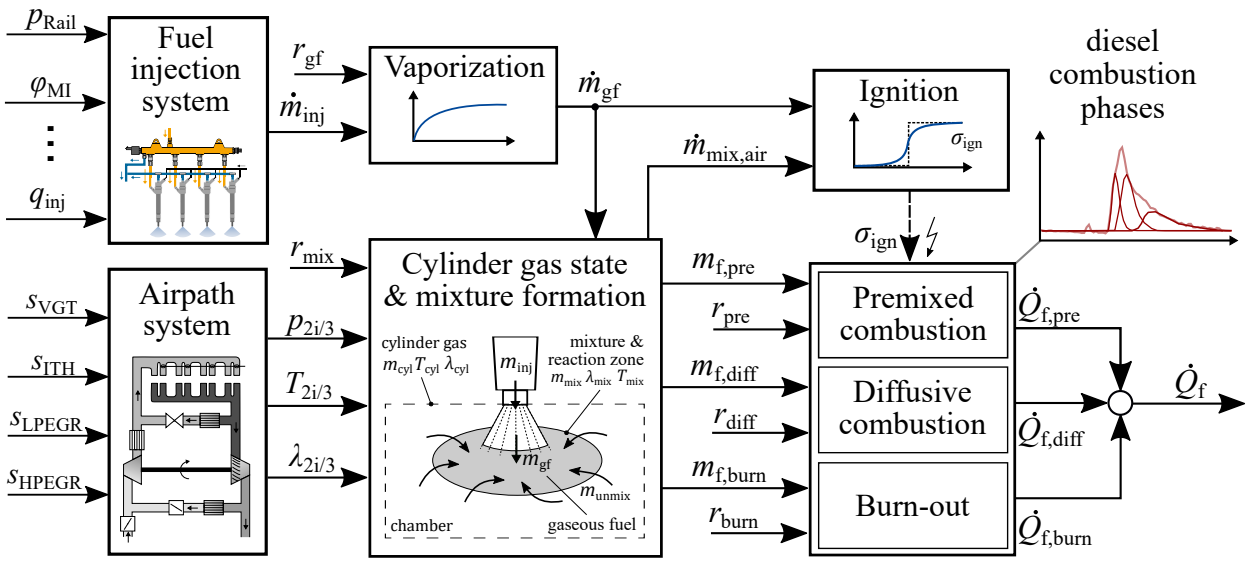

Figure 4.22: Structure of semi-physical combustion model with underlying submodels for the fuel vaporization, the mixture formation and the ignition. Fuel injection model (Appx. A.3) and airpath model (Chap. 3) provide the inputs for the combustion model.

The Fig. 4.22 shows the structure of the overall combustion model, consisting of the submodels for the fuel vaporization, the mixture formation and the ignition. The characteristic diesel combustion phases are modeled by separated transfer functions. In the following sections, theses submodels and experimental modeling of its rate parameters $r_i = 1/\tau_i = f_{exp}(\cdots)$ are described in more detail. Combining both models finally leads to the semi-physical diesel combustion model.

Fuel Vaporization

Vaporization describes the phase change from the injected liquid fuel m_{inj} to the gaseous fuel m_{gf}. It is a highly complex process, which is usually simulated using 1D/3D-fluid mechanics models describing the physical effects of droplet decomposition in the injection jet (inertia, friction and viscosity, surface tension, heat transfer).

In J. B. Heywood (1988), Hiroyasu, Arai, et al. (1989), Constien (1991), Barba (2001), and Kozuch (2004) and Grill (2006), the spray atomization model according to Varde et al. (1984) is used, which describes atomization of injection jet into continuously growing number of fuel droplets characterized by their primary droplet diameter. This mean droplet diameter is formulated as a function of the nozzle cross-section area and the dimensionless Reynolds and Weber number. These two parameters require in return the temperature and pressure dependent fuel properties, such as density, viscosity and surface tension. An initial value for the mean droplet diameter and an empirical equation for the rate of droplet diameter decrease must be chosen, see i.e. Barba (2001). Depending on the author, different parameters are assumed for the rate of droplet decay. With decreasing droplet diameter, the number of droplets and the sum of the droplet surface increases, leading finally to the complete vaporization. Mass balance equation can then be used to determine the vaporized fuel mass.

These vaporization models are originally intended to provide an input for more detailed spray combustion models, such as e.g. Hiroyasu, Kadota, et al. (1983) and Stiesch (1999). However, if only the temporal behavior of conversion from liquid to gaseous fuel is of interest, a simpler and an easier to identify model approach would be more effective. Simulation results of these vaporization models show a dynamic delay between the injected and the vaporized fuel quantity, see i.e. Barba (2001). This process strongly depends on the injection jet velocity w_{inj} and the gas properties of the medium into which the liquid fuel is injected. In modeling fuel injection, this relationship is taken into account by forming the pressure differences between the injection pressure and the cylinder gas pressure. Injection jet velocity and its build-up, depending on the injector nozzle geometry and the injector dynamics, is implicitly taken into account by the injection process model by describing the course of fuel injection rate. Influence of the engine speed is also included through conversion into crank angle domain, see Appx. A.3.

Since the evaporation process is subject to similar influences and thus behaves proportionally to injection rate, it appears to be reasonable to model the evaporation as a succeeding dynamic process. In the simplest case, this behavior is approximated by a first-order transfer function. In Pischinger et al. (2009) a simplified vaporization model is also proposed, representing a first order lag element

$$m'_{\mathrm{gf}}(\varphi) = \frac{\mathrm{d}m_{\mathrm{gf}}(\varphi)}{\mathrm{d}\varphi} = \frac{1}{\tau_{\mathrm{gf}}} \left(m_{\mathrm{inj}}(\varphi) - m_{\mathrm{gf}}(\varphi)\right) = r_{\mathrm{gf}} \left(m_{\mathrm{inj}}(\varphi) - m_{\mathrm{gf}}(\varphi)\right), \tag{4.51}$$

where m_{gf} is the mass of vaporized, gaseous fuel and τ_{gf} is the characteristic angle constant of the vaporization process. The parameter $r_{\mathrm{gf}} = 1/\tau_{\mathrm{gf}}$ describes the vaporization rate and is generally not constant. According to the discussed detailed vaporization models, it can be assumed that r_{gf} must be a function of the engine speed, the injection pressure and the properties of cylinder gas. Modeling this parameter is treated in Sect. 4.5.

Mixture formation and auto-Ignition

The inhomogeneities in the combustion chamber are an important characteristic of diesel engine combustion. The description of mixture formation is a central component for modeling the combustion phases of diesel combustion.

Immediately after the start of the fuel injection, at the periphery of the injection jets occur a boundary layer, in which a reactive mixture of vaporized fuel and surrounding cylinder air first forms and then eventually ignites. Exact modeling of mixture formation in these boundary layers usually requires spatial modeling of the material flows, heat flows and reaction kinetics inside combustion chamber. Since no spatial distributions in the combustion chamber can be verified and measured with conventional test bench measurement technology, an alternative but representative modeling approach must be found for describing inhomogeneous mixture formation.

In the following, all boundary layers, which are formed at several locations in the combustion chamber (depending on the number of injection nozzle holes), are summarized globally in one mixture zone. This leads to a quasi-dimensional modelling of the inhomogeneities.

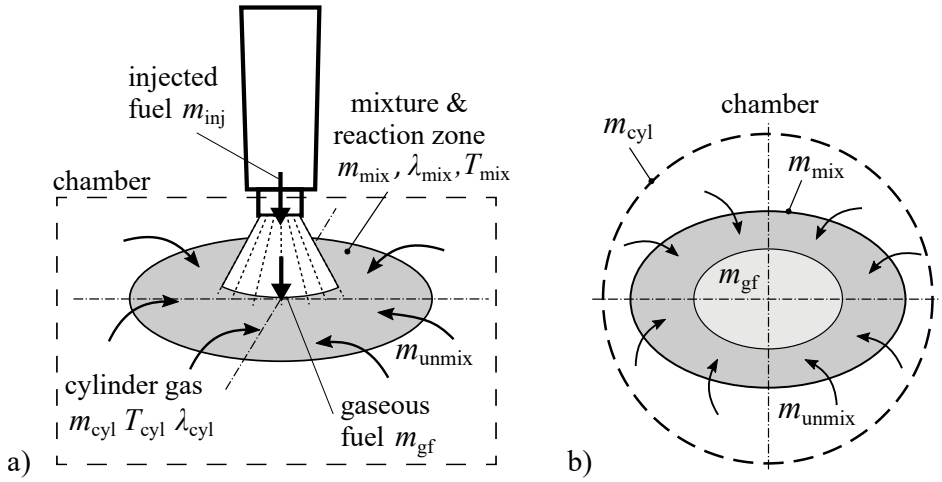

Figure 4.23: a) Illustration of the formation of mixture/reaction zone; b) Quasi-dimensional illustration (top view) of the masses in the mixture zone and the mass flow entering during its formation

a) *Definition of mixture zone*

The combustion chamber is thus divided into the *mixture/reaction zone* and the surrounding cylinder gas regarded as *unmixed zone*[17], defined by their masses m_{mix} and m_{unmix}. The formation of mixture zone is initiated by the occurrence of vaporized, gaseous fuel m_{gf}. It is assumed that the mixture zone only increases in mass during its formation by ongoing fuel vaporization m_{gf} or by air entrainment of surrounding cylinder gas $m_{unmix \to mix}$. By admixing the surrounding combustion gas $m_{unmix \to mix}$, the mixture zone builds up around the vaporized fuel m_{gf}. The latter is also denoted as air entrainment.

$$m'_{mix}(\varphi) = \frac{dm_{mix}}{d\varphi} = \sum_{i=1}^{p} \frac{dm_{in,i}}{d\varphi} = \frac{dm_{gf}}{d\varphi} + \frac{dm_{unmix \to mix}}{d\varphi} \tag{4.52}$$

Process of mixture formation ends when all vaporized fuel and all surrounding cylinder mass have entered the mixture zone $m_{mix} = m_{cyl}$ ($m_{unmix} = 0$). Fig. 4.23 illustrates the formation of the mixture zone in the combustion chamber.

For further simplification, the mixing and reaction zone is described as mixture of two components defined by their mass fractions: fresh unburned air X and inert gas $(1 - X)$, considering burned gas from EGR and burned residual gas mass from prior work cycle remaining inside the cylinder

$$X_{mix} = \frac{m_{air}}{m_{air} + m_{inert}} = \frac{m_{air}}{m_{mix}}; \qquad 1 - X_{mix} = \frac{m_{inert}}{m_{air} + m_{inert}} = \frac{m_{inert}}{m_{mix}} \tag{4.53}$$

The mass fraction of fresh air $X = m_{air}/m_{mix}$ represents an essential state variable for describing the formation of the mixture zones. Generally, the change in the air mass fraction within a two-

[17] unmixed in terms of not being mixed with injected fuel. However, surrounding cylinder gas is in fact also a mixture of fresh air and residual gas

component system separated by system boundaries can be described by the following equation

$$\frac{\mathrm{d}X_{\mathrm{mix}}}{\mathrm{d}\varphi} = \frac{1}{m_{\mathrm{mix}}}\left[\sum_{i=1}^{p}(X_{\mathrm{mix}} - X_{\mathrm{in},i})\frac{\mathrm{d}m_{\mathrm{in},i}}{\mathrm{d}\varphi} + \sum_{j=1}^{q}(X_{\mathrm{mix}} - X_{\mathrm{out},j})\frac{\mathrm{d}m_{\mathrm{out},j}}{\mathrm{d}\varphi}\right] \tag{4.54}$$

It is assumed that the two-component mixture is instantly homogeneously mixed. In this case, the outflowing mass has the same composition as the mixture within the system boundaries ($X_{\mathrm{out}} = X_{\mathrm{mix}}$). Thus, only the air mass fractions $X_{\mathrm{in},i}$ of inflowing mass flows $\mathrm{d}m_{\mathrm{in},i}/\mathrm{d}\varphi$ cause a change in the air mass fraction X_{mix}. Additionally, since mixture zone can only expand, an outflow is neglected. The air mass fraction in the mixture zone is described by the following differential equation rewritten from mass balance

$$\frac{\mathrm{d}X_{\mathrm{mix}}}{\mathrm{d}\varphi} = \frac{1}{m_{\mathrm{mix}}}\left[\sum_{i=1}^{p}(X_{\mathrm{mix}} - X_{\mathrm{in},i})\frac{\mathrm{d}m_{\mathrm{in},i}}{\mathrm{d}\varphi}\right] \tag{4.55}$$

b) *Air entrainment*

The dynamics of mixture formation is determined by the admixtures of vaporized fuel and surrounding cylinder gas. Both mass flows have an influence on the duration of the ignition delay and the burning rate during the diffusive combustion and burn-out. The admixture of fuel is determined by the rate of vaporization, which is mainly driven by the injection rate. The dynamics of air entrainment requires considering the turbulence and air availability inside the cylinder. Therefore, modeling the dynamics of air entrainment is important for connecting the combustion model with the in-cylinder gas state.

The basic idea of modeling the admixture of surrounding cylinder gas is based on the assumption that the mass concentration difference between the mixed zone and the surrounding gas is the driving forces for the air entrainment. Since the presence of fuel vapor first initiates mixture formation, the rate of air entrainment must also be proportional to the amount of fuel in the mixture zone. With the constraint that the mass inside the cylinder must remain constant $m_{\mathrm{cyl}} = m_{\mathrm{mix}} + m_{\mathrm{unmix}}$, the cylinder gas mass flow into the mixed zone is defined as a first order differential equation with respect to crankshaft angle φ

$$\begin{aligned}\frac{\mathrm{d}m_{\mathrm{unmix}\to\mathrm{mix}}}{\mathrm{d}\varphi} &= r_{\mathrm{mix}}\frac{L_{\mathrm{st}}m_{\mathrm{gf}}}{m_{\mathrm{cyl}}}m_{\mathrm{unmix}} \\ &= r_{\mathrm{mix}}\frac{L_{\mathrm{st}}m_{\mathrm{gf}}}{m_{\mathrm{cyl}}}\Big(m_{\mathrm{cyl}} - m_{\mathrm{mix}}\Big) \\ &= \frac{1}{\tau_{\mathrm{mix}}}\frac{L_{\mathrm{st}}m_{\mathrm{gf}}}{m_{\mathrm{cyl}}}\Big(m_{\mathrm{cyl}} - m_{\mathrm{mix}}\Big)\end{aligned} \tag{4.56}$$

whereas $r_{\mathrm{mix}} = 1/\tau_{\mathrm{mix}}$ denotes the mixing rate representing the turbulence intensity inside the combustion chamber. The term $(L_{\mathrm{st}}m_{\mathrm{gf}})/m_{\mathrm{cyl}}$ considers the fuel to cylinder gas mass ratio inside the cylinder. Additionally, the difference of the gas masses $(m_{\mathrm{cyl}} - m_{\mathrm{mix}})$ ensures that the m_{mix}

converges for $\varphi \to \infty$ to the cylinder gas mass m_{cyl}.

$$\begin{aligned}\frac{\mathrm{d}m_{\mathrm{mix}}}{\mathrm{d}\varphi} &= \frac{\mathrm{d}m_{\mathrm{gf}}}{\mathrm{d}\varphi} + \frac{\mathrm{d}m_{\mathrm{unmix}}}{\mathrm{d}\varphi} \\ &= r_{\mathrm{gf}}\left(m_{\mathrm{inj}} - m_{\mathrm{gf}}\right) + r_{\mathrm{mix}}\frac{L_{\mathrm{st}}m_{\mathrm{gf}}}{m_{\mathrm{cyl}}}\left(m_{\mathrm{cyl}} - m_{\mathrm{mix}}\right)\end{aligned} \tag{4.57}$$

The ratio between fuel and air admixture determines the air-fuel ratio λ_{mix} inside the mixture

$$\begin{aligned}\lambda_{\mathrm{mix}} &= \frac{X_{\mathrm{mix}}m_{\mathrm{mix}} - m_{\mathrm{air,burned}}}{L_{\mathrm{st}}m_{\mathrm{gf}}} \\ &= \frac{X_{\mathrm{mix}}m_{\mathrm{mix}} - L_{\mathrm{st}}\lambda_{\mathrm{b}}m_{\mathrm{bf}}}{L_{\mathrm{st}}m_{\mathrm{gf}}},\end{aligned} \tag{4.58}$$

with the stoichiometrically burned air mas $m_{\mathrm{air,burned}} = L_{\mathrm{st}}\lambda_{\mathrm{b}}m_{\mathrm{bf}}$, determined from the already burned fuel m_{bf} and the stoichiometric air requirement $L_{\mathrm{st}}(= 14.5$ for diesel). The combustion is assumed to be stoichiometric with $\lambda_{\mathrm{b}} = 1$.

$$\frac{\mathrm{d}m_{\mathrm{bf}}}{\mathrm{d}\varphi} = \frac{1}{H_{\mathrm{l}}}\frac{\mathrm{d}Q_{\mathrm{f}}}{\mathrm{d}\varphi} \tag{4.59}$$

The variable X_{mix} represents the air mass fraction inside the mixture. The change of the air mass fraction within a two-component system, separated by system boundaries, can be described by the following equation

$$\begin{aligned}\frac{\mathrm{d}X_{\mathrm{mix}}}{\mathrm{d}\varphi} = \frac{1}{m_{\mathrm{mix}}}\Big[&(X_{\mathrm{cyl}} - X_{\mathrm{mix}})\frac{\mathrm{d}m_{\mathrm{unmix}\to\mathrm{mix}}}{\mathrm{d}\varphi} \\ &- X_{\mathrm{mix}}\frac{\mathrm{d}m_{\mathrm{gf}}}{\mathrm{d}\varphi} - X_{\mathrm{mix}}L_{\mathrm{st}}\lambda_{\mathrm{b}}\frac{\mathrm{d}m_{\mathrm{bf}}}{\mathrm{d}\varphi}\Big]\end{aligned} \tag{4.60}$$

There are essentially two effects that are taken into account by this air entrainment model. The lower the oxygen availability in the combustion chamber, the longer it takes until sufficient fresh air is admixed. This leads to longer ignition delays. Additionally, due to the lower oxygen content, more surrounding cylinder gas must be mixed in order to fulfill ignition conditions. In this way, the effects of exhaust gas recirculation on the ignition delay can be modeled and the effect of lowering nitrogen oxide formation is taken into account.

c) *Auto-ignition*

In general, the auto-ignition is rather a continuous process than a discrete event. Chemiluminescence imaging in Dec (1997) show that ignition is occurring progressively at multiple locations accross the downstream regions of all fuel jets, beginning well before the start of premixed combustion peak. Since the ignition is equated with the start of combustion and is detected by analyzing the pressure rise after injection, ignition is treated as an abruptly occuring event.

Commonly used ignition modeling approaches separate the overall ignition process into a physical and a chemical delay component, see Eq. (4.43). The physical delay component considers injection delay and fuel vaporization. However, injection delay is already considered by the injection model

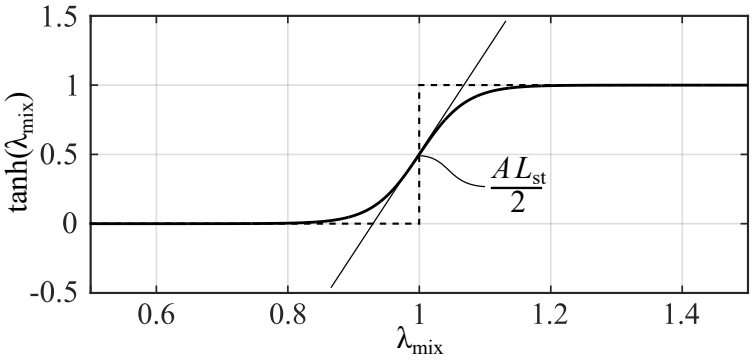

Figure 4.24: Modeling of ignition event σ_{ign} as function of the air-fuel ratio λ_{mix} in the mixture zone by a tangent hyperbolicus function

in Appx. A.3. Modeling of dynamic delay of fuel vaporization is treated in the beginning of this section. What is left over is the chemical delay component, which considers mixture formation and the temperature driven reaction kinetics of ignition. Consequently, the ignition condition has to be formulated as function of the state variables of the mixture.

Simulations have shown a good compliance with measurements when only air-fuel ratio of the mixture λ_{mix} is used as ignition condition. Although the reaction kinetics are usually described based on the pressure- and temperature-dependent Arrhenius equation, it is assumed that it is the admixture of hot cylinder gas that causes the necessary increase in pressure and temperature in the mixture zone, which leads eventually to ignition. In addition, the reaction kinetics run several time scales faster than the mixing, which is why the reaction kinetics become quasi-stationary compared to the slower mixing dynamics, see Sect. 4.4.2. As consequence, the influence of pressure and temperature is neglected in the formulation of the ignition condition.

Assuming that an air-fuel-mixture becomes ignitable when reaching $\lambda_{\text{ign}} = 1$, the following ignition condition for the start of combustion is formulated

$$\sigma_{\text{ign}}(\varphi) = \begin{cases} 0 & \text{, for } \lambda_{\text{mix}} < \lambda_{\text{ign}} \\ 1 & \text{, for } \lambda_{\text{mix}} \geq \lambda_{\text{ign}}, \end{cases} \tag{4.61}$$

where the air-fuel ratio λ_{mix} in the mixed zone is given by $(m_{\text{mix}} X_{\text{mix}})/m_{\text{gf}}$. Such a discontinuous function as Eq. (4.61) is not particularly suitable in connection with parameter estimation methods, especially in case of gradient-based estimation methods. A continuously differentiable activation function is therefore preferable.

In the field of experimental modeling, validity functions are used in order to switch between local submodels or to activate only particular submodels of the overall model (Sect. 2.2). Besides typically used Gaussian or pyramidal validity functions, tangent hyperbolic functions have proven to be useful in cases where the transition between the validity areas has not only to be abruptly, but also continuously differentiable. The following equation describes the ignition event on the basis of a tangent hyperbolic function

$$\sigma_{\text{ign}}(\varphi) = \frac{1}{2} + \frac{1}{2} \tanh\Big(A \cdot L_{\text{st}}\big(\lambda_{\text{mix}} - \lambda_{\text{ign}}\big)\Big) \tag{4.62}$$

The parameter A offers the adjustment of the slope of the tanh-function at $\lambda_{mix} = \lambda_{ign}$ and has to be chosen in advance. Fig. 4.24 shows the course of Eq. 4.62 in dependence of the air-fuel ratio of the mixture zone.

Using this model approach, the ignition delay only depends on the rate of vaporization r_{gf} and mixture formation rate r_{mix}. This allows the determination of these two parameters based on the measured ignition event (Sect. 4.5). In case of multiple injections, one separate ignition model is required for each injection.

d) *Division into fuel proportions*

In order to determine the share of each combustion phases, it is necessary to determine the fuel mass fraction involved in the combustion phases. Although the combustion phases run partially in parallel, their origin can be described by the temporal modeling of the fuel mass flow. Therefore, assumptions must be made in order to divide fuel injection into corresponding fractions, acting as model inputs of the combustion model.

Premixed fuel mass fraction builds up during fuel vaporization prior to ignition ($\varphi \leq \varphi_{soi}$)

$$m_{gf,pre}(\varphi) = \int_{\phi=\varphi_{soi}}^{\varphi} \left(1 - \sigma_{ign}(\varphi)\right) \cdot m'_{gf}(\varphi) \mathrm{d}\varphi. \tag{4.63}$$

At ignition ($\varphi = \varphi_{ign}$), the entire amount of gaseous fuel $m_{gf,pre}(\varphi = \varphi_{ign})$ in the mixture zone is accounted to the premixed combustion and activated by ignition signal $\sigma_{ign}(\varphi)$

$$m_{pre}(\varphi) = m_{gf,pre}(\varphi) \cdot \sigma_{ign}(\varphi). \tag{4.64}$$

This corresponds to an abrupt excitation of the premixed combustion by the premixed fuel mass m_{pre} built-up until then, which is activated by the ignition signal $\sigma_{ign}(\varphi)$ in Eq. (4.62). The amount of premixed fuel mass fraction m_{pre} is proportional to the rate of vaporization and the duration of the ignition delay. The fuel amount, which is vaporized after ignition ($\varphi \geq \varphi_{ign}$) during ongoing injection ($u_{inj} \neq 0$) is accounted to the diffusive combustion

$$m_{diff}(\varphi) = \int_{\varphi=\varphi_{soi}}^{\varphi} u_{inj}(\varphi) \cdot \sigma_{ign}(\varphi) \cdot m'_{gf}(\varphi) \mathrm{d}\varphi. \tag{4.65}$$

The rate of diffusively burned fuel mass flow $\mathrm{d}m_{diff}(\varphi)/\mathrm{d}\varphi$ corresponds to the rate of vaporization. The temporal overlap between active fuel injection, described by activation signal $u_{inj}(\varphi)$, and the ignition event activated by the ignition signal $\sigma_{ign}(\varphi)$ determines *diffusive fuel mass* fraction

$$\frac{\mathrm{d}m_{diff}(\varphi)}{\mathrm{d}\varphi} = m'_{diff}(\varphi) = u_{inj}(\varphi) \cdot \sigma_{ign}(\varphi) \cdot m'_{gf}(\varphi) \tag{4.66}$$

But this also means, if ignition takes place after the end of injection ($\varphi_{soc} \geq \varphi_{eoi}$), then the diesel combustion is premixed only. Injection activation signal $u_{inj}(\varphi)$ represents a binary signal $\sigma_{inj}(\varphi)$ that indicates non-zero value of injection rate

$$u_{inj}(\varphi) = \begin{cases} 1 & \text{for } m'_{inj} \geq m'_{min} \\ 0 & \text{for } m'_{inj} \leq m'_{min} \end{cases} \tag{4.67}$$

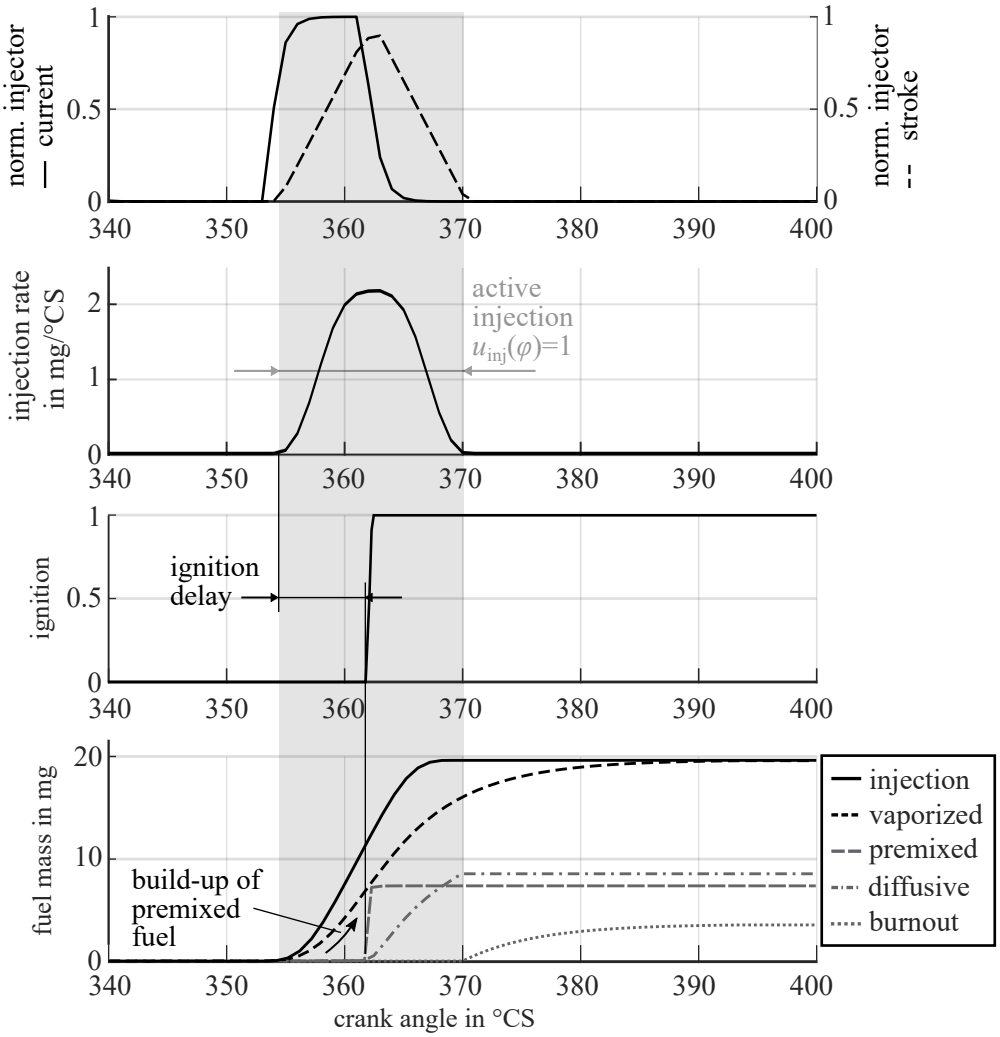

Figure 4.25: Division into fuel mass proportions: Course of injector current and stroke (top), fuel injection rate and ignition signal (middle), and fuel masses of injected fuel, vaporized fuel and mass fractions involved in combustion phases (bottom)

A threshold value $\dot{m}_{\min}$ for injection rate can be used to neglect small injection rates. The *burnout mass flow* results from the remaining mass flow of vaporized fuel after the end of the injection. The dynamics of the burn-out mass flow is also controlled by the vaporization rate.

$$m_{\text{burn}}(\varphi) = \int_{\phi=\varphi_{\text{soi}}}^{\varphi} \big(1 - u_{\text{inj}}(\varphi)\big) \cdot \sigma_{\text{ign}}(\varphi) \cdot m'_{\text{gf}}(\varphi) \mathrm{d}\varphi. \tag{4.68}$$

Since the vaporization is modeled by an first order lag and the rate of fuel evaporation decreases at the end of injection, the burnout mass flow is slower than the diffusive mass flow, see Eq. (4.51)

$$\frac{\mathrm{d}m_{\text{burn}}(\varphi)}{\mathrm{d}\varphi} = m'_{\text{burn}}(\varphi) = \big(1 - u_{\text{inj}}(\varphi)\big) \cdot \sigma_{\text{ign}}(\varphi) \cdot m'_{\text{gf}}(\varphi) \tag{4.69}$$

If burnout is not considered, the activation signal can be neglected ($u_{\text{inj}}(\varphi) = 1$), so that the mass fraction involved in the burnout disappears and is accounted to the diffusive combustion. Using these assumptions does not violate the law of mass conservation. The sum of all three fuel masses

leads to the total injected fuel mass m_{inj}

$$m_{\mathrm{inj}} = m_{\mathrm{gf}} = m_{\mathrm{pre}} + m_{\mathrm{diff}} + m_{\mathrm{burn}} \tag{4.70}$$

Figure 4.25 shows exemplarily the injection process and the breakdown of vaporized fuel into fuel mass proportions involved in each diesel combustion phase. The dynamics of these different mass flows are decisive for the parameter estimation of the combustion model. In fact, it is the division of fuel injection into mass fractions that makes it possible to determine the various combustion phases in the first place.

Modeling of burning rates

In the case of modeling the combustion process by only one linear dynamic process, as it is shown in Fig. 4.20, it is not possible to match both, characteristic shape (increase, decrease and peak value) of the burn rate curve $\mathrm{d}Q_{\mathrm{f}}(\varphi)/\mathrm{d}\varphi$ as well as the total amount of burning energy $Q_{\mathrm{f}}(\varphi)$. At least a two-phase-model approach is required for modeling a characteristic diesel combustion. Matching of burn rate curve allows for prediction of center of combustion and pressure gradient, while matching of total amount of burning energy is required for the prediction of fuel consumption and combustion efficiency.

In compliance with the aforementioned fuel path model, the injected fuel mass is divided into a premixed fuel amount m_{pre}, non-premixed diffusive fuel m_{diff} and burn-out amount m_{burn}, see Fig. 4.25. These fuel mass flows act as inputs for each combustion phase which are modeled as transfer function based on Eq. (4.50). The course of premixed mass flow $m_{\mathrm{pre}}(\varphi)$ corresponds to abrupt step excitation, while the courses of diffusive $m_{\mathrm{diff}}(\varphi)$ and burn-out mass flow $m_{\mathrm{burn}}(\varphi)$ is determined by the dynamics of mixture formation.

The process order n_i (degree of nominator polynomial) of the transfer function describing the combustion phases is chosen empirically with the goal to match the characteristic shape of burn rate curve. A first order transfer function ($n = 1$) does not allow to reproduce the continuous increase in burn rate $\mathrm{d}Q/\mathrm{d}\varphi$ at the beginning of combustion (premixed), see Fig. 4.19 b) (top). Therefore, at least a second order transfer function is required to model the characteristic curve of premixed combustion. The higher the system order n, the less abrupt is the increase of the burn rate at the beginning. On the other hand, a high system order leads to a lengthening of the burning time (stretching of the curve). To describe a rapid drop in burn rate (after reaching peak value), this dynamic behavior may be unwanted.

The choice of system order n can also be justified by considering the physical fluid dynamics and chemical reaction kinetics involved in each combustion phase, see previous sections 4.4.1 and 4.4.2 regarding characteristics of diesel combustion and its phenomenological modeling.

With regard to an accurate mapping of the increase in the burn rate at the beginning of the combustion, see Fig. 4.20, the calculation step size in °CS of the simulation model or real-time processing hardware must also be taken into account when choosing the process order. In the case real-time processing hardware runs with a higher crank angle resolution ($\varphi_{\mathrm{s}} < 1°$ CS), an adequate

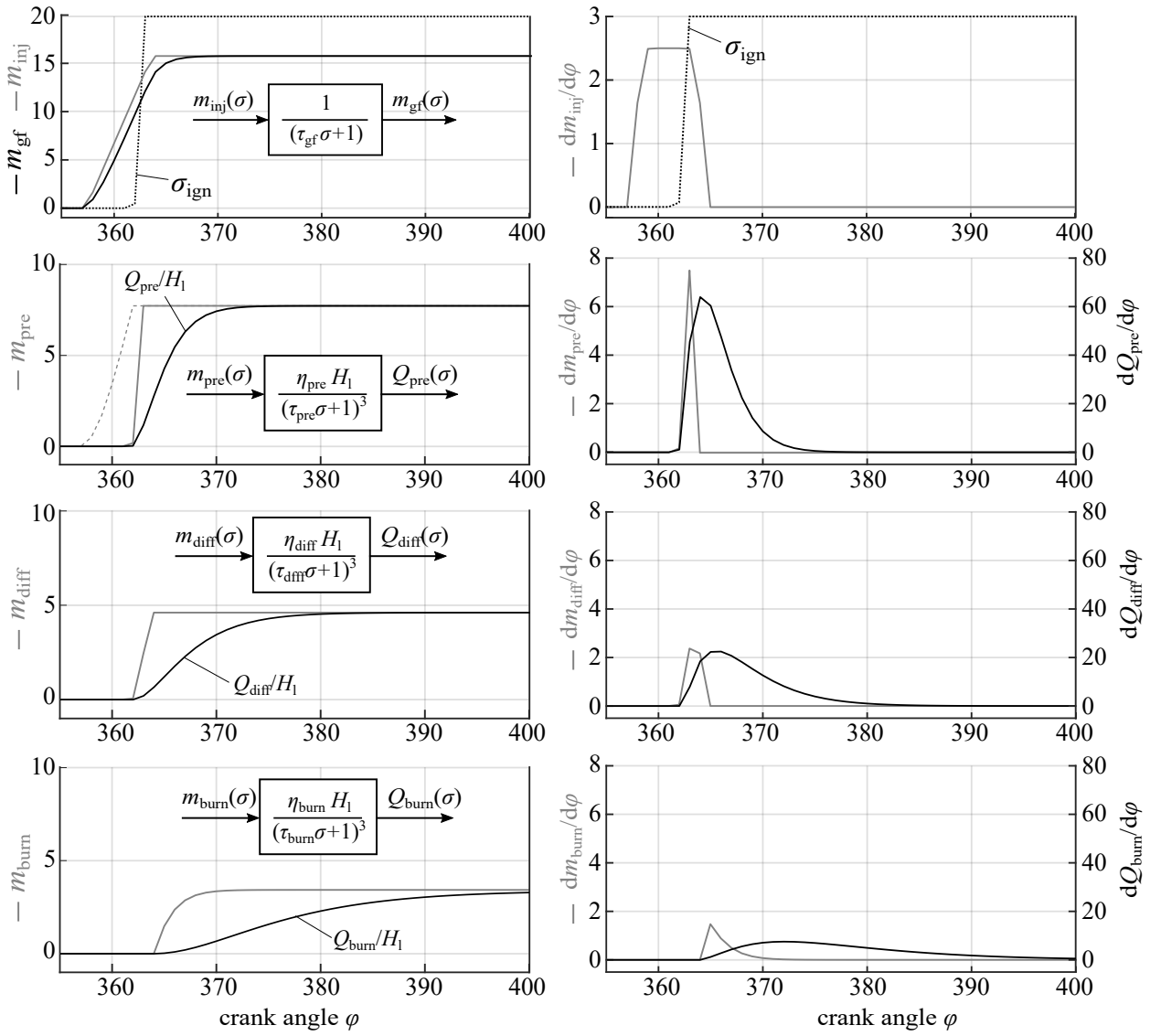

Figure 4.26: Simulation results for semi-physical diesel combustion model: Courses of injection, ignition and fuel masses involved in the combustion phases *premixed*, *diffusive combustion* and burn-out

approximation of the burn rate increase at the SOC would require a higher order process model. However, this would lead to a more complex state and parameter estimation problem.

An alternative approach to achieve a better approximation of the burn rate increase at SOC (while maintaining lower process order), could be carried out by adjusting the parameter A of the ignition model (4.62). Since premixed, diffusive and burnout fuel mass flows Eqs. (4.64), (4.66) and (4.69) are activated by ignition signal $\sigma_{\mathrm{ign}}(\varphi)$, its steepness can be adjusted by parameter A in Eq. (4.62), see Fig. 4.24. It is recommended to do so according to the engine speed.

a) *Premixed combustion*

The premixed combustion is the initial and usually the fastest combustion phase. Since the fuel-gas-mixture is already homogenously mixed in the reaction zone, chemical kinetics determine rate of

premixed combustion. Modeling the underlying chemical chain reactions would inevitably lead to a complex system of nonlinear coupled equations. For this reason alone, the premixed combustion can be considered as higher order dynamic process. A speed-limiting factor is the propagation of pressure and temperature inside the combustion chamber. Since pressure and temperature propagation are subject of a spatial expansion, an at least third order dynamic process is assumed in order to approximate the increasing slope at the beginning of the premixed combustion

$$\frac{1}{r_{\text{pre}}^3} Q_{\text{pre}}'''(\varphi) + \frac{3}{r_{\text{pre}}^2} Q_{\text{pre}}''(\varphi) + \frac{3}{r_{\text{pre}}} Q_{\text{pre}}'(\varphi) + Q_{\text{pre}}(\varphi) = \eta_{\text{pre}} H_{\text{l}} m_{\text{pre}}(\varphi) \tag{4.71}$$

whereas r_{pre} represents the rate parameter in $1/^\circ$ crankshaft angle degree and η_{pre} the efficiency parameter of premixed combustion.

b) *Diffusive combustion and Burn-out*

In contrast to premixed combustion, the process dynamics of the diffusive combustion and burnout are mixing controlled and thus dominated by the dynamics of vaporization and mixing. The diffusive combustion takes place while the temperature inside the reaction zone is already increased due to the already started premixed combustion. For this reason, the reaction kinetics are significantly faster than the mixing process, so that the kinetics can be regarded as quasi-stationary compared to the mixing process. Although, the same complex process of chemical reactions take place during these phases, the reaction kinetics are hidden due to dominance of the slower mixing dynamics. Therefore, the process order of diffusion combustion and burn-out is considered to be lower than the order of premixed combustion

$$\frac{1}{r_{\text{diff}}^2} Q_{\text{diff}}''(\varphi) + \frac{2}{r_{\text{diff}}} Q_{\text{diff}}'(\varphi) + Q_{\text{diff}}(\varphi) = \eta_{\text{diff}} H_{\text{l}} m_{\text{diff}}(\varphi), \tag{4.72}$$

$$\frac{1}{r_{\text{burn}}^2} Q_{\text{burn}}''(\varphi) + \frac{2}{r_{\text{burn}}} Q_{\text{burn}}'(\varphi) + Q_{\text{burn}}(\varphi) = \eta_{\text{burn}} H_{\text{l}} m_{\text{burn}}(\varphi) \tag{4.73}$$

with the rate parameters $r_{\text{diff}} = 1/\tau_{\text{diff}}$ and $r_{\text{burn}} = 1/\tau_{\text{burn}}$ in $1/^\circ$ of crankshaft angle and the efficiency parameters η_{diff} and η_{burn} representing the proportion of fully burned fuel. All three combustion phase-models are formulated in such a way that they have only one multiple eigenvalue. Thus, the course of the corresponding combustion phase is described by only one rate parameter that represents a measure for the reaction speed. This formulation represents a model simplification that later facilitates the parameter estimation problem significantly.

The total burn rate and total released burn energy results from the sum of the contributions of the combustion phases, represented in Fig. 4.27

The rate parameters shown in the overall signal flow scheme in Fig. 4.22 allow the adaptation of combustion model according to the real combustion process.

$$\theta_{\text{r}} = \begin{bmatrix} r_{\text{gf}} & r_{\text{mix}} & r_{\text{pre}} & r_{\text{diff}} & r_{\text{burn}} \end{bmatrix}^{\text{T}} \tag{4.74}$$

Parameters r_{gf} and r_{mix} serve mainly for the adjustment of ignition event and the fuel split between premixed and diffusive or burnout combustion, while r_{pre}, r_{diff} and r_{burn} serve for mapping the total burn rate curve. Note that rate parameters $r_i (= 1/\tau_i)$ are the reciprocals of the angle constants in Fig. 4.26.

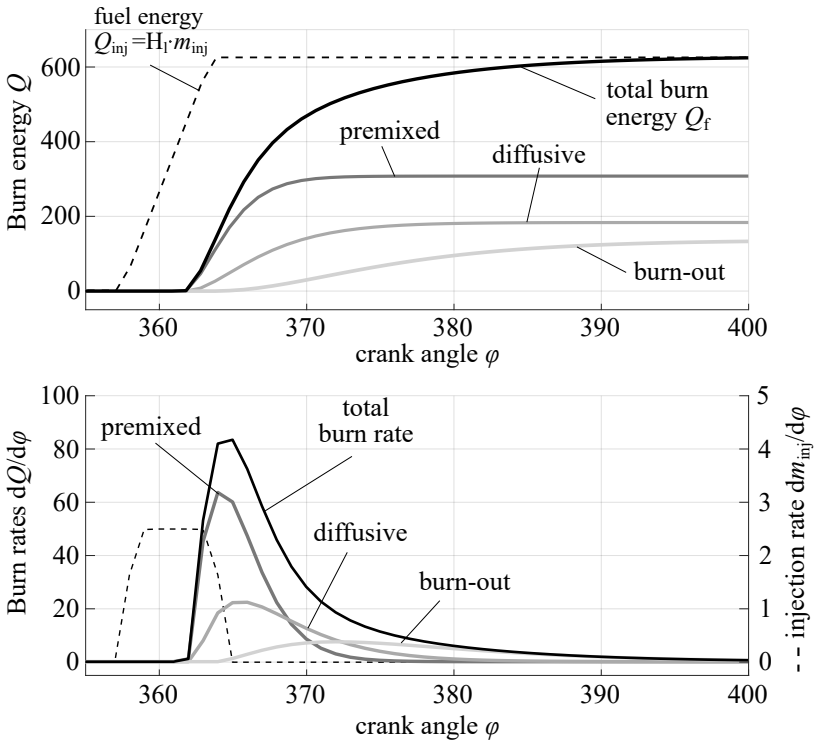

Figure 4.27: Simulation results for the release of burn energy (upper plot) and the burn rate (lower plot) of the semi-physical diesel combustion model: Courses of injection rate, combustion phases *premixed*, *diffusive combustion* and burn-out, and the total burn energy/rate

Experimental modeling of parameters

An experimental modeling method is used for modeling and storing of rate parameters as function of the engine operation point (look-up table, neuro-fuzzy model), which leads to a semi-physical diesel combustion model. Each i-th rate parameter of (4.74) is modeled by a *pyramidal radial basis function* as follows, see Fig. 4.28 and Sect. 2.2,

$$r_i(\mathbf{u}) = f_{\mathrm{r,i}}(\mathbf{u}) = \sum_{j=1}^{L} \Phi_j(\mathbf{u}) w_j . \tag{4.75}$$

The input variables $\mathbf{u}$ must be selected for each rate parameter. Considered inputs are engine operation point defining variables i.e. engine speed, injection quantity or the initial in-cylinder gas state, represented by the in-cylinder gas mass, in-cylinder gas temperature and the air content inside the combustion chamber prior to injection.

The model formulations in Eqs. (4.71), (4.72) and (4.73) are strong simplifications compared to a detailed combustion modeling approach. For instance, the rate parameters of chemically controlled reactions, i.e. auto-ignition or premixed combustion, are strongly pressure and temperature dependent. Both, pressure and temperature varies locally inside the combustion chamber and change during the engine work cycle. The mixing-controlled process, i.e. mixture formation or diffusive combustion, are strongly influenced by the turbulent flow conditions inside combustion chamber, which also varies locally.

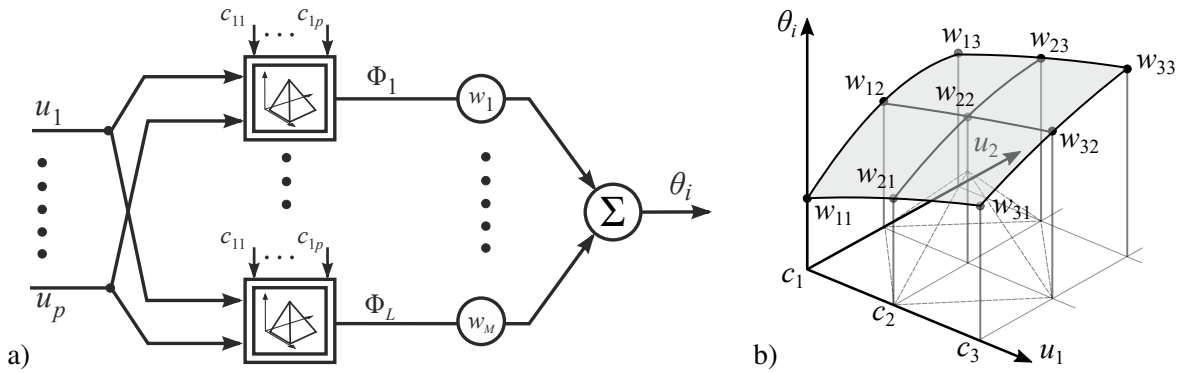

Figure 4.28: a) Scheme of experimental modeling approach using pyramidal basis function; b) Example of 2-D experimental model of the parameter θ_i

However, the course of the cylinder gas pressure and temperature or the turbulent flow conditions inside combustion chamber is already determined before the start of combustion process by the engine operation point, i.e. engine speed, charging pressure and temperature, rail pressure, etc. This means, the engine operation point defines the initial situation, which determines the course of the combustion process and all sub-processes involved. Furthermore, the processes inside the combustion chamber are much faster compared to dynamics of engine operation point variables(i.e. engine speed changes, airpath dynamics, etc.). Consequently, engine operation point variables are regarded as constant during one engine operation cycle. If an model approximation with a particular set of model parameters can be found for an engine operation point, it is legitimate to assume that the parameters only depend on the operation point. Thus, the following experimental model approach for modeling and storing a rate parameter variable r_i is given as

$$\begin{aligned} r_i &= f_{\mathrm{r}}(\mathbf{u}) = f_{\mathrm{r}}\left(n_{\mathrm{eng}}, p_{\mathrm{rail}}, \varphi_{\mathrm{mi}}, \mathbf{x}_{\mathrm{cyl}}\right), \\ \frac{\mathrm{d}r_i}{\mathrm{d}\varphi} &= \frac{\mathrm{d}\, f_{\mathrm{r}}(\mathbf{u})}{\mathrm{d}\varphi} = 0. \end{aligned} \tag{4.76}$$

If all influences on the combustion have to be considered, the number of input variables in Eq. 4.76 becomes relatively large. A high number of input variables significantly complicates the identification of the parameter model. Additional knowledge about the physical relation between the model parameters and the operation point variables shall be used to reduce the input dimension of experimental parameter model. For instance, it is not reasonable to use all in-cylinder gas state variables (pressure, temperature and mass) as inputs, since these variables are already related to each other via the ideal gas law. In this case, the cylinder gas mass is best suited as an input variable, since it is approximately constant during combustion.

Influence of piston speed and on reaction rate

From first investigations of influences of different engine operating point variables on the shape of combustion rate, it is obvious that the rate parameters must be functions of engine speed, injection rate and the cylinder filling (gas density). Additionally, the location of combustion with respect to TDC has also a significant influence on burn rate. The earlier combustion starts with respect to

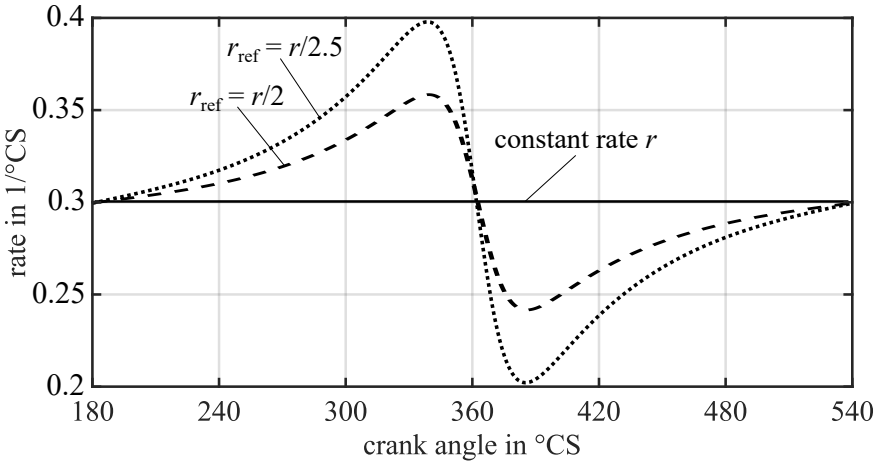

Figure 4.29: Crank angle resolved course of reaction rate $r_{dV}(\varphi)$ in Eq. (4.80) including the influence of change of volume (with $r = 0.3$)

top dead center, the higher the values for combustion rate and in-cylinder pressure. The modeling approach described so far for the burn rates in Eqs. (4.71) to (4.73) describes only the conversion of unburned to burned fuel mass. To describe the reaction rate in reciprocating piston engines, the influence of the density change must be taken into account via the rate parameters.

The kinetics of a chemical reaction is typically formulated as a function of time t and using the material concentrations c_i of the reactants involved. With the aid of material-specific molar masses M in kg/mol, material densities ρ_i can be used instead of molar concentrations. Assuming a simple chemical reaction $A_1 \rightarrow A_2$ with time-related rate r_t in 1/s

$$\frac{d\rho_i}{dt} = -r_t \rho_i = -r_t \left(\frac{m_i}{V}\right) \tag{4.77}$$

On the other hand, the change of material density in reciprocating piston engines is given with respect to mass m_i and volume V as

$$\frac{d\rho_i}{dt} = \frac{d}{dt}\left(\frac{m_i}{V}\right) = \frac{1}{V}\frac{dm_i}{dt} - \frac{m_i}{V^2}\frac{dV}{dt} \tag{4.78}$$

Combining both Eqs. (4.77) and (4.78) and rearranging with respect to the change of mass leads to

$$\frac{dm_i}{dt} = \left(r_t + \frac{1}{V}\frac{dV}{dt}\right) m_i = r_t \left(1 + \frac{1}{r_t V}\frac{dV}{dt}\right) m_i \tag{4.79}$$

The rate parameter r_t still covers the influence of density or engine speed on combustion rate, while the term in the brackets represents the influence of volume change with respect to TDC. By replacing the factor $1/r_t$ within the brackets by a reference rate constant r_{ref} allows adjusting the effect of volume change

$$\frac{dm_i}{dt} = r_t \left(1 + \frac{1}{r_{ref} V}\frac{dV}{dt}\right) m_i = r_t r_{dV} m_i \tag{4.80}$$

The crank angle resolved course of $r_{dV}(\varphi)$ is depicted in Fig. 4.29.

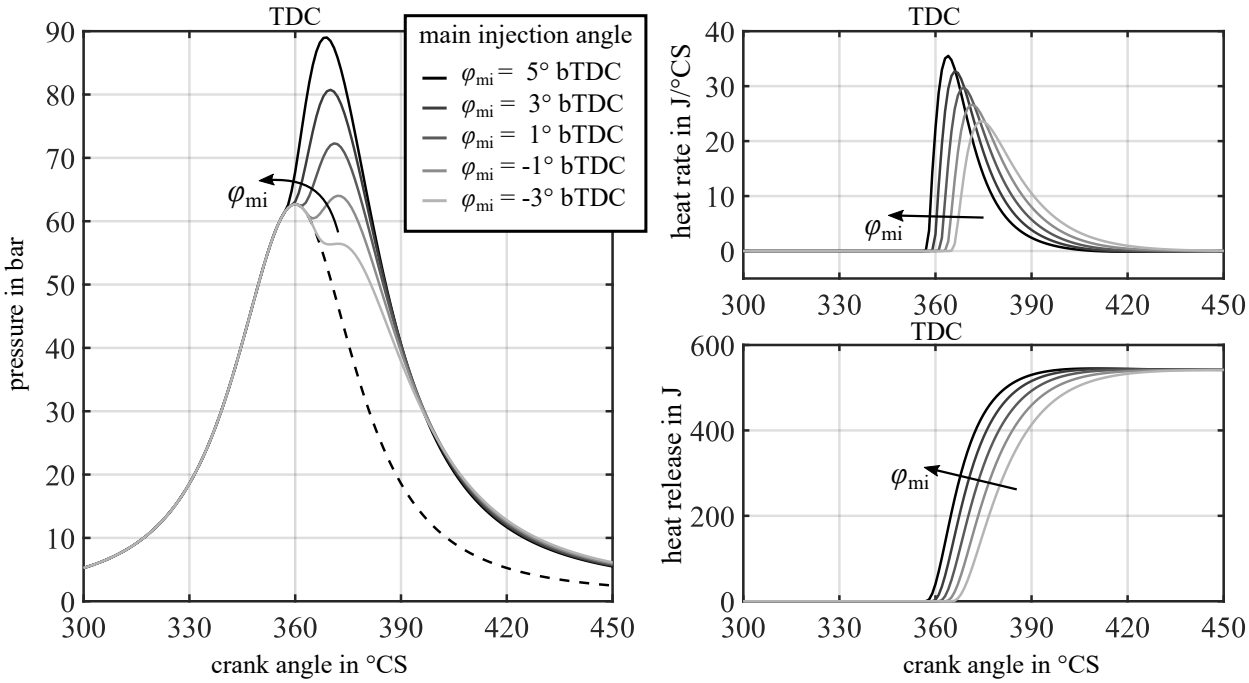

Figure 4.30: Simulation of variations of main injection angle φ_{mi} on reaction rate parameter $r_{dV}(\varphi)$ depicted in Fig. 4.29: Influence on in-cylinder gas pressure (left); Influence on heat rate and heat release (right)

During compression phase before TDC, the molecules are squeezed together, reducing the distance between the molecules and thus leading to a higher conversion rate (increasing collision probability between the molecules). On the other hand, in the expansion phase after TDC, the molecules are being pulled apart again, causing the speed of the reaction to decrease again. The effect of using r_{dV} from Eq. (4.80) for modeling the rate parameter of combustion model in Eqs. (4.71) to (4.73) is shown in Fig. 4.30 by means of the courses of burn rate and cylinder gas pressure. Using Eq. (4.80) allows modeling the influence of injection angle on rate parameters, so that injection angle does not to be considered as input variables of experimental parameter model in Eq. (4.76).

4.5 Cylinder estimation

In the following, two use cases for identifying a semi-physical cylinder model are presented, see Fig. 4.2. In both cases, the estimation of non-measurable cylinder variables and physical-interpretable model parameters is first performed by combined state and parameter estimation based on the Kalman filter algorithm. The estimated physical-interpretable parameters of the semi-physical model are modeled in parallel by experimental modeling. This results in a semi-physical real-time model in the form described by the Eqs. (2.63) and (2.64) in Sect. 2.4.

The *first approach* described in Sect. 4.5.1 deals with the exclusive estimation of diesel combustion. The goal is to estimate the unknown combustion phases (burn rates) and its parameter (rate parameters/characteristic angle constants) simultaneously based on the burn rate $\mathrm{d}Q_{f,m}$ reconstructed

from measured cylinder pressure signal and by using Eq. (A.8) or (A.11) for determining the heat rate $\Delta Q_{\mathrm{h,m}}$ and Eq. (A.33) for wall heat transfer rate ΔQ_{w}, compare Fig. 4.2 with measurements $y_{\mathrm{m}} = \mathrm{d}Q_{\mathrm{f,m}}$ (for each cylinder)[18]. The combustion phases and rate parameters are determined online using a combined state and parameter estimation (joint estimation approach) based on an extended Kalman filter (EKF).

The *second approach* in Sect. 4.5.2 represents a global estimation approach where the cylinder pressure is used directly for estimation, compare Fig. 4.2 with the measurement $y_{\mathrm{m}} = p_{\mathrm{cyl}}$ instead of the calculated $\mathrm{d}Q_{\mathrm{f,m}}$ (for each cylinder). Compared to the first approach, estimation of the combustion phases and rate parameters is embedded within a cylinder gas state estimation including cylinder gas state and heat transfer model, which are described in Sect. 4.2 and 4.3. This corresponds to an overall cylinder estimation in which the cylinder gas state, cylinder mass flows, and the combustion phases as well as the wall heat exchanges are simultaneously determined.

The real application at the engine test bench of these methods described in the following is shown in Sect. 5.2 in the context of the so-called model-based online combustion analysis.

4.5.1 Diesel combustion estimation

Fig. 4.31 shows the signal flow of the joint state and parameter estimator of the semi-physical diesel combustion model. The course of total burn rate $\mathrm{d}Q_{\mathrm{f,m}}$ and burning energy $Q_{\mathrm{f,m}}$ are used as measurements for the estimation. Burn rate results from the sum of the heat rate $\mathrm{d}Q_{\mathrm{h,m}}$, calculated based on measured cylinder gas pressure and volume by using Eq. (A.11), and the wall heat transfer rate $\mathrm{d}Q_{\mathrm{w}}$. Instead of the crank angle φ, in the following the variables are written as a function of the angular step k, as it is common in the discrete notation. In discrete-angle representation, the burn rate ($\mathrm{d}Q_{\mathrm{f,m}}/\mathrm{d}\varphi \approx \left(Q_{\mathrm{f,m}}(k) - Q_{\mathrm{f,m}}(k-1)\right)/\varphi_{\mathrm{s}} = \Delta Q_{\mathrm{f}}$) is given as

$$\Delta Q_{\mathrm{f,m}}(k) = \Delta Q_{\mathrm{h,m}}(k) + \Delta Q_{\mathrm{w}}(k). \tag{4.81}$$

The course of total cumulated burn energy $Q_{\mathrm{f,m}}(k)$ is obtained using Euler forward integration with crank angle based calculation step size φ_{s}

$$Q_{\mathrm{f,m}}(k) = Q_{\mathrm{f,m}}(k-1) + \varphi_{\mathrm{s}} \Delta Q_{\mathrm{f,m}}(k) = Q_{\mathrm{f,m}}(k-1) + \varphi_{\mathrm{s}} \left(\Delta Q_{\mathrm{h,m}}(k) + \Delta Q_{\mathrm{w}}(k)\right). \tag{4.82}$$

Wall heat losses are calculated by using an empirical heat transfer model such as proposed by Woschni (1970), Hohenberg (1980) or Bargende (1991), see previous Sect. 4.3. Calculations of heat rate and heat transfer are performed online using a self-developed indication system IndiSPACE, which allows crank angle synchronous processing of in-cylinder pressure signals by using a down-sampled crankshaft signal as measurement trigger signal (incremental speed sensor), see Appx. A.1.2 for more information.

Since the estimation of the combustion phases and their parameters is based on the calculated heat rate $\Delta Q_{\mathrm{h,m}}$ and the wall heat transfer rate ΔQ_{w}, the accuracy of the estimation depends on the

[18] Burn rate $\mathrm{d}Q_{\mathrm{f,m}}$ is not directly measured. However, in the context of Kalman filtering, *measurements* y_{m} are variables used within the correction step (*measurement update*)

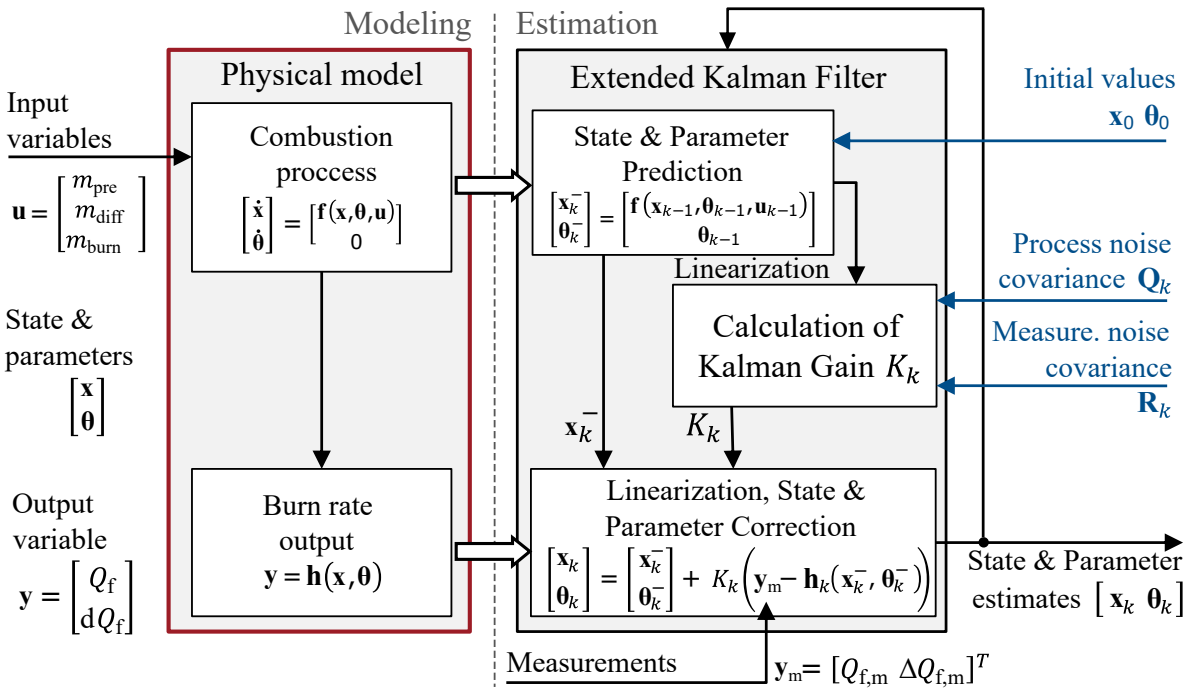

Figure 4.31: Structure and signal flow of the joint estimation of combustion phases and their rate parameters: State variables $\mathbf{x}$ are defined by Eq. (4.85) and parameters $\boldsymbol{\theta}$ by Eq. (4.88), burn rate $Q_{\text{f,m}}$ and burn release $\Delta Q_{\text{f,m}}$ determined from cylinder pressure signals are used as measurements $\mathbf{y}_{\text{m}}$

quality and reliability of these variables. Especially for the online application of this approach, appropriate precautions, such as pressure signal filtering and zero-line correction of the heat rate $\Delta Q_{\text{h,m}}$, must consequently be taken to ensure sufficient quality of the estimation results at all times during operation.

When calculating the heating rate, the signal quality of the combustion chamber pressure signal is very important. Due to the measurement principle of the pressure sensors the relative in-cylinder pressure is only measured. Thus, either the pressure change $\mathrm{d}p_{\text{cyl}}/\mathrm{d}\varphi$ has to be used as reference variable and a method for pegging the pressure measurement value needs to be applied, see for offset correction methods e.g. Beidl (2011b), Klein et al. (2007) or Zydek et al. (2016). In general, the measured in-cylinder pressure signals are very noisy and must consequently be reduced to a minimum with the aid of signal filters. Special care must be taken to ensure that the useful signal is not distorted too much by the filtering. Furthermore, used pressure sensor is designed for the high pressure range (Kistler 2003), the measuring accuracy of the pressure sensors is assumed to be better during compression and combustion while the accuracy is more error-prone during the gas exchange phase, especially due to the installation position close to the cylinder valves, see Fig. 4.7 in Sect. 4.2.2. Cylinder pressure filtering and offset correction is typically performed in the context of cylinder pressure analysis described in Appx. A.1.2.

To improve the estimation, the ignition signal σ_{ign} can be introduced as an additional model output variable. The ignition signal σ_{ign} is calculated using Eq. (4.62). This allows a faster adjustment of

the rate parameters r_{gf} and r_{mix} of the mixture formation at the very beginning of the estimation process, so that the modeled ignition matches the measured ignition signal $\sigma_{\mathrm{ign,m}}$ before the rate parameters of the combustion phase are adjusted.

Normally, the ignition event is determined as the location of the 5%-fraction of total released heat $\varphi_{\mathrm{Q5\%}}$. The location of the ignition is defined by threshold checking of the $5\%Q_{\mathrm{h,total}}$-limit ($\varphi_{\mathrm{soc}} = \varphi_{\mathrm{Q5\%}}$). However, this method is unable to cope with the unavoidable signal noises caused by the cylinder pressure sensors. By using the location of 5%-mass fraction burned leads to rather late SOCs. Additionally, the detection of multiple injections and ignitions remains not possible. For this reason an alternative method is described in Weber (2019b), which applies the threshold checking method on the recursively calculated estimate of the correlation function between the set of multiple time-shifted injection rate signals and the heat rate (index m for measured)

$$\sigma_{\mathrm{ign,m}}(\varphi) = \begin{cases} 0, & \text{for } \varphi < \varphi_{\mathrm{soc}}, \\ 1, & \text{for } \varphi \geq \varphi_{\mathrm{soc}}. \end{cases} \tag{4.83}$$

Using the correlation function instead of the heat release, allows to cope with the signal noise and is able to detect reliably actual start of combustion. Even the start of combustion of minor injection quantities (i.e. of pilot-injections) can be detected. Such small injection quantities would normally lead to heat releases below the 5%−limit of the total amount. For more detailed information see the corresponding the technical reports, Weber (2019a) and Weber (2019b).

The model output must match with the reference values from measurements. The "measurement" for the estimation is then given as follows (index m for measured)

$$\mathbf{y}_{\mathrm{m}}(k) = \begin{bmatrix} \sigma_{\mathrm{ign,m}}(k) & Q_{\mathrm{f,m}}(k) & \Delta Q_{\mathrm{f,m}}(k) \end{bmatrix}^{\mathrm{T}}. \tag{4.84}$$

State and parameter estimation model

The formulation of the state and parameter space model is done according to the modeling assumptions and definitions of the previous section 4.4. The relevant state variables are summarized in the state vector, which is composed of the variables of mixture mass, fuel masses, and burning energies and rates of the combustion phases

$$\mathbf{x}_{\mathrm{r}} = \begin{bmatrix} m_{\mathrm{gf}} & m_{\mathrm{mix}} & m_{\mathrm{pre}} & m_{\mathrm{diff}} & m_{\mathrm{burn}} & Q_{\mathrm{pre}} & \Delta Q_{\mathrm{pre}} & \dots & Q_{\mathrm{burn}} & \Delta Q_{\mathrm{burn}} \end{bmatrix}^{\mathrm{T}} \tag{4.85}$$

By discretization of the differential equations of the mixture formation and the combustion model with respect to crank angle, a discrete-angle difference equation system is obtained. The state space representation of the overall combustion model is written as

$$\begin{aligned} \mathbf{x}_{\mathrm{r}}(k) &= \mathbf{f}_{\mathrm{r}}\left(\mathbf{x}_{\mathrm{r}}(k-1), \boldsymbol{\theta}_{\mathrm{r}}(k-1), \mathbf{u}(k-1)\right), \\ \mathbf{y}_{\mathrm{r}}(k) &= \mathbf{h}_{\mathrm{r}}\left(\mathbf{x}_{\mathrm{r}}(k)\right) \end{aligned} \tag{4.86}$$

Discretization of the continuous parameter model in Eq. (4.76) leads to following crank angle discrete parameter model

$$\boldsymbol{\theta}_{\mathrm{r}}(k) = \boldsymbol{\theta}_{\mathrm{r}}(k-1) + \mathbf{w}_{\mathrm{r}}(k-1) \tag{4.87}$$

with additive random process variable $\mathbf{w}_\mathrm{r}$ representing uncorrelated white process noise. The parameter vector $\boldsymbol{\theta}_\mathrm{r}$ is composed of the rate parameters r_gf, r_mix, r_pre, r_diff, r_burn only

$$\boldsymbol{\theta}_\mathrm{r} = \begin{bmatrix} r_\mathrm{gf} & r_\mathrm{mix} & r_\mathrm{pre} & r_\mathrm{diff} & r_\mathrm{burn} \end{bmatrix}^\mathrm{T} \tag{4.88}$$

This model corresponds to an first order Markovian Process with white noise as disturbances w.

$$\mathbf{w}_\mathrm{r} = \begin{bmatrix} w_{r_\mathrm{gf}} & w_{r_\mathrm{mix}} & w_{r_\mathrm{pre}} & w_{r_\mathrm{diff}} & w_{r_\mathrm{pre}} \end{bmatrix}^\mathrm{T} \tag{4.89}$$

As it can be seen in Eq. (4.87), parameters stay constant If the corresponding parameter process noise variables w_i are set to zero. Consequently, adaptation of the parameters is enabled by modeling the parameter noise w_i. To accelerate estimation process and improve its convergence, an adequate choice for initial values for the state variables $\mathbf{x}_0$ must be made.

To reduce the complexity of the estimation of rate parameter, the combustion efficiency η is determined outside the estimation algorithm by calculating the ratio between the total released burning energy and the sum of fuel mass involved in the combustion process after the end of combustion

$$\eta = \frac{Q_\mathrm{f,m}}{H_\mathrm{l} m_\mathrm{gf}} = \frac{Q_\mathrm{f,pre} + Q_\mathrm{f,diff} + Q_\mathrm{f,burn}}{H_\mathrm{l}(m_\mathrm{pre} + m_\mathrm{diff} + m_\mathrm{burn})} \tag{4.90}$$

For the sake of simplicity, the efficiency parameters η_pre, η_diff and η_burn of each combustion phase ($Q_{\mathrm{f},i}$) are merged together to one single parameter describing the overall efficiency. [19]

$$\eta = \eta_\mathrm{pre}\eta_\mathrm{diff}\eta_\mathrm{burn} \tag{4.91}$$

This parameter η is used during estimation to account for uncertainties in the amount of injected fuel ($Q_\mathrm{f,meas} = \eta H_\mathrm{l} m_\mathrm{inj}$). To accelerate the estimation process and improve its convergence, an adequate choice for initial values for the state variables $\mathbf{x}_0$ and the parameters $\boldsymbol{\theta}_0$ must be made.

Joint state and parameter estimation

By merging all model equation together into one state space representation, a discrete-angle linear state space model of n-th order ($n = n_x + n_\theta$) is obtained, which is used for combustion state and parameter estimation.

$$\begin{aligned} \begin{bmatrix} \mathbf{x}_\mathrm{r}(k) \\ \boldsymbol{\theta}_\mathrm{r}(k) \end{bmatrix} &= \begin{bmatrix} \mathbf{f}\big(\mathbf{x}_\mathrm{r}(k-1), \boldsymbol{\theta}_\mathrm{r}(k-1), \mathbf{u}(k-1)\big) \\ \mathbf{I} \cdot \boldsymbol{\theta}_\mathrm{r}(k-1) \end{bmatrix} + \begin{bmatrix} \mathbf{w}_{\mathrm{r,x}}(k) \\ \mathbf{w}_{\mathrm{r},\theta}(k) \end{bmatrix}, \\ \mathbf{y}_\mathrm{r}(k) &= \mathbf{h}_\mathrm{r}\big(\mathbf{x}_\mathrm{r}(k)\big) + \mathbf{v}(k), \end{aligned} \tag{4.92}$$

where $\mathbf{w}_{\mathrm{r,x}}$ is the process state noise, $\mathbf{w}_{\mathrm{r},\theta}$ the parameter noise and $\mathbf{v}$ the measurement noise affecting the joint state vector or model output, respectively. EKF algorithm is here applied for joint estimation (Sect. 2.3.2). The structure of this joint estimation approach is shown in Fig. 4.31.

[19] fuel conversion efficiency η is typically $> 95\%$

Alternatively, an dual estimation approach could also be used for this estimation problem, see Sect. 2.3.3. The estimation error to be minimized is described by the equation

$$\begin{aligned}\mathbf{e}_{\mathrm{Q_f}}(k) &= \mathbf{y}_{\mathrm{m}}(k) - \hat{\mathbf{y}}_{\mathrm{r}}(k) \\ &= \begin{bmatrix} \sigma_{\mathrm{ign,m}}(k) \\ Q_{\mathrm{f,m}}(k) \\ \Delta Q_{\mathrm{f,m}}(k) \end{bmatrix} - \begin{bmatrix} \sigma_{\mathrm{ign}}(k) \\ Q_{\mathrm{f,pre}}(k) + Q_{\mathrm{f,diff}}(k) + Q_{\mathrm{f,burn}}(k) \\ \Delta Q_{\mathrm{f,pre}}(k) + \Delta Q_{\mathrm{f,diff}}(k) + \Delta Q_{\mathrm{f,burn}}(k) \end{bmatrix}.\end{aligned} \tag{4.93}$$

Since the states $\mathbf{x}_{\mathrm{r}}$ of semi-physical combustion model (combustion phases) are not directly observable based on the information determined from cylinder pressure signal, estimation of state variables is mainly dominated by the state prediction step and less by the state correction step of the Kalman filter algorithm. Their corresponding diagonal elements in the initial error covariance matrix $\mathbf{P}_{x0}$ as well as the process noise covariance matrix $\mathbf{Q}_{x0}$ - have to be set to very small value close to zero (non-zero values to avoid numerical issues). But this means also that the overall combustion model is mainly adapted via estimation of the parameters $\boldsymbol{\theta}_{\mathrm{r}}$ based on the measurements. Therefore, the process noise w_i of each i-th rate parameter must be modeled adequately in order to estimate the overall combustion model.

Since all parameters are assumed to be constant but unknown, each process noise variable w_i is modeled as a function of an assumed parameter error at the beginning of the estimation. This is done by using the square of standard deviation (variance), which represents a measure for the initial parameter error e_{θ_i}

$$w_i(k) = \varphi_s(e_{\theta_i})^2. \tag{4.94}$$

This results in a correction of the parameter corresponding to its assumed initial parameter error during the estimation. To ensure that the adaptation only takes place at a certain period of the combustion, the process noise is controlled via an activation function.

Additionally, the initial process noise model is updated from cycle to cycle by the final error covariance values $\mathbf{P}(k)$ of the previous cycle. The cycle-to-cycle update of the error covariance leads to cycle-to-cycle improvement of the estimation result. Based on the fact that the relevant influences on the parameter (engine operating point) do not change abruptly from cycle to cycle, this method also allows a more robust setting of covariances, which not reacts to sensitive to the cycle-to-cycle fluctuations.

However, the process noise model has to be able to react to changes of the engine operation point. This is done by modeling the initial standard deviation as a function of the relevant influence factor, i.e. the engine speed or the in-cylinder mass, etc.

$$\Delta\theta_i(k) = f(n_{\mathrm{eng}}, m_{\mathrm{cyl}}, ...) \tag{4.95}$$

The process noise models are used to build the diagonal matrix of the process covariance $\mathbf{Q}(k)$, which is used within the Kalman filter algorithm

$$\mathbf{Q}_r(k) = \begin{bmatrix} \Delta r_{\mathrm{gf}}^2 & \cdots & 0 \\ \vdots & \ddots & \vdots \\ 0 & \cdots & \Delta r_{\mathrm{burn}}^2 \end{bmatrix}. \tag{4.96}$$

The covariance matrix for the process noise is then given as

$$\mathbf{Q}(k) = \begin{bmatrix} \mathbf{Q}_x(k) & \mathbf{0} \\ \mathbf{0} & \mathbf{Q}_r(k) \end{bmatrix}. \tag{4.97}$$

Modeling of the measurement noise covariance matrix $\mathbf{R}(k)$ requires making assumption regarding the effect of the pressure signal noise on reconstructed burn rate and sum of burning energy used as measurement with Kalman filter. By means of these assumptions it is possible to influence on which signal the state and parameter estimator should rely more. One objective could be the exact matching of the characteristic course of increase and decrease of the burn rate. Another objective might be the exact matching of the total amount of released burning energy. The relation between the corresponding elements in the measurement covariance matrix $\mathbf{R}(k)$ determines the compromise between matching the shape or matching the total amount of burning energy. Therefore, the corresponding elements of the measurement covariance matrix supposed to be set in relation to each other. Besides this consideration, each element of the matrix of the measurement covariance $\mathbf{R}(k)$ is chosen according to an assumed standard deviation of the corresponding (constant) measurement noise v_i

$$\mathbf{R}(k) = \begin{bmatrix} v_{\text{ign}}^2 & 0 & 0 \\ 0 & v_{\text{Q}}^2 & 0 \\ 0 & 0 & v_{\text{dQ}}^2 \end{bmatrix} = \begin{bmatrix} r_{\text{ign}}^2 & 0 & 0 \\ 0 & (R_{\text{Q/dQ}} \cdot v_{\text{dQ}})^2 & 0 \\ 0 & 0 & v_{\text{dQ}}^2 \end{bmatrix} \tag{4.98}$$

The diagonal elements corresponding to burn rate and burning energy are set in relation to each other by introducing the ratio factor $R_{\text{Q/dQ}}$.

Fig. 4.32 shows the working principle and results of the combustion phases estimator based on the examples of two engine operating points. Thereby, real-time capability of this method has been verified on a prototyping real-time system, see Ch. 5. On this real-time system, the measurement data processing and the estimation computations are implemented and executed crank angle synchronously with the calculation step size φ_{s}. Estimation is performed cycle-by-cycle, but only during high pressure phase of engine's working cycle. At the beginning of each cycle, the estimation results from previous cycle are set as initial parameter values θ_0 for the next cycle. However, initial values of the state variables must reset to zero $\mathbf{x}_0 = \mathbf{0}$. For the sake of a better readability and interpretability, the characteristic angle constant $\tau_i = 1/r_i$ are shown in Fig. 4.32 instead of the actual estimated rate parameters r_i. Within the first engine working cycles, the ignition model is adjusted in order to match with the ignition signal by adapting the rate parameter of mixture formation r_{mix}. The adaptation of premixed angle constant is carried out faster than the adaptation of angle constants of diffusion combustion and burn-out. This can be manipulated by defining a higher initial process noise covariance value for the diagonal element in $\mathbf{Q}$ corresponding to the rate parameter of premixed combustion r_{pre}. In the examples in Fig. 4.32 c), premixed rate parameter r_{pre} is determined within 2 to 5 cycles. Estimation of r_{diff} and r_{burn} takes usually longer. Both parameters converge usually within 30 to 60 cycles, depending on the operating point and on how close the initial value is compared to its actual value.

The efficiency parameter η is determined after the first couple cycles based on the steady-state value at the end of combustion by using Eq. (4.91). In case of sufficient approximation by premixed

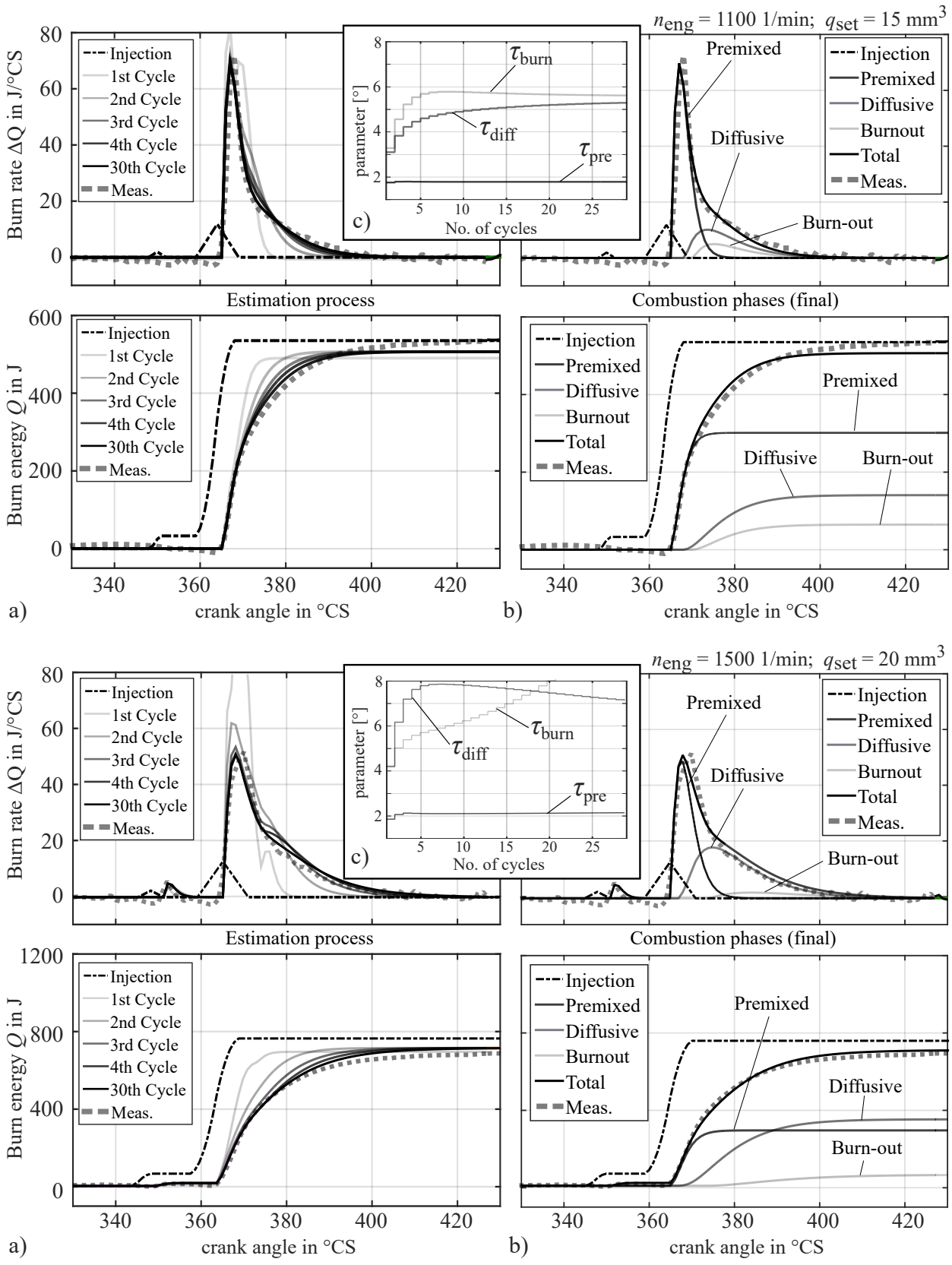

Figure 4.32: Simulation results for the estimation of diesel combustion phases for two engine operation points: a) estimation process for total burn rate ΔQ_f and released burn energy Q_f; b) estimation results for the combustion phases Q_i,ΔQ_i after 30th; c) courses of estimated parameters τ_i during cycle-to-cycle adaptation

and diffusion combustion model only, the EKF-estimator tends to reduce the influence of burn-out model by further increasing of the angle constant τ_{burn}, resulting into very small contribution burn-out (see Fig. 4.32, second operation point, bottom). Furthermore, termination conditions are be defined, on whose occurrence the estimation is switched off by nulling the corresponding values of process noise covariance.

4.5.2 Overall cylinder state and parameter estimation

In principle, the combustion phase can also be estimated directly on the basis of the measured relative cylinder gas pressure. For this purpose, the combustion model must be embedded in a one-zone cylinder model which is capable of reproducing the cylinder gas pressure. This cylinder model includes, in addition to the semi-physical combustion model, a model of the thermodynamic cylinder gas state, models for the incoming and outgoing cylinder mass flows, and a wall heat transfer model that describes the heat transfer between the cylinder inner walls and the cylinder gas, see Fig. 4.3 illustrating all relevant variables of an one-zone cylinder model. The model equations for the thermodynamic cylinder gas state and cylinder mass flows are described in Sect. 4.2. A model approach for heat transfer in internal combustion engines, based on a new semi-physical model approach for the heat transfer coefficient, is presented in Sect. 4.3.

The main advantage of this overall approach is that neither heat rate, wall heat losses nor cylinder gas state variables must be determined in advance for the estimation of the combustion phases and their rate parameters, compared to the method in Sect. 4.5.1. The calculation of the heat rate based on the measured cylinder pressure generally requires filtering of the measured pressure signal as well as offset correction to determine the absolute pressure. Furthermore, the empirical wall heat model which is required to reconstruct the burn rate does not have to be parameterized in advance either. Both filter settings and the offset correction method significantly affect the heat rate calculation. Also the identification of the parameters of the wall heat model requires extensive measurement over a wide engine operating range. Tuning all these parameters is necessary to obtain a sufficiently accurate calculation of the burn rate curve, which is eventually used as a reference variable for the estimation the semi-physical combustion model. All of this is omitted with this holistic approach. Instead, the holistic approach allows the estimation of the in-cylinder gas state, the engine mass flows, and the wall heat transfer together in connection with their parameters. Fig. 4.33 shows the signal flow scheme of the overall cylinder estimation.

The goal is to determine all relevant cylinder state variables and model parameters based on the measured cylinder pressure, as shown in Fig. 4.2. Since the measured cylinder pressure signal is affected by signal offset, only the change of cylinder gas pressure $\Delta p_{\text{cyl,m}}$ is used as a measurement for the estimation

$$\mathbf{y}_{\text{m}}(k) = \Delta p_{\text{cyl,m}}(k) = \frac{p_{\text{rel,m}}(k) - p_{\text{rel,m}}(k-1)}{\varphi_{\text{s}}}. \tag{4.99}$$

In addition, besides the engine speed n_{eng}, the injection rate $\mathrm{d}m_{\text{inj}}/\mathrm{d}\varphi$ and the engine cooling water temperature T_{h2o}, the gas states in the intake manifold and in the exhaust manifold are provided to

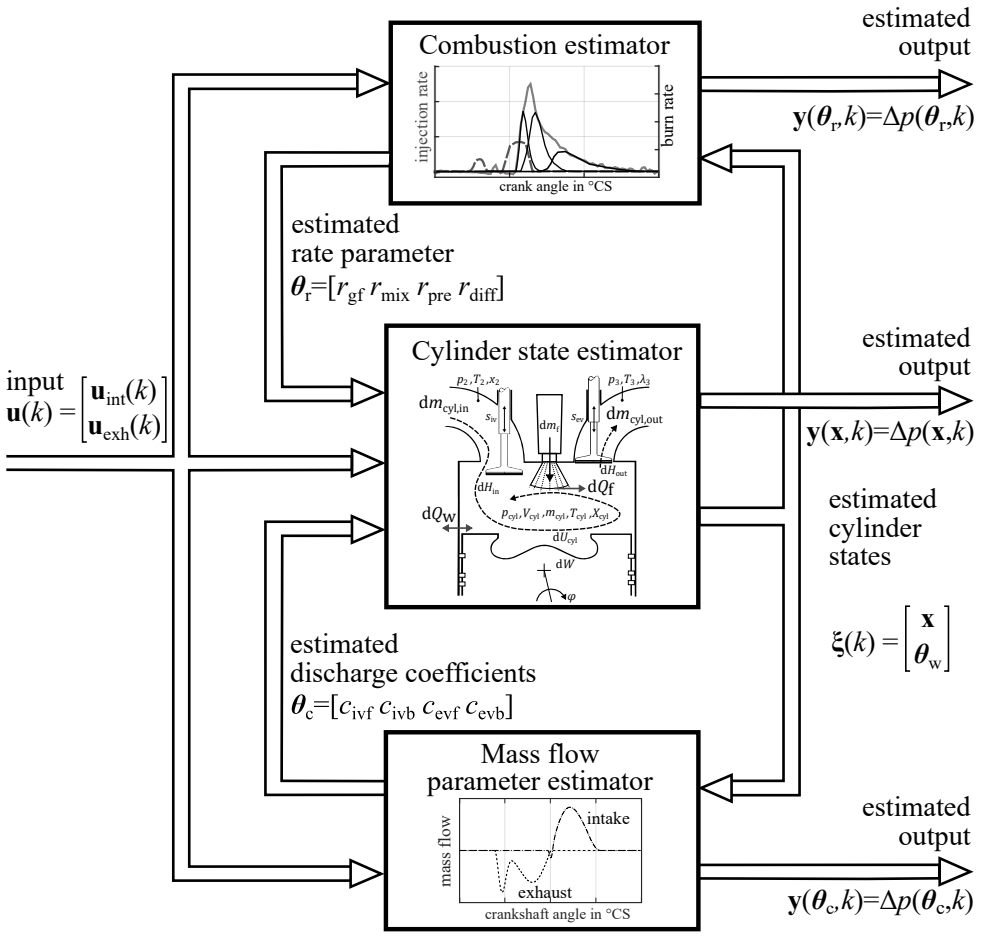

Figure 4.33: Signal flow of dual estimation scheme for overall cylinder estimation including cylinder gas state estimation and combustion estimation

the estimation algorithm

$$\begin{aligned}\mathbf{u}_{int}(k) &= \begin{bmatrix}p_{2i}(k) & T_{2i}(k) & X_{2i}(k)\end{bmatrix}^T\\ \mathbf{u}_{exh}(k) &= \begin{bmatrix}p_3(k) & T_3(k) & \lambda_3(k)\end{bmatrix}^T\end{aligned} \tag{4.100}$$

However, the exhaust gas temperature T_3 and the air-fuel ratio λ_3 only serve the purpose of verification and validation and are not necessary for the cylinder estimator considered here. Cylinder volume $V_{cyl}(k)$ is calculated as function of φ by using Eq. (A.53). Instead of the volume's derivative, the difference quotient $\Delta V_{cyl}(k)$ is used to describe the change of cylinder volume

$$\Delta V_{cyl}(k) = V_{cyl}(k) - V_{cyl}(k-1). \tag{4.101}$$

State and parameter estimation model

The pressure change as the model output is described by Eq. (4.8). Discretization of Eq. (4.8) results in the following model output equation

$$\begin{aligned}\Delta p_{\mathrm{cyl}}(k) = \frac{1}{V_{\mathrm{cyl}}(k)}\Big[&- \kappa p_{\mathrm{cyl}}(k)\Delta V_{\mathrm{cyl}}(k) + \kappa R T_{\mathrm{in}}\Delta m_{\mathrm{in}}(k) - \kappa R T_{\mathrm{cyl}}(k)\Delta m_{\mathrm{out}}(k) \\ &+ (\kappa - 1)\big(\Delta Q_{\mathrm{f}}(k) + \Delta Q_{\mathrm{w}}(k)\big)\Big].\end{aligned} \tag{4.102}$$

Although, the absolute pressure is not available as measurement, the signal curve of the pressure change contains information about the pressure increase caused by the combustion (last term within brackets of Eq. (4.102)) as well as the influence of the volume change caused by the piston movement (first term within brackets of Eq. (4.102)). During gas exchange phase, the pressure change is almost zero despite the volume change, since it is balanced by the incoming and outgoing valve mass flows (second and third term within brackets of Eq. (4.102)). This process behavior is exploited to estimate cylinder mass change caused by intake and exhaust valve mass flows.

Since the valve mass flows are modeled as a functions of the pressure difference between cylinder gas and intake/exhaust manifold, the absolute pressure level of the cylinder gas pressure can be determined within the estimation by forward integration of Eq. (4.102)

$$p_{\mathrm{cyl}}(k) = p_{\mathrm{cyl}}(k-1) + \varphi_{\mathrm{s}}\Delta p_{\mathrm{cyl}}(k) \tag{4.103}$$

The cylinder gas temperature is determined from cylinder pressure, mass and volume using the ideal gas law

$$T_{\mathrm{cyl}}(k) = \frac{p_{\mathrm{cyl}}(k)V_{\mathrm{cyl}}(k)}{m_{\mathrm{cyl}}(k)R}. \tag{4.104}$$

This relation is further used to replace $T_{\mathrm{cyl}}(k)$ in Eq. (4.102). The discrete-angle difference equation for the cylinder gas mass is obtained by discretization of mass balance equation (4.4).

$$\begin{aligned}m_{\mathrm{cyl}}(k) &= m_{\mathrm{cyl}}(k-1) + \varphi_{\mathrm{s}}\Delta m_{\mathrm{cyl}}(k) \\ &= m_{\mathrm{cyl}}(k-1) + \varphi_{\mathrm{s}}\left(\Delta m_{\mathrm{in}}(k) + \Delta m_{\mathrm{out}}(k) + \Delta m_{\mathrm{f}}(k)\right)\end{aligned} \tag{4.105}$$

The difference quotient of intake valve mass flow $\Delta m_{\mathrm{in}}(k)$ and exhaust valve mass flow Δm_{exh} are given by Eqs. (4.15) and (4.16), where the flow coefficients are the parameter to be estimated

$$\boldsymbol{\theta}_{\mathrm{c}}(k) = \begin{bmatrix} c_{\mathrm{ivf}}(k) & c_{\mathrm{ivb}}(k) & c_{\mathrm{evf}}(k) & c_{\mathrm{evb}}(k)\end{bmatrix}^{\mathrm{T}} \tag{4.106}$$

Using the mass flows, the air mass fraction $X_{\mathrm{cyl}}(k)$ of the cylinder gas can be further calculated by using discretized form of Eq. (4.14). With Eqs. (4.103), (4.104), (4.105) and discretized Eq. (4.14) the thermodynamic cylinder gas state is fully described.

The state and parameter estimation model of the burn rate ΔQ_{f} is the same as in Sect. 4.5.1. The heat transfer between cylinder wall and cylinder gas has a direct effect on the cylinder pressure change as well (last term within brackets of Eq. (4.102)). Modeled by Newton's law (4.19), the cylinder wall heat is transferred to the incoming gas during the intake phase, resulting in a reduction

of the cylinder charge (assuming $T_\mathrm{w} > T_\mathrm{2i}$). During the compression and combustion phase, the cylinder gas temperature increases significantly, so that the direction of the mean heat flow changes direction, resulting in wall heat losses. The heat transfer rate ΔQ_w is given in discrete notation as

$$\Delta Q_\mathrm{w}(k) = \frac{1}{\omega_\mathrm{eng}} \alpha_\mathrm{w}(k) A_\mathrm{w}(k) \left(T_\mathrm{cyl}(k) - T_\mathrm{w}\right) \tag{4.107}$$

whereby the heat transfer coefficient α_w is modeled by Eq. (4.26) proposed in Sect. 4.3.2 and the cylinder wall temperature T_w by Eq. (4.20).

$$\alpha_\mathrm{w}(k) = C \frac{p_\mathrm{cyl}(k)}{T_\mathrm{cyl}(k)} w_\mathrm{t}(k). \tag{4.108}$$

The heat transfer coefficient further relates the heat transfer rate to the other system states cylinder gas pressure $p_\mathrm{cyl}(k)$ and gas temperature $T_\mathrm{cyl}(k)$ (scaling constant $C = 10^3$). The mean gas velocity w_t describes the intensity of charge motion and therefore represents a system state. State equation for the average gas velocity w_t as measure for the turbulence, results through discretization of Eq. (4.34) and applying Euler forward integration rule

$$w_\mathrm{t}(k) = w_\mathrm{t}(k-1) + \varphi_\mathrm{s} \Delta w_\mathrm{t}(k) \tag{4.109}$$

with the average gas velocity change $\Delta w_\mathrm{t}(k)$

$$\begin{aligned} \Delta w_\mathrm{t}(k) = &- \frac{1}{3} w_\mathrm{t}(k) \frac{\Delta V_\mathrm{cyl}(k)}{V_\mathrm{cyl}(k)} - c_\mathrm{diss} \frac{w_\mathrm{t}(k)^2}{l_\mathrm{char}} + \frac{1}{2} \frac{c_\mathrm{int}}{l_\mathrm{char}(k)} \left(\frac{\Delta m_\mathrm{iv,f}(k)}{\rho_\mathrm{2i} A_\mathrm{iv,th}(k)} \right)^2 \\ &+ \frac{1}{2} \frac{c_\mathrm{inj}}{l_\mathrm{char}(k)} \left(\frac{\Delta m_\mathrm{inj}(k)}{\rho_\mathrm{f} A_\mathrm{inj,th}(k)} \right)^2 + \frac{1}{2} \frac{c_\mathrm{comb}}{l_\mathrm{char}(k)} \left(\frac{\Delta Q_\mathrm{f}(k)}{H_\mathrm{l} \rho_\mathrm{f} A_\mathrm{p}} \right)^2, \end{aligned} \tag{4.110}$$

considering the influences of volume change, inflowing intake mass flow and injection, as well as combustion turbulence on the average gas velocity w_t. The parameters of this model are summarized by the parameter vector $\boldsymbol{\theta}_\mathrm{w}$ defined as

$$\boldsymbol{\theta}_\mathrm{w} = \begin{bmatrix} c_\mathrm{diss} & c_\mathrm{int} & c_\mathrm{inj} & c_\mathrm{comb} \end{bmatrix}^\mathrm{T} \tag{4.111}$$

Combining Eqs. (4.107) to (4.109) allows eventually the calculation of wall heat transfer rate $\Delta Q_\mathrm{w}(k)$ over the whole operating cycle.

Dual state and parameter estimation

A CKF algorithm, Eqs. (2.42) to (2.53), is used to estimate the states and parameters. Compared to the EKF, the CKF algorithm provides a more robust estimation behavior in strongly nonlinear systems, see Sect. 2.3.2. Due to the introduction of additional system states and the model parameters to be estimated, the system order increases significantly. High-dimensional matrix operations lead to an excessive increase of the computational effort and should consequently be avoided in real-time applications. For this reason, both a joint and a dual estimation approach is used for the combined state and parameter estimation, where the states and parameters of individual model parts

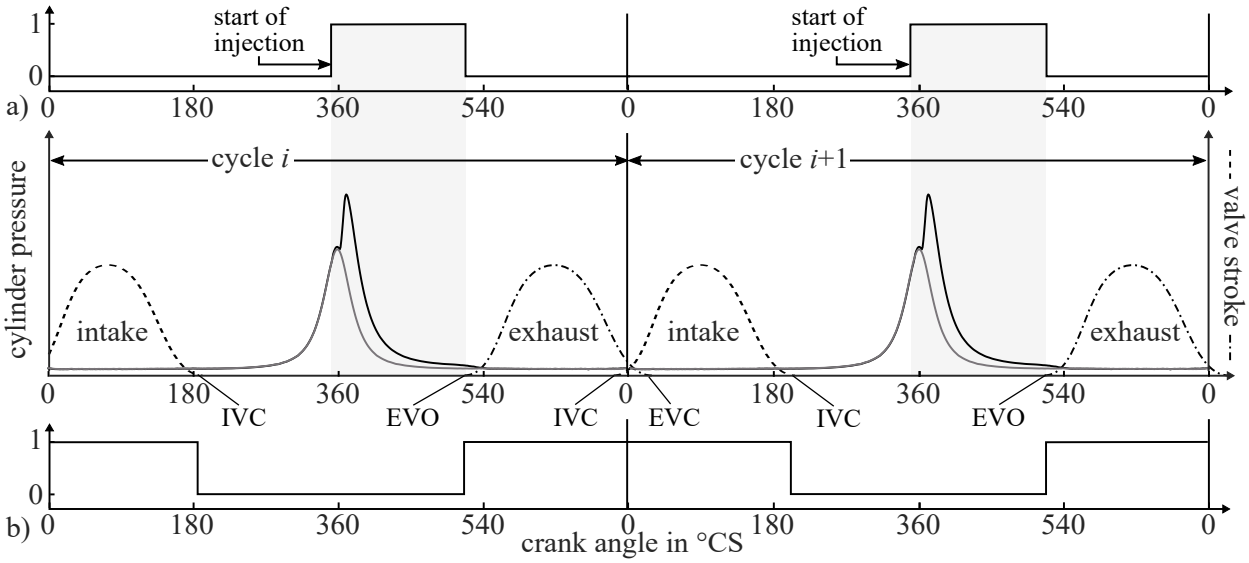

Figure 4.34: Task handling of overall cylinder estimation: activation of a) combustion phase estimator and b) mass flow parameter estimator

are estimated separately from each other. This decreases the system order of individual estimators, resulting in less computational effort.

In addition, it is possible to take advantage of the fact that the calculation of certain model components as well as estimators only need to be executed at certain phases of engine's working cycle. For example, estimation of the combustion phases can be switched off during the gas exchange phase, whereas the estimation of the parameters of the cylinder mass flow models is inactive during the high-pressure phase. The total burn rate $\Delta Q_{\mathrm{f}}(k)$, that is required to calculate the pressure change in Eq. (4.102), is estimated via a separate combustion estimator based on the joint estimation approach as described in the previous Sect. 4.5.1. In return, the state variables required for the estimation of combustion phases and rate parameters, such as the cylinder gas mass m or the air mass fraction X, are provided by the cylinder state estimator.

The task handling of cylinder estimation is shown in Fig. 4.34. The active and inactive phases of combustion phase and mass flow parameter estimators are indicated by means of their activation signals in in Fig. 4.34 a) and b). While combustion estimation is initialized by the start of injection (SOI) and runs until exhaust valve opens, the mass flow estimator is activated during both active intake and active exhaust phase.

For the estimation of the cylinder gas state a joint estimation approach is chosen. The system state $\mathbf{x}$ includes the gas state variables: cylinder gas pressure p, pressure change Δp, gas mass m and the mean gas flow velocity w_{t} of cylinder charge [20]

$$\mathbf{x} = \begin{bmatrix} p & \Delta p & m & w_{\mathrm{t}} \end{bmatrix}^{\mathrm{T}}. \tag{4.112}$$

The cylinder pressure, pressure change, and cylinder mass are described by Eqs. (4.102),(4.103) and (4.105), while the mean gas velocity is given by inserting (4.110) into (4.109). The parameter of

[20] For the sake of simplicity the index cyl of in-cylinder gas state variables p_{cyl}, T_{cyl}, etc. is neglected

wall heat transfer model $\boldsymbol{\theta}_{\mathrm{w}}$ are modeled as first-order Markovian processes according to Eq. (2.55). Since $\boldsymbol{\theta}_{\mathrm{w}}$ must be estimated over the entire working cycle, the system state vector $\mathbf{x}$ and $\boldsymbol{\theta}_{\mathrm{w}}$ are merged together in the joint state, leading to following state space estimation model

$$\begin{aligned}\begin{bmatrix}\mathbf{x}(k)\\ \boldsymbol{\theta}_{\mathrm{w}}(k)\end{bmatrix} &= \begin{bmatrix}\mathbf{f}\big(\mathbf{x}(k-1),\boldsymbol{\theta}_{\mathrm{w}}(k-1),\mathbf{u}(k-1)\big)\\ \mathbf{I}\cdot\boldsymbol{\theta}_{\mathrm{w}}(k-1)\end{bmatrix} + \begin{bmatrix}\mathbf{w}_{\mathrm{x}}(k)\\ \mathbf{w}_{\mathrm{w}}(k)\end{bmatrix},\\ \mathbf{y}_{\mathrm{x}}(k) &= \mathbf{h}_{\mathrm{x}}\big(\mathbf{x}(k)\big) + \mathbf{v}_{\mathrm{x}}(k)\end{aligned} \tag{4.113}$$

Similar to the combustion parameters, the flow coefficients $\boldsymbol{\theta}_{\mathrm{c}}(k)$ in Eq. (4.106) are only estimated during the gas exchange phase, the estimation of $\boldsymbol{\theta}_{\mathrm{c}}$ is therefore excluded from the cylinder state estimation scheme and addressed by a separate parameter estimator, see Fig. 4.33. Within the parameter estimator, flow coefficient estimates are modeled as constants and independent of other inputs or state variables

$$\begin{aligned}\boldsymbol{\theta}_{\mathrm{c}}(k) &= \boldsymbol{\theta}_{\mathrm{c}}(k-1) + \mathbf{w}_{\mathrm{c}}(k-1),\\ \mathbf{y}_{\mathrm{c}}(k) &= \mathbf{j}\left(\boldsymbol{\theta}_{\mathrm{c}}(k),\mathbf{x}(k)\right) + \mathbf{v}_{\mathrm{c}}(k)\end{aligned} \tag{4.114}$$

The estimated gas state variables $\mathbf{x}(k)$ from the gas state estimation model (4.113) serves as inputs of the mass flow parameter estimator and are used to calculate the model output.

In principle, in the dual estimation approach, different formulations for the estimation error $e = y_{\mathrm{m}} - y$ can be chosen for each estimator. For the joint estimation of the joint state $[\mathbf{x}, \boldsymbol{\theta}_{\mathrm{w}}]$, the estimation error equation is given by the difference between measured pressure change $\Delta p_{\mathrm{m}}(k)$ and modeled value $\Delta p(k)$

$$e_{\mathrm{x}}(k) = y_{\mathrm{m}}(k) - y(\mathbf{x},k) = \Delta p_{\mathrm{m}}(k) - \Delta\hat{p}(\mathbf{x},k), \tag{4.115}$$

For estimation of the coefficients $\boldsymbol{\theta}_{\mathrm{c}}$ of mass flow models, two different estimation error formulation can be applied. [21] The first approach is to use the error between measured and estimated pressure change as given in Eq. (4.115), whereby the modeled pressure change Δp is calculated based on the parameter estimates after the prediction step of the CKF-algorithm, see Sect. 2.3.2.

$$e_{\mathrm{c}}(k) = y_{\mathrm{m}}(k) - y(\boldsymbol{\theta}_{\mathrm{c}},k) = \Delta p_{\mathrm{m}}(k) - \Delta\hat{p}(\boldsymbol{\theta}_{\mathrm{c}},k). \tag{4.116}$$

The second approach is to use a calculated absolute pressure $\hat{p}_{\mathrm{m}}$ as "measurement". This is determined by forward integration of measured pressure change $\Delta p_{\mathrm{m}}(k)$ using the estimated pressure $p(k-1)$ from previous estimation step. The estimation error equation is then given by

$$e_{\mathrm{c}}(k) = [p(k-1) + \varphi_{\mathrm{s}} y_{\mathrm{m}}(k)] - y(\boldsymbol{\theta}_{\mathrm{c}},k) = \hat{p}_{\mathrm{m}} - \hat{p}(\boldsymbol{\theta}_{\mathrm{c}},k). \tag{4.117}$$

For the estimation of the combustion phases and their rate parameters it is reasonable to exclude the component of the pressure change that is caused by the volume change instead of using the raw

[21] Additionally, the modeled output can also be used for parameter estimation instead of the actual measurement. This way, the parameter estimation is completely relying on the result of the state estimation. It must be noted that large estimation errors are more likely to lead to instabilities (e.g. large error in the initial state at the beginning of the estimation).

measurement of cylinder pressure change $y_\mathrm{m} = \Delta p_\mathrm{m}$. For this, the Eq. (A.8) is used for heat rate calculation.

$$\begin{aligned}\Delta Q_\mathrm{h,m} &= \frac{c_\mathrm{v}}{R}\frac{V(k)+V(k-1)}{2}y_\mathrm{m} + \left(1+\frac{c_\mathrm{v}}{R}\right)\left[\hat{p}(k-1)+\varphi_\mathrm{s}y_\mathrm{m}(k)\right]\Delta V(k)\\ &= \frac{1}{\kappa-1}\frac{V(k)+V(k-1)}{2}y_\mathrm{m} + \frac{\kappa}{\kappa-1}p_\mathrm{m}(k)\Delta V(k) = \Delta Q_\mathrm{h,m}\end{aligned} \tag{4.118}$$

Similar to the combustion phase estimator in Sect. 4.5.1, the ignition signal σ_ign detected from measured pressure signal curve. However, compared to Eq. (4.84), the cumulative heat release $Q_\mathrm{h,m}$ is not used as further "measurements" for estimation, because the calculated ΔQ_m is a function of estimated pressure $\hat{p}(k-1)$ and larger state estimation errors in $\mathbf{x}$ would lead to large errors in cumulated heat energy $Q_\mathrm{m}$which significantly weakens the robustness of the combustion phase estimator. The "measurement" for the combustion phase estimation results then in

$$\mathbf{y}_\mathrm{m} = \begin{bmatrix}\sigma_\mathrm{ign}(k)\\ \Delta Q_\mathrm{h,m}(k)\end{bmatrix} \tag{4.119}$$

Since ΔQ_m represents the "measured" heat rate $\Delta Q_\mathrm{h,m}$, this approach is corresponding to a heat rate estimation. Correspondingly, the heat rate is used as model output instead of the pressure change, given as

$$\begin{aligned}\hat{\mathbf{y}}_\mathrm{r} = \begin{bmatrix}\hat{\sigma}_\mathrm{ign}(k)\\ \Delta\hat{Q}_\mathrm{h}(k)\end{bmatrix} &= \begin{bmatrix}\hat{\sigma}_\mathrm{ign}(k)\\ \Delta\hat{Q}_\mathrm{f}(k)+\Delta\hat{Q}_\mathrm{w}(k)\end{bmatrix}\\ &= \begin{bmatrix}\hat{\sigma}_\mathrm{ign}(k)\\ \Delta\hat{Q}_\mathrm{f}(\mathbf{x}_\mathrm{r},\boldsymbol{\theta}_\mathrm{r},k)+\Delta\hat{Q}_\mathrm{w}(\mathbf{x},\boldsymbol{\theta}_\mathrm{w},k)\end{bmatrix},\end{aligned} \tag{4.120}$$

where the total burn rate $\Delta\hat{Q}_\mathrm{f}$ is determined based on the predicted combustion phases $\hat{\mathbf{x}}_\mathrm{r}$ and rate parameters $\hat{\boldsymbol{\theta}}_\mathrm{r}$ and the wall heat transfer $\Delta\hat{Q}_\mathrm{w}$ is determined based on the gas state variables $\hat{\mathbf{x}}$ and the heat transfer parameters $\hat{\boldsymbol{\theta}}_\mathrm{w}$. The estimation error equation for the combustion phase estimator then becomes

$$\begin{aligned}e_{\mathrm{Q_h}}(k) &= y_\mathrm{m}(k) - \mathbf{y}(\hat{\mathbf{x}}_\mathrm{r},\hat{\boldsymbol{\theta}}_\mathrm{r},\hat{\mathbf{x}},\boldsymbol{\theta}_\mathrm{c},k)\\ &= \begin{bmatrix}\sigma_\mathrm{ign}(k)\\ \Delta Q_\mathrm{h,m}(k)\end{bmatrix} - \begin{bmatrix}\hat{\sigma}_\mathrm{ign}(k)\\ \Delta\hat{Q}_\mathrm{f}(\mathbf{x}_\mathrm{r},\boldsymbol{\theta}_\mathrm{r},k)+\Delta\hat{Q}_\mathrm{w}(\mathbf{x},\boldsymbol{\theta}_\mathrm{w},k)\end{bmatrix}.\end{aligned} \tag{4.121}$$

The modeling of the process noise and measurement noise covariance matrices follows generally the same procedures as for the combustion phase estimator. However, due to the different estimation error formulations to be used, different measurement noise covariance matrices $\mathbf{R}$ must be modeled as well. Furthermore, it is recommended to dimension the estimation variables and parameters in all estimation models to a similar value range, e.g. Δp in MPa, m in g and T in 10^3 K.

For the joint estimation of $\mathbf{x}$ and $\boldsymbol{\theta}_w$, the measurement noise covariance is chosen according to the signal noise of the measured cylinder pressure. Measurements of cylinder pressure show that the noise amplitude is significantly larger in the gas exchange phase than during the compression and

combustion phases. Refer to Sect. 4.2.2 for more details and see Fig. 4.7. During the high pressure phase, it can be assumed that the signal integrity of the pressure measurement is better, since the pressure values lie in the mid-range of the pressure sensor, where a better signal-to-noise ratio can be observed. Consequently, the measurement noise covariance $R(k)$ is switched to a multiple of the high pressure phase value for the gas exchange phase ($C > 2$)

$$R(k) = \begin{cases} R_{\mathrm{hp}} & \text{, for } \varphi_{\mathrm{ivc}} < \varphi < \varphi_{\mathrm{evo}} \text{ (high-pressure phase),} \\ CR_{\mathrm{hp}} & \text{, for } \varphi_{\mathrm{ivc}} \leq \varphi \geq \varphi_{\mathrm{evo}} \text{ (low-pressure phase).} \end{cases} \tag{4.122}$$

Since the mass flow estimation is performed only during the gas exchange phase, the same measurement noise covariance can be used. The measurement noise covariances for the combustion phase estimator is chosen according to the noise amplitude observable in the calculated ΔQ_{m} signal; compare to Eq. (4.98).

Fig. 4.35 shows simulation results of overall cylinder gas state estimator, which comprises the estimation of the pressure change Δp, the absolute in-cylinder gas pressure p, the temperature T, and the mass m inside the cylinder as well as the cylinder mass flows entering and exiting the cylinder through intake and exhaust valves. Only the estimation results of the first, the second, the fifth and final (30^{th}) working cycle are depicted, since the estimated courses converge after 5-10 working cycles (for a constant working point) and consequently change only marginally. In the two top graphs of Fig. 4.35, the courses of the measurements of absolute pressure p_{m} and pressure change Δp_{m} are compared with the pressure $\hat{p}$ and pressure change $\Delta \hat{p}$ estimated by the cylinder gas state estimator. The measured absolute pressure curve shown is taken from a cylinder pressure analysis and is therefore filtered and offset-corrected using the zero-line method, see Appx.A.1.2.

During the gas exchange, it can be seen from the estimated pressure curves that the cylinder estimator notably suppresses the noise as well as corrects the pressure level. This is particularly noticeable in the exhaust phase, where the cylinder pressure measurement lies below the mean gas pressure p_3 in the exhaust manifold. However, this is not physically plausible. A pressure difference $p_{\mathrm{cyl}} - p_3 < 0$ during the exhaust phase would lead to a mass flow in the wrong direction. The cylinder gas state estimator, on the other hand, corrects the pressure curve on the basis of the underlying physical state estimation model in such a way that it lies in the physically plausible value range above the pressure in the exhaust manifold. During the intake phase, the cylinder pressure is marginally corrected as well. The degree of the correction in the particular engine strokes is determined by the modeled course of the measurement noise covariance.

In the two lower graph in Fig. 4.35, the estimated curves of cylinder gas temperature T and mass m are compared with the reference curves denoted as “measurements” since they are determined from measurements. In addition, the final estimated intake and exhaust mass flows through the valves are depicted. The reference cylinder gas mass is determined from stationary measurements using the measurements from the HFM sensor and the lambda probe. It is plotted as constant line over the entire operating cycle (dashed line). However, its value is only valid for high-pressure phase (closed system). Only the injected fuel mass is added in the process of injection. Reference course for the gas temperature is determined based on cylinder pressure measurement, reference value of

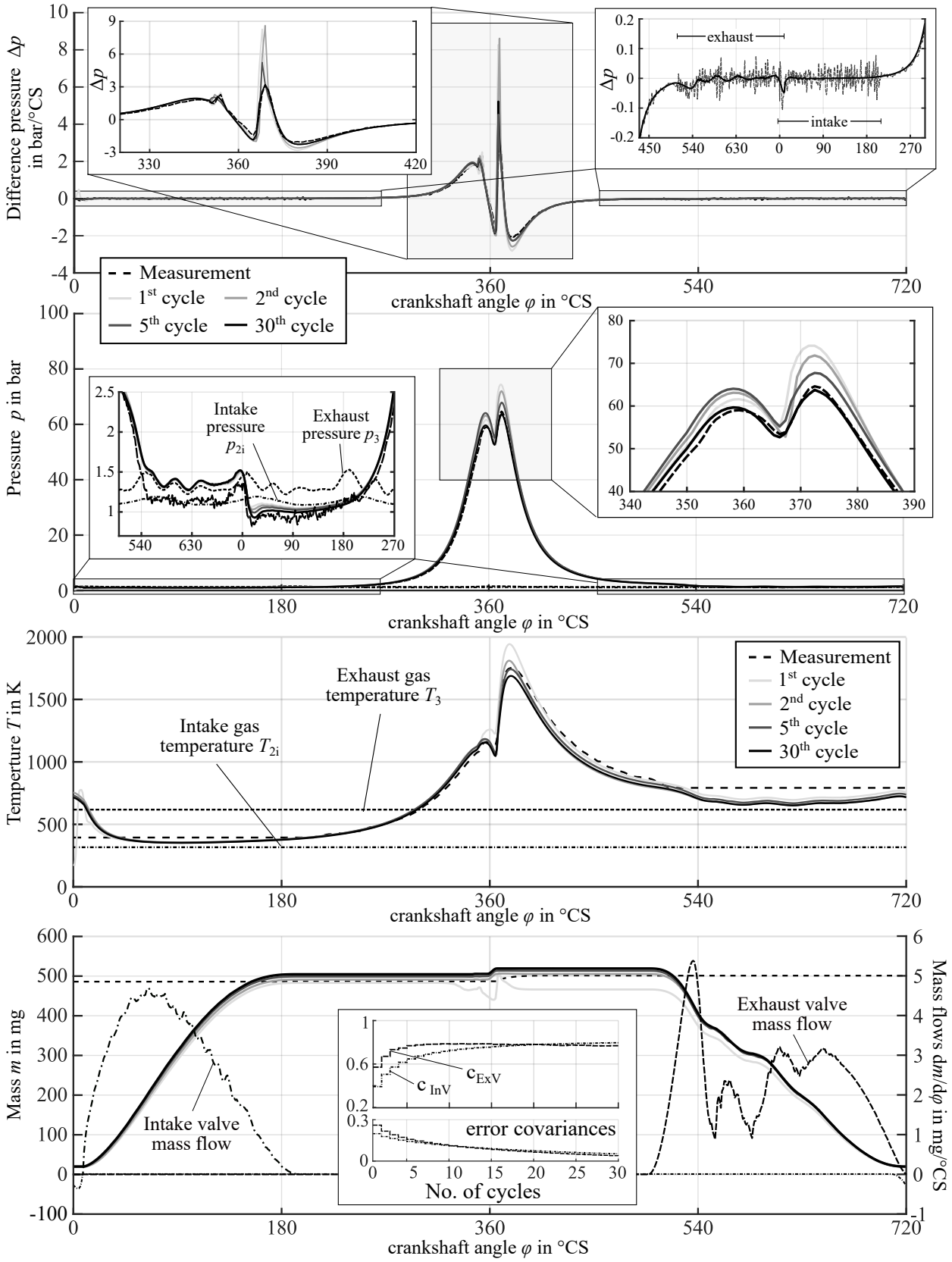

Figure 4.35: Simulation results of the cylinder estimation over 30 working cycles ($n_{\mathrm{eng}} = 1400$ 1/min, $q_{\mathrm{inj}} = 16$ mm^3): Comparison of estimated cylinder gas states with reference courses determined from measurements

cylinder gas mass and cylinder volume using ideal gas law (A.17). Consequently, the temperature "measurement" is also only valid for the high-pressure phase.

The cylinder state estimator is able to estimate the course of cylinder gas temperature and gas mass over the entire working cycle. By comparison with the measured gas temperatures in the intake manifold T_{2i} and exhaust manifold T_3, the course of the cylinder gas temperature during the gas exchange phase can be plausibilized. By estimating the parameters $\boldsymbol{\theta}_c$ and $\boldsymbol{\theta}_c$ and correcting the cylinder gas pressure, the cylinder gas temperature and mass adapt to the corresponding reference curves (high-pressure phase). In the bottom graph of Fig. 4.35, the cycle-to-cycle change of the estimates of flow coefficients $\boldsymbol{\theta}_c = [c_{iv}, c_{ev}]$ are plotted over the duration of the estimation (number of cycles). With each cycle, the error covariance of the parameter estimates decreases towards zero, causing the parameters to converge to a fixed value.

Fig. 4.36 shows further simulation results for the same engine operating point as shown in Fig. 4.35. At the two top graphs, the final estimation results of estimated burn rates and burn energy are shown. The cycle-to-cycle behavior of the combustion phase estimator is not depicted here for the sake of better readability. The procedure of estimation corresponds to the behavior described in Sect. 4.5.1. In addition, the components of premixed combustion $\Delta Q_{f,pre}$ and diffusive combustion ΔQ_f are plotted, which contribute to the total burn rate ΔQ_f and burn energy Q_f, respectively. The modeling of the burnout $\Delta Q_{f,burn}$ was omitted in this simulation. Along with the combustion phase, the courses of the corresponding rate parameters over the first 30 working cycles of the estimation are depicted in a separate graph. For reference, the "measured" heat rate $\Delta Q_{h,m}$ is also plotted, since $\Delta Q_{h,m}$ is used for estimation, compare to Eq. (4.121). Compared to the burn rate ΔQ_f, the heat rate $\Delta Q_{h,m}$ is reduced by the wall heat rate ΔQ_w.

In the middle graphs of Fig. 4.36 the estimated courses of the heat rate, the wall heat transfer rate, and their corresponding courses of the released heat energy are shown. In both graphs, the estimated courses are compared with the corresponding reference courses $\Delta Q_{h,m}$ and $\Delta Q_{w,m}$ denoted as "measurements" (dashed curves). The heat rate $\Delta Q_{h,m}$ is calculated from the measured cylinder pressure, whereas the wall heat transfer rate $\Delta Q_{w,m}$ is determined by a phenomenological model approach, see Appx. A.1.2 and A.2.3. By estimating the rate parameters $r_{pre} = 1/\tau_{pre}$ and $r_{diff} = 1/\tau_{diff}$ (angular constant τ increase, thus rates decrease), the estimated heat rate ΔQ_h and wall heat transfer rate ΔQ_w adjust to the reference curves of "measurements".

The bottom two graphs of Fig. 4.36 show the estimate of the average gas velocity w_t (charge motion) over the entire working cycle and the cycle-to-cycle change of the estimated parameter c_{diss}, that parameterized the dissipation term in Eq. (4.110) that eventually causes the change in the estimated average gas velocity w_t. Dissipation term in Eq. (4.110) determines the decay of average gas velocity w_t in the cylinder. Therefore, parameter c_{diss} affects the level of gas velocity w_t over the entire working cycle. To reduce the complexity of estimation problem, the parameters c_{int}, c_{inj}, and c_{comb} of the charge motion producing terms in Eq. (4.110) are excluded from the parameter vector to be estimated $\boldsymbol{\theta}_w$. A good agreement with measurements results from setting all these parameters to a constant value $c_{prod} = 0.5$.

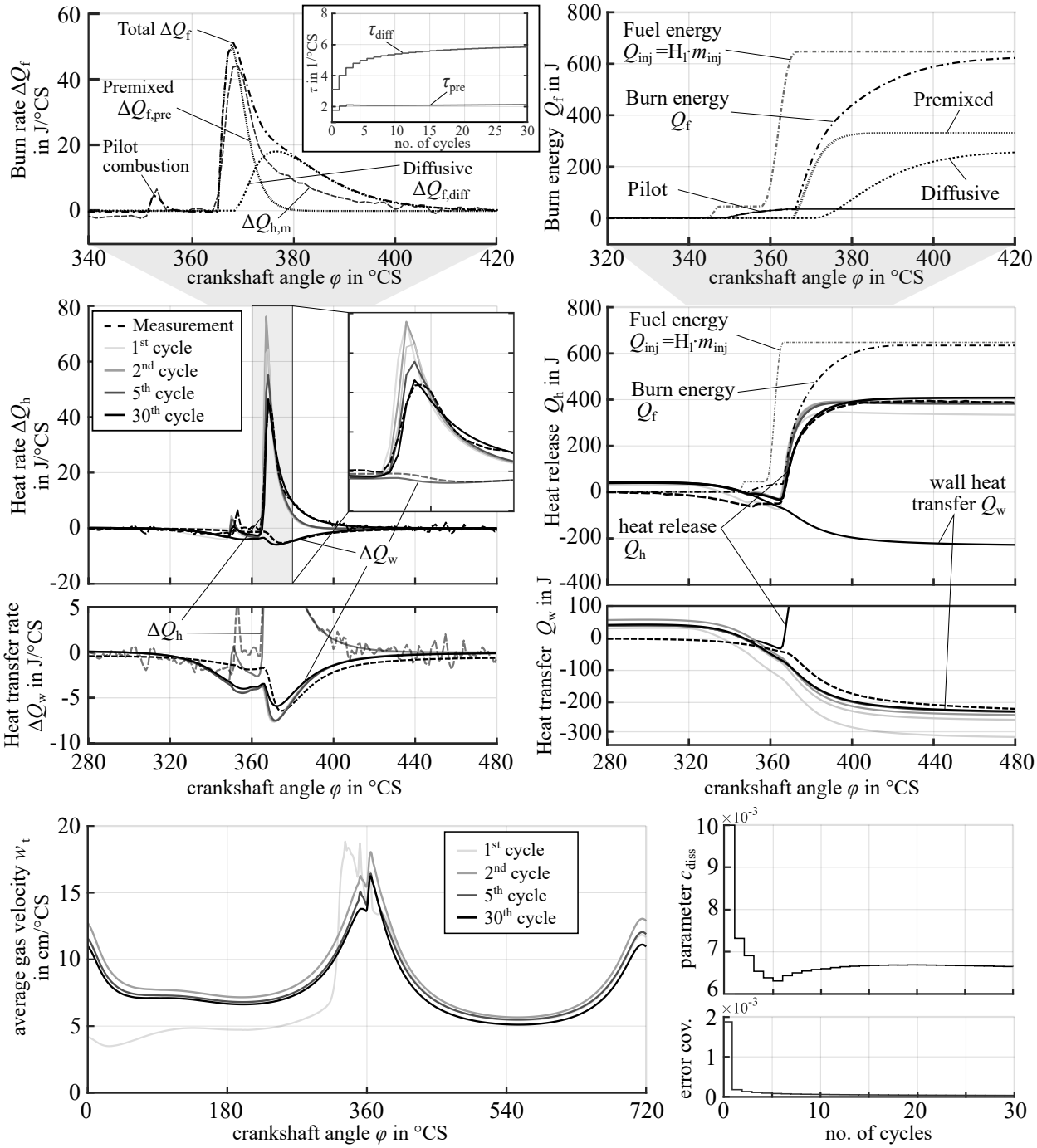

Figure 4.36: Simulation results of overall cylinder estimation for the engine operation point $n_{eng} = 1400$ 1/min, $q_{inj} = 16$ mm^3: Comparing of combustion and heat transfer estimation (within 30 working cycles) with reference courses based on cylinder pressure measurements

In most cases, the parameters to be estimated converge to a constant value after 10-20 working cycles. In real engine operation at the engine speed of 1400 min^{-1} this corresponds to a duration of about 1-2 seconds. As soon as a minimum number of working cycles have been passed and the relative cycle-to-cycle change of a parameter falls below a predefined threshold, the estimation is switched off by zeroing the corresponding covariance matrices. This turns off the correction step of the Kalman algorithm and the estimation is then based only on a model-based prediction; which eventually corresponds to a pure model simulation.

Afterwards, the parameter estimation results of each i-th parameter of $\boldsymbol{\theta}_{\mathrm{w}}$, $\boldsymbol{\theta}_{\mathrm{c}}$ and $\boldsymbol{\theta}_{\mathrm{r}}$ are modeled via experimental modeling approach as follows

$$\theta_i(\mathbf{z}) = \mathbf{g}_i(\mathbf{z})^{\mathrm{T}}\mathbf{w}, \tag{4.123}$$

where the weighting factor $\mathbf{w}$ are identified using a local parameter estimation approach based on RLS-algorithm, see Sect. 2.4. The estimated parameter $\boldsymbol{\theta}_{\mathrm{w}}$, $\boldsymbol{\theta}_{\mathrm{c}}$ and $\boldsymbol{\theta}_{\mathrm{r}}$ are mapped as functions of operating point variables $\mathbf{z}$, see e.g. Fig. 2.16. Through combining these experimental parameter models with the model equation within the cylinder estimator results the semi-physical cylinder gas state model that is able to reproduce the cylinder gas states, the cylinder flows, the characteristic combustion phases of diesel combustion as well as the wall heat transfer.

4.6 Identification of parameter models

The identification of the parameter models (4.123) is performed online by using a recursive least square algorithm described in Sect. 2.3.1. Since the objective is to model and store the estimated parameters $\boldsymbol{\theta}_{\mathrm{w}}$, $\boldsymbol{\theta}_{\mathrm{c}}$ and $\boldsymbol{\theta}_{\mathrm{r}}$ as functions of engine operating point variables, the identification of parameter models must be performed in a slower computation rate than the cylinder estimation or combustion estimation, respectively. Therefore, a cycle-by-cycle calculation at engine speed rate, and subsequent to the crank-angle-resolved estimation, is sufficient for the identification of parameter models.

Fig. 4.37 shows parameter estimation results in the form of parameter maps. The estimated rate parameters are shown as functions of engine speed and injection quantity (burnout is neglected). The engine operation area is varied over a engine speed range n_{eng} from idle mode to 3000 1/min and a load range represent by fuel injection quantity q_{inj} from 3 to 30 mm^3. 51 steady state engine operating points are additionally marked as reference measurement data.

Since the phase parameters represent a measure for the dynamics of combustion processes in angle frequency domain, various measurements confirm that they are highly affected by engine speed due to the relation between time domain and crank angle domain. In Fig. 4.37, it can be seen that all rate parameters show an engine speed dependent behavior. The relation between the change of engine speed n_{eng} and the change of rate parameter is approximately linear. To further reduce the candidates for parameter model inputs, the linear relation to the engine speed can be extracted by using the relation between time and crank angle domain in Eq. (2.4).

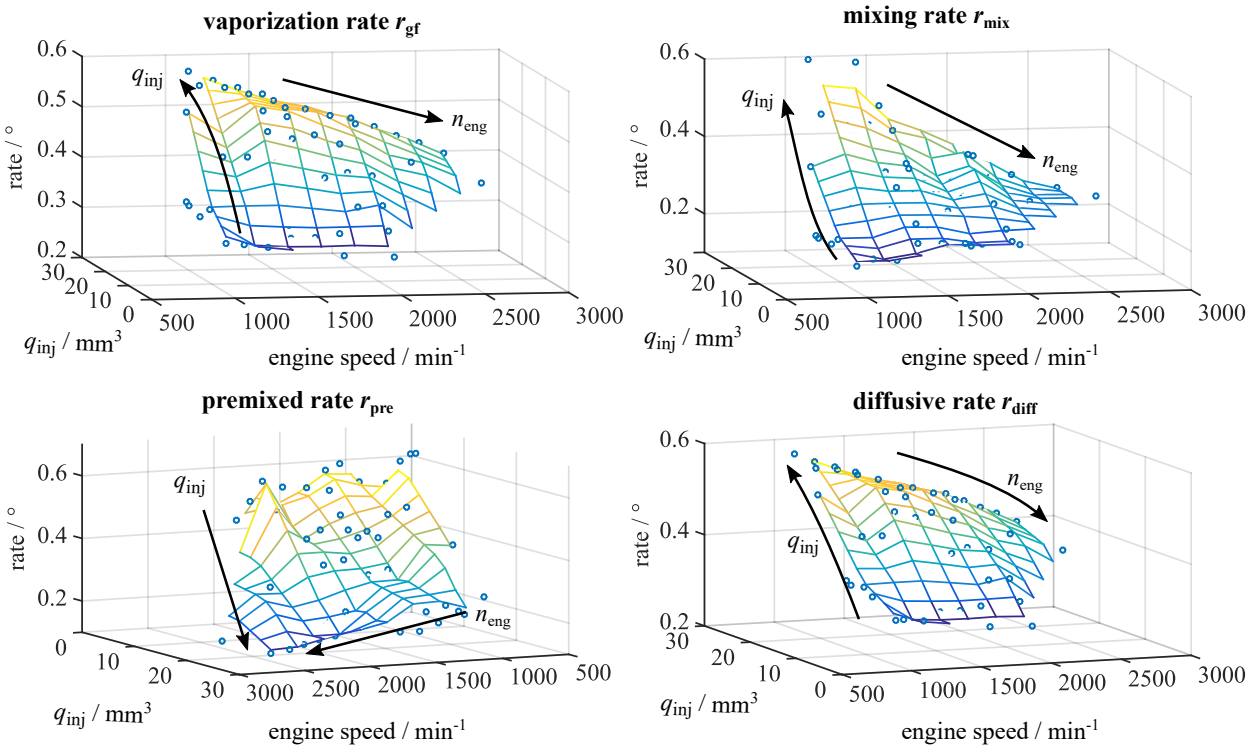

Figure 4.37: Results of identified rate parameter models showing the rate parameters as functions of engine speed and injection quantity (engine load); interpolated estimation results of 51 steady state engine operation (blue circles)

Both vaporization rate parameter r_{gf} and mixing rate parameter r_{mix} are related to injection quantity q_{inj}. Increasing injection quantity accompanied with increasing rail pressure p_{rail} (injection rate) leads to higher vaporization and mixing rates, although, rail pressure is typically also adjusted proportionally to engine speed n_{eng}.

Additionally, an increase in engine speed leads to a reduction of premixing duration due to the limitations of fuel path dynamics (vaporization and mixture formation). The temporal overlap between the injection process and the start of combustion determines the ratio between homogeneous (premixed) and inhomogeneous combustion (diffusive, burn-out). In general, an increase in injection quantities causes longer injection durations and a shift from homogeneous to inhomogeneous combustion. This is why, the reaction rates of premixed r_{pre} and diffusive combustion phase r_{diff} behave in contrary to each other with regard to the influence of injection quantity; see parameter maps for r_{pre} and r_{diff} in Fig. 4.37 (bottom). An increase injection quantity lowers reaction rate of premixed combustion, while reaction rate of diffusive combustion increases with higher quantities. This is consistent with the observations described in section 4.4.1, which show that the share of premixed combustion decreases at higher loads, while the share of diffusion combustion increases. The cylinder gas mass m_{cyl} has influence on reaction rate r_{pre}, vaporization rate r_{gf} and mixing rate parameter r_{mix}, whereby the vaporization rate r_{gf} is less affected by cylinder gas mass m_{cyl}.

For the online-identification of the overall cylinder model, the flow coefficients c_{InV}, c_{ExV} of the cylinder mass flow models and the dissipation coefficient c_{diss} of the wall heat transfer model are

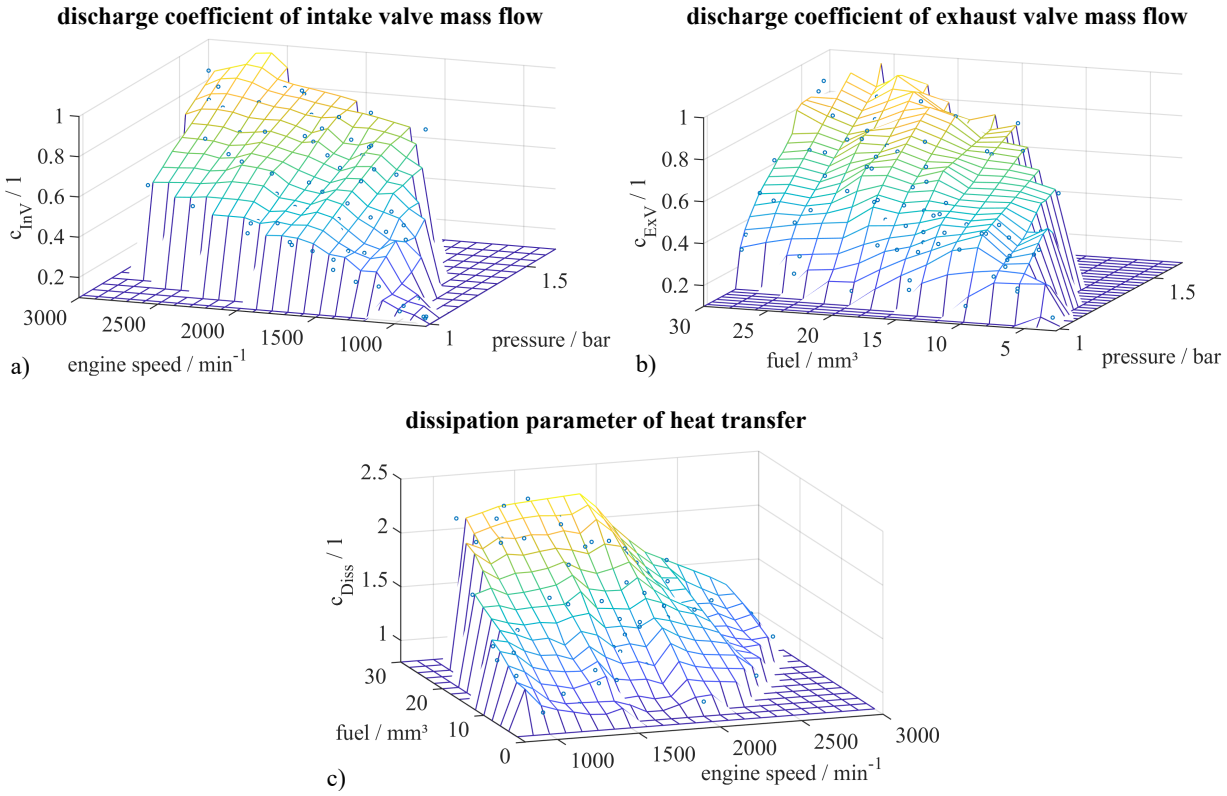

Figure 4.38: Results of identified parameter models of discharge coefficients of a) intake valve, b) exhaust valve model, and c) of dissipation coefficient of heat transfer model; interpolated estimation results of 92 steady state engine operation points (blue circles)

identified as functions of the engine operating point variables. From the operating point variables, the most influencing variables are identified and used as input variables of the experimental parameter models. By varying the engine operating point variable during the combined state and parameter estimation described in Sect. 4.5, the relevant influence variables that serve as inputs for the estimated parameter models are identified.

The estimated flow coefficients c_{InV}, c_{ExV} of the valve mass flow models correlate with engine speed n_{eng} and upstream pressure $p_{2\mathrm{i}}$ at intake manifold. A higher intake pressure also raises the pressure level of the in-cylinder pressure, so that both flow coefficients c_{InV} and c_{ExV} relate to each other depending on ratio between the corresponding valve disc diameter A_{iv} and A_{ev}, see Eqs. 4.15 and 4.16. However, a higher injection quantity q_{inj} (engine load) significantly increases the pressure and temperature level of the combustion gas after combustion, leading to a higher upstream pressure at the exhaust valve during the exhaust process. Therefore, the effect of injection quantity has to be taken into account for modeling the flow coefficient c_{ExV} of the exhaust valve. Since the relation between engine speed n_{eng} and boost pressure $p_{2\mathrm{i}}$ can change in turbocharged diesel engines and is therefore not unique, the engine speed must also be considered as an input variable for the parameter models of the flow coefficients.

Fig. 4.38 shows the results of online-identification of the experimental parameter models of intake and exhaust valve flow coefficients as funtions of the measured engine speed n_{eng}, intake pressure

p_{2i} and injection quantity q_{inj}. For modeling of the flow coefficient of exhaust valves, the influence of engine speed is neglected. Instead, the injection quantity q_{inj} is used as second input variable. The heat transfer model in Sect. 4.3 is parameterized by the dissipation coefficient c_{diss} which determines the level of in-cylinder charge motion (gas velocity).

4.7 Summary

Modeling of combustion comprises the crank-angle resolved description of the in-cylinder state variables and processes during the engine operating cycle (Fig. 4.3). This involves modeling the in-cylinder gas state variables, the valve mass flows, the heat transfer to the cylinder walls, and the heat release during combustion. A particular difficulty lies in modeling of the combustion process consisting of *mixture formation*, *ignition* and the *instationary release of burning energy* (burn rate of combustion).

The modeling of combustion is based on a novel semi-physical approach. With this approach, it is possible to reproduce the crank angle resolved courses of the characteristic combustion phases of diesel combustion as a function of the injection course and the operating point. In simplified terms, the combustion process is described as a delayed system response to the injection process. The delay between the start of injection and the start of combustion is interpreted as dead time and the combustion rate curve as a dynamic process of higher order. The three overlapping combustion phases premixed combustion, diffusive combustion and burn-out, are modeled by separate transfer functions in a crank angle frequency domain. A quasi-dimensional mixture formation model is used to describe the ignition delay and serves for the division of the injection quantity into three parts, which act as inputs for the combustion phases. The mixture formation is determined by the vaporization rate and the rate of air entrainment (mixing rate). The rate parameters of the transfer functions and the mixture formation are modeled as a functions of the engine operating point (injection quantity and speed) using experimental map models.

This system theoretical model approach allows simplified modeling, in means of reduced number of equations, simpler mathematical formulations and reduced number of parameters. Compared to other combustion models from the literature, which usually involve complex couplings of equations and states, with the presented modeling approach the engine combustion is very easy to calculate using the few setting parameters for model adjustment (angular constants/rate parameters).

The identification of the derived semi-physical combustion models is performed according to the methodology presented in Sect. 2.4. State and Parameter estimation is mainly based on *in-cylinder gas pressure* and the *crankshaft angle position*, and supported by *additional variables*, such as cylinder volume or valve lifts. Two approaches for the determination of a semi-physical cylinder model were considered in this work.

The first approach focuses solely on the semi-physical modeling and identification of the combustion process. This approach requires that the real heat rates and heat losses are already obtained from

the measured and pre-processed cylinder pressure signals and thus are available as input variables ("measurement") for the estimation and identification of the semi-physical combustion model.

In the second approach, the whole operating cycle is modeled additionally to the combustion. This includes the in-cylinder gas pressure, gas temperature and gas mass, as well as the intake and exhaust valve mass flows and the wall heat losses. Although this makes the online identification more complicated, the measured cylinder pressures can be used directly as a reference signal for the identification of the semi-physical cylinder model without the need to calculate the heat rate and wall heat losses in advance. The second approach shall be used whenever the pressure indication system at the engine test bench does not include a post-processing of the cylinder pressure signals and functions of the heat rate analysis. Another advantage is that the models for the valve mass flows and the wall heat losses can also be determined on the basis of in-cylinder pressure sensor signals.

The calculations of the model equations and estimation algorithms are performed crank angle synchronously (1° resolution) and perpetually over several engine operating cycles. Online identification of the real-time semi-physical models is performed using steady-state engine measurements. The identification process is completed within 20 to 30 operating cycles (40 to 60 revolutions). Depending on the engine speed, this corresponds to a few seconds in real time. According to the scheme represented in Fig. 2.14, the semi-physical cylinder model results after concluding the identification of the experimental parameter models.

5 Applications

This chapter deals with the practical implementation of the semi-physical modeling methodology at the engine test bench. First, the setup of the engine test bench including the test engine, the available measurement technology and the real-time prototyping hardware is presented. The real-time development environment of the prototyping hardware, which is used for the development and validation of the modeling methodology, is described on functional level. Here, software architecture of the real-time environment and the main aspects of the implementation of the model calculations and estimation algorithms are treated in more detail. Then, the measurement procedure for generating semi-physical real-time models is briefly explained.
Furthermore, two possible applications of the modeling methodology in the context of the model-based development process are presented. First application example is the model-based online combustion analysis which represents a functional extension of the conventional pressure and combustion process analysis. Second application example is the use of the semi-physical models for real-time engine simulation at a hardware-in-the-loop test bench.

In the development of engine control function, model-based methodology has proven to be promising for handling increasing complexity of future control design and calibration process. In this context, the use of simulation models (virtualization) facilitates development tasks and reduces costs and efforts for e.g. prototypes and testing facilities. In particular, real-time and physically interpretable models, such as those treated in this work, can be deployed to increase efficiency in many areas and stages of development process.

Fig. 5.1 reflects the content and structure of this chapter. Sect. 5.1 treats the setup of the engine test bench at the Institute of Automation and Mechatronics (IAT) and the implementation of the methodology on the rapid prototyping system, as well as the procedure for generating semi-physical real-time models on the engine test bench, see Fig. 5.1 a).

The first and most evident application example results directly from the implementation of the semi-physical modeling methodology on the test bench automation system. This application is referred to as model-based online combustion analysis and is presented in Sect. 5.2. Sect. 5.3 treats the use of the semi-physical models for real-time engine simulation on a hardware-in-the-loop test bench that was also set up at IAT, see Fig. 5.1 b).

An important feature of the test benches shown in Fig. 5.1 is the fact that the electrical interfaces to the RCP system or ECU were kept identical on both the engine test bed and the HIL test bench. A second RCP system identical to the one in Fig. 5.1 a) was set up at the HIL test bench. This allowed the models and estimators developed in the chapters 3 and 4 to be first implemented and

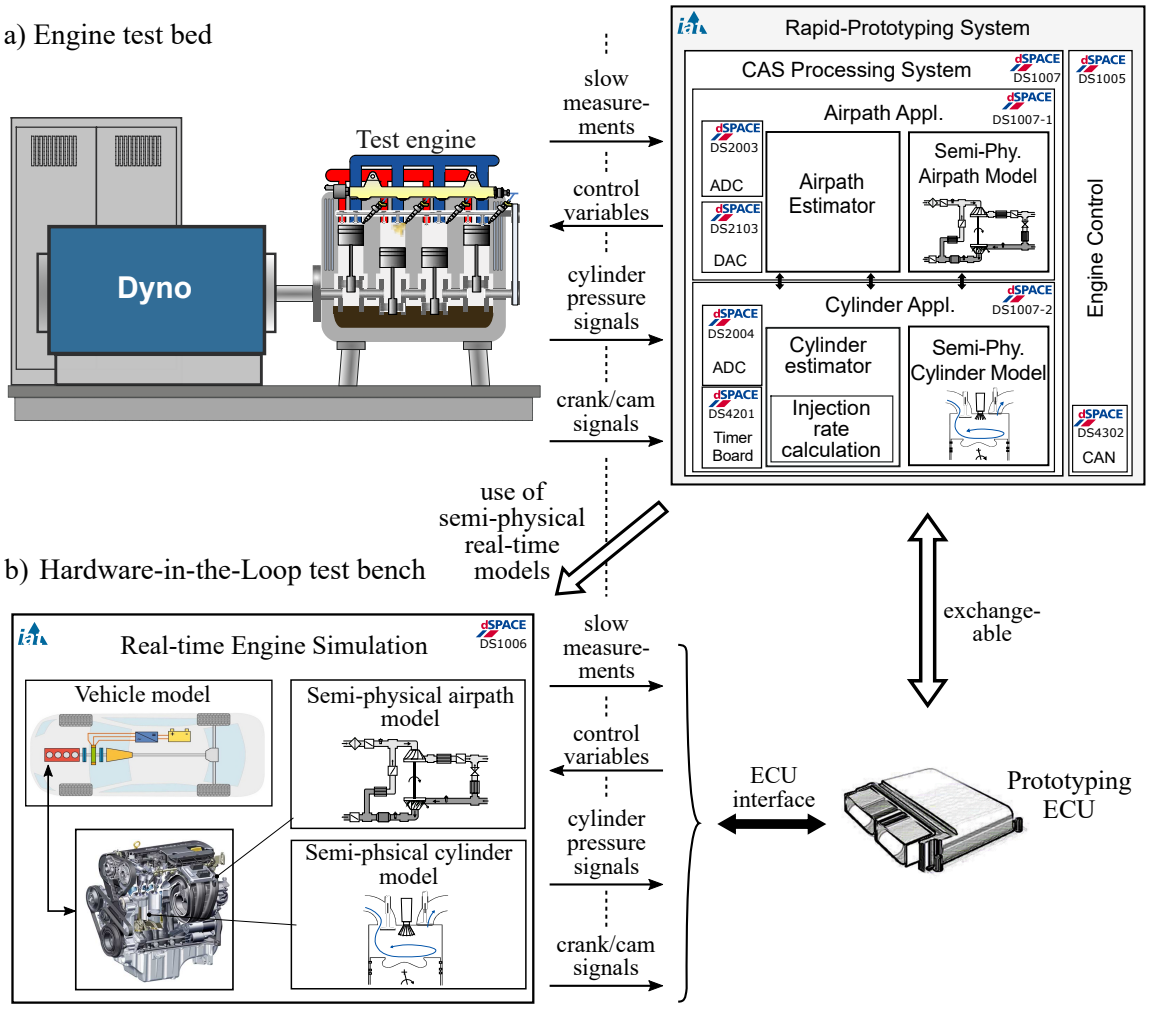

Figure 5.1: Overview of test benches: a) Engine test bench controlled via Rapid Control Prototyping System (RCP) and b) Hardware-in-the-Loop test bench (HIL); electrical interfaces of both test benches are identical, so that the identical RCP system can be used at the HIL test bench

tested under constant and reproducible conditions on the HIL test bench before migrating to the identical RCP system on the engine test bench.

5.1 Implementation on the engine test bench

All experiments and measurements are carried out on the engine test bench of the Institute for Automatic Control and Mechatronics (IAT) of the Technical University of Darmstadt. Details regarding the hardware setup of the engine test bed can be found in the Appx. A.1. The test bench is equipped with a 1.9l test diesel engine of the type GM/Opel Z19DTH connected to a speed-controlled load machine. Specifications of test engine and load machine are also listed in the Appx. A.1 in Tab. A.1 .

For the application of the methods described in chapter 3 and 4, the engine test bench is equipped with several sensors, such as the cylinder pressure sensors required for cylinder state and parameter estimation and the numerous pressure and temperature sensors at the various locations in the air system that are required for the airpath estimation. An overview of the sensors used is shown in Fig. A.1. The test bench control and the control of the fuel and exhaust gas measurement technology is implemented on a separate test bench PC. Processing of the sensor signals and the control of the engine actuators is handled by the Rapid-Control-Prototyping system.

5.1.1 Real-time environment for control function development

The RCP system, shown in Fig. 5.1 a), is a modular real-time system equipped with two processor boards for the execution of real-time applications, and several I/O boards for the processing of different I/O signals, such as analog-in/out, digital-I/O or CAN communication. One processor boards executes the engine controller, which allows manipulation the injection parameters, such as injection quantities and injection angles, and controlling the actuator positions of the airpath system. A second processor board serves as a real-time development environment for implementing the semi-physical models and the state and parameter estimation algorithms. This second processor board has an integrated Dual-core CPU, which allows the parallelization of two real-time applications of each of the two CPU core.

A simplified scheme of the software architecture implemented on the Dual-core processor board is shown in Fig. 5.2. The semi-physical model calculations and estimation algorithms for the airpath system and in-cylinder processes are each assigned to one of the two CPU cores as separate real-time software applications. The *airpath application* performs the computations of the airpath state and parameter estimation described in Sect. 3.3, while the *cylinder application* is performs the corresponding cylinder estimation described in Sect. 4.5.

The cylinder application includes the functionalities of a conventional pressure indication system, such as filtering and pegging of cylinder pressure signals, heat rate calculation and ignition detection, which is able to detect reliably the ignition events during the ongoing work cycle (also minor pre-combustions of pilot injections), see Weber (2019b). More details about the feature set and the specific functions are described in the Appx. A.1.2.

Furthermore, the injection rate is calculated using a semi-physical injection model as function of measured injector current I_{inj}. Details regarding the semi-physical injection model are given in the Appx. A.3. The injection rate model is main input variable of the semi-physical combustion model and there required for the estimation of the diesel combustion phases and their parameters.

The execution of both real-time applications is crank-angle synchronously triggered via an external trigger signal. The pulse trigger signal is generated using the pulse signal of the engine speed sensor (incremental encoder), where the pulse width corresponds to the crank angle resolution and can be configured via the timer board. The cylinder application is executed with a resolution of 1° degree crank angle. This calculation step size $\varphi_{\mathrm{s}} = 1°$ is the minimum crank angle resolution required for a reasonable consideration of the in-cylinder processes in the cylinder. The step size φ_{s} (in °CS)

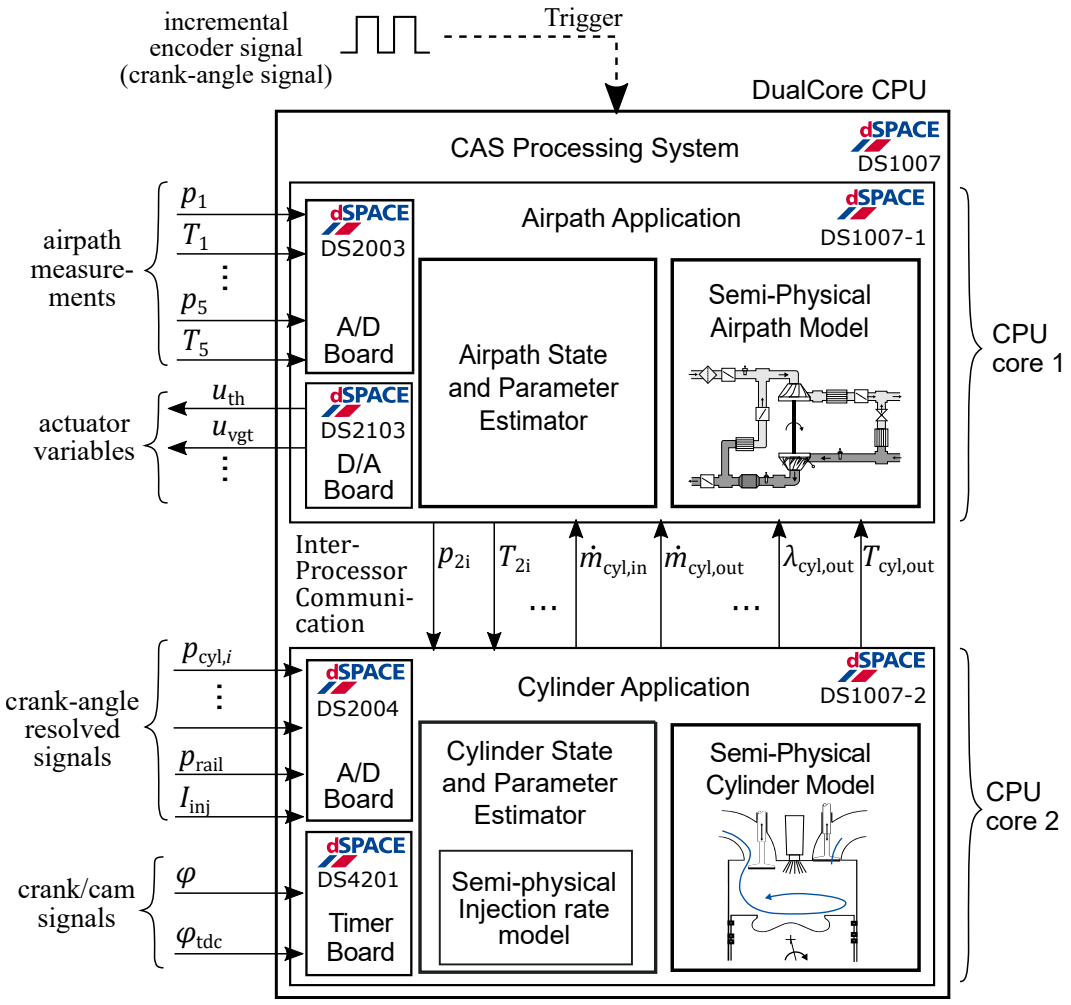

Figure 5.2: Software architecture of the Dual-core processor board DS1007 of the Rapid-Control Prototyping system at the engine test bench: Real-time applications of airpath and cylinder group (incl. computations of semi-physical models and estimation algorithms) are distributed on two separate CPU cores of the processor board; the execution of the real-time applications is triggered crank-angle synchronously by the engine speed sensor (incremental encoder) with a predefined crank-angle resolution configurable by the Timer board

also defines the available time interval as function of the engine speed (in 1/min), in which the real-time application must be executed, denoted as turn-around time in s

$$t_{\text{turn-around}} < \frac{\varphi_s}{360°} \frac{60\text{s}}{n_{\text{eng}}}$$

Since the airpath behavior is less dynamic, it is sufficient to execute the airpath application with a higher crank angle resolution[1](e.g. every 10/20/30 ° CS), which is why the airpath application is less critical with respect to the requirement for real-time capability.

[1]The signals of the pressure sensors in the intake and exhaust manifolds should be averaged over several degrees of crank angle to eliminate the influence of the engine strokes (oscillations)

With the real-time hardware used in this work, real-time capability could be achieved up to a engine speed of approximately 3000 1/min, which corresponds to an available time interval of 55.5μs. The turn-around time of the cylinder application is not constant over the entire operating cycle due to the engine stroke dependent computation load. The turn-around time is highest in the crank angle range 340° to 540○, where the high-dimensional system of equations for the three combustion phases is calculated in parallel. A marginal reduction of the turn-around time can be achieved by omitting the burn-out phase.

5.1.2 Measurement procedure for model identification

In this work, a stationary point measurement was considered for the identification of the semi-physical models. In order to identify the model parameters, the engine states must be in steady state so that the slow thermal processes are already finished.

A steady state engine operating point is defined by a constant engine speed and engine load. Engine load is represented by the injection quantity q_{inj}. Since the injection control is subordinate to the torque control, the injection quantity can be manipulated more easily via ECU-Bypassing. Furthermore, the injection quantity relates to the total heat release and is more suitable for the interpretation of the measurement results.

In stationary engine operation mode, the online state and parameter estimation is activated by switching on initial error covariance matrices $\mathbf{P}_0 = \mathbf{P}(0)$ and setting the entries in the covariance matrices $\mathbf{Q}(k)$ associated to the states and parameters, see 2.3.4. During estimation, the initial error covariances are minimized. By monitoring the diagonal elements of the error covariance matrix $\mathbf{P}(k)$, the time at which the error covariances no longer change ($\mathbf{P}(k) = \mathbf{P}_{\text{min}}$) is detected and experimental parameter modeling is started. Nulling the error covariance matrices deactivates the online identification for the operating point. By resetting the covariances, the identification process can be restarted with the last estimated values. This whole process is completed after about 20 to 30 engine operating cycles, so that the next engine operating point can be targeted and the identification process restarted.

The measurement sequence for the online identification of semi-physical model is illustrated in Fig. 5.3 a). The test engine was operated within a speed range of 850 up to 2800 min^{-1} and the injection quantity was varied within a range of 3 mm^3 (idle mode) to 30 mm^3. During measurement, the engine was operated in series ECU mode. In this mode, other engine states such as boost pressure and temperature or rail pressure were also varied in dependence on speed and load.

After the considered engine operation range is fully covered and the online identification of the experimental parameter models is done, the correction step of the state and parameter estimator can be switched off, so that the predictor-corrector mode of the Kalman filter is switched to pure prediction mode, which then represents the physical model part $\mathbf{x}_k = \mathbf{f}(\mathbf{x}_{k-1}, \boldsymbol{\theta}_k, \mathbf{u}_k)$ of the semi-physical model, see Fig. 5.4 and compare with Fig. 2.12. The model parameters are obtained from the experimental parameter model $\boldsymbol{\theta}_k = \mathbf{g}(\mathbf{w}, \mathbf{w}_k, \mathbf{u}_k)$.

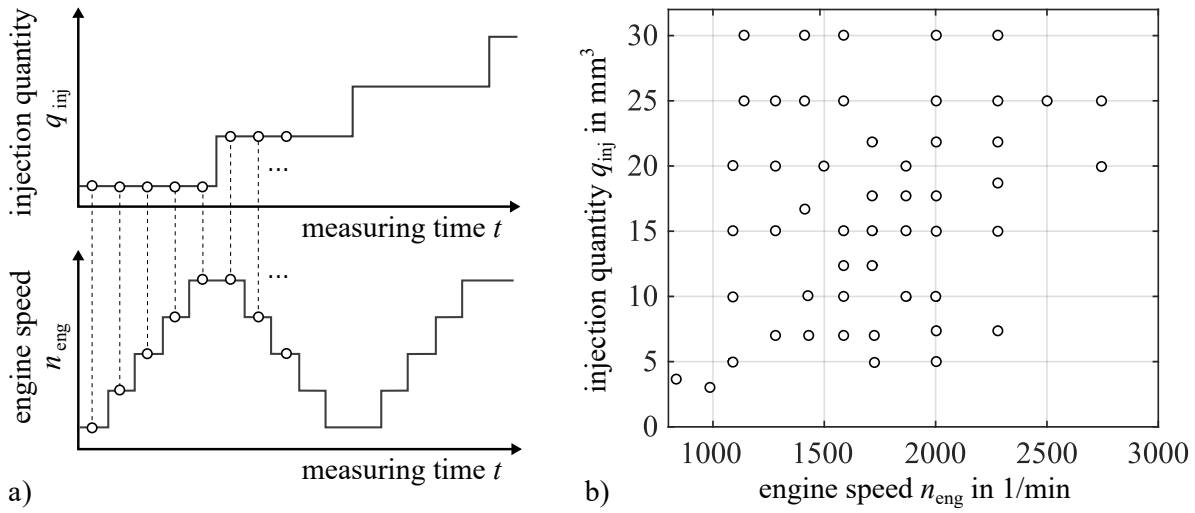

Figure 5.3: Illustration of measurement sequence from which the data of stationary engine operation points is extracted: a) Sequences of injection quantity q_{inj} and engine speed n_{eng} over time, and b) stationary engine operation points depicted in speed-load engine map (injection quantity represents engine load)

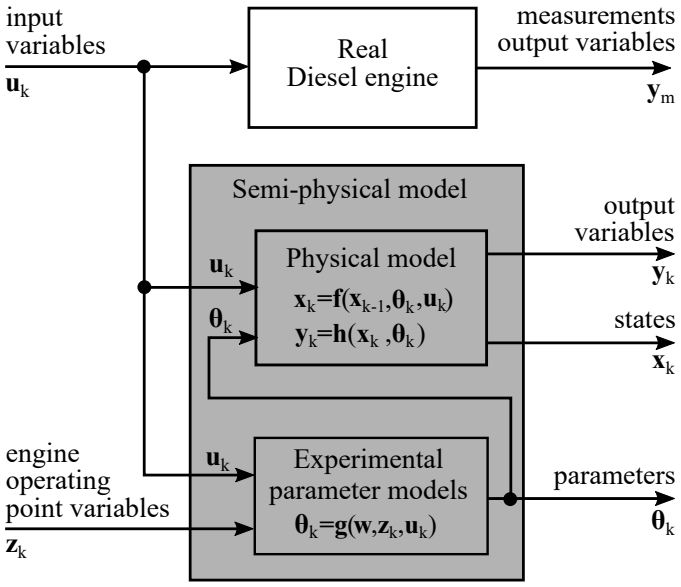

Figure 5.4: Scheme of semi-physical model after experimental parameter models are identified online (compare with Fig. 2.12): The correction step is deactivated, so that prediction step of the state and parameter estimation represent the physical model. Adding experimental parameter model results in a semi-physical model

For verification of the semi-physical diesel combustion model, the modeled burn rates of premixed and diffusive combustion are compared with the total burn rate reconstructed from the measured cylinder pressure in Fig. 5.5. The identified semi-physical combustion model is simulated online and in parallel to the total burn rate determined from cylinder pressure measurements on the RCP-System.

In Fig. 5.6, a comparison of the combustion features of the identified semi-physical combustion model and the combustion features obtained from cylinder pressure analysis (heat rate analysis) is shown. Note that due to the relatively large computational step size of $\varphi_s = 1°CS$, the angle-related characteristic values of model and measurements are overlapping or show a multiple of φ_s as quantification error. Both the total released combustion energy and the CA50 are well matched by the semi-physical model.

The total experiment duration required for the generation of the semi-physical model is rather affected by the settling duration until the steady-state operation is reached than by the duration of the parameter identification. The implementation of a more efficient design of experiments was not the focus of this work and was therefore not further examined. For more information regarding efficient online methods for engine measurement see e.g. Bredenbeck (1999), Mitterer and Zuber-Goos (2000), and Kowalczyk (2018).

5.2 Model-based online combustion analysis

In the engine development, the thermodynamic analysis of combustion process, referred to as combustion analysis, has been applied for more than 40 years now (Bargende 2014). Over the last decades the computational power of test bed computers has significantly increased, so that 0D/1D- thermodynamic calculations of the engine operating cycle is now performed online at the engine test bench using information from in-cylinder pressure sensors. A *pressure indication system* processes the signals of in-cylinder pressure sensors with respect to crankshaft angle and calculates based on their signal traces different signal features and the rate of heat release during combustion. The analysis of pressure features and heat rate profile at the engine test bench is referred to as *online combustion analysis*. It offers the investigation and optimization of the combustion process regarding fuel efficiency and emission behavior.

In this work, the functionalities of the pressure indication system were implemented on the RCP real-time system used at the engine test bench. This enables model calculations and state and parameter estimation algorithms to be implemented right next to the crank angle synchronous processing of the measured cylinder pressure signals, see Fig. 5.2.[2] By implementing these additional calculations, the basic functionalities of the online combustion analysis are extended. More details regarding implemented functionalities can be found in Appx. A.1.2.

[2]Model calculations and estimation algorithms are performed in the same calculation task as the crank angle synchronous sampling of the cylinder pressure signals, the injection currents, and the intake and exhaust manifold pressure signals

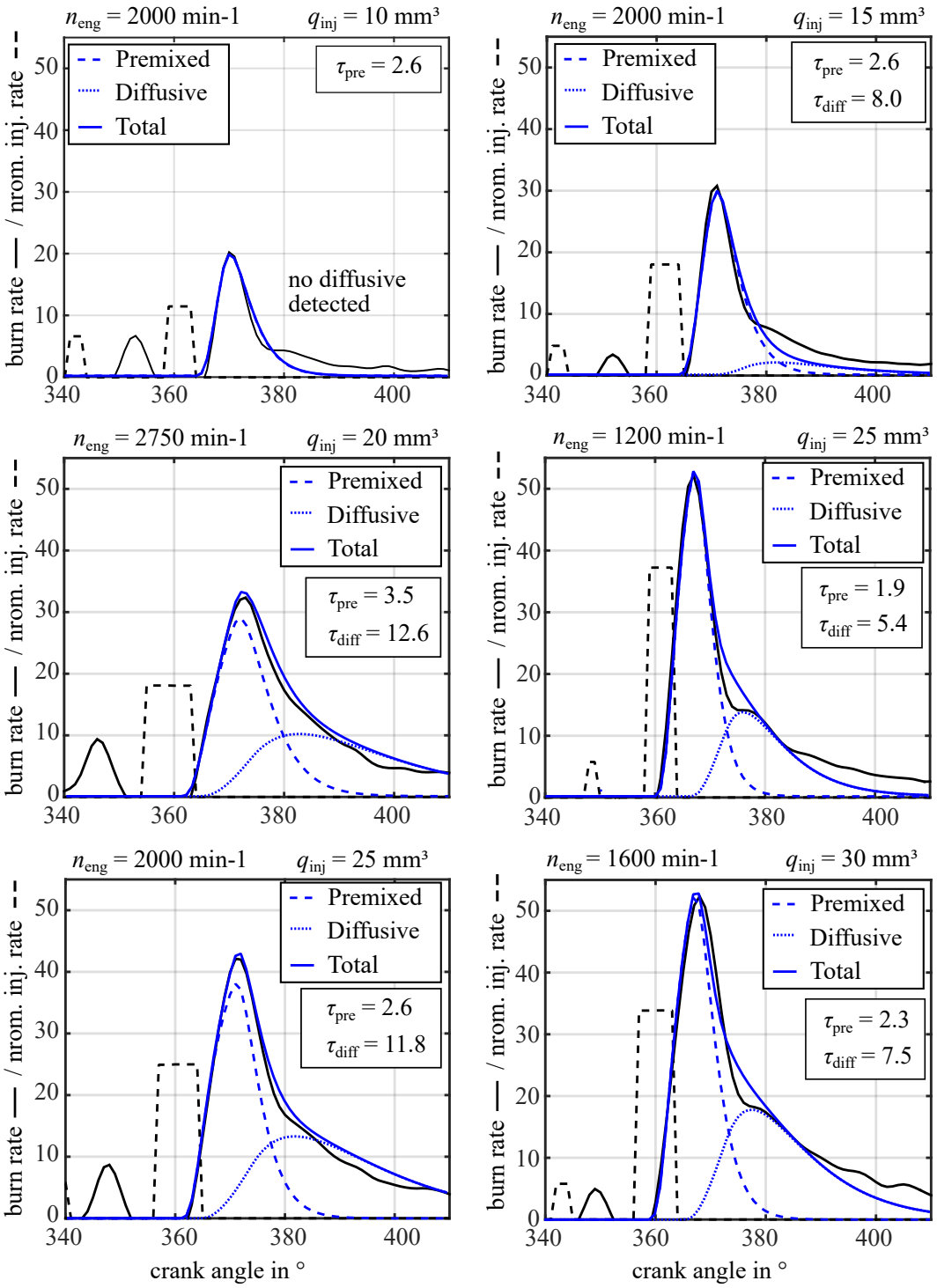

Figure 5.5: Comparison of the simulation of the identified semi-physical combustion model (blue) with the total burn rate (black) reconstructed from measured in-cylinder pressure signals using Eq. (A.11) for six different stationary engine operation points; burn rates of premixed and diffusive combustion are modeled using third order transfer functions and the parameters τ_{pre}, τ_{diff} represent their characteristic angle constants; injection rates are formulated with respect to crank angle and normalized for better readability

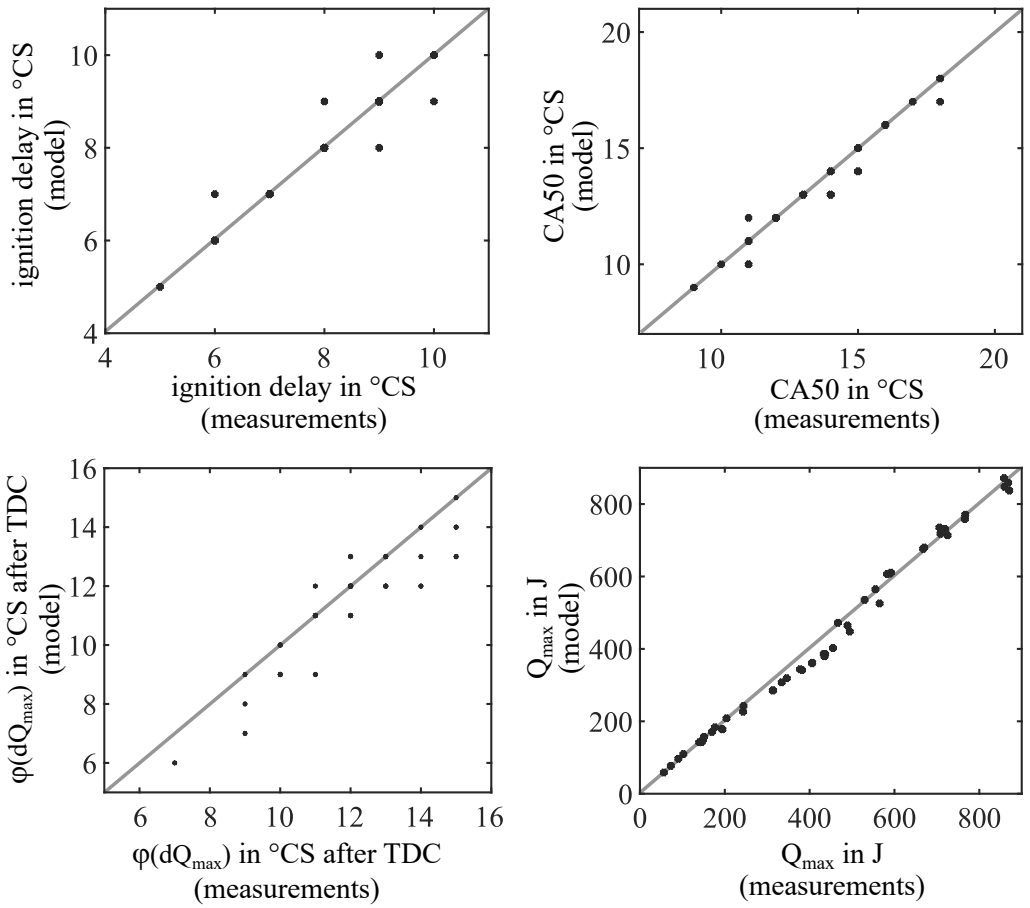

Figure 5.6: Model verification via comparison of the combustion features of the identified semi-physical combustion model with the characteristics obtained from cylinder pressure and combustion analysis (51 measurement points), compare Fig 4.11

This extension is here referred to as *Model-based online combustion analysis* (MBCA). The Fig. 5.7 illustrates the principle of MBCA by depicting measured and modeled variables available at the engine test bench. Using model-based state and parameter estimators allows to determine additional non-measurable system states and characteristic values based on the measured in-cylinder pressure. These additional estimated information serve then as virtual sensors providing calibration engineers deeper insight into the engine behavior during measurements and support them during development and calibration of control functions at the test bed.

The Kalman filter-based state and parameter estimation combines model-based prediction and correction by measurement and thus fills the gap between pure simulation and available measurements. Even though not all modeled in-cylinder quantities can be verified directly by measurements on the test rig, these quantities are nevertheless governed by physical laws and provide useful information in addition to cylinder pressure information.

Since most engine states are physically related to each other, changes in control parameters or engine speed cause multiple engine states to change simultaneously in dynamic engine operation. The time-related correlation of the causalities between the change of specific control parameters

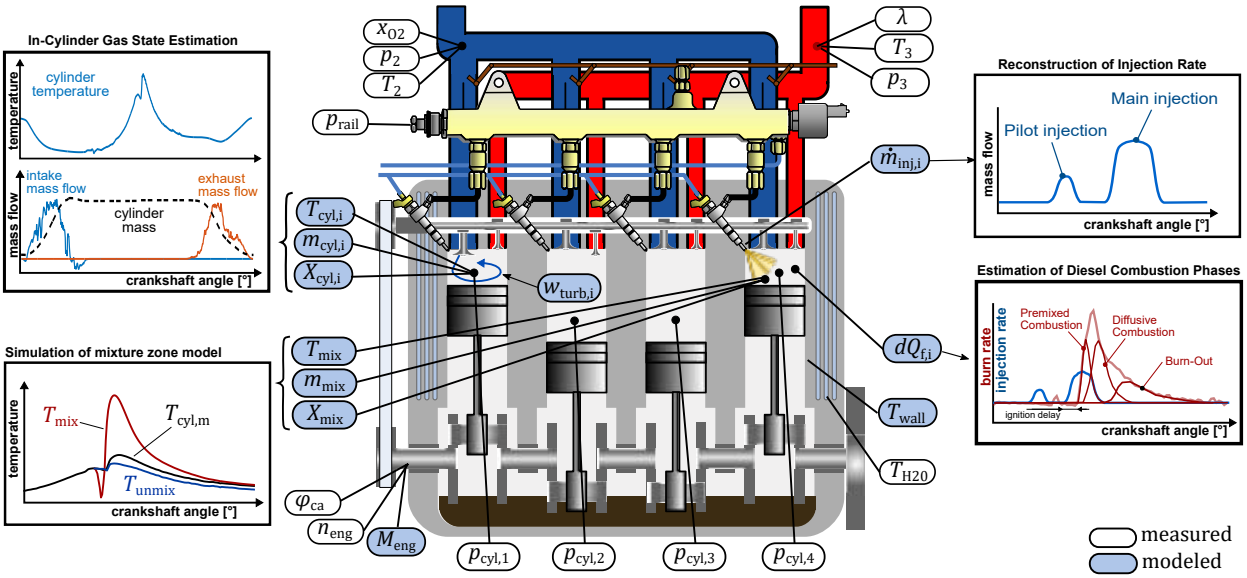

Figure 5.7: Model-Based Online Combustion Analysis: Illustration of measured signals and modeled variables (virtual sensors) determined with model-based state and parameter estimators (Kalman filters) and semi-physical models based on available measurements

and its impact on the engine's outputs, such as torque, fuel consumption and emissions, represents a major challenge for test bench engineers. Different dynamics of the processes in the combustion engine and limitations of the measurement technology (sensor dynamics) further complicate the time-related correlation, so that an exact determination of the cause responsible for e.g. resulting emission measurements cannot be made. Using cycle-resolved virtual sensors and pre-processed measured variables can support handling of different dynamics and help to overcome the limits of the measuring technology.

The crank angle resolved in-cylinder gas state estimator (Sect. 4.5) can be applied to determine the in-cylinder gas mass, gas temperature and air mass fraction as well as the intake and exhaust valve mass flows, see Fig. 5.7. Additionally, other virtual variables are present, such as the mean charge motion (Sect. 4.3.1 or the mixture formation model, which provides the gas temperature and oxygen fraction within the virtual mixing and reaction zone (Sect. 4.4.3). Using these cycle-resolved variables allows investigating of the cycle-to-cycle behavior of the thermodynamic in-cylinder gas state (before start of combustion), which is known to have significant influence on the formation of raw emissions during transient engine operation.

The combustion phases and their characteristic rate parameters provide additional information about the characteristics of the combustion and offer an analysis tool for evaluating and comparing the combustion process. In this way there is a direct relation between the injection and the resulting division of the combustion phases. The effects of injection variations (injection angle, injection pressure, etc.) on e.g. the relationship between premixed combustion, diffusive combustion and burn-out are then not only qualitatively but also quantitatively visible for the experienced engine developer. The rate parameters are a measure for the dynamics of the individual combustion phase.

Since both their shares and parameters have an influence on the resulting nitrogen oxide and soot emissions, these quantitative variables can be used to investigate dynamic emission behavior.

5.3 Real-time engine simulation on Hardware-in-the-Loop test bench

After semi-physical real-time engine models are identified at the engine test bed, they can be applied in the context of HiL testing of ECUs for *real-time simulation* of the engine or even test driving cycle (driver, driving maneuver, environmental, powertrain simulation). In this way, controller functions or new ECU software versions can first be extensively tested on the target hardware in a real-time environment before being used on the real system, see Fig. 5.1 b). This significantly reduces costs and effort in the development process and allows critical corner cases to be tested under safe and reproducible conditions (Ch. 1).

In order to prove the applicability of the developed semi-physical models in real-time simulation, a hardware-in-the-loop simulation test bench based on a real-time system was set up in this work. For the real-time simulation of the engine model (*plant model*), a Processor Board equipped with an AMD Opteron QuadCore Processor with 2.8 GHz is used. The plant model is divided among the four CPU cores. Fig. 5.8 shows the structure of the overall Hardware-in-the-Loop simulation model implemented as a multi-core real-time application.

The semi-physical cylinder model including combustion model with stored parameter maps of the angular constants is calculated crank angle synchronously on CPU 2 of the quad core processor at a resolution of 1° CS. The clock rate at which the model is executed increases in relation to the time with increasing engine speed ($\Delta t = 1°/(6 \cdot n_{\mathrm{eng}})$). The crank angle-resolved variables, such as in-cylinder gas states, burn rate, etc., are simulated for one lead cylinder only. Further cylinders are realized by 180° shift of the lead cylinder variable (4-cylinder diesel engine is considered). To simulate the cylinder pressure sensors, the calculated cylinder pressures are output as an analog signal via a D/A board with 1° CS crank angle resolution. To simulate the cylinder pressure sensors, the calculated cylinder pressures are also output with 1° CS crank angle resolution as analog signals via a D/A board.

The models described in Chapters 3 and 4 (incl. semi-physical injection model Appx. A.3) are simulated on the used real-time hardware without any limitations up to an engine speed of 6000 1/min. The limiting factor is not so much the computational effort of the cylinder model but rather the crank angle resolved output of the cylinder pressure, limited by the data transfer between processor board and D/A board and by the converter rate of the D/A board.

Further details regarding the real-time hardware and the model implementation are given in Appx. A.1.3.

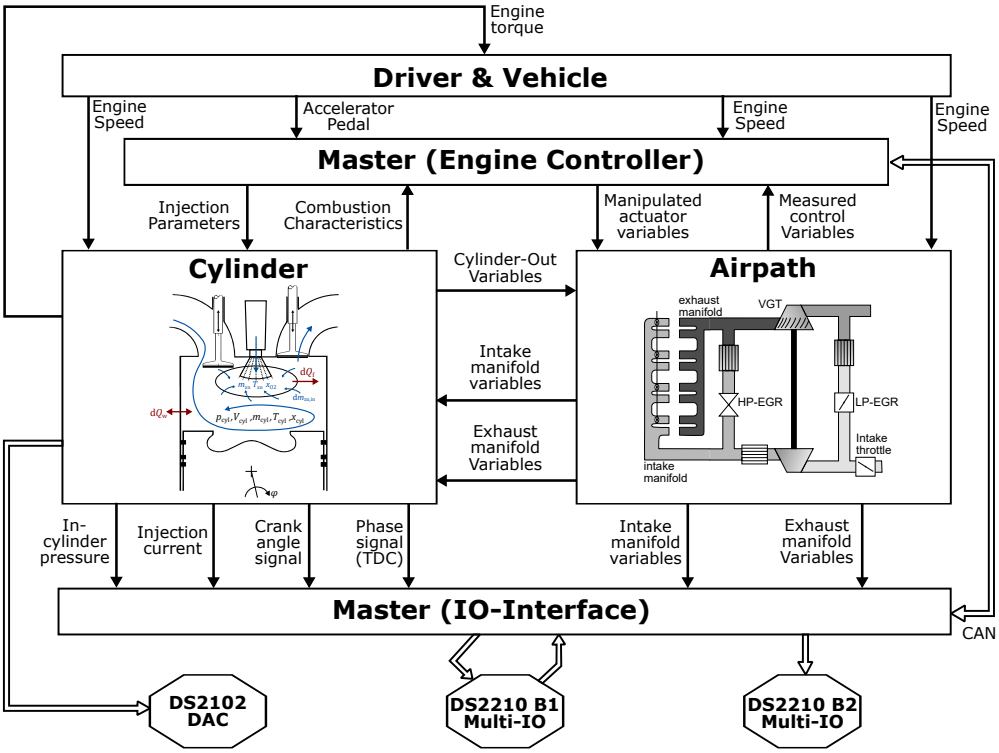

Figure 5.8: Structure and interfaces of the HIL simulation model implemented on a real-time system based on hardware from the company *dSPACE GmbH*; semi-physical airpath model from Ch. 3, cylinder model from Ch. 4, and injection model from Appx. A.3 are used as simulation models, see Appx. A.1.3 for more details

6 Conclusions

In this work, a modeling methodology for the systematic and efficient generation of semi-physical real-time models of a diesel engine is proposed. For the modeling and identification of the semi-physical real-time models, only online-capable, recursive identification methods are used, which makes this methodology particularly suitable for the online-application at the engine test bench. This allows the semi-physical real-time models to be obtained directly online during the measurement.

The modeling methodology is based on three steps. The first step is the derivation of a lean semi-physical model structure based on basic physical equations with unknown physical parameters. In the second step, these model equations are used for model-based state and parameter estimation to determine both unmeasured state variables and unknown parameters online based on available measurements. The third step involves experimental modeling of the estimated parameters to store their behavior as a function of the operating point. The implementation of these three steps leads to a semi-physical and real-time capable model in which the essential system behavior is described by simple physically interpretable equations and the matching to the real behavior is achieved by experimental (map-based) modeling of the parameters as functions of engine operating point.

Semi-physical modeling exploits the advantages of physical and experimental (data-based) modeling and offers a good compromise between good physical interpretability and the exact reproduction of the measured system behavior. When deriving a semi-physical model, the goal is to find simple physical equations that can be used to accurately describe the real system behavior for a constant operating point[1] with a particular set of constant parameters. The prerequisite is that it must be possible to model a changed system behavior, caused by a changed operating point, by simply adapting the parameters of the derived physical model equations.

A major issue in modeling (both physical and experimental) is the lack of system information required for model identification and the uncertainty of the available measurements. Kalman filtering methods offer the possibility of combing behavioral models with uncertainty assumptions regarding variables and measurements to allow both, the estimation of unknown system states and the filtering and correction of measured signals. In the case of nonlinear systems, the use of a Sigma-point Kalman filter is recommended for estimation, since it offers advantages (over the extended Kalman filter) such as a derivative-less and more accurate propagation of the statistical properties and an easier implementation for nonlinear systems.

To enable parallel, simultaneous estimation of both unknown states and parameters, the Kalman filter is extended by corresponding equations for the parameters (modeled as constant states). Depending on the dimension of the estimation problem and how the state variables and parameters are mathematically related, the combined state and parameter estimation is carried out as a joint

[1] or within a sufficiently small operating range

estimation or as a dual estimation. In the joint estimation, the uncertainties of states and parameters can be described more easily relative to each other using the filter noise parameters. For high-dimensional systems, where the relationships between state variables and parameters to be estimated are not so strong, it is recommended to split them into a dual estimation approach. In both case, the estimation behavior is controlled and adapted situation-wise via the filter noise parameters of the Kalman filter. However, the appropriate modeling of the noise parameter remains a major challenge.

The experimental modeling of the estimated parameters as a function of the engine operating point leads finally to the online identification of a semi-physical model. In this way, the variability of a parameter is stored in a purely mathematical model which allows the mapping of the real measured behavior. Since the dynamic system behavior is already described by the physical model part of the semi-physical real-time model, it is sufficient to use a local estimation approach for the identification of the operating point-dependent parameter model.

The modeling methodology is developed and applied to a common-rail diesel engine with dual-EGR and a variable exhaust gas turbocharger. It is applied to the two main subsystems of an internal combustion engine, the airpath system and the cylinder group.

Semi-physical airpath modeling

It was shown that the semi-physical modeling approach is well suited for modeling the airpath. This is mainly due to two reasons. On the one hand, the essential physical system behavior of the airpath can be separated from the engine speed-dependent behavior, and on the other hand, a physical mean-value airpath model can be assembled modularly using idealized basic elements such as ducts, flow resistors and heat exchangers. The first system property allows an easy online identification of the semi-physical airpath model in steady-state engine operation and the second property, the modularity, ensures that the overall state and parameter estimation problem can be split into multiple estimators, significantly reducing the implementation and computational workload of airpath estimation. Furthermore, thanks to this modularity, almost any arbitrary air system topologies with/without low-pressure EGR and multiple turbocharger stages, for both diesel and gasoline engines, can be modeled.

Semi-physical cylinder and combustion modeling

The greatest challenge in engine modeling is the generation of accurate but also real-time capable models of the complex physical and chemical processes inside the combustion chambers of the cylinder group. On the one hand, this is due to the high complexity and speeds of the chemical reaction and molecular transport processes in the cylinder. On the other hand, the processes in the combustion chamber are discontinuous, event-driven and strongly influenced by the engine operating cycle. Consequently, cycle-resolved model representation in the crank angle domain is chosen to model the processes inside the cylinder.

The modeling of combustion is based on a novel semi-physical approach. With this approach, it is possible to reproduce the crank angle resolved courses of the characteristic combustion phases of diesel combustion as a function of the injection course and the operating point. In simplified terms, the combustion process is described as a delayed system response to the injection process. The delay between the start of injection and the start of combustion is interpreted as dead time and the combustion rate curve as a dynamic process of higher order. A quasi-dimensional mixture model is derived that allows the decomposition of the fuel injection into three fuel mass fractions, which serve as input variables for the combustion phases. The courses of the combustion phases are described by semi-physical models, in which the crank angle resolved course of the release of burning energy is modeled by transfer functions in a crank angle frequency domain. The rate parameters or angular constants of these transfer functions are modeled as a function of the operating point (injection quantity and speed) using experimental map models.

This system theoretical model approach allows simplified modeling, in means of reduced number of equations, simpler mathematical formulations and reduced number of parameters. Compared to other combustion models from the literature, which usually involve complex couplings of equations and states, with this modeling approach the engine combustion is very easy to calculate using the few setting parameters (angular constants/rate parameters) for model adjustment. Additionally, this modeling approach is also feasible for the combination with less computing-intensive, recursive parameter estimation algorithms, allowing the model to be adapted online to real engine behavior.

The state and parameter estimation is mainly based on the in-cylinder gas pressure and the crankshaft angle, supported by additional variables which are reconstructed by using physics-based models in combination with state estimation techniques. The use of online state and parameter estimation methods for the estimation of cycle-resolved in-cylinder processes represents an additional scientific contribution of this work. The calculations of model equations and estimation algorithms are performed crank angle synchronously with a resolution of 1 degree.[2]

Applications

The methodology for generating the semi-physical real-time models was developed and tested on a prototyping real-time system (RCP) on the engine test bench. The real-time capability of model generation method using online methods, such as state and parameter estimation and recursive paramater estimator, is proven on the RCP system equipped with Dual-Core processor running each at 1 GHz clock rate. The computations of the airpath model and the cylinder model were distributed between the two processor cores.

The online identification of the semi-physical real-time models for the air system and the cylinder group is carried out in stationary engine operation. Estimated results are obtained within 20 to 30 duty cycles (40 to 60 revolutions), which corresponds to only a few seconds depending on the engine speed. This way, an efficient model generation can be realized during a stationary engine

[2] At least a crankshaft angle resolution of 1° is required for modeling heat release during combustion

measurement on the engine test bench. But it remains to be investigated whether this modeling methodology can also be used in more efficient measuring strategies.

With a crank-angle resolution of 1° CS, the cylinder estimation calculations can be performed up to a engine speed of 3000 1/min (calculation step size of $\approx 55\mu$s). Since the computations of the airpath models and estimator are executed with a higher calculation step size, it is possible to execute them up to the engine speed limit of 6000 1/min. For smaller crank angle resolutions <1 ° CS and higher engine speed, the calculations of the cylinder models and estimator must be implemented on more powerful computation hardware, e.g. FPGA-based real-time systems.

The lean physical model structure combined with the low computational effort of experimental models allows semi-physical real-time models to be used in many stages of the model-based development process. In this work, two applications of semi-physical real-time models are demonstrated.

As an application example in the context of combustion diagnostics at the test bench, the model-based combustion analysis (MBCA) is introduced. This can be seen as an extension of the commonly used cylinder pressure based combustion analysis provided by commercial pressure indication systems. Typical functionalities of pressure indication systems such as cylinder pressure analysis and heat rate calculation are then extended by the use of model-based state and parameter estimation providing additional information such as the dynamics of mixture formation or the shares and rates of the combustion phases based on the in-cylinder pressure sensor signals. The estimated variables and parameters allow the combustion processes to be characterized and compared with respect to the engine operating point; giving test bench engineers a better insight into the system behavior and supporting them in ECU calibration.

The application of the semi-physical models for real-time engine simulation was demonstrated on a hardware-in-the-loop test bench. The semi-physical real-time models of airpath and cylinder allow simulation of a combustion engine, including the highly time-resolved simulation of the analog signals of the cylinder pressure sensors. This enables testing and validation of cylinder pressure-based ECU function on the HIL test bench.

Outlook

A major advantage of semi-physical models is their good transferability to other systems which are based on the same fundamental physical principles. Thus, the treated methods are supposed to be suited for the modeling of spark-ignition combustion in gasoline engines as well as for the modeling of combustion of any liquid fuels like bio fuel or synthetic fuel and gases. This requires the engine-specific design parameters and the material constants of the used fuel to be adjusted. A prerequisite is that the course of heat release caused by combustion can be expressed by one or more overlapping transfer functions. However, proof of transferability to gasoline engines and other engine types is still pending, but should be the subject of future studies. It also remains to be evaluated whether the presented model approach can be used for multiple injection with highly dynamic piezo fuel injectors.

Furthermore, the proposed modeling approach provides a physical interpretability and characterization of the combustion dynamics based on the combustion phases and their angular constants. These parameters correspond to the rate at which the combustion energy is released locally in the combustion chamber. Consequently, the parameter of the combustion phase can be interpreted as a measure of local temperature gradients in the mixture and reaction zone. The higher the rate of heat release, the higher tends to be the local peak temperature occurring in the combustion chamber and leading to high local temperatures (> 2500 K), which are known to be the main cause for the formation of nitrogen oxide emissions. On the contrary, an increase of diffusive combustion leads to an increase of soot formation. Investigations of the relations between combustion phases, their characteristic angle constants and emission behavior shall be the scope of future research work.

Further, the presented mixture formation model can be used as basis for a two-zone model which is required for physical modeling the inhomogeneities in the combustion chamber causing the generation of nitrogen emissions and soot particles. The mixture formation must then be extended by equations for the temperature and oxygen inside the virtual mixing and reaction zone. The second zone (non-reaction) zone results then from mass and energy balance. A first modeling approach for the emission formation based on transfer functions rather than Arrhenius equations is presented in Weber (2019a) and Weber (2019b). There, the formation of nitrogen oxide and particulate emissions is modeled based on the modeled gas states of the mixture zone and on the shares of the diesel combustion phases. However, crank-angle resolved emission modeling requires smaller calculation step size (crank angle resolution smaller than $< 1°$) and additional measurement technology for model validation such as optical combustion analysis.

Semi-physical real-time models are also applicable in the design of ECU functions. They can be integrated into control functions to implement a model-based feedforward control that allows to impose a certain dynamic behavior to a system or to serve as virtual sensors of unmeasured system states that can be used for sensorless control.

In case of a model-based feedforward combustion control, the center of combustion and the peak value of heat rate can be predicted using the semi-physical combustion model. Measuring the cylinder pressure would then only be necessary at the test bench for the identification of the combustion model and the calibration of the model-based controller. The in-cylinder pressure sensors can then be omitted in series engines.

If in-cylinder pressure sensors are used in series engines, the method treated here can be used for combustion diagnosis and adaptation of combustion control during engine operation.[3] Knowing the combustion characteristics from cylinder estimation allows adjustment and optimization of injection and airpath control according to the properties and composition of the used fuel. Additionally, it enables fault detection in the injection system or the detection of fuel type and properties.

[3] Especially for heavy duty vehicle or marine engines, where the fuel might change depending on the geographical region the engine is operating

Appendix

A.1 Test benches

The research project for the development and validation of semi-physical real-time engine models was carried out with the use of two test benches. First, models and estimators were developed offline on the office PC and then implemented and tested on a hardware-in-the-loop engine simulator. The HIL simulator is connected to an RCP real-time system on which the models and estimators are implemented and tested. The RCP system is technically equivalent to the RCP system on the engine test bench, see Appx. A.1.2.

A.1.1 Engine test bench

The hardware setup of the engine test bed at the Institute of Automatic Control and Mechatronics at the Technische Universität Darmstadt is shown in Fig. A.1. The engine test bench is equipped with a 1.9L test diesel engine of the type GM/Opel Z19DTH (110 kW) connected to a speed-controlled 160 kW load machine. The specifications of the test engine GM/Opel Z19DTH are listed in Tab. A.1.

The setup of the engine test bench with all sensors and measurements is shown in Fig. A.1. Besides the series sensors, the test engine is equipped with additional sensors for pressure, temperature and actuator positions. Exhaust gas characteristics are measured by several measurement systems. Additional Bosch lambda sensors are installed at different positions at the exhaust pipe and the intake manifold. Nitrogen oxide is measured by NGK-Sensors and soot measurement is given by AVL 439 Opacimeter, AVL 483 MicroSoot and AVL 415S Smoke meter. Fuel mass flow can be measured by AVL 735 Mass Flow Meter and fuel temperature is controlled by AVL 753S.

Structure of the Test bed control, the measurement systems, and the used real-time system for prototyping are shown Fig. A.2. The test bed is equipped with three modular real-time systems (see Fig. A1). A dSPACE system is used for control and supervision of the load machine. Two further dSPACE systems are connected as multi-processor systems for Rapid Control Prototyping (RCP). One RCP system undertakes the task of engine control, including an air path control as well as an injection control via ETK-Bypassing and ETAS ES1000.

The second dSPACE system consists of a DS1007 Dual-Core Processor board connected to a DS2004 high speed A/D board and a DS4201 Prototyping board, which is customized to a Timer board. The Timer board processes the signals from incremental encoder mounted to the crankshaft, and generates an adjusted trigger signal depending on the preconfigured crank angle resolution. The trigger signal is then used for crank angle synchronous (CAS) data acquisition and as function call

Table A.1: Specifications of test engine and load machine

test engine	
Manufacturer	GM Powertrain Z19DTH
No. of cylinders	4
Displacement	1910 cm^3
Power	110 kW
Max. torque	315 Nm
Compression ratio	17.5
Injection system	Bosch CP1H
Turbo charger	Exhaust gas driven with VTG
EGR	High and low pressure EGR
Pressure sensors	KISTLER Type 6056A Kistler 2003
	Calibrated range 0 ... 100 bar
	Linearity $\leq \pm 0.3$ % / FSO (23°C)
	Hysteresis < 1 % / FSO
load machine	
Manufacturer/type	ABB Asynchronous machine
Max. power	160 kW
Max. torque	300 Nm
Max. speed	5000 1/min
Inertia	0.38 kgm^2

trigger signal for crank angle synchronous calculations on the DS1007 Dual-Core Processor board. On one of the processor cores runs an online indication system (Software package IndiSPACE), which provides, apart from acquisition of cylinder pressure and characteristics (pressure gradient, IMEP, etc.), also calculations of the rate of heat release as well as in-cylinder gas masses and temperatures for each cylinder. The second processor core is executed synchronously to the indication system, so that further parallel calculations can be performed. CAS-calculations are running on this processor core. These model calculations are the central element of the model-based combustion analysis. Via fast inter-processor communication, calculations of cylinder pressure traces and in-cylinder gas states from indication can be directly incorporated into the model calculations on the second processor core.

A.1.2 Rapid-Control Prototyping System

For the FVV research project, a real-time system equipped with a DS1007 processor board was set up. The DS1007 provides a dual core processor (each at 1 GHz clock rate) and low latency in terms of read/write access to the I/O boards. A high-speed A/D board and a Timer board are connected via Peripheral High Speed (PHS) bus to the processor board. The real-time system is connected to the host PC via an integrated Gigabit Ethernet port, providing the build and download of user-specific applications onto the two CPU core of the DS1007.

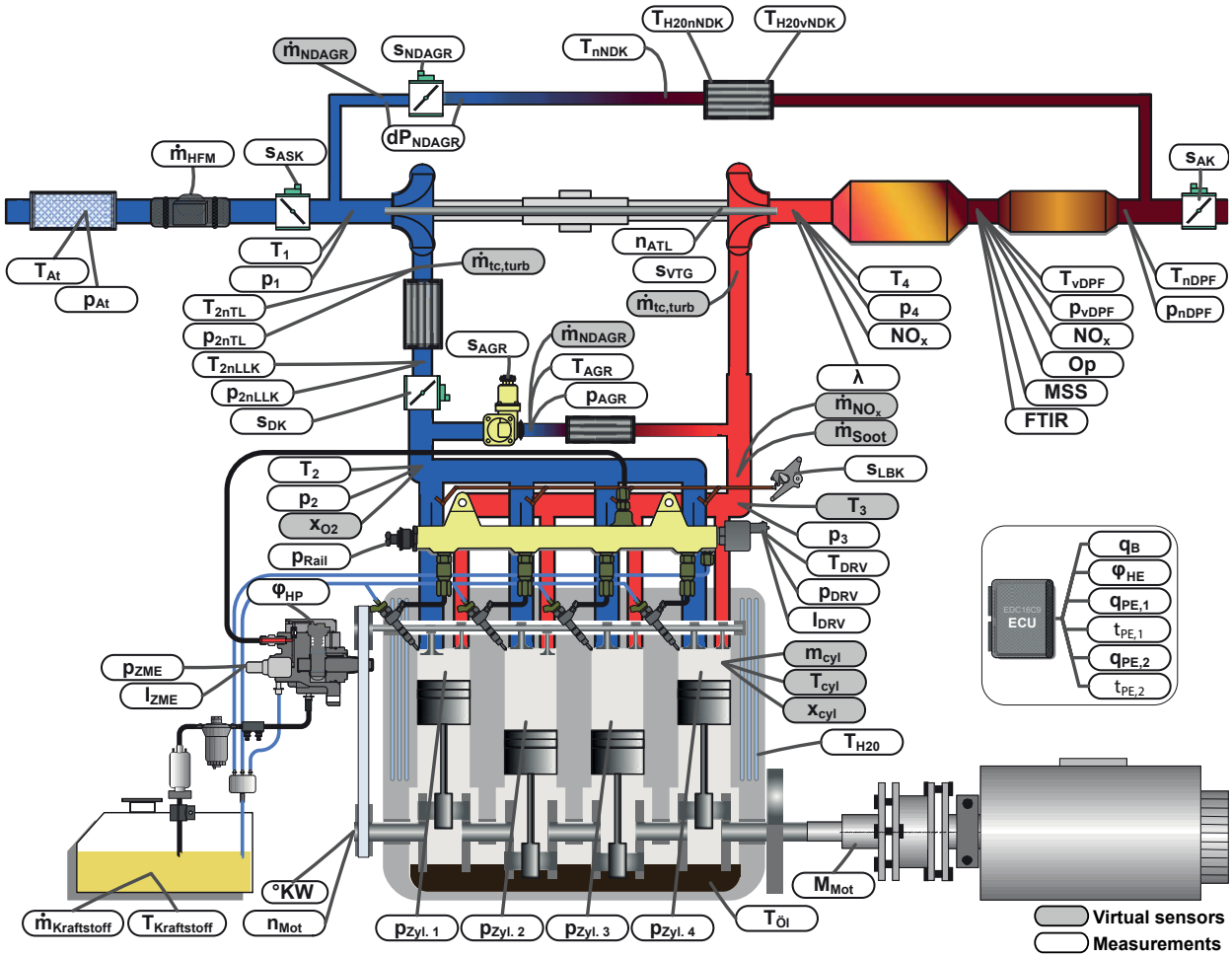

Figure A.1: Overview of the test engine with the available sensors and virtual sensors determined by real-time models or state estimators

A timer board developed at IAT, based on a DS4201S prototyping board, is used to convert the incremental encoder signal (pulse signal) into trigger signal, which is used to trigger the AD conversion of the DS2004 high-speed A/D board with preconfigured crank angle resolution. Using the crank angle synchronous trigger signal for A/D conversion enables crank-angle synchronous data processing of measured cylinder pressure signals. Therefore, the functionalities of a pressure indication system are implemented on of the two cores of the DS1007 processor board. The crank angle resolution can be set in the timer board (0.1°, 0.25°, 0.5°, 1°, 3°,...). A total of 16 independent analog signals with 16-bit resolution can be read in via the DS2004 (conversion time of approx. 800 ns).

Crank-angle synchronous data processing (CAS)

The incremental encoder usually outputs a high-resolution pulse signal, whereby the pulse width corresponds to a constant crank angle. The crankshaft speed can be determined on the basis of the pulse signal and knowledge of its pulse width. The phase signal serves as a reference for determining the absolute, cylinder-specific crankshaft angle. It usually indicates the top dead center

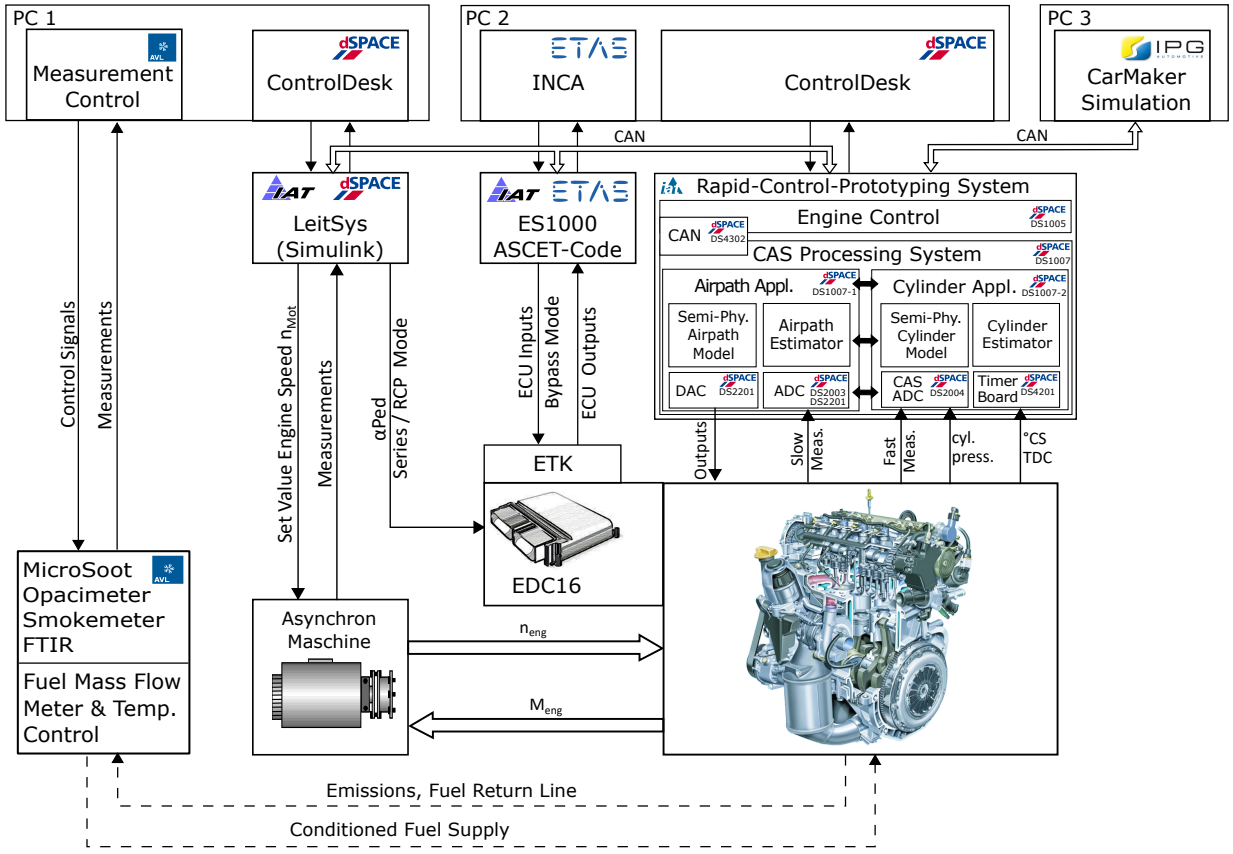

Figure A.2: Scheme of test bench automation, measurement systems and real-time hardware for Rapid Control Prototyping

of the master cylinder, with which the absolute crankshaft position of all engine cylinders can be determined according to the cylinder sequence and the offset. For four stroke engines it must be differed between the combustion TDC and the gas exchange TDC. This can be carried out be simple value check of the in-cylinder pressure at TDC excitation. While in-cylinder pressure values during combustion phase (closed system) are above 5 bar, the values lie below this mark during gas exchange phase (open system).

Pressure indication system

The basic functions of the pressure indication system *indiSPACE*-program are

- crank-angle synchronous data processing: Determining the crank angle of each cylinder and A/D-conversion of the measured signals with respect to current crank angle
- calculation of auxiliary in-cylinder variables as volume, intake and exhaust valve lift
- reconstruction of injection rate curve
- cylinder pressure analysis including the filtering and offset correction of measured in-cylinder pressure and the calculation of pressure characteristics, e.g. maximal pressure gradient, indicated mean pressure, difference pressure, etc.

- combustion analysis including the determination of the curves of heat rate and heat losses as well as the determination of combustion characteristics, e.g. start and center of combustion, efficiency, etc.

Cylinder pressure analysis

The cylinder pressure analysis is performed to calculate pressure characteristics and the heat release rate $\mathrm{d}Q_\mathrm{h}/\mathrm{d}\varphi$ during combustion, see Fig. A.3. Analysis is based on signals of in-cylinder gas pressure sensors, incremental encoder sensor, and phase sensor indicating the top dead center (TDC) of each cylinder.

Cylinder pressure sensor generally measure only the relative pressure. To achieve the absolute pressure, the sensor offset must be compensated. The offset can be calculated with the following equation

$$p_\mathrm{off} = p_\mathrm{m}(\varphi) - \frac{\Delta p(\varphi - 1)}{\left(\frac{V(\varphi-1)}{V(\varphi)}\right)^\kappa - 1} \tag{A.1}$$

during the phase 100° to 80° crank angle degrees before firing TDC. The characteristic values of the pressure curve are usually described by peak pressure p_max and the angle at which the peak pressure occurs φ_pmax, as well as the peak value of the pressure gradient $\mathrm{d}p_\mathrm{max}/\mathrm{d}\varphi$ and the angle φ_dpmax at which it occurs.

The indicated mean effective pressure (IMEP) p_mi is relevant for determining the indicated torque M_ind. This results from the integration of the cylinder gas pressure p_cyl along the volume change during a working cycle (Isermann 2014)

$$p_\mathrm{mi} = \frac{W}{V_\mathrm{d}} = \frac{1}{V_\mathrm{d}} \int_{\varphi=0°}^{720°} p_\mathrm{cyl}(\varphi) \frac{\mathrm{d}V(\varphi)}{\mathrm{d}\varphi} \mathrm{d}\varphi. \tag{A.2}$$

Mean indicated torque is given as

$$M_\mathrm{ind} = \frac{V_\mathrm{d}}{4\pi} p_\mathrm{mi}. \tag{A.3}$$

Based on the indicated torque and the engine speed, results the engine power

$$P_\mathrm{eng} = \eta_\mathrm{eff} M_\mathrm{ind} \omega_\mathrm{eng} \qquad \text{in kW} \tag{A.4}$$

and the specific fuel consumption

$$b_\mathrm{sfc} = \frac{m_\mathrm{f}}{P_\mathrm{eng}} = \frac{m_\mathrm{f}}{\eta_\mathrm{eff} M_\mathrm{ind} \omega_\mathrm{eng}} \qquad \text{in g/kW} \tag{A.5}$$

Pressure-based combustion analysis

The cylinder pressure-based combustion analysis includes the calculation of the rate of heat release (ROHR) and the calculation of characteristic values such as start/end of combustion (SOC/EOC), the centre of combustion (COC/CA50) and the maximum heat rate.

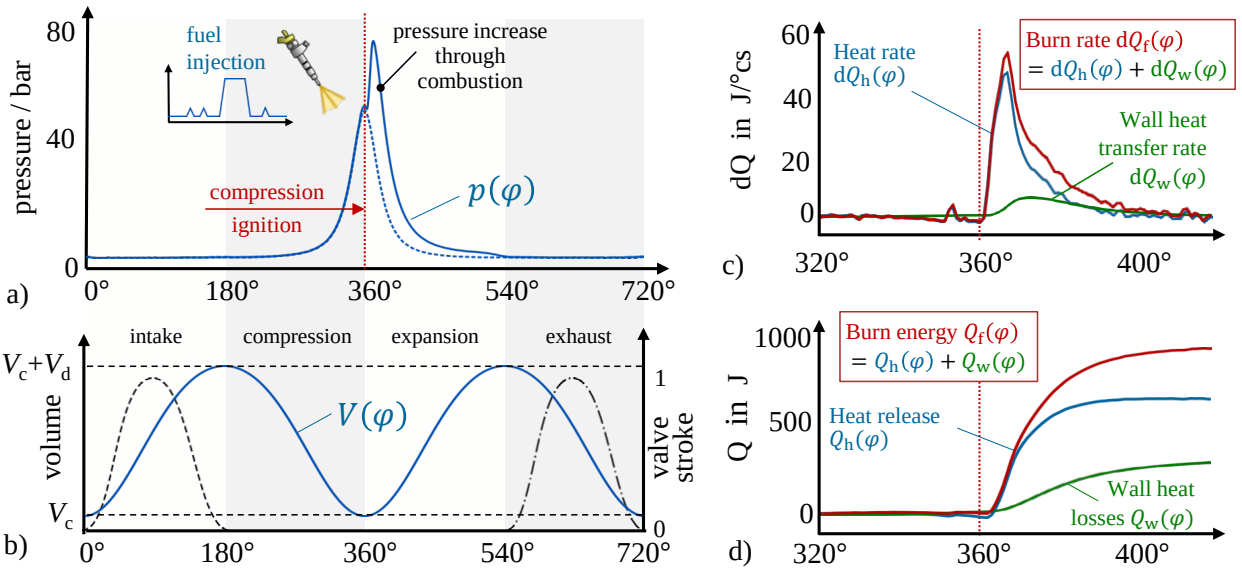

Figure A.3: Cylinder pressure and heat rate analysis for engine operating cycle: a) cylinder pressure curve $p(\varphi)$ (dashed line for towed (non-firing) mode); b) cylinder volume $V(\varphi)$ and intake/exhaust valve strokes; heat rate $\mathrm{d}Q_\mathrm{h}(\varphi)$, burn rate $\mathrm{d}Q_\mathrm{f}(\varphi)$ and wall heat transfer rate $\mathrm{d}Q_\mathrm{w}(\varphi)$ determined from cylinder pressure $p(\varphi)$ and volume $V(\varphi)$; d) cumulative/released heat energy Q_h, burn energy $Q_\mathrm{f}(\varphi)$ and wall heat energy $Q_\mathrm{w}(\varphi)$

There are two calculation rules for determination of heat release based on in-cylinder pressure and volume. First heat release calculation rule is based on the first law of thermodynamics

$$\frac{\mathrm{d}Q_\mathrm{f}}{\mathrm{d}\varphi} + \frac{\mathrm{d}Q_\mathrm{w}}{\mathrm{d}\varphi} + \frac{\mathrm{d}W_\mathrm{cyl}}{\mathrm{d}\varphi} = \frac{\mathrm{d}Q_\mathrm{h}}{\mathrm{d}\varphi} + \frac{\mathrm{d}W_\mathrm{cyl}}{\mathrm{d}\varphi} = \frac{\mathrm{d}U_\mathrm{cyl}}{\mathrm{d}\varphi} = m_\mathrm{cyl} c_\mathrm{v}(T_\mathrm{cyl}) \frac{\mathrm{d}T_\mathrm{cyl}}{\mathrm{d}\varphi} \tag{A.6}$$

Assuming that cylinder gas mass is constant, substitution the unknown temperature by ideal gas law in differential form

$$p_\mathrm{cyl} \frac{\mathrm{d}V_\mathrm{cyl}}{\mathrm{d}\varphi} + V_\mathrm{cyl} \frac{\mathrm{d}p_\mathrm{cyl}}{\mathrm{d}\varphi} = m_\mathrm{cyl} R \frac{\mathrm{d}T_\mathrm{cyl}}{\mathrm{d}\varphi} \tag{A.7}$$

and using the relation $\kappa = c_\mathrm{p}/c_\mathrm{v}$, results

$$\begin{aligned} \frac{\mathrm{d}Q_\mathrm{h}}{\mathrm{d}\varphi} &= \left(1 + \frac{c_\mathrm{v}}{R}\right) p_\mathrm{cyl} \frac{\mathrm{d}V_\mathrm{cyl}}{\mathrm{d}\varphi} + \frac{c_\mathrm{v}}{R} V \frac{\mathrm{d}p_\mathrm{cyl}}{\mathrm{d}\varphi} \\ &= \left(1 + \frac{1}{\kappa - 1}\right) p_\mathrm{cyl} \frac{\mathrm{d}V_\mathrm{cyl}}{\mathrm{d}\varphi} + \frac{1}{\kappa - 1} V_\mathrm{cyl} \frac{\mathrm{d}p_\mathrm{cyl}}{\mathrm{d}\varphi} \\ &= \frac{\kappa}{\kappa - 1} p_\mathrm{cyl} \frac{\mathrm{d}V_\mathrm{cyl}}{\mathrm{d}\varphi} + \frac{1}{\kappa - 1} V_\mathrm{cyl} \frac{\mathrm{d}p_\mathrm{cyl}}{\mathrm{d}\varphi} \end{aligned} \tag{A.8}$$

Using discrete formulation the heat rate is then determined from measured cylinder pressure $p(k)$, volume $V(k)$ and their difference quotients

$$\begin{aligned} \Delta Q_\mathrm{h}(k) &= \left(1 + \frac{1}{\kappa - 1}\right) p_\mathrm{cyl}(k) \Delta V_\mathrm{cyl}(k) + \frac{1}{\kappa - 1} V_\mathrm{cyl}(k) \Delta p_\mathrm{cyl}(k) \\ &= (1 + A(k))\, p_\mathrm{cyl}(k) \Delta V_\mathrm{cyl}(k) + A(k) V_\mathrm{cyl}(k) \Delta p_\mathrm{cyl}(k) \end{aligned} \tag{A.9}$$

Since the caloric value are generally temperature dependent, different approaches for the factor $A(k)$ are proposed by i.e. Bargende (1991), Beidl (2011b).

$$A(k) = 2.39 + 0.0008 \frac{T_{\varphi=240°\mathrm{CS}}}{[K]} \frac{p_{\mathrm{cyl}}(k) V_{\mathrm{cyl}}(k)}{p_{\varphi=240°\mathrm{CS}} V_{\varphi=240°\mathrm{CS}}} \tag{A.10}$$

The second way to calculated the heat release is based on the assumption of an isentropic state change proposed by Hohenberg (1982). Using isentropic state change equation leads to following equation

$$\begin{aligned} \Delta Q_{\mathrm{h}}(k) &= \frac{1}{\kappa - 1} V_{\mathrm{cyl}}(k) \left[p_{\mathrm{cyl}}(k) - p_{\mathrm{cyl}}(k-1) \left(\frac{V_{\mathrm{cyl}}(k-1)}{V_{\mathrm{cyl}}(k)} \right)^{\kappa} \right] \\ \Delta Q_{\mathrm{h}}(k) &= \frac{c_{\mathrm{v}}(T_{\mathrm{cyl}}(k)}{R} V_{\mathrm{cyl}}(k) \left[p_{\mathrm{cyl}}(k) - p_{\mathrm{cyl}}(k-1) \left(\frac{V_{\mathrm{cyl}}(k-1)}{V_{\mathrm{cyl}}(k)} \right)^{\kappa} \right] \end{aligned} \tag{A.11}$$

The specific heat capacity at constant volume can be calculated by using following approximation equation (Hohenberg 1982)

$$c_{\mathrm{v}}(T) = \frac{\mathrm{d}u}{\mathrm{d}T} = 0.7 + 10^{-3} \, (0.155 + A) \quad \text{in J/(kg K)} \tag{A.12}$$

with in-cylinder gas temperature T in K and gas pressure $p_{2\mathrm{i}}$ in the intake manifold in Pa (V_{d} in m, $Q_{\mathrm{h,total}}$ in J)

$$A_{\mathrm{SI}} = 0.1 \text{ for SI-engines} \tag{A.13}$$

$$A_{\mathrm{CI}} = \frac{Q_{\mathrm{h,total}} \cdot 56}{V_{\mathrm{d}} \cdot p_{2\mathrm{i}}} \text{ for CI-engines} \tag{A.14}$$

A comparison of different methods for fast, real-time capable heat rate calculation is carried out in Knerr et al. (2016).

Another way to calculate the heat flow during engine's operating cycle is proposed by J. B. Heywood (1988).

$$\frac{\mathrm{d}Q_{\mathrm{h}}(\varphi)}{\mathrm{d}\varphi} = \frac{n - \kappa}{n - 1} \frac{p(\varphi) V(\varphi)}{\kappa - 1} \left[\left(\frac{p(\varphi + \Delta\varphi)}{p(\varphi)} \right)^{\frac{n-1}{n}} - 1 \right]. \tag{A.15}$$

The isentropic coefficient κ is assumed to be constant and the polytropic coefficient n is given as

$$n(\varphi) = \frac{\lg\left(p(\varphi + \Delta\varphi)\right) - \lg\left(p(\varphi)\right)}{\lg\left(V(\varphi)\right) - \lg\left(V(\varphi + \Delta\varphi)\right)} \tag{A.16}$$

Hereby, the polytropic coefficient serves as characteristic value for the heat transfer during the particular working cycle phase. There are four special cases for the polytropic coefficient between which a distinction is made (Stephan et al. 2013):

- $n = 0$: isobaric state change
- $n = 1$: isothermic state change
- $n = \infty$: isochoric state change
- $n = \kappa$: isentropic or adiabatic state change, corresponds to Eq. (A.11)

By applying the Eqs. (A.15) and(A.16) to the overall working cycle, one obtains not only the heat transfer behavior during the high pressure phase in the closed cylinder, but also the characteristics of the heat transfer during the gas exchange process.

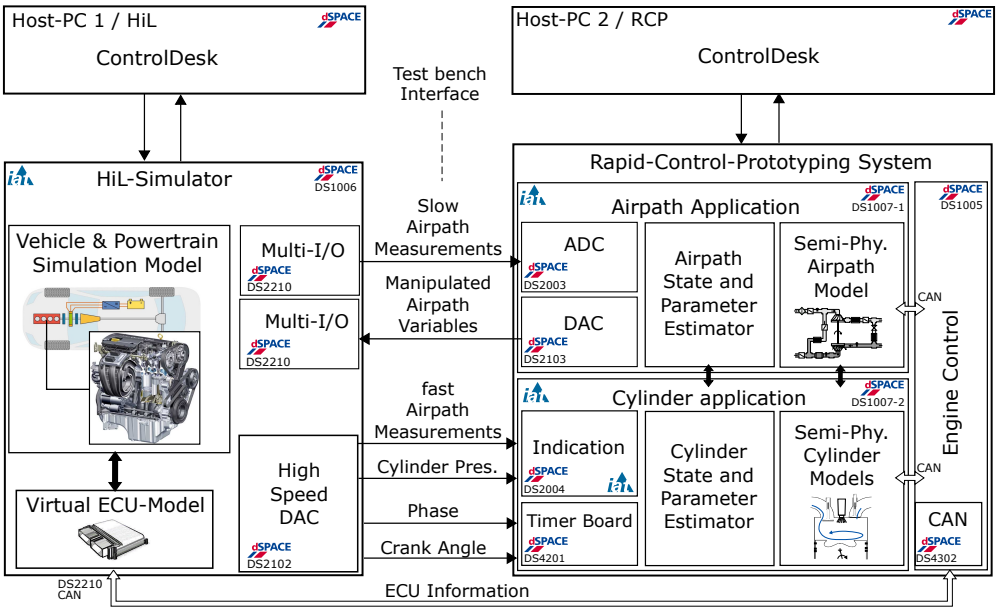

Figure A.4: Scheme of hardware and signal flow of Hardware-in-the-Loop test bench

A.1.3 Hardware-in-the-Loop test bench

The hardware-in-the-loop simulation test bench is also based on real-time systems from dSPACE. For more efficient development and testing of control functions, a replica of the RCP system was also set up at a hardware-in-the-loop test bench, see Appx A.1.3. The HIL simulator is connected to an RCP system that corresponds to the RCP system on the engine test bench in terms of both hardware and software. This means that newly developed software functions can first be tested in the real-time environment on the HIL test bench under repeatable conditions before they are tested on the real test engine on the engine test bench.

In contrast to the usual HiL application, where the engine is simulated with real actuator components and the real injection system, the RCP system is understood as the "hardware" of the HiL test bench instead of the real or prototyping ECU, see Fig. A.4. The interfaces were defined in such a way that a transition from the HiL to the engine test bench is possible without major changes. The interconnection of the development hardware and the HiL hardware is shown in Fig. A.4.

For the real-time simulation of the engine model (plant model), a Processor Board equipped with an AMD Opteron QuadCore Processor with 2.8 GHz is used. The plant model is divided among the four CPU cores. Fig. 5.8 shows the structure of the overall Hardware-in-the-Loop simulation model implemented as a multi-core real-time application.

One CPU core is dedicated for the simulation of the air system (CPU 1) and one CPU core to the simulation of the cylinder group (CPU 2). The analog sensor signals of the cylinder pressures as well as the crankshaft and camshaft signals are simulated on the CPU 2 and output via a separate D/A card (DS2102).

On the third CPU core, a vehicle model is calculated, which consists of the drivetrain model, from which the engine speed results and where the engine torque acts on. In addition, a driver is simulated who can follow a predefined test cycle. In a simplified way, the driver model represents a speed controller that uses the accelerator and brake pedals to control a predefined speed profile. Special algorithms are implemented within the driver model for the start-up (clutch engagement) and the shifting behavior. The powertrain model represents a longitudinal vehicle model that simulates the transmission, the clutch, the drive shaft and the tire-road contact (via Pajecka Magic Formula). The fourth CPU core (CPU 4) is used for I/O handling and simulation of the ECU interface (sensor and actuators). Furthermore, the base functions of the series ECU are implemented in order to be able to simulate the calibrated Series ECU mode as it is possible at the real engine test bed.

With the HiL Simulator it is also possible to simulate driving cycles, such as NEDC or WLTC or any other test cycle by specifying the vehicle speed profile.

A.2 Fundamentals on engine modeling

A.2.1 Thermodynamics

The *ideal gas law* [4] represents an algebraic equation connecting the thermodynamic gas state variables to each other (Stephan et al. 2013)

$$p\ V = m\ R\ T, \tag{A.17}$$

where $R = R(p, T, \lambda)$ in J/(kg K) is the general gas constant for air, which depends on the gas pressure p in Pa, the gas temperature T in Kand the air fuel ratio λ. If three of four gas state variables are known, the fourth can be determined using the ideal gas law. The differential form of the ideal gas law (A.17) is given as following (assuming $R \approx$ const.)

$$p\frac{\mathrm{d}V}{\mathrm{d}t} + V\frac{\mathrm{d}p}{\mathrm{d}t} = R\ T\frac{\mathrm{d}m}{\mathrm{d}t} + m\ R\frac{\mathrm{d}T}{\mathrm{d}t}. \tag{A.18}$$

The differential form is particularly useful in combination with assumptions regarding gas state change behavior, i.e. in case of a closed system with a constant volume $\mathrm{d}V/\mathrm{d}t = 0$ or mass $\mathrm{d}m/\mathrm{d}t = 0$, or if negligibly small changes in temperature $\mathrm{d}T/\mathrm{d}t \approx 0$ can be assumed, the corresponding terms in Eq. (A.18) can then be eliminated which allows a simplified calculation of the state variables.

Fundamental law for energy balance denoted as *first law of thermodynamics*

$$\mathrm{d}W_\mathrm{t} + \mathrm{d}Q_\mathrm{a} + \sum \mathrm{d}m_i\ (h_i + e_{\mathrm{a},i}) = \mathrm{d}U + \mathrm{d}E_\mathrm{a} \tag{A.19}$$

Where W_t is the technical work performed across the system boundary, Q_a is the heat flowing across the system boundary, $\mathrm{d}m_i$ are the masses flowing across the system boundary, h_i is the

[4] Ideal gas laws holds only for pressures $p < 5$ bar (VDI-Wärmeatlas 2013), which is sufficient for the air path system of combustion systems.

specific enthalpy of the mass $\mathrm{d}m_i$ flowing across the system boundary, $e_{\mathrm{a},i}$ is the specific external energy (e.g. kinetic or potential energy) of the mass m flowing across the system boundary, U the internal energy of the system, and E_a the external energy of the system (e.g., kinetic or potential energy).

A.2.2 Engine work cycle

The gas exchange process can be interpreted as an instationary process with open system boundaries. The energy balance of such instationary process is given by the first law of thermodynamics (Stephan et al. 2013)

$$\frac{\mathrm{d}W}{\mathrm{d}\varphi} + \frac{\mathrm{d}Q_\mathrm{h}}{\mathrm{d}\varphi} + \frac{\mathrm{d}H_\mathrm{in}}{\mathrm{d}\varphi} + \frac{\mathrm{d}H_\mathrm{out}}{\mathrm{d}\varphi} = \frac{\mathrm{d}U_\mathrm{cyl}}{\mathrm{d}\varphi} \tag{A.20}$$

On the right-hand side, U_cyl represents the internal energy of the gas inside the combustion chamber, calculated by using caloric gas properties of the gas. The caloric gas properties are generally pressure-, temperature- and air-fuel-ratio-dependent.

$$\frac{\mathrm{d}U_\mathrm{cyl}}{\mathrm{d}\varphi} = m_\mathrm{cyl}\left(\frac{\partial u_\mathrm{cyl}}{\partial T}\frac{\mathrm{d}T_\mathrm{cyl}}{\mathrm{d}\varphi} + \frac{\partial u_\mathrm{cyl}}{\partial \lambda}\frac{\mathrm{d}\lambda_\mathrm{cyl}}{\mathrm{d}\varphi} + \frac{\partial u_\mathrm{cyl}}{\partial p}\frac{\mathrm{d}p_\mathrm{cyl}}{\mathrm{d}\varphi}\right) + u_\mathrm{cyl}\frac{\mathrm{d}m_\mathrm{cyl}}{\mathrm{d}\varphi}. \tag{A.21}$$

The partial differentiations are determined by using polynomial formula $f(p, T, \lambda)$ proposed e.g. by Justi (1938) or Zacharias (1966), see Appx. A.2.4.

However, the pressure dependency $\partial u_\mathrm{cyl}/\partial p \approx 0$ and the influence of the air-fuel ratio $\partial u_\mathrm{cyl}/\partial \lambda \approx 0$ can be neglected for $\lambda >> 1$, so that the change of internal energy of the cylinder gas yields to

$$\frac{\mathrm{d}U_\mathrm{cyl}}{\mathrm{d}\varphi} = m_\mathrm{cyl}\frac{\partial u_\mathrm{cyl}}{\partial T}\frac{\mathrm{d}T_\mathrm{cyl}}{\mathrm{d}\varphi} + u_\mathrm{cyl}\frac{\mathrm{d}m_\mathrm{cyl}}{\mathrm{d}\varphi}. \tag{A.22}$$

Since the gas temperature in the combustion chamber changes significantly during the operating cycle, the temperature dependence must be taken into account. Alternatively, this can be done by using isochoric heat capacities $c_\mathrm{v} = \partial u_\mathrm{cyl}/\partial T|_{V=\mathrm{const.}}$ in J/(kg K). By using the heat capacities, the specific internal energy of the cylinder gas u_cyl yields to

$$u_\mathrm{cyl} \approx c_\mathrm{v} T_\mathrm{cyl} \tag{A.23}$$

The internal energy of the in-cylinder gas is then

$$\frac{\mathrm{d}U_\mathrm{cyl}}{\mathrm{d}\varphi} = m_\mathrm{cyl}c_\mathrm{v}\frac{\mathrm{d}T_\mathrm{cyl}}{\mathrm{d}\varphi} + c_\mathrm{v}T_\mathrm{cyl}\frac{\mathrm{d}m_\mathrm{cyl}}{\mathrm{d}\varphi} \tag{A.24}$$

The change of cylinder gas mass m_cyl results from the incoming $\dot{m}_\mathrm{in}$ and outgoing mass flow $\dot{m}_\mathrm{out}$, and the injected fuel $\dot{m}_\mathrm{f}$ (= injection rate$\dot{m}_\mathrm{inj}$), see Fig. 4.3 a). With respect to crank angle the cylinder gas mass is determined from mass balance equation as follows

$$\frac{\mathrm{d}m_\mathrm{cyl}}{\mathrm{d}\varphi} = \frac{\mathrm{d}m_\mathrm{in}}{\mathrm{d}\varphi} + \frac{\mathrm{d}m_\mathrm{out}}{\mathrm{d}\varphi} + \frac{\mathrm{d}m_\mathrm{f}}{\mathrm{d}\varphi}. \tag{A.25}$$

The left-hand side of (A.20) represents the energies entering and exiting across the system boundaries. Since the system boundary is drawn around the cylinder gas, the change of volume $\mathrm{d}V_{\mathrm{cyl}}/\mathrm{d}\varphi$ during the piston movement leads to volume work

$$\frac{\mathrm{d}W}{\mathrm{d}\varphi} = -p_{\mathrm{cyl}}\frac{\mathrm{d}V_{\mathrm{cyl}}}{\mathrm{d}\varphi}. \tag{A.26}$$

The indicated torque caused by pressure increase during combustion can be determined in similar way; see Appx A.1.2. Detailed information about how mechanical variables such as engine torque M_{eng} (and if necessary engine speed n_{eng}) can be calculated based on in-cylinder pressure and volume can be found in Isermann (2014).

The heat release rate $\mathrm{d}Q_{\mathrm{h}}/\mathrm{d}\varphi$ describes the change of heat energy of the cylinder gas. It is given by sum of burn rate $\mathrm{d}Q_{\mathrm{f}}/\mathrm{d}\varphi$ of the combustion and the heat transfer $\mathrm{d}Q_{\mathrm{w}}/\mathrm{d}\varphi$ between the in-cylinder gas and the cylinder walls

$$\frac{\mathrm{d}Q_{\mathrm{h}}}{\mathrm{d}\varphi} = \frac{\mathrm{d}Q_{\mathrm{f}}}{\mathrm{d}\varphi} + \frac{\mathrm{d}Q_{\mathrm{w}}}{\mathrm{d}\varphi}. \tag{A.27}$$

During the combustion process, injected fuel mass is converted to burning energy Q_{f}. The release of burning energy is described total burn rate $\mathrm{d}Q_{\mathrm{f}}/\mathrm{d}\varphi$. Since combustion energy is added, Q_{f} is accounted with a positive sign. Depending on the current temperature gradient between gas temperature T_{cyl} and wall temperature T_{w}, the heat transfer rate $\mathrm{d}Q_{\mathrm{w}}/\mathrm{d}\varphi$ is either positive or negative. For instance, in a warmed-up internal combustion engine, there is usually a heat transfer from the hot inner cylinder walls to the cooler gas inflowing through the intake valves during. Compression and combustion cause the gas temperature to exceed the cylinder wall temperature, so that the heat flow reverses and heat losses occur. Both heat release through combustion and heat transfer between cylinder gas and wall are subject to complex physical processes. Detailed modeling of these processes is not reasonable for real-time applications. Therefore, only zero- or quasi-dimensional modeling approaches are considered. Wall heat transfer model is treated in Sect. 4.3 and combustion modeling in Sect. 4.4.

Enthalpy flows $\mathrm{d}H$ are also entering and leaving through the intake and exhaust valves proportional to the corresponding valve mass flows

$$\frac{\mathrm{d}H_{\mathrm{in}}}{\mathrm{d}\varphi} = h_{\mathrm{in}}\frac{\mathrm{d}m_{\mathrm{in}}}{\mathrm{d}\varphi} = \left(u_{\mathrm{in}}(T_{\mathrm{in}}) + RT_{\mathrm{in}}\right)\frac{\mathrm{d}m_{\mathrm{in}}}{\mathrm{d}\varphi}, \tag{A.28}$$

$$\frac{\mathrm{d}H_{\mathrm{out}}}{\mathrm{d}\varphi} = h_{\mathrm{out}}\frac{\mathrm{d}m_{\mathrm{out}}}{\mathrm{d}\varphi} = \left(u_{\mathrm{cyl}} + RT_{\mathrm{cyl}}\right)\frac{\mathrm{d}m_{\mathrm{out}}}{\mathrm{d}\varphi}. \tag{A.29}$$

While the specific intake enthalpy $h_{2\mathrm{i}}$ depends on the intake gas temperature $T_{\mathrm{in}}(\approx T_{2\mathrm{i}})$, the specific exhaust enthalpy h_{out} is a function of in-cylinder gas temperature T_{cyl} during the exhaust phase. The internal energies of intake and in-cylinder gas are either determined from polynomial formulas or lookup-tables as functions of temperature. Alternatively, the specific enthalpies can be determined based on isobaric heat capacity c_{p} $(= c_{\mathrm{v}} + R)$ in J/(kg K),

$$h_{\mathrm{in}} = c_{\mathrm{p}}T_{\mathrm{in}} = (c_{\mathrm{v}} + R)T_{\mathrm{in}}, \tag{A.30}$$

$$h_{\mathrm{cyl}} = c_{\mathrm{p}}T_{\mathrm{cyl}} = (c_{\mathrm{v}} + R)T_{\mathrm{cyl}}. \tag{A.31}$$

Finally, through insertion of Eqs. (A.24) to (A.31) into the energy balance equation (A.20) results the following relation

$$- p_{\mathrm{cyl}} \frac{\mathrm{d}V_{\mathrm{cyl}}}{\mathrm{d}\varphi} + \frac{\mathrm{d}Q_{\mathrm{f}}}{\mathrm{d}\varphi} + \frac{\mathrm{d}Q_{\mathrm{w}}}{\mathrm{d}\varphi} + c_{\mathrm{p}} T_{\mathrm{in}} \frac{\mathrm{d}m_{\mathrm{in}}}{\mathrm{d}\varphi} - c_{\mathrm{p}} T_{\mathrm{cyl}} \frac{\mathrm{d}m_{\mathrm{out}}}{\mathrm{d}\varphi} = m_{\mathrm{cyl}} c_{\mathrm{v}} \frac{\mathrm{d}T_{\mathrm{cyl}}}{\mathrm{d}\varphi} + c_{\mathrm{v}} T_{\mathrm{cyl}} \frac{\mathrm{d}m_{\mathrm{cyl}}}{\mathrm{d}\varphi}. \quad \text{(A.32)}$$

A.2.3 Heat transfer

The stationary heat transfer between two mediums i and j and their corresponding temperature T_i and T_j can be determined with the help of Newton's law as follows

$$\dot{Q}_{i \to j} = \alpha_{i \to j} A_{i \to j} \left(T_i - T_j \right) \quad \text{(A.33)}$$

with the heat transfer coefficient $\alpha_{i \to j}$ in J/(m^{2}Ks) and the heat transfer surface $A_{i \to j}$ in m^2. The stationary heat transfer between the in-cylinder gas and the surrounding cylinder wall surface is then

$$\begin{aligned} \frac{\mathrm{d}Q_{\mathrm{w}}}{\mathrm{d}\varphi} = \frac{\mathrm{d}q_{\mathrm{w}}}{\mathrm{d}\varphi} A_{\mathrm{w}} &= \alpha_{\mathrm{w}} A_{\mathrm{w}} \left(T_{\mathrm{cyl}} - T_{\mathrm{w}} \right) \frac{\mathrm{d}t}{\mathrm{d}\varphi} \\ &= \alpha_{\mathrm{w}}(\varphi) A_{\mathrm{w}}(\varphi) \left(T_{\mathrm{cyl}}(\varphi) - T_{\mathrm{w}} \right), \end{aligned} \quad \text{(A.34)}$$

with $\alpha_{\mathrm{w}}(\varphi)$ representing the heat transfer coefficient, $A_{\mathrm{w}}(\varphi)$ the effective heat transfer surface, and the temperature difference $\left(T_{\mathrm{cyl}}(\varphi) - T_{\mathrm{w}} \right)$ as driving force for the heat transfer

Cylinder wall temperature

In Sargenti (2004), a generally applicable wall temperature model is presented that allows the calculation of the wall temperature at several locations in the combustion chamber (valves, liners, etc.). Due to its model complexity, this model is not suitable for use in real time applications. Additionally, model validation is not possible since series engines are not equipped with temperature sensors inside the combustion chamber. An alternative to a rather detailed wall temperature model is the empirical formula given by H. Müller and Bertling (1971)

$$T_w = 360 + 9 \lambda_{\mathrm{air}}^{0.4} \sqrt{d_{\mathrm{p}} n_{\mathrm{eng}}} \quad \text{in K}, \quad \text{(A.35)}$$

with the air excess factor λ_{air}, the piston diameter d_{p} in m, and the engine speed n_{eng} in 1/min. However, this calculation formula represents rather a rough estimate, since it does not consider relevant influencing factors such as those occurring in turbocharged engines with direct injection. In addition, a model of the excess air factor must be given.

The heat transfer surface $A_{\mathrm{w}}(\varphi)$ yields from the cylinder liner surface $A_{\mathrm{l}}(\varphi) = \pi d_{\mathrm{b}} s_{\mathrm{p}}(\varphi)$ depending on the bore diameter d_{b} and the piston stroke $s_{\mathrm{p}}(\varphi)$, the cylinder head surface A_{h}, the piston surface A_{p} and the its top land $A_{\mathrm{top}} = 2\pi d_{\mathrm{p}} h_{\mathrm{top}}$ with a correction factor 0.25 (Hohenberg 1980)

$$\begin{aligned} A_{\mathrm{w}}(\varphi) &= A_{\mathrm{l}}(\varphi) + A_{\mathrm{h}} + A_{\mathrm{p}} + 0.25 A_{\mathrm{top}} \\ &= \pi d_{\mathrm{b}} s_{\mathrm{p}}(\varphi) + A_{\mathrm{h}} + A_{\mathrm{p}} + 0.5 \pi d_{\mathrm{p}} h_{\mathrm{top}}. \end{aligned} \quad \text{(A.36)}$$

Heat transfer coefficient

The developed approaches for the calculation of the heat transfer coefficient α_w can be divided into two categories: *empirical approaches* such as that developed by Nusselt (1923), where the coefficient is determined empirically from experiments, and approaches based on the *similarity theory*, see Pflaum and Mollenhauer (1977, p. 41 ff.) for more details. However, only the latter can be applied to different engines (Bargende 1991). The first and most commonly used approach for the heat transfer coefficient is the equation of Woschni (1970).[5]

The derivation of the heat transfer coefficient α is based on the similarity theory proposed by Nusselt (1910) and starts from the correlation of *dimensionless numbers* to describe the phenomena of the heat transfer. In case of forced heat transfer the correlation of dimensionless number is generally given as

$$\mathrm{Nu} = C \cdot \mathrm{Re}^{\mathrm{m}} \cdot \mathrm{Pr}^{\mathrm{n}}, \tag{A.37}$$

with the dimensionless numbers

$$\begin{aligned} \mathrm{Nu} &= \frac{\alpha \cdot d}{\lambda}, \\ \mathrm{Re} &= \frac{w \cdot d \cdot \rho}{\eta}, \\ \mathrm{Pr} &= \frac{\nu}{a} = \frac{c_{\mathrm{p}} \cdot \eta}{\lambda} = \frac{\nu \cdot \rho \cdot c_{\mathrm{p}}}{\lambda}. \end{aligned} \tag{A.38}$$

The *Nusselt number* Nu describes convective heat transfer in the temperature boundary layer at the gas-wall heat transition. It relates between the heat transfer coefficient α multiplied by a characteristic length d and the heat conductivity λ. Even though in the case of forced convection the heat at the wall can only be transferred by heat conduction $\dot{q} = -\lambda(\partial T/\partial y)$, it is still referred to as convection, since the temperature gradient $(\partial T/\partial y)$ is influenced by the flow velocity of the fluid (Pischinger et al. 2009). The *Reynolds number* Re describes the flow conditions at the boundary layer. The *Prandtl number* Pr describes the physical material properties of fluids by the kinematic viscosity ν and the heat conductivity λ and thus provides the connection between these two boundary layer at the heat transition.

Woschni is treating the flow inside internal combustion engines as turbulent pipe flow. For this heat transfer problem, the following exponents have been found to be generally valid:

$$\mathrm{m} = 0.78 \qquad \mathrm{n} = 0.33$$

Since the value of $\mathrm{Pr}^{0.33}$ does not change significantly within the engine-relevant temperature and pressure range, $\mathrm{Pr}^{0.33}$ can assigned to the constant factor C.

By substituting the Nu and Re into (A.37) and rearranging the equation regarding the heat transfer coefficient α, results

$$\alpha = C \cdot d^{m-1} \cdot \lambda \cdot \left(\frac{w \cdot \rho}{\eta}\right)^{m}. \tag{A.39}$$

[5] it is also the first approach applied within a computer-aided calculation of the working cycle

The thermal conductivity $\lambda = f(T)$, the dynamic viscosity $\nu = f(T)$ and the density $\rho \approx$ const. $\cdot\, p/T$ are described by polynomials depending on gas temperature T and gas pressure p. The characteristic length d and the velocity w must be defined engine-specifically as a function of motor parameters or variables. Despite the complex processes involved in heat transfer, e.g. different engine types/geometries, locally varying temperature gradients, etc., the approach for the mean heat transfer coefficient based on similarity theory has proven to be successful in many engineering applications. However, the appropriate consideration of the changing gas properties and flow conditions during the working cycle is main issue in modeling the heat transfer coefficient.

The global wall heat transfer coefficient α_w is given by Woschni (1970)

$$\alpha_\mathrm{w} = 130 \cdot d_\mathrm{p}^{-0.2} \cdot p^{0.8} \cdot T^{-0.53} \cdot w^{0.8}. \tag{A.40}$$

Woschni's approach for the local average velocity in the cylinder w is composed of an engine speed-dependent term, represented by the mean piston speed c_m in m/s, and a term considering the influence of the combustion

$$w = C_1 c_\mathrm{m} + C_2 V_\mathrm{d} \frac{T_\mathrm{ivc}}{p_\mathrm{ivc} V_\mathrm{ivc}} \left(p - p_\mathrm{drag}\right) \tag{A.41}$$

Combustion has an impact on the inhomogeneities of the gas state and on the flow conditions during combustion causing an increase of turbulence. The turbulence increase through combustion is described by the pressure difference $p_\mathrm{diff} = p - p_\mathrm{drag}$. Woschni gives different constants C_1, C_2 for the individual phases of the work cycle:

$$C_1 = 6.18 + 0.417 \frac{c_\mathrm{u}}{c_\mathrm{m}} \qquad \text{gas exchange phase (low pressure phase)}$$
$$C_1 = 2.28 + 0.308 \frac{c_\mathrm{u}}{c_\mathrm{m}} \qquad \text{compression and expansion (high pressure phase)}$$

with the swirl velocity c_u in m/s for the consideration of intake swirl,

$$C_2 = 3.24 \cdot 10^{-3} \qquad \text{for DI-engines and SI-engines}$$
$$C_2 = 6.22 \cdot 10^{-3} \qquad \text{for pre-chamber engines}$$

However, experiments have shown repeatedly that the heat transfer coefficient is too low in towed engine operation mode and at low load, so K. Huber (1990) adjusted the velocity term as follows

$$w = c_\mathrm{m} \left[1 + 2 \left(\frac{V_\mathrm{c}}{V(\varphi)} \right)^2 p_\mathrm{mi}^{-0.2} \right], \qquad p_\mathrm{mi}(\text{in bar}) \geq 1. \tag{A.42}$$

A notable improvement is the consideration of the crank angle resolved cylinder volume $V(\varphi)$. Hohenberg (1980) proposed also an equation for the heat transfer coefficient, in which the variable cylinder volume $V(\varphi)$ is considered as characteristic length instead of the piston diameter d_p.

$$\alpha_\mathrm{w} = 130 \cdot V^{-0.06} \cdot p^{0.8} \cdot T^{-0.4} \cdot (c_\mathrm{m} + 1.4)^{0.8} \quad \text{(in SI units)}. \tag{A.43}$$

The approach of Bargende (1991) was originally developed for gasoline engines[6]. Similar to Hohenberg the variable cylinder volume is used as characteristic length to consider the specific engine geometry and crank angle dependence. For the calculation of the temperature dependent material constants of the heat transfer coefficient, the mean temperature $T_\mathrm{m} = (T_\mathrm{cyl} + T_\mathrm{w})/2$ is used instead of the gas temperature and the current gas composition is taken into account by the air content.

$$\alpha_\mathrm{w} = C \cdot V^{-0.073} \cdot p^{0.78} \cdot T_\mathrm{m}^{-0.477} \cdot w^{0.78} \cdot \Delta \quad \text{(in SI units).} \tag{A.44}$$

The velocity term w in the Reynolds number is described by means of the actual piston speed $w_\mathrm{p}(\varphi)$ m/s and the turbulent kinetic energy k in $\mathrm{m}^2/\mathrm{s}^2$

$$w = \frac{1}{2}\sqrt{\frac{8}{3}k + w_\mathrm{p}(\varphi)^2}. \tag{A.45}$$

The turbulent kinetic energy k is modeled by a simplified, global k-ε model

$$\frac{\mathrm{d}k}{\mathrm{d}t} = \left[-\frac{2}{3}\frac{k}{V}\frac{\mathrm{d}V}{\mathrm{d}t} - \varepsilon\frac{k^{1.5}}{l} + \varepsilon_\mathrm{q}\frac{k^{1.5}}{l}\right] \tag{A.46}$$

Since the heat transfer is strongly influenced by the instantaneous flow field, the mean piston velocity c_m in the velocity term of the Re number does not represent sufficiently accurate the crank angle dependent turbulence and heat transfer. Therefore, the approaches of Woschni (1970), Hohenberg (1980) and K. Huber (1990) do not adequately describe the heat transfer coefficient during the charge exchange phase. A solution is to replace the mean piston velocity c_m by the actual inlet and outlet flow velocities in order to achieve a better agreement.

In Robert Pivec and Sams (1998), an approach for the heat transfer at the inlet and outlet, developed by Zapf (1969), is investigated by means of comparisons with experiments and CFD simulation in more detail. In Zapf's approach, the Nusselt equation (A.37) is formulated separately for the inlet and outlet ports, respectively. The velocity term in the Re number is described by the mass flows, and the characteristic length dimension is included in the calculation of the heat transfer coefficient by the valve lift history. The heat transfer coefficients for the intake process α_iv and the exhaust process α_ev are given in $\mathrm{W}/(\mathrm{m}^2\mathrm{K})$ as

$$\begin{aligned}
\alpha_\mathrm{iv} &= 2.152\left(1 - 0.765\frac{s_\mathrm{iv}}{d_\mathrm{iv}}\right)\dot{m}_\mathrm{iv}^{0.5}T^{0.33}d_\mathrm{2i}^{1.5} \\
\alpha_\mathrm{ev} &= 1.785\left(1 - 0.797\frac{s_\mathrm{ev}}{d_\mathrm{ev}}\right)\dot{m}_\mathrm{ev}^{0.5}T^{0.41}d_3^{1.5}
\end{aligned} \tag{A.47}$$

with valve strokes s_i and diameters d_i in mm, temperature T in K, and valve mass flows in kg/s (Robert Pivec and Sams 1998). Investigations of Zapf's approach in Robert Pivec and Sams (1998) and later in Wimmer et al. (2000) show, compared to Woschni's approach for the gas exchange phase, good compliance with experimentally determined heat transfer coefficient during both intake and exhaust phase. In Wimmer et al. (2000) it is also shown that the heat transfer coefficients

[6] it was later also applied to diesel engines (Kozuch 2004)

in the inlet and outlet have a nearly linear-proportional relationship to the respective mass flow. However, the investigations of Wimmer et al. (2000) also show that the approach according to Zapf requires slight adjustments of the constants in (A.47) when transferred to different engine types and geometries.

A.2.4 Material constants

To calculate the gas states in the air path, the properties of the combustion gas and the fuel are necessary. The combustion gas consists of a mixture of fresh air and the returned burnt fuel-air mixture or residual gas remaining in the combustion chamber. Relevant for the calculation are the caloric properties, which change depending on temperature, pressure and composition of the mixture. Besides Justi's approach, there is the also widely used approach of Zacharias (1966), which additionally considers the pressure dependence. In the context of an online calculation, however, this has the consequence that an iterative calculation of the caloric property becomes necessary due to the inclusion of pressure. Furthermore, the comparison of both approaches does not show a significant increase in accuracy by including the pressure.

Caloric Properties of combustion gas

The caloric properties such as internal energy u and the heat capacity c_v of the combustion gas are calculated using the established empirical formula proposed by Justi (1938), which is a polynomial function of temperature T in K and air-fuel ratio λ

$$\begin{aligned} u(T,\lambda) = 0.1445\Big[1356.8 &+ \left(489.6 + \frac{46.4}{\lambda^{0.93}}\right)(T - T_{\text{ref}})\,10^{-2} \\ &+ \left(7.768 + \frac{3.36}{\lambda^{0.8}}\right)(T - T_{\text{ref}})^2\,10^{-4} \\ &- \left(0.0975 + \frac{0.0485}{\lambda^{0.75}}\right)(T - T_{\text{ref}})^3\,10^{-6}\Big] \end{aligned} \tag{A.48}$$

in kJ/kg and with respect to the reference temperature $T_{\text{ref}} = 273.15$ K. The heat capacity c_{v} is determined via derivation of (A.48) with respect to temperature

$$c_{\text{v}}(T,\lambda) = \frac{\mathrm{d}u(T,\lambda)}{\mathrm{d}T}. \tag{A.49}$$

The influence of changes in air fuel ratio $\mathrm{d}u(T,\lambda)/\mathrm{d}\lambda$ can be considered by using the derivate of (A.48) regarding λ.

These equations apply to $\lambda > 1$ and temperatures. Since diesel engine combustion is generally carried out over-stoichiometric and the mean cylinder gas temperature lies below < 2000 K, the use of Justi's equations for calculation of the caloric properties within the one-zone model is valid (Merker and Schwarz 2009).

A.2.5 Mechanical system

Piston displacement and speed

The displacement of a piston s_p in dependence on the crankshaft angle ϕ in rad ($= \varphi$ [°CS] $\cdot \frac{\pi}{180}$) can be described by

$$s_p(\phi) = r_{cs}\left[1 + \frac{1}{\lambda_{cr}} - \cos\phi - \frac{1}{\lambda_{cr}}\sqrt{1 - \lambda_{cr}^2 \sin^2\varphi}\right] \text{ in m} \tag{A.50}$$

with the stroke-to-connection rod ratio between

$$\lambda_{cr} = \frac{r_{cs}}{l_{cs}},$$

where r_{cs} is the crankshaft radius and l_{cs} represents the connection rod length. The current piston speed w_p in dependence on ϕ results from differentiation of Eq. (A.50) as follows

$$\frac{ds_p(\phi)}{d\varphi} = w_p(\phi) = r_{cs}\left(\sin(\phi) + \frac{\lambda_{cr}}{2}\frac{\sin(2\phi)}{\sqrt{1 - \lambda_{cr}^2 \sin^2(\phi)}}\right) \text{ in m/rad.} \tag{A.51}$$

The average piston speed over one stroke is determined as follows

$$\overline{w}_p = \frac{1}{\pi}\int_0^{\pi} w_p(\phi)d\phi = \frac{2r_{cs}\omega_{eng}}{\pi} = 4r_{cs}n_{eng} \tag{A.52}$$

Cylinder volume

The cylinder volume and its change can be determined individually for each cylinder based on the absolute crank angle φ and engine geometry parameter. The volume is a function of the current crankshaft angle position and therefore is independent of the other gas states.

$$V_{cyl}(\varphi) = V_c + \frac{V_d}{2}\left[1 - \cos(\phi) + \frac{1}{\lambda_{cr}}\left(1 - \sqrt{1 - \lambda_{cr}^2 \sin^2(\phi)}\right)\right] \tag{A.53}$$

The change of cylinder volume results from its derivation regarding the crankshaft angle φ

$$\frac{dV_{cyl}(\varphi)}{d\varphi} = \frac{V_d}{2}\left(\sin(\phi) + \frac{\lambda_{cr}}{2}\frac{\sin(2\phi)}{\sqrt{1 - \lambda_{cr}^2 \sin^2(\phi)}}\right), \tag{A.54}$$

whereas $\lambda_{cr} = r_{cs}/l_{cr}$ represents the ratio between crankshaft radius r_{cs} and connecting rod length l_{cr}.

Calculation of valve lift

The curve of the intake and exhaust valve strokes are determined based on the approach given by Urlaub (1995). There, the course of the valve stroke movement is modeled with the help of several curve segments of a circle that merge into one another. In order to achieve the smoothest possible curve, the cam shape is designed in such a way that no acceleration changes occur. The principle is illustrated in Fig. A.5.

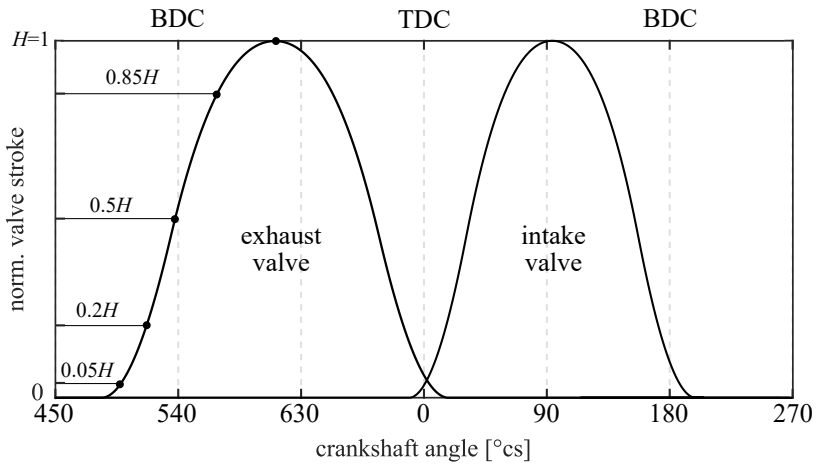

Figure A.5: Courses of intake and exhaust valve strokes with respect to crankshaft angle of the test engine GM/Opel Z19 DTH (A.1.1)

A.2.6 Air system

The inputs of the storage elements are the mass flow rates of the inflowing $\dot{m}_{\text{in},i}$ and outflowing gas mass $\dot{m}_{\text{out},j}$, the inflow temperatures $T_{\text{in},i}$) (representing the enthalpy $h(T_{\text{in},i})$ of the inflows) and the inflow air mass fraction $X_{\text{in},i} \in [0; 1]$. Outputs are the gas states inside the gas storage defined by its mass m_{st}, pressure p_{st}, temperature T_{st} and air content X_{st}.

Gas storages with ideal mixture

The gas storage element can be regarded as open thermodynamic system with p inflows and q outflows of mass and energy crossing system boundaries, see Fig. 3.3 a). The gas mixture inside the storage is ideally mixed and assumed to be uniform in composition and state at each point of time (J. B. Heywood 1988), which stands in accordance with the lumped parameter modeling approach. The gas storage mass results from conservation law of mass

$$\frac{\mathrm{d}m_{\text{st}}}{\mathrm{d}t} = \sum_{i=1}^{p} \dot{m}_{\text{in},i} - \sum_{j=1}^{q} \dot{m}_{\text{out},j} \tag{A.55}$$

For the intake and exhaust system, the storage volume is assumed to be fixed ($\mathrm{d}V/\mathrm{d}t = 0$) and that the change of potential and kinetic energy can be omitted. The energy balance is given as

$$\frac{\mathrm{d}U_{\text{st}}}{\mathrm{d}t} = \sum_{i=0}^{p} h_{\text{in},i}\dot{m}_{\text{in},i} - \sum_{j=0}^{q} h_{\text{out},j}\dot{m}_{\text{out},j} + \dot{Q}_{\text{w,st}}, \tag{A.56}$$

where $\mathrm{d}U_{\text{st}}/\mathrm{d}t$ is the change of internal energy of the stored gas in J, h is the specific enthalpy in [J/(kg K)] of the inflows and outflows, and $\dot{Q}_{\text{w,st}}$ represents the wall heat losses. The internal energy U_{st} of the stored gas results from the product of the gas mass m_{st} and the specific internal energy u_{st} in [J/kg]. The change of internal energy yields according to the product rule to

$$\frac{\mathrm{d}U_{\text{st}}}{\mathrm{d}t} = \frac{\mathrm{d}}{\mathrm{d}t}\left(m_{\text{st}}u_{\text{st}}\right) = m_{\text{st}}\frac{\mathrm{d}u_{\text{st}}}{\mathrm{d}t} + u_{\text{st}}\frac{\mathrm{d}m_{\text{st}}}{\mathrm{d}t}. \tag{A.57}$$

The specific energy u_{st} is generally a function of the gas temperature T_{st}, gas pressure p_{st} and the air-fuel ratio λ_{st},

$$u_{\mathrm{st}} = u_{\mathrm{st}}\left(T_{\mathrm{st}}, p_{\mathrm{st}}, \lambda_{\mathrm{st}}\right) \approx u_{\mathrm{st}}\left(T_{\mathrm{st}}, \lambda_{\mathrm{st}}\right). \tag{A.58}$$

However, for temperatures lower than 1800 K, the dependency on the pressure can be neglected (Pischinger et al. 2009). By using partial derivation of u_{st} with respect to temperature T and air-fuel-ratio λ, the change in specific energy yields to

$$\frac{\mathrm{d}u_{\mathrm{st}}}{\mathrm{d}t} = \left(\frac{\mathrm{d}u_{\mathrm{st}}}{\mathrm{d}T_{\mathrm{st}}}\right)\Big|_{\lambda_{\mathrm{st}}} \frac{\mathrm{d}T_{\mathrm{st}}}{\mathrm{d}t} + \left(\frac{\mathrm{d}u_{\mathrm{st}}}{\mathrm{d}\lambda_{\mathrm{st}}}\right)\Big|_{T_{\mathrm{st}}} \frac{\mathrm{d}\lambda_{\mathrm{st}}}{\mathrm{d}t} \tag{A.59}$$

The specific internal energy and its partial derivatives are either calculated by a polynomial approach according to Justi (1938) or Zacharias (1966), or are determined from tabulated data by mean of look-up tables (Pischinger et al. 2009). For the specific enthalpies of the inflows and outflows holds

$$h_{\mathrm{in},i} = u_{\mathrm{st}}\left(T_{\mathrm{in},i}, \lambda_{\mathrm{in},i}\right) + RT_{\mathrm{in},i} \qquad \text{and} \qquad h_{\mathrm{out}} = u_{\mathrm{st}}\left(T_{\mathrm{st}}, \lambda_{\mathrm{st}}\right) + RT_{\mathrm{st}} \tag{A.60}$$

Note that by assuming an ideal mixture in the gas storge, the gas temperature of the outflowing gas equals the temperature of the stored gas (Guzzella and Onder 2010).

Substituting the Eqs. (A.55) to (A.63) into the energy balance (A.56), the differential equation for the gas temperature T_{st} is obtained

$$\frac{\mathrm{d}T_{\mathrm{st}}}{\mathrm{d}t} = \frac{1}{m_{\mathrm{st}} u_{\mathrm{st}}} \left[\sum_{i=0}^{p} h_{\mathrm{in,i}} \dot{m}_{\mathrm{in},i} - \sum_{j=0}^{q} h_{\mathrm{out,j}} \dot{m}_{\mathrm{out},j} - u_{\mathrm{st}} \dot{m}_{\mathrm{st}} + \dot{Q}_{\mathrm{w,st}} \right] \tag{A.61}$$

After numerical integration of the differential equations for the storage mass m_{st} (3.1) and temperature T_{st} (A.61), the third unknown gas state variable, the gas pressure p_{st} in the storage, is determined by the ideal gas law (A.17)

$$p_{\mathrm{st}} = \frac{m_{\mathrm{st}} R T_{\mathrm{st}}}{V_{\mathrm{st}}}, \tag{A.62}$$

whereas V_{st} represents the known storage volume, which must be derived from construction parameters or identified experimentally.

The heat flow $\dot{Q}_{\mathrm{w,st}}$ of the wall heat losses from storage gas to the environment are described by Newton's law (Pflaum and Mollenhauer 1977)

$$\dot{Q}_{\mathrm{w,st}} = k_{\mathrm{w,st}} A_{\mathrm{w,st}} \left(T_{\mathrm{st}} - T_{\mathrm{a}}\right), \tag{A.63}$$

with the storage wall surface $A_{\mathrm{w,st}}$, the heat transfer coefficient $k_{\mathrm{w,st}}$ and the ambient temperature T_{a}. For the sake of simplicity, modeling the heat storage of walls and the wall temperature is not considered.

The Eqs. (A.55)-(A.63) apply generally to all storage elements of the intake and exhaust path of the airpath system. However, some reasonable model simplifications can be made. Since the temperature level in the intake system varies only marginally, the temperature dependency can be

neglected when calculating the specific internal energy and the specific enthalpies of the inflows and outflows. The specific internal energy can be calculated in a simplified way by using the isochoric heat capacity c_v in [J/(kg K)]

$$u_\mathrm{st} = c_\mathrm{v} T_\mathrm{st}. \tag{A.64}$$

Correspondingly, the specific enthalpies are calculated based on the isobaric heat capacity c_p in [J/(kg K)]

$$h_{\mathrm{in},i} = c_\mathrm{p} T_{\mathrm{in},i} \qquad \text{and} \qquad h_{\mathrm{out},i} = c_\mathrm{p} T_{\mathrm{out},i} \approx c_\mathrm{p} T_\mathrm{st}. \tag{A.65}$$

The specific heat capacities c_p and c_v of ideal gases differ by the gas constant R (Stephan et al. 2013). It is also advantageous to use the ratio of the two specific heat capacities, called *isentropic exponent*

$$c_\mathrm{p} - c_\mathrm{v} = R \qquad \text{and} \qquad \kappa = \frac{c_\mathrm{p}}{c_\mathrm{v}}. \tag{A.66}$$

Furthermore, it can be assumed that for some storage elements of the intake systems the transported heat through the storage is much larger than the heat flow to the walls, so that the wall heat losses can be neglected ($\dot{Q}_\mathrm{w,st} \approx 0$) (Isermann 2014). With this assumption and by using the simplified assumption regarding the caloric properties of the gas, the differential equations for the storage pressure and temperature can be simplified to

$$\frac{\mathrm{d}p_\mathrm{st}}{\mathrm{d}t} = \frac{\kappa R}{V_\mathrm{st}} \left[\sum_{i=1}^{p} \dot{m}_{\mathrm{in},i} T_{\mathrm{in},i} - \sum_{j=1}^{q} \dot{m}_{\mathrm{out},j} T_\mathrm{st} \right] \tag{A.67}$$

$$\frac{\mathrm{d}T_\mathrm{st}}{\mathrm{d}t} = \frac{1}{m_\mathrm{st}} \left[\sum_{i=1}^{p} \left(\kappa T_{\mathrm{in},i} - T_\mathrm{st}\right) \dot{m}_{\mathrm{in},i} - \sum_{j=1}^{q} (\kappa - 1) T_\mathrm{st} \dot{m}_{\mathrm{out},j} \right] \tag{A.68}$$

These differential equations are mutually coupled and describe the dynamic behavior of the pressure p_st and temperature T_st in case of an adiabatic state change, which represents an extreme scenario where no heat transfers between the stored gas and the walls is taken place. This approximation is reasonable for storage elements of the intake system, where the difference between the storage gas temperature and the engine compartment temperature is negligibly small.

On the contrary, for storage elements of the exhaust system, where the temperature gradients are high and the heat losses are significant, the calculation of the storage temperature must either consider wall heat losses additionally ($\dot{Q}_\mathrm{w,st} \neq 0$) or if cooler elements, such as intercooler or EGR-cooler, are included in the storage elements, the wall heat losses are accounted to the cooling capacity of the cooler and the separate calculation of the wall heat losses becomes obsolete.

The other extreme scenario is the isothermal case ($\kappa = 1$), where only small temperature changes occur ($\mathrm{d}T_\mathrm{st}/\mathrm{d}t \approx 0$), so that for the storage temperature holds $T_\mathrm{st} \approx T_{\mathrm{in},i}$. A better approximation for the gas pressure inside the storage is then given by

$$\frac{\mathrm{d}p_\mathrm{st}}{\mathrm{d}t} = \frac{R_\mathrm{air} T_\mathrm{st}}{V_\mathrm{st}} \left[\sum_{i=1}^{p} \dot{m}_{\mathrm{in},i} - \sum_{j=1}^{q} \dot{m}_{\mathrm{out},j} \right]. \tag{A.69}$$

This simplification decouples the calculations of pressure and temperature, but also neglects the dynamic behavior of the storage temperature. For storage elements with small volume and negligible wall heat losses, this represents a good modeling approach. In case of larger storage volumes ($\dot{m}_{\mathrm{in},i}/m_{\mathrm{st}} << 1$) and, particularly, storages with more than one inflowing gas masses with differing inflow temperatures, the storage temperature is better approximated by the following differential equation

$$\frac{\mathrm{d}T_{\mathrm{st}}}{\mathrm{d}t} \approx \frac{1}{m_{\mathrm{st}}} \left[\sum_{i=1}^{p} (T_{\mathrm{in},i} - T_{\mathrm{st}})\, \dot{m}_{\mathrm{in},i} + \dot{Q}_{\mathrm{w,st}} \right]. \tag{A.70}$$

This differential equation represent a first order lag element with the ratio $\dot{m}_{\mathrm{in},i}/m_{\mathrm{st}}$ as dwell time constant. In steady state operation the dynamic behavior of the storage temperature converges towards the temperature of the inflows corresponding proportionally to the mass inflow rates.

The air mass fraction X_{st} inside the storage element is given by the ratio between mass of fresh air $m_{\mathrm{st,air}}$ and the total gas mass m_{st}

$$X_{\mathrm{st}} = \frac{m_{\mathrm{st,air}}}{m_{\mathrm{st}}} \tag{A.71}$$

The change of air mass fraction is determined solely by the air mass fraction $X_{\mathrm{in},i}$ of the entering mass flows. The differential equation is given as

$$\frac{\mathrm{d}X_{\mathrm{st}}}{\mathrm{d}t} = \frac{1}{m_{\mathrm{st}}(t)} \left[\sum_{i=0}^{p} (X_{\mathrm{in},i} - X_{\mathrm{st}}) \dot{m}_{\mathrm{in},i}(t) \right] \tag{A.72}$$

Heat exchanger

Heat exchangers in the intake and exhaust system are generally modeled as stationary flow process in an open thermodynamic system

$$\dot{m}_{\mathrm{gas}}\,(h_{\mathrm{in}} - h_{\mathrm{out}}) + \dot{Q}_{\mathrm{cl}} = 0 \tag{A.73}$$

with a heat transfer $\dot{Q}_{\mathrm{cl}}$ causing a change in specific enthalpy of the inflowing gas $\dot{m}_{\mathrm{gas}}$, compare Fig. 3.3 c). Depending on the direction of heat flow $\dot{Q}_{\mathrm{cl}}$, the outflow temperature Tout is lowered or raised compared to the temperature T_{in}. The output temperature T_{out} of the heat exchanger follows from specific output enthalpy $h_{\mathrm{out}} = c_{\mathrm{p}} T_{\mathrm{out}}$

$$T_{\mathrm{out}} = T_{\mathrm{in}} + \frac{\dot{Q}_{\mathrm{cl}}}{\dot{m}_{\mathrm{gas}} c_{\mathrm{p}}} \tag{A.74}$$

According to VDI-Wärmeatlas (2013), a heat exchanger is modeled based on a lumped parameter approach as a heat transfer between two fluids through a wall. The heat transfer $\dot{Q}_{\mathrm{gas,w}}$ between the gas to be cooled $\dot{m}_{\mathrm{gas}}$ with inflowing temperature T_{in} and the heat exchanger wall with temperature T_{w} is given by Newton's law as

$$\dot{Q}_{\mathrm{gas,w}} = \alpha_{\mathrm{gas,w}}(\dot{V}_{\mathrm{gas}}) A_{\mathrm{gas,w}}\,(T_{\mathrm{in}} - T_{\mathrm{w}})\,, \tag{A.75}$$

whereas $A_{\mathrm{gas,w}}$ represents the heat transfer surface and $\alpha_{\mathrm{gas,w}}(\dot{V}_{\mathrm{gas}})$ the heat transfer coefficient, depending on the volume flow rate of the gas to be cooled $\dot{V}_{\mathrm{gas}}$. Correspondingly, the heat transfer $\dot{Q}_{\mathrm{w,cl}}$ between heat exchanger wall and coolant fluid with temperature T_{cl} is given as

$$\dot{Q}_{\mathrm{w,cl}} = \alpha_{\mathrm{w,cl}}(\dot{V}_{\mathrm{cl}}) A_{\mathrm{w,cl}} \left(T_{\mathrm{w}} - T_{\mathrm{cl}}\right), \tag{A.76}$$

with heat transfer coefficient $\alpha_{\mathrm{w,cl}}(\dot{V}_{\mathrm{cl}})$ depending on the volume flow rate of the coolant $\dot{V}_{\mathrm{cl}}$ and the heat transfer surface $A_{\mathrm{w,cl}}$.

In the stationary case, the wall heat dynamics can be neglected, so that the specific heat flows become equal $\dot{Q}_{\mathrm{w,cl}} = \dot{Q}_{\mathrm{gas,w}}$. With the assumption of an averaged surface area $A_{\mathrm{cl}} = A_{\mathrm{gas,w}} = A_{\mathrm{w,cl}}$ and by rearranging Eq. (A.75) regarding T_{w} and inserting into Eq. (A.76) results after some algebraic manipulations

$$\dot{Q}_{\mathrm{cl}} = k_{\mathrm{cl}}(\dot{V}_{\mathrm{gas}}, \dot{V}_{\mathrm{cl}}) A_{\mathrm{cl}} \left(T_{\mathrm{in}} - T_{\mathrm{cl}}\right) \tag{A.77}$$

with the overall heat coefficient

$$k_{\mathrm{cl}}(\dot{V}_{\mathrm{gas}}, \dot{V}_{\mathrm{cl}}) = \frac{1}{\frac{1}{\alpha_{\mathrm{gas,w}}(\dot{V}_{\mathrm{gas}})} + \frac{1}{\alpha_{\mathrm{w,cl}}(\dot{V}_{\mathrm{cl}})}} = \frac{\alpha_{\mathrm{gas,w}}(\dot{V}_{\mathrm{gas}})\, \alpha_{\mathrm{w,cl}}(\dot{V}_{\mathrm{cl}})}{\alpha_{\mathrm{gas,w}}(\dot{V}_{\mathrm{gas}}) + \alpha_{\mathrm{w,cl}}(\dot{V}_{\mathrm{cl}})} \tag{A.78}$$

A.3 Semi-physical injection modeling

The task of the injection system is to inject a desired amount of fuel at a specific time (relative to the current angular position of the cylinder piston) and with a desired injection rate into the compressed gas inside the combustion chamber. Generally, an injection system consists of a pressure supply and an injection nozzles. The pressure supply is typically realiszed by an high-pressure piston pump, which is driven via timing belt by the engine speed. The pump is responsible for building up and maintaining a desired injection pressure during the injection process to achieve precise fuel injection.

In modern Diesel engines, pressure pump and injector nozzle are electronically controlled, which allows an additional degree freedom by means of a variable control of injection quantity, timing and pressure level (Wintrich et al. 2017). Light duty vehicle engines and also increasingly heavy duty and marine engines are typically equipped with common rail injection system (CR-Diesel engines) (Leonhard et al. 2011). In common-rail injection systems, pressure generation and fuel injection are separated from each other by using a intermediate volume as pressure reservoir (common rail) between the high pressure pump and the injection nozzle. The injection nozzles are connected to the pressure reservoir via equal length high-pressure pipe lines to ensure an identical behavior of all injector (Reif 2012). The volume of the common rail is sufficiently large to ensure an almost constant injection pressure during injection, even for larger injection quantities and at low engine speed. Additionally, such injection systems allow manipulating the injection parameters (quantity, timing, pressure) independent of the engine speed within the whole engine operation range. Fig. A.6 shows the setup and components of the common rail injection system.

The fact that pressure generation and injection timing can be manipulated almost independently from each other, made the application of multiple injections with nearly constant injection rate possible (Wintrich et al. 2017). Additional pilot and post injections allow to reduce combustion noise and optimize the trade-off between nitrogen oxide and soot emissions (Hammer 2014). Therefore, the injector development was focused on improving the dynamic behavior in order to enable several small injections within short period of time. For emission reduction, the injection pressure level also plays an important role. To meet increasing emissions requirements, further development of common-rail systems has also been driven toward higher injection pressures of up to 3000 bar, see e.g. Shinohara et al. (2011).

Injectors consist of a nozzle with multiple injection holes and a hydraulic servo system with a electrically actuated valve. In modern CR-systems there are two types of valve actuators used - *solenoid valve* and *piezo valve* actuators. The setup of solenoid valve injector is depicted in Fig. A.7 a). In the first generations of CRS-injectors, solenoid valve injector were used, which generally are less expensive but have slower injector dynamics than piezo injectors. The higher dynamics of piezo injectors allows an improved multiple injection capability and steeper increase of injection rates. With modern solenoid valve injectors, up to 5 injections are possible. An example of injection pattern is shown in Fig. A.6. In contrast, piezo injectors allow up to 10 injections within one injection cycle. Furthermore, the time period between injections can be set short enough, so that a so-called rate shaping of the combustion is possible, see e.g. Jörg, Zubel, et al. (2017), Jörg,

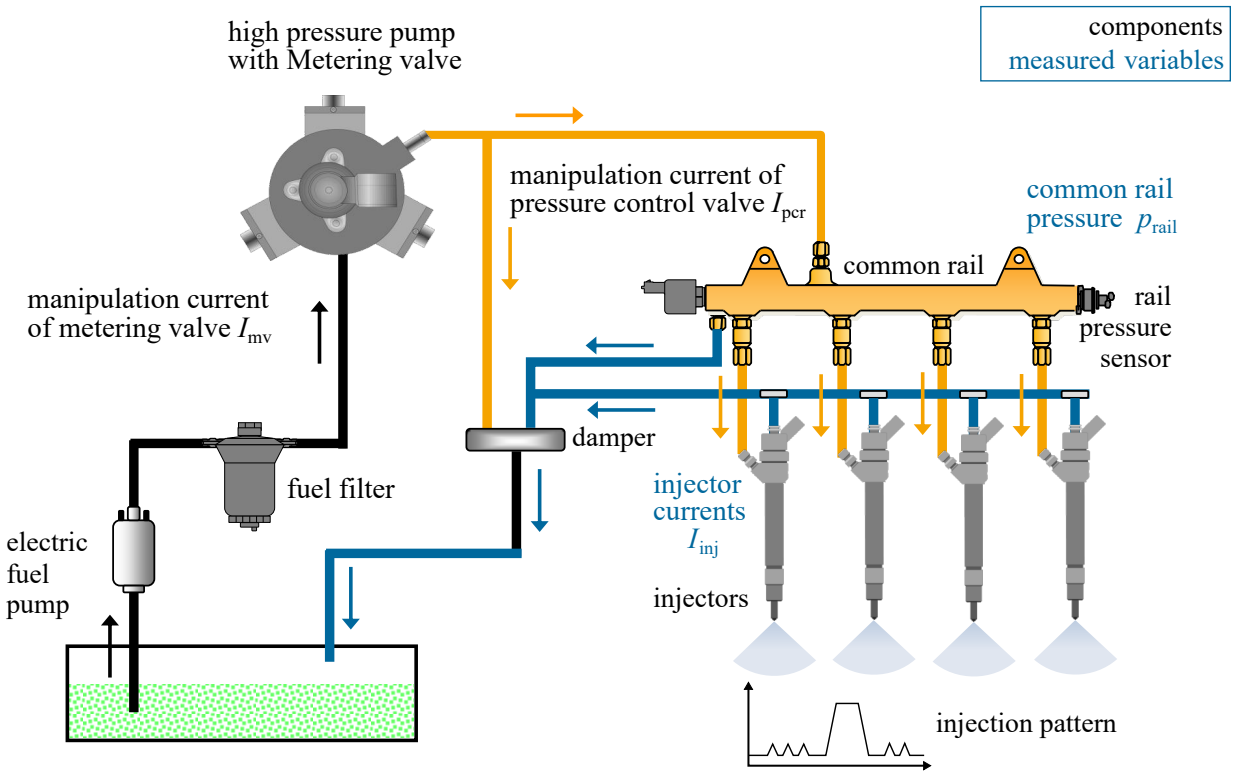

Figure A.6: Scheme of common rail injection system of a four cylinder Diesel engine: working principle of engine speed independent injection rate (pattern)

Schaub, et al. (2018) and Jörg, Schnorbus, et al. (2015). Due to the cost pressure further effort was invested into the improvement of injector dynamics of solenoid injector, so that system pressure and multiple injection capabilities of solenoid injectors come close to those of piezo injectors (Wintrich et al. 2017).

In order to meet the requirements of stricter emission legislation, additional system functions of fuel injectors, such as injector quantity balancing and zero quantity calibration, which allow a precise adjustment and drift compensation over the whole lifetime, have led to a continuous quantity increase with activation time. After the first μs of injector energizing (fully open injector nozzles) results a linear relation between activation duration and injection quantity, see Fig. A.7 a) and b). In the literature, e.g. Seykens et al. (2005), Reif (2012), and Payri et al. (2016), it is shown that the slope of this linear relation (maximal injection rate) correlates with the injection (rail) pressure p_{rail}. However, there is not a strictly proportional relation (quasi-stationary) between injection pressure and injection rate since the injector dynamics as well as the nonlinear flow condition at the nozzle have an significant influence on the shape of the injection rate. For small injection quantities, as in the case of pilot injection, it is the nonlinear behavior during the opening and closing phase that is decisive for the course of the injection rate and the resulting injection quantity, see Fig. A.7 a). The determination of such small injection quantities requires a more precise modeling of injection process that goes beyond a simple injection model with e.g. rectangular model.

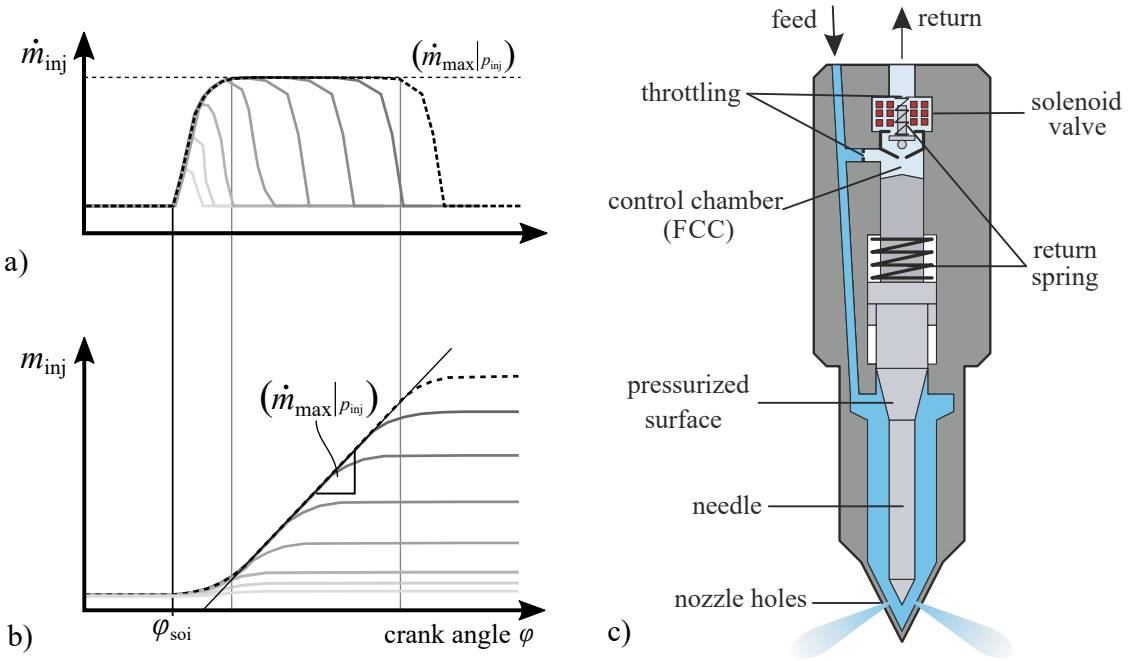

Figure A.7: Illustration of a) different injection rates and b) corresponding cumulative injected fuel mass for different injection duration; c) schematic diagram of solenoid valve injector during active injection process

A.3.1 Modeling of fuel injection

The solenoid valve consists of a coil winding and a valve plunger, see Fig. A.7 c). The valve plunger is connected to the housing via spring bearing, which supports the valve actuator returning to closed position. Fig. A.7 c) shows the injector in open state.

Energizing the solenoid coil opens the control chamber and the fuel inside flows back via the return line into the tank. The outflow via return line must be higher than the volume flow into the control chamber in order to cause a pressure drop and to avoid a pressure compensation. The pressure difference between the control chamber and the nozzle pre-chamber generates a force acting on pressurized surface which causes an upwards movement of the injector needle and to the opening of the injection nozzles. Here, the pressure force must first overcome the preload force of the return spring in order to cause needle movement. The closing of the injector nozzle follows the reverse principle. By closing the control volume the pressure inside the control chamber builds up ($\approx p_{rail}$) and causes an downwards movement back to the initial position (Gauthier 2009). Upwards movement of injector needle is assisted by a return spring, therefore the closing of the nozzles generally takes place faster than the opening. Pressure drop and pressure rebuild inside the control volume is determined by the cross-sectional areas of its feed and return throttles. Both throttle orifices are designed to allow a smooth upwards and downwards movement of injector needle.

This indirect control with the use of servo-hydraulic amplification is necessary to achieve the required forces for sufficiently high dynamics of the injector needle; despite using a small electro-mechanical actuator for activation (Reif 2012). However, this working principle leads to the fact

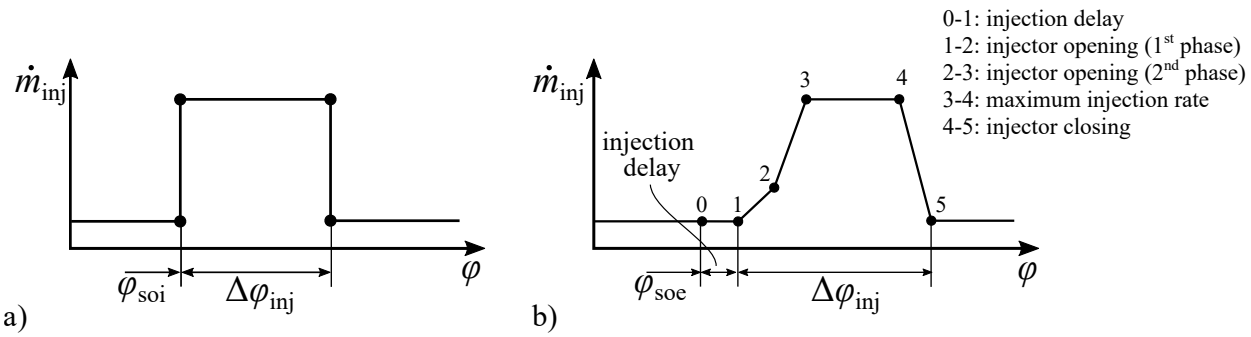

Figure A.8: Illustration of a) a rectangular injection rate model; b) trapezoidal injection rate model by Barba (2001), injection duration Δt_{inj} (time based) is proportional to $\Delta\varphi_{inj}$ (angle based)

that the movement of the injector needle and the opening of the nozzle do not directly correspond to the energizing timing. The needle movement is generally delayed due to the pressure dynamics of the control volume and takes longer than the energizing time.

The fuel injection is characterized by the curve of the injection rate, which is typically given as fuel mass flow rate $\dot{m}_{inj}(\varphi)$ with respect to crank angle φ, see an example for a pilot injection and a main injection in Fig. A.9 c) (bottom). These injection rate curves are characterized by a steep rate increase at the start of injection (SOI), an almost constant rate level during the injection and an equally steep rate drop at the end of injection (EOI). The angles of SOI and EOI are usually formulated with respect to the crank angle where the piston is at the top dead center. However, due to hydraulic delay and the nozzle needle dynamics, the actual start and end of injection is unknown. Therefore, ECUs use the angle of the start of injector energizing φ_{soe} and its energizing time Δt_{et} in μs as injection parameters.

The simplest way to model the injection rate is by approximating the curve by a rectangular injection rate model, see Fig. A.8 a). Start and duration of injection are assume to be equal to the ECU injection parameters start of injector energizing $\varphi_{soe}(= \varphi_{soi})$ and the energizing time Δt_{et} ($\propto \Delta\varphi_{inj}$. The height of the injection rate is determined from the total injection quantity q_{inj}/stroke divided by the energizing time Δt_{et}. The total injection quantity is either provided by the ECU parameter maps as function of engine load and speed or must be determined from measurements. Generally, the actual fuel injection is delayed to the SOE and lasts longer than the injector energizing, therefore, such simple model is not sufficient as input for more sophisticated combustion model. Since the energizing duration is shorter than the actual fuel injection, rectangular approximation tends to overestimate the injection rate level.

Although, this simple model approach allows an easy and fast calculation of the injection rate, a more detailed modeling of the characteristic Diesel combustion, including premixed and spray combustion, requires modeling the overlap between injection phase and combustion phase (occurring for higher injection quantities and durations). Therefore, an accurate modeling of the injection duration is required to model the characteristics of Diesel combustion.

Barba (2001) proposes an empiric model approach based on a polygonal or trapezoidal curve shown in Fig. A.8 b). The shape of the injection rate is modeled by sequential phases of the injection processes: injection delay, stepwise rate increase, maximum rate level and abrupt rate drop. Each phase is described by a corresponding parameters (phase duration or slope), which are determined as function of the rail pressure as the driving force for the whole injection process. To determine the parameters, the injection rate must be known from measurements or detailed injection model calculations. Due to this phase-by-phase modeling of the injection curve, this empirical injection rate model reproduces the real shape of the injection rate very well in a wide range and is therefore suitable as an input variable for a combustion model.

A simplified 0D injection model is developed in Payri et al. (2016) which is able to reproduce the injection rate, focusing on the shape and the injected mass and by using the inputs: rail pressure, backpressure and energizing time. In general, the main injection has rather a trapezoidal shape and the shorter pilot and post have a rather a triangular shape. The model approach is based on the idea to model the injection rate by using mathematical expressions e.g. straight slopes, first/second order system responses or other mathematical function as exponential or trapezoidal functions.

D. Ritter et al. (2019) follows a similar approach as Payri et al. (2016) and presents a control-oriented injector model for the purpose of cycle-to-cycle control of Diesel engine equipped with piezo injectors. The model approach is based on piece-wise defined and physically motivated basis functions. This injector model makes it possible to reproduce a smooth course of the injection rate of both small triangular pilots and trapezoidal main injections.

Physical modeling of the injection rate requires modeling of electro-hydraulic system of the injector nozzle. The injection pressure and the energizing timing of the injection nozzles act as input variables. Constien (1991) models the injection process in a direct-injection Diesel engine based on a flow equation for incompressible fluids (Bernoulli equation) and a differential equation for the injector needle dynamics. Since the modeled injection system is a unit injector system, opening and closing of the injector is pressure-controlled. Constien (1991) shows the influence of nozzle orifice cross section and injection pressure on the discharge coefficient of the flow equation. Constien (1991) shows on the basis of experimental investigation at a modified injection pump test rig[7] the influence of nozzle opening cross-section and injection pressure on the discharge coefficient in the flow equation.

Poetsch (2014) presents similar model approach for a common rail injection system. The injection rate is also modeled by a Bernoulli equation, whereby the discharge coefficient is described as a series of flow resistances. The injection delay (hydraulic delay) between injector currents and needle movement is assumed to be constant. A triangular course for the needle lift is assumed, whereas the slope depends on the rail pressure, and the duration on the energizing time of the injector. Needle lift and needle drop can have different slopes. The injection model calculates injection quantity and rate profile from the input of the ECU target values for injection pressure and injection timing. The model also accounts for pressure oscillations in the injection system (Poetsch 2014).

[7] Injection pump test rig provides measurements of injection rate, injector needle stroke and needle stop force

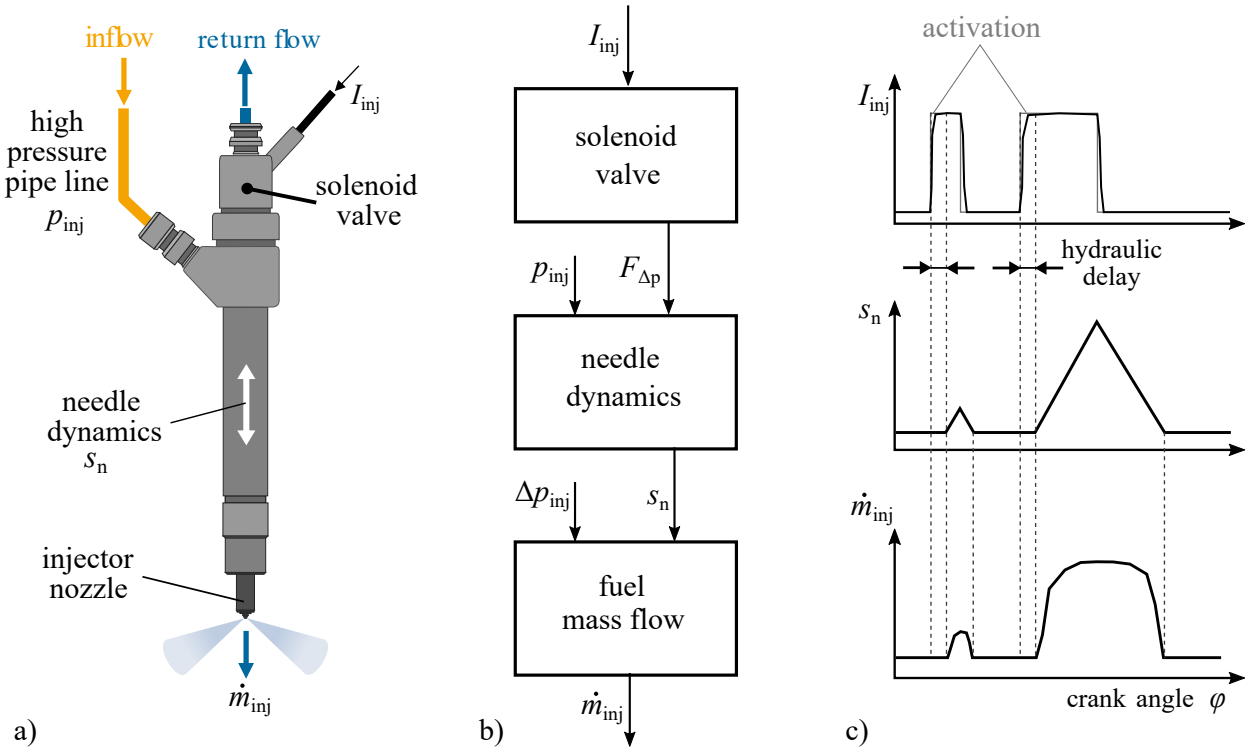

Figure A.9: a) Illustration of a solenoid valve injector; b) scheme of injector block diagram and c) simulated courses of injector activation by means of activation signal U_{inj} and injector current I_{inj}, (triangular) needle stroke s_n and fuel injection rate $\dot{m}_{inj}$

In general, accurate modeling of the injection process and model identification requires highly time-resolved measurements of needle position and injection rate in dependence of injection pressure and injection rate. For modeling the characteristics of Diesel combustion, the modeling of the injection delay and injection duration is required. However, in series engines, neither the needle lift nor the curve of the injection rate are generally known. The measurement of the injection rate and needle lift is only possible on specially designed injection nozzle test benches. As no such measurement is available for this work, simplifications regarding the sub-processes of the injection must be made in order to be able to identify system parameters based on available measurements.

In the following, a semi-physical modeling approach for the injection rate of a solenoid valve injector [8] is presented. The structure and working principle is shown in Fig. A.7 c).

A.3.2 Semi-physical fuel injector model

The semi-physical injector model consists of three sub-models connected in series, see Fig. A.9 b). The first sub-model is an electro-hydraulic system including the solenoid valve with servo-hydraulic amplification. The solenoid valve is energized via activation signal U_{inj} leading to a injector current I_{inj}. The output of the electrohydraulic system is a normalized pressure force

[8] Even though *solenoid valve* and *piezoelectric actuated injectors* differ in their properties, both work on the same working principle. This modeling approach can also be applied to piezo injectors with the same mode of operation

$F_{\Delta p}$ acting on the injector needle. Second sub-model describes the injector needle dynamics in dependence of normalized pressure force $F_{\Delta p}$ and the injection pressure p_{inj}. The mass flow rate $\dot{m}_{inj}$ is then calculated based on the Bernoulli equation and as function of the needle stroke s_{inj} and the difference pressure Δp_{inj} between injection pressure p_{inj} and in-cylinder counter pressure p_{cyl}. For the sake of simplicity, the injection pressure in the nozzle is assumed to be equal to the system pressure in the common rail $p_{inj} \approx p_{rail}$.

Modeling of the dynamic behavior of the solenoid valve (hydraulic delay) and injector needle movement are developed in the electro-hydraulic subsystem in Sect. A.3.2. The model for the injector needle dynamics and the theoretical cross-sectional flow area is described in Sect. A.3.2. The modeling of fluid mechanical subsystem, including the calculation of fuel injection rate and the flow conditions through the injector nozzle, is described in section A.3.2.

Electrohydraulic subsystem

Physical modeling of the solenoid actuator would result in a third-order dynamical system. The coil current can be described by a first order differential equation and the valve plunger dynamics by a second order motion equation. Since the characteristic time constants of both subsystems (determined by the coil inductance and the mass of the plunger) are negligible compared to the time resolution of the calculation, it is sufficient to approximate the dynamics of the solenoid valve by a first order lag element[9]

$$G_v(\sigma) = \frac{I_{inj}(\sigma)}{U_{inj}(\sigma)} = \frac{K_v}{\tau_v \sigma + 1}, \tag{A.79}$$

with crank angle frequency $\sigma = j\omega_\varphi$ in 1/°. Since the valve displacement cannot be measured, it is assumed that the valve displacement behaves quasi-stationary to the valve current I_{inj}. K_v represents the gain factor describing the stationary relation between binary activation signal $U_{inj} \in [0; 1]$ and injector current I_{inj} in 1/A. The parameter τ_v summarizes the characteristic time constants of the overall solenoid valve dynamics.

A detailed modeling of the hydraulic amplification would require the physical modeling of the pressure dynamics in the control chamber including the inflowing and outflowing flows. However, with regard to the objective of this work, it is not the representation of the force amplification but rather the delaying effect on the opening and closing of the injector nozzles that is of importance. Consequently, a simplified approach is applied for modeling this hydraulic delay.

The hydraulic delay can be investigated based on in-cylinder pressure measurements and heat release analysis. The point of negative heat release[10] relative to the start of energizing ($I_{inj} \neq 0$) indicates the start of injection. It can be observed that the time delay is almost constant, but it is influenced by the relation of injection pressure and engine speed. With an increase in rail pressure (at constant engine speed), the hydraulic delay shortens slightly. This observation also corresponds

[9] Measurements of the injector current at a high sampling rate (crank angle resolved) have shown that the injector current does not change stepwise, but also exhibits certain low-pass behavior

[10] Fuel injection causes a reduction in cylinder gas pressure due to the cooling effect of fuel evaporation

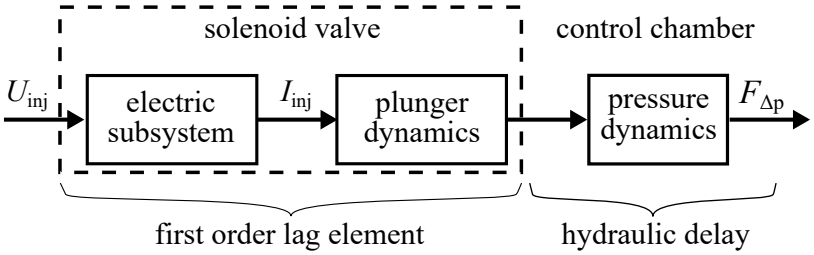

Figure A.10: Scheme of the signal flow of the electrohydraulic subsystem including the dynamic behavior of the solenoid valve and the control chamber

to the expected physical behavior of the hydraulic amplification, since the rail pressure corresponds to the system pressure within the injector, which is the driving force for the movement of the injector needle.

In Barba (2001), the hydraulic delay of the injector is also given as a function of the rail pressure. The characteristic opening time t is derived from Newton's law of motion

$$t = \frac{c}{\sqrt{p_{\text{rail}}}}. \tag{A.80}$$

Based on this approach and by using the crank angle velocity, the hydraulic delay τ_{id} can be written with respect to crank angle as a function of both the engine speed n_{eng} in min^{-1} and the rail pressure p_{rail} in Pa

$$\tau_{\text{id}} = \frac{360}{60} n_{\text{eng}} \frac{c_{\text{id}}}{\sqrt{p_{\text{rail}}}}. \tag{A.81}$$

The parameter c_{id} in $\sqrt{\text{kg/m}}$ represents a tuning parameter for model adjustment according to the fuel injector.

Note that the needle is also connected to the housing via spring bearing. Therefore, the spring force must first be overcome before the needle deflects. During the closing process, the return spring support the upwards movement of the needle. This results in a dynamically lagged needle movement, which is accounted with the hydraulic delay.

Finally, the entire effect chain from energizing the solenoid valve, over the pressure drop in the control volume and up to the overcoming of the preload force of the return spring is approximated by a first order lag element for the solenoid valve and a hydraulic delay τ_{id} representing the pressure drop inside the control chamber which leads to the pressure force acting on the injector needle, see Fig. A.10.

Injector needle dynamics

In accordance to Poetsch (2014), the needle movement is described in a simplified way by a triangular course, see Fig. A.9 c). A ballistic needle movement without stop is assumed. The

gradient is described as a function of the injection pressure

$$\frac{\mathrm{d}s_\mathrm{n}}{\mathrm{d}t} = \begin{cases} +c_\mathrm{n} p_\mathrm{inj} & \text{für } I_\mathrm{inj} \geq I_\mathrm{min} \\ -c_\mathrm{n} p_\mathrm{inj} & \text{für } I_\mathrm{inj} \approx 0 \end{cases} \tag{A.82}$$

The parameter c_n is used to parameterize the rate at which the injector needle moves. It is also used to normalize the rate with respect to the injection pressure. The conversion into crank angle domain is done by using the angular velocity of the engine ω_eng

$$\frac{\mathrm{d}s_\mathrm{n}}{\mathrm{d}t}\frac{\mathrm{d}t}{d\varphi} = \frac{\mathrm{d}s_\mathrm{n}}{\mathrm{d}\varphi} = \frac{1}{\omega_\mathrm{eng}} \begin{cases} +c_\mathrm{n} p_\mathrm{inj} & \text{für } I_\mathrm{inj} \geq I_\mathrm{min} \\ -c_\mathrm{n} p_\mathrm{inj} & \text{für } I_\mathrm{inj} \approx 0 \end{cases} \tag{A.83}$$

Consequently, the injector needle stroke results from the integration of the needle velocity

$$s_\mathrm{n}(\varphi) = c_\mathrm{n} \int_{\varphi_\mathrm{soi}}^{\varphi_\mathrm{eoi}} \frac{\mathrm{d}s_\mathrm{n}}{\mathrm{d}\varphi} \mathrm{d}\tau \tag{A.84}$$

Flow equation

The mass flow injection rate is determined based on the continuity equation by using the *Bernoulli equation for incompressible fluids*

$$\frac{\mathrm{d}m_\mathrm{inj}}{\mathrm{d}\varphi} = A_\mathrm{inj} w_\mathrm{inj} = \frac{A_\mathrm{inj}}{\omega_\varphi} \sqrt{2\rho(p_\mathrm{inj} - p_\mathrm{cyl})}, \tag{A.85}$$

where A_inj is the effective cross sectional area of the nozzle orifice and w_inj represents the mass flow density with respect to crankshaft angle in kg/(m^{2}cs°) resulting from the root term. The angular velocity ω_φ is used for the transformation from time-based to crank angle-based formulation. The difference between the injection pressure p_inj and the in-cylinder pressure p_cyl determines the maximal injection rate through the injector nozzle. Fuel density is generally depending on injection pressure and fuel temperature and can be determined based on lookup tables $\rho = \rho(p, T)$ (Kolev 2007). The injection pressure is assumed to be equal to the rail pressure ($p_\mathrm{inj} \approx p_\mathrm{rail}$).

The theoretical cross-sectional area $A_\mathrm{th,tot}$ of the injector nozzle depends on the number n_nozzle and diameter d_nozzle of the injector nozzle holes

$$A_\mathrm{th,tot} = n_\mathrm{nozzle} \left(\frac{d_\mathrm{nozzle}}{2} \right)^2. \tag{A.86}$$

For passengers car engines the diameter d_nozzle of a multi-hole injector nozzle is between 0.10 and 0.15 mm (Tschöke et al. 2018). Considering the design and operating principle of an injector nozzle, it can be assumed that the injector nozzle is already fully open after a rather short energizing duration. After that initial opening period, a further injector needle displacement s_n does no have any effect on the cross sectional area $A_\mathrm{th}(s_\mathrm{n})$ at the nozzle orifices. This assumption is also in line with experimental studies in the literature. In Constien (1991), a curve of the effective cross-sectional area with respect to needle position is shown, which was averaged over many measuring points.

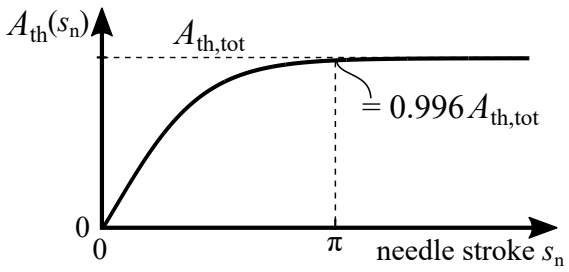

Figure A.11: Illustration of course of the cross sectional area of the injector nozzle as function of the injector needle displacement s_n

This curve has a descending slope, which can be described by a root or tangent hyperbolic function. Therefore, a tangent hyperbolic function is proposed to describe the nonlinear relation between needle position and cross sectional area

$$A_{th}(s_n) = A_{th,tot} \tanh\left(2\pi s_n^2\right), \tag{A.87}$$

The needle stroke from Eq. (A.84) serves as input and must be normalized $s_n \in \{0, 1\}$ by means of its parameter c_n in order to adjust the input dimension of the tangent hyperbolic function to the value range $\{0; 2\pi\}$ (e.g. $\tanh(\pi) = 0.996$). Since for $x \to \infty$ holds $\tanh(x) = 1$, the effective cross sectional area converges towards the total theoretical area $A_{inj,th}$. Fig. A.11 shows the course of the effective cross sectional area as function of needle stroke. However, this cross-sectional area is rather theoretical. During injection process occur flow losses resulting in a smaller effective cross-sectional area A_{inj}. In addition, wear and coking at the injector nozzle can lead to additional geometrical constrictions of the nozzles over lifetime. To describe the effective flow cross-section A_{inj}, a non-dimensional discharge coefficient α_{inj} is introduced, which represents the ratio between the effective and the theoretical cross sectional area

$$\alpha_{inj} = \frac{A_{inj}}{A_{th}(s_n)}. \tag{A.88}$$

From the product of theoretical cross sectional area (A.87) and discharge coefficient α_{inj} results the effective cross sectional area as function of the injector needle displacement

$$A_{inj}(s_n) = \alpha_{inj} A_{th}(s_n). \tag{A.89}$$

Consequently, the discharge coefficient α_{inj} represents a further tuning parameter of the injection rate model and serves also for dimensioning purposes if the injector-specific parameters (nozzle diameter and nozzle number) are unknown.

A.3.3 Identification of injector model parameters

The identification of the semi-physical injector model requires the determination of parameter c_{id} of the electrohydraulic subsystem, parameter c_n of needle stroke dynamics, and the discharge coefficient α_{inj} of the injection rate model.

The identification of injection model requires the variation of injection quantities q_{inj}, rail pressure p_{rail}, start of injection φ_{mi} (injection angle) and duration $\Delta\varphi_{\mathrm{mi}}$. Injection quantity, injection angle and timing is set constant in relation to main injection. Fuel quantity of pilot injection is set to $q_{\mathrm{pi}} = 1\ \mathrm{mm}^3$. The start of pilot injection φ_{pi} is manipulated proportional to main injection angle φ_{mi}.

The parameters are determined based on a total of $N = 280$ measurement data points, each with a small pilot injection varying in the quantity range of 0.5 to 1.2 mm^3 and a main injection in the range of 2.3 to 28.7 mm^3. Concerning the engine speed, the measuring points cover the range from idle speed of 850 up to 5000min^{-1}. The rail pressure was set in the range of 293.5 bar up to 1200 bar according to the ECU base map which is given as function of engine speed and engine load.

The *fmincon*-optimization algorithm of *MATLAB*® is used to determine the injector model parameters. The model error equation to be minimized is formulated as

$$V = \frac{1}{N}\left[\sum_{i=1}^{N}\frac{|m_{\mathrm{pi,ref},i} - m_{\mathrm{pi},i}|}{m_{\mathrm{pi,ref},i}} + \sum_{i=1}^{N}\frac{|m_{\mathrm{pi,ref},i} - m_{\mathrm{pi},i}|}{m_{\mathrm{pi,ref},i}}\right]. \tag{A.90}$$

Measurement points with one pilot and one main injection were chosen intentionally as a reference values, so that the non-proportional relationship between injection duration × injection rate and injection quantity, which can be observed in the area of opening and closing, is reproduced sufficiently by the model, compare to Fig A.7 a) and b). Since the injection quantities of pilot and main injection cannot be measured separately at the engine test bench, the set points from the ECU are used as a reference for the injection quantities. However, the total injection quantity was validated using an AVL mass flow meter in steady-state engine operation.

For the test engine, in Appx. A.1.1, the parameter optimization returns as result the parameters

$$c_{\mathrm{id}} = 0.487, \qquad c_{\mathrm{n}} = 0.2362, \qquad \alpha_{\mathrm{inj}} = 0.844$$

A comparison of the injection masses from the model calculation and the reference values from the 280 measurement points is represented in Fig. A.12. As it is shown, the semi-physical injection model is capable of reproducing a realistic shape of injection rate (hydraulic injection delay, injector dynamics) with accurate resulting injection quantities. However, the accuracy of the model decreases for calculation step sizes > 0.5.

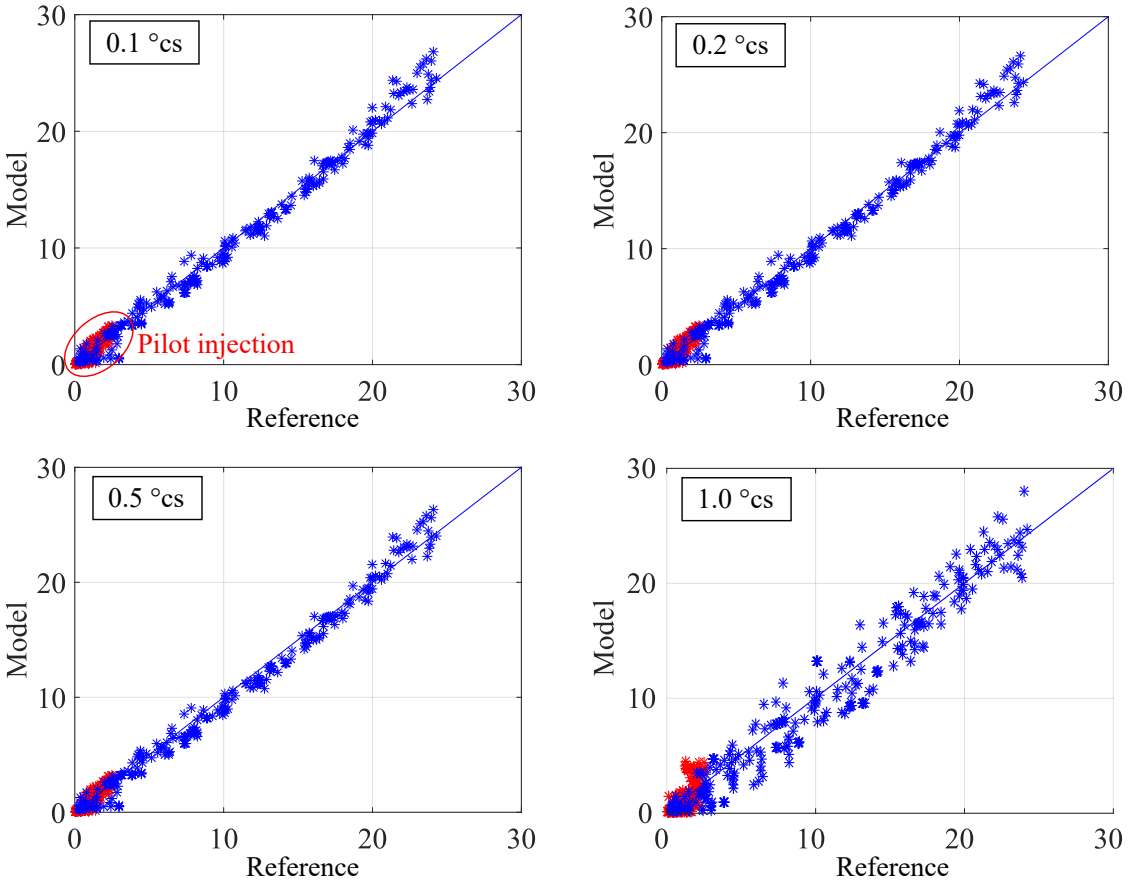

Figure A.12: Comparison of injection quantities [mg] from model calculations with different step sizes (0.1/0.2/0.5/1.0°cs) with ECU set set points of 280 stationary measurement points

A.4 Used tools for the thesis

The tools used to create this work are listed in the following table:

Software tool	Description and usage
TeXnicCenter 2.02, MiKTeX 2.9	Creating and editing thesis document (document preparation)
Inkscape 0.91	Vector graphics editor used for creating and editing all figures of this thesis
DeepL Translator	Translator used as a support for writing in English
MATLAB Simulink	Programming environment for modeling and simulation, and creating plots of simulation and measurement results
dSPACE Real-Time Interface	Compiling MATLAB Simulink models to run them on dSPACE real-time target hardware
dSPACE ControlDesk	Experimentation and Instrumentation software used for recording of measurements at the test bench

Bibliography

Ammann, M. (2003). Modellbasierte Regelung des Ladedrucks und der Abgasrückführung beim aufgeladenen PKW-Common-Rail-Dieselmotor. Dissertation. ETH Zürich.

Arasaratnam, I. (2009). Cubature Kalman Filtering: Theory & Applications. PhD thesis. McMaster University.

Arasaratnam, I. and S. Haykin (2008). Square-Root Quadrature Kalman Filtering. In: *IEEE Transactions on Signal Processing* 56 (6), pp. 2589–2593.

Arasaratnam, I. and S. Haykin (2009). Cubature Kalman Filters. In: *IEEE Transactions on Automatic Control* 54 (6), pp. 1254–1269.

Ayoubi, M. (1996). Nonlinear system identification based on neural networks with locally distributed dynamics and application to technical processes. Dissertation. TU Darmstadt.

Barba, C. (2001). Erarbeitung von Verbrennungskennwerten aus Indizierdaten zur verbesserten Prognose und rechnerischen Simulation des Verbrennungsablaufes bei Pkw-DE-Dieselmotoren mit Common-Rail-Einspritzung. Dissertation. ETH Zürich.

Bargende, M. (1991). Ein Gleichungsansatz zur Berechnung der instationären Wandwärmeverluste im Hochdruckteil von Ottomotoren. Dissertation. TU Darmstadt.

Bargende, M. (2014). Zukunft der Motorprozessrechnung und 1D-Simulation. In: *MTZ - Motorentechnische Zeitschrift* 75 (15), pp. 108–113.

Bechtloff, J. (2018). Schätzung des Schwimmwinkels und fahrdynamischer Parameter zur Verbesserung modellbasierter Fahrdynamikregelungen. Dissertation. TU Darmstadt.

Beidl, C. (2011a). Verbrennungskraftmaschinen I. Vorlesungsskript, Institut für Verbrennungskraftmaschinen und Fahrzeugantriebe, TU Darmstadt.

Beidl, C. (2011b). Verbrennungskraftmaschinen II. Vorlesungsskript, Institut für Verbrennungskraftmaschinen und Fahrzeugantriebe, TU Darmstadt.

Björck, Å. (1996). Numerical Methods for Least Squares Problems. Society for Industrial and Applied Mathematics.

Bredenbeck, J. (1999). Statistische Versuchsplanung für die Online-Optimierung von Verbrennungsmotoren. In: *MTZ - Motortechnische Zeitschrift* 60 (11), pp. 740–744.

Chmela, F., G. Orthaber, and W. Schuster (1998). Die Vorausberechnung des Brennverlaufs von Dieselmotoren mit direkter Einspritzung auf der Basis des Einspritzverlaufs. In: *MTZ - Motortechnische Zeitschrift* 59 (7-8), pp. 484–492.

Chmela, F., G. Pirker, and A. Wimmer (2007). Zero-dimensional ROHR simulation for DI diesel engines - A generic approach. In: *Energy, Conversion and Management* 48 (11), pp. 2942–2950.

Chui, C. K. and G. Chen (2017). Kalman Filtering with Real-Time Applications. 5th ed. Springer Verlag Berlin Heidelberg.

Constien, M. (1991). Bestimmung von Einspritz- und Brennverlauf eines direkteinspritzenden Dieselmotors. Dissertation. TU München.

Cox, H. (1964). On the Estimation of State Variable and Parameters for Noisy Dynamic Systems. In: *IEEE Transactions on Automatic Control* 9 (1), pp. 5–12.

Dec, J. E. (1997). A Conceptual Model of DI Diesel Combustion Based on Laser-Sheet Imaging. In: *SAE Transactions* 106, pp. 1319–1348.

El Tahry, S. H. (1982). k-Epsilon Equation for Compressible Reciprocatin Engine Flows. In: *Journal of Energy* 7 (4), pp. 345–353.

Elbert, P., C. Barro, and A. Amstutz (2016). Emission-optimised diesel engine - Optimal emission strategies for diesel engines with virtual emission sensors. Abschlussbericht 1440. FVV Research Association for Combustion Engines e.V., Frankfurt am Main.

Eriksson, L. (2007). Modeling and Control of Turbocharged SI and DI Engines. In: *Oil & Gas Science and Technology* 62 (4), pp. 523–538.

Föllinger, O. (2013). Regelungstechnik - Einführung in die Methoden und ihre Anwendung. Ed. by U. Konigorski, B. Lohmann, G. Roppenecker, and A. Trächtler. VDE Verlag GmbH, Berlin.

Gauthier, Y. (2009). Einspritzdruck bei modernen PKW-Dieselmotoren: Einfluss auf die Russemissionen. Vieweg+Teubner Research, GWV Fachverlage GmbH, Wiesbaden.

Gelb, A. et al. (1974). Applied optimal estimation. The MIT Press, Cambridge, MA, USA and London, England.

Golub, G. and F. Van Loan (1996). Matrix Computations. The John Hopkins University Press, Baltimore, MD, USA.

Goodwin, G. C. and K. S. Sin (1984). Adaptive Filtering, Prediction and Control. Prentice-Hall, Englewood Cliffs, NJ, USA.

Gordon, D. et al. (2018). Development and Validation of a Real-Time Capable FPGA Based Gas-Exchange Model for Negative Valve Overlap. In: *International Journal of Engine Research* 21 (3), pp. 421–436.

Greitzer, E. (1976). Surge and Rotating Stall in Axial Flow Compressor - Part I: Theoretical Compression System Model. In: *ASME Journal of Engineering for Power* 98, pp. 190–198.

Grewal, M. S. and A. P. Andrews (2008). Kalman Filtering: Theory and Practice Using MATLAB. 4thd Edition. John Wiley & Sons, Hoboken, NJ, USA.

Grill, M. (2006). Objektorientierte Prozessrechnung von Verbrennungsmotoren. Dissertation. Uni Stuttgart.

Guzzella, L. and C. H. Onder (2010). Introduction to modeling and control of internal combustion engine systems. 2nd ed. Springer Verlag, Berlin.

Hadler, J. et al. (2008). Volkswagen's New 2.0 l TDI Engine for the Most Stringent Emission Standards. In: *MTZ worldwide* 69, pp. 12–18.

Hammer, J. (2014). Dieseleinspritztechnik beim PKW – Zukunft mit Tradition. In: *MTZ - Motortechnische Zeitschrift* 75, pp. 102–107.

Heywood, J. B. (1988). Internal Combustion Engine Fundamentals. Mc-Graw Hill, New York, USA.

HGHH-Project (2022). Hamburg Green Hydrogen Hub. https://www.hghh.eu/ (accessed: 2022-04-04).

Hiroyasu, H., T. Kadota, and M. Arai (1983). Development and use of a spray combustion modeling to predict diesel engine efficiency and pollutant emissions: Part 1 combustion modeling. In: *Bulletin of JSME* 26 (214), pp. 569–575.

Hiroyasu, H., M. Arai, and M. Tabata (1989). Empirical Equations for the Sauter Mean Diameter of a Diesel Spray. In: *SAE Technical Paper* (No. 890464), pp. 1–12.

Hohenberg, G. (1980). Berechnung des gasseitigen Wärmeübergangs in Dieselmotoren. In: *MTZ - Motortechnische Zeitschrift* 41 (7/8), pp. 321–326.

Hohenberg, G. (1982). Der Verbrennungsverlauf - ein Weg zur Beurteilung des motorischen Prozesses. In: *4. Wiener Motorensymposium*, pp. 71–88.

Hopp, M. and U. Pfeiffer (1998). Entwicklung eines Rechenprogramms zur Simulation der dieselmotorischen Russoxidation. Abschlussbericht 659. FVV Research Association for Combustion Engines e.V., Frankfurt am Main.

Huber, K. (1990). Der Wärmeübergang schnelllaufender, direkteinspritzender Dieselmotoren. Dissertation, TU München.

Huber, T., T. Kruse, and G. Cornetti (2014). Simulation of diesel engine emissions by coupling 1-D with data-based models. In: *14. Internationales Stuttgarter Symposium*. Ed. by W. J. Bargende M. Reuss HC. Springer Vieweg, Wiesbaden, pp. 821–834.

Isermann, R. (1989). Digital Control Systems - Volume 1: Fundamentals, Deterministic Control. Vol. 1. Springer Verlag, New York, USA.

Isermann, R. (2007). Mechatronic Systems - Fundamentals. 1st ed. Springer Verlag, London, England.

Isermann, R. (2014). Engine Modeling and Control: Modeling and Electronic Management of Internal Combustion Engines. Springer Verlag, Berlin, Heidelberg.

Isermann, R. and M. Münchhof (2011). Identification of Dynamic Systems: An Introduction with Applications. Springer Verlag, Berlin, Heidelberg.

Jörg, C., M. Zubel, et al. (2017). Digital combustion rate shaping control as a tool to identify modern fuel injection strategies. In: *26. Aachener Kolloquium Fahrzeug- und Motorentechnik*. Aachen: Aachener Kolloquium Fahrzeug- und Motorentechnik GbR, pp. 535–564.

Jörg, C., J. Schaub, D. Neumann, and S. Pischinger (2018). Diesel Combustion Control via Rate Shaping. In: *MTZ worldwide* 79, pp. 16–21.

Jörg, C., T. Schnorbus, et al. (2015). Feedforward Control Approach for Digital Combustion Rate Shaping Realizing Predefined Combustion Processes. In: *SAE International Journal of Engines*. Vol. 8. 3. SAE International, Detroit, MI, USA, pp. 1041–1054.

Julier, S. J. and J. K. Uhlmann (1996). A General Method for Approximating Nonlinear Transformations of Probability Distributions. Tech. Report. Robotics Research Group, Department of Engineering Science, University of Oxford.

Julier, S. J. and J. K. Uhlmann (1997). A new extension of the Kalman filter to nonlinear systems. In: *Signal Processing, Sensor Fusion, and Target Recognition VI*. Vol. 3068, pp. 182–193.

Julier, S. J. and J. K. Uhlmann (2002). Reduced sigma point filters for the propagation of means and covariances through nonlinear transformations. In: *Proceedings of the 2002 American Control Conference (Cat. No.CH37301)*. Vol. 2. Anchorage, AK, USA, pp. 887–892.

Julier, S. J. and J. K. Uhlmann (2004). Unscented filtering and nonlinear estimation. In: *Proceedings of the IEEE* 92 (3), pp. 401–422.

Jung, M. (2003). Mean-Value Modelling and Robust Control of the Airpath of a Turbocharged Diesel Engine. PhD thesis. University of Cambridge.

Justi, E. (1938). Spezifische Wärme, Enthalpie, Entropie und Dissoziation technischer Gase. Springer Verlag, Berlin.

Kalman, R. (1960). A New Approach to Linear Filtering and Prediction Problems. In: *Transactions of the ASME - Journal of Basic Engineering* 82, pp. 35–45.

Kistler (2003). High temperature pressure sensor for cylinder pressure measurements in glow plug adapter. Online Manual (accessed: 2023-09-05). Kistler Instrumente AG, Winterthur, Switzerland.

Klein, P. (2009). Zylinderdruckbasierte Füllungserfassung für Verbrennungsmotoren. Dissertation. Uni Siegen.

Klein, P., M. Schmidt, and O. Loffeld (2007). Estimation of the cylinder pressure offset and polytropic exponent using extended Kalman filter. In: *IFAC Proceedings Volumes*. Vol. 40. 10, pp. 175–182.

Kluesener, P., I. Pyc, and G. Zimmermann (2022). e-Methanol - A universal green fuel. White paper: www.siemens-energy.com/hydrogen (accessed: 2022-03-27). München: Siemens Energy Global GmbH & Co. KG, pp. 15–18.

Kocher, L. et al. (2011). Control-oriented modeling of diesel engine gas exchange. In: *Proceedings of American Control Conference*. San Francisco, pp. 1555–1560.

Kolev, N. I. (2007). Multiphase Flow Dynamics 3 - Turbulence, Gas Absorption and Release, Diesel Fuel Properties. Springer Verlag, Berlin, Heidelberg, New York.

Konigorski, U. (2017). Modellbildung und Simulation. Vorlesungsskript, Institut für Automatisierungstechnik und Mechatronik, TU Darmstadt.

Kopp, R. E. and R. J. Orford (1963). Linear regression applied to system identification for adaptive control systems. In: *AIAA Journal* 1 (10), pp. 2300–2306.

Kowalczyk, M. (2018). Online-Methoden zur effizienten Vermessung von statischen und dynamischen Verbrennungsmotormodellen. Dissertation. TU Darmstadt.

Kozuch, P. (2004). Ein phänomenologisches Modell zur kombinierten Stickoxid- und Russberechnung bei direkteinspritzenden Dieselmotoren. Dissertation. Uni Stuttgart.

Leonhard, R., M. Parche, and C. Kendlbacher (2011). Einspritztechnik für Schiffsdieselmotoren. In: *MTZ - Motortechnische Zeitschrift* 72 (11), pp. 262–269.

Leonhardt, S. (1996). Modellgestützte Fehlererkennung mit Neuronalen Netze - Überwachung von Radaufhängung und Diesel-Einspritzanlagen. Dissertation. TU Darmstadt.

Ljung, L. and T. Söderström (1983). Theory and Practice of Recursive Identification. MIT press, Cambridge, MA, USA.

Ljung, L. (1999). System Identification: Theory for the User. 2nd ed. Prentice Hall Information and System Sciences Series. Prentice-Hall, Englewood Cliffs, NJ, USA.

Magnussen, B. and B. Hjertager (1977). On Mathematical Modeling of Turbulent Combustion with Special Emphasis on Soot Formation and Combustion. In: *International Symposium on Combustion*. Vol. 16, pp. 719–729.

Maschmeyer, H., M. Kluin, and C. Beidl (2015). Real driving emissions—a paradigm change for development. In: *MTZ - Motortechnische Zeitschrift* 76 (2), pp. 16–21.

Maschmeyer, H., C. Beidl, T. Düser, and B. Schick (2016). RDE-Homologation - Herausforderungen, Lösungen und Chancen. In: *MTZ - Motortechnische Zeitschrift* 77 (10), pp. 84–91.

Maus, W. (2019). Zukünftige Kraftstoffe - Energiewende des Transports als ein weltweites Klimaziel. ATZ/MTZ-Fachbuch, Springer Vieweg, Berlin.

Maybeck, P. (1979). Stochastic Models, Estimation, and Control. Vol. 1. Academic Press, New York, USA.

Mayer, M. and G. Krämer (2011). Abgasturbolader - Sinnvolle Nutzung des Abgasenergie. 6th ed. Vol. 103. Landsberg/Lech: Verlag moderne Industrie AG.

Mehra, R. K. (1970). On the identification of variances and adaptive Kalman filtering. In: *IEEE Transactions on Automatic Control* 15 (2), pp. 175–184.

Mehra, R. K. (1972). Approaches to adaptive filtering. In: *IEEE Transactions on Automatic Control* 17 (5), pp. 693–698.

Merker, G., C. Schwarz, G. Stiesch, and F. Otto (2006). Simulating Combustion: Simulation of combustion and pollutant formation for engine-development. 1st ed. Springer Verlag, Berlin.

Merker, G. (2014). Grundlagen Verbrennungsmotoren - Funktionsweise, Simulation, Messtechnik. 7.,vollständig überarbeitete Auflage. ATZ/MTZ Fachbuch. Springer Vieweg, Wiesbaden.

Merker, G. and C. Schwarz (2009). Grundlagen Verbrennungsmotoren. 5., vollst. überarb., aktualisierte und erw. Aufl. ATZ/MTZ Fachbuch. Vieweg + Teubner Verlag, Wiesbaden.

Mitterer, A. and F. Zuber-Goos (2000). Modellgestützte Kennfeldoptimierung - Ein neuer Ansatz zur Steigerung der Effizienz in der Steuergeräteapplikation. In: *ATZ - Automobiltechnische Zeitschrift* 102 (3), pp. 188–196.

Moraal, P. and I. Kolmanovsky (1999). Turbocharger Modeling for Automotive Control Applications. In: *International Congress and Exposition, Paper No.1999-01-0908*. SAE International, Detroit, MI, USA, pp. 1–15.

Mrosek, M. and R. Isermann (2010). Dynamic Reference Value Generation for the Control of a Diesel Engine with HP and LP-EGR. In: *Proceedings of ASME 2010 Dynamic Systems and Control Conference*. Vol. 1. Cambridge, MA, USA, pp. 109–116.

Mrosek, M. (2017). Model-Based Control of a Turbocharged Diesel Engine with High- and Low-Pressure Exhaust Gas Recirculation. Dissertation. TU Darmstadt.

Müller, H. and H. Bertling (1971). Programmierte Auswertung von Druckverläufen in Ottomotoren. Fortschr.-Ber. VDI Reihe 6 Nr. 30., VDI Verlag, Düsseldorf.

Müller, N. (2003). Adaptive Motorregelung beim Ottomotor unter Verwendung von Brennraumdrucksensoren. Dissertation. TU Darmstadt.

Münz, M. et al. (2016). Oxymethylene Ether (OME1) as Synthetic Low Emission Fuel for DI Diesel Engines. In: *3. Internationaler Motorenkongress*. Springer Vieweg, Baden-Baden, pp. 537–553.

Nelles, O. (2001). Nonlinear System Identification: From Classical Approaches to Neural Networks and Fuzzy Models. Springer Berlin, Heidelberg.

Nelles, O. (1999). Nonlinear System Identification with Local Linear Neuro-Fuzzy Models. Dissertation. TU Darmstadt.

Nelson, A. T. (2000). Nonlinear estimation and modeling of noisy time-series by dual Kalman filtering methods. PhD thesis. Dept. of Electrical and Computer Engineering, Oregon Graduate Institute of Science & Technology.

Neumann, K. (1934). Untersuchungen an der Dieselmaschine - Einfluss der Verbrennungsgeschwindigkeit auf das Arbeitsverfahren. In: *Forschung auf dem Gebiete des Ingenieurwesens A*. Vol. 5. 6. VDI, Berlin, pp. 173–180.

Neumann, K. (1936). Kinetische Analyse des Verbrennungsvorgangs in der Dieselmaschine. In: *Forschung auf dem Gebiete des Ingenieurwesens A*. Vol. 7. 3. VDI, Berlin, pp. 57–65.

Nusselt, W. (1923). Der Wärmeübergang in der Verbrennungskraftmaschine. Forschungsarbeiten auf dem Gebiet des Ingenieurwesens, VDI-Forsch.-Heft 264, Springer Verlag, Berlin.

Payri, R., J. Gimeno, R. Novella, and G. Brancho (2016). On the rate of injection modeling applied to direct injection compression ignition engines. In: *International Journal of Engine Research* 17 (10), pp. 1015–1030.

Pflaum, W. and K. Mollenhauer (1977). Wärmeübergang in der Verbrennungskraftmaschine. Springer Verlag, Wien, New York.

Pischinger, R., M. Klell, and T. Sams (2009). Thermodynamik der Verbrennungskraftmaschine. Vol. 3. Springer Verlag, Wien.

Poetsch, C. (2014). Crank-Angle Resolved Modeling of Fuel Injection and Mixing Controlled Combustion for Real-Time Application in Steady-State and Transient Operation. In: *SAE Technical Paper* (No. 2016-01-0558), pp. 1–14.

Poulos, S. and J. Heywood (1983). The Effect of Chamber Geometry on Spark-Ignition Engine Combustion. In: *SAE Technical Paper* (No. 830334), pp. 1–27.

Puskorius, G. V. and L. A. Feldkamp (1991). Decoupled extended Kalman filter training of feedforward layered networks. In: *International Joint Conference on Neural Networks (IJCNN)*. Vol. 1. Seattle, WA, USA, pp. 771–777.

Reif, K. (2012). Dieselmotor-Management: Systeme, Komponenten, Steuerung und Regelung. 5., überar. u. erw. Aufl. 2012. Springer+Teubner Verlag, Wiesbaden.

Reinhardt, H. (2008). Modellierung des Zündverzugs bei Mehrfacheinspritzung aufgeladener Dieselmotoren. Abschlussbericht 876. FVV Research Association for Combustion Engines e.V., Frankfurt am Main.

Rether, D. (2012). Modell zur Vorhersage der Brennrate bei homogener und teilhomogener Dieselverbrennung. Dissertation. Uni Stuttgart.

Ritter, B. (2020). Nonlinear State Estimation and Noise Adaptive Kalman Filter Design for Wind Turbines. Dissertation. TU Darmstadt.

Ritter, D. et al. (2019). Optimization-based fuel injection rate digitalization for combustion rate shaping. In: *2019 American Control Conference (ACC)*. Philadelphia, PA, USA, pp. 5103–5110.

Robert Pivec, A. W. and T. Sams (1998). Wärmeübergang im Ein- und Auslasssystem. In: *MTZ - Motortechnische Zeitschrift* 59 (10), pp. 658–663.

Sargenti, R. (2004). Entwicklung eines allgemeingültigen Modells zur Berechnung der Brennraumwandtemperaturen bei Verbrennungsmotoren. Abschlussbericht 779. FVV Research Association for Combustion Engines e.V., Frankfurt am Main.

Schaffnit, J. (2002). Simulation und Control Prototyping zur Entwicklung von Steuergerätefunktionen für aufgeladene Nutzfahrzeug-Dieselmotoren. Dissertation. TU Darmstadt.

Scharpf, J. S. (2011). Modellbasierte Methodik zur Optimierung der Sensorkonfiguration am Beispiel Dieselmotor. Dissertation. TU München.

Schmitt, M. (1995). Untersuchung zur Realisierung mehrdimensionaler lernfähiger Kennfelder in Großserien-Steuergeräten. Dissertation. TU Darmstadt.

Sequenz, H. (2013). Emission Modelling and Model-Based Optimisation of the Engine Control. Dissertation. TU Darmstadt.

Seykens, X., L. Somer, and R. Baert (2005). Detailed Modeling of Common Rail Fuel Injection Process. In: *MECCA Journal of Middle European Construction and Design of Cars* 3 (2-3), pp. 30–39.

Shinohara, Y., K. Takeuchi, O. Herrmann, and H. Laumen (2011). Common-Rail-Einspritzsystem mit 3000 Bar. In: *MTZ -Motortechnische Zeitschrift* 72 (1), pp. 10–15.

Sidorow, A. (2014). Model-based fault diagnosis of the air path and turbocharger of a diesel engine. Dissertation. TU Darmstadt.

Sigloch, H. (2008). Technische Fluidmechanik. 6th ed. Berlin, Heidelberg, New York: Springer.

Singhal, S. and L. Wu (1989). Training multilayer perceptrons with the extended Kalman algorithm. In: *Advances in neural information processing systems*. Bell Communications Research, Inc., Morristown, New Jersey, USA, pp. 133–140.

Sinsel, S. (2000). Echtzeitsimulation von Nutzfahrzeug-Dieselmotoren mit Turbolader zur Entwicklung von Motormanagementsystemen. Dissertation. TU Darmstadt.

Sitkei, G. (1964). Kraftstoffaufbereitung und Verbrennung bei Dieselmotoren. Springer, Berlin, Heidelberg.

Sjöberg, J. et al. (1995). Nonlinear black-box modeling in system identification: a unified overview. In: *Automatica* 31 (12), pp. 1691–1724.

Song, Q., Z. Jiang, and J. Han (2007). Noise Covariance Identification Based Adaptive UKF with Application to Mobile Robot Systems. In: *Proceedings 2007 IEEE International Conference on Robotics and Automation*. Roma, Italy, pp. 4164–4169.

Song, Q., J. Qi, and J. Han (2006). An Adaptive UKF Algorithm and Its Application in Mobile Robot Control. In: *2006 IEEE International Conference on Robotics and Biomimetics*. Kunming, China, pp. 1117–1122.

Steiner, R. (2004). Modellbildung und strömungsmechanische Simulation der dieselmotorischen Verbrennung. Dissertation. Uni Karlsruhe (TH).

Steinhaus, T., A. Mokros, and C. Beidl (2021). Einsatz von OME-Reinkraftstoff am Serienmotor: Analyse der Abgasemissionen in unterschiedlichen Applikationsstrategien. In: *18. FAD-Konferenz. Herausforderung-Abgasnachbehandlung*. Dresden, pp. 169–183.

Stephan, P., K. Schaber, K. Stephan, and F. Mayinger (2013). Thermodynamik - Grundlagen und technische Anwendungen Band 1: Einstoffsystem. 19. Auflage. Springer Vieweg Verlag, Berlin, Heidelberg.

Stiesch, G. (1999). Phänomenologisches Multizonen-Modell der Verbrennung Schadstoffbildung im Dieselmotor. Dissertation. Uni Hannover.

Stiesch, G. (2003). Modeling Engine Spray and Combustion. Springer Verlag, Berlin, Heidelberg.

Töpfer, S. (2002). Hierarchische neuronale Modelle für die Identifikation nichtlinearer Systeme. Dissertation. TU Darmstadt.

Töpler, J. and J. Lehmann (2017). Wasserstoff und Brennstoffzelle - Technologien und Marktperspektiven. 2nd ed. Springer Vieweg Verlag, Berlin, Heidelberg.

Torkzadeh, D. D. (2003). Echtzeitsimulation der Verbrennung und modellbasierte Reglersynthese am Common-Rail-Dieselmotor. Dissertation. ETH Zürich.

Tschanz, F., A. Amstutz, C. Barro, and P. Obrecht (2012). Soot-controlled diesel engine – Control-orientated modelling of soot emissions and control of harmful emissions in engine operation. Abschlussbericht 986. FVV Research Association for Combustion Engines e.V., Frankfurt am Main.

Tschöke, H., K. Mollenhauer, and R. Maier (2018). Handbuch Dieselmotoren. 4. Auflage. Springer Vieweg Verlag, Wiesbaden.

Uhlmann, J. K. (1995). Dynamic Map Building and Localization: New Theoretical Foundations. PhD thesis. University of Oxford.

Urlaub, A. (1995). Verbrennungsmotoren - Grundlagen, Verfahrenstheorie, Konstruktion. 2. neubearbeitete Auflage. Springer Verlag, Berlin, Heidelberg.

Van der Merwe, R. (2004). Sigma-Point Kalman Filters for Probabilistic Inference in Dynamic State-Space Models. PhD thesis. OGI School of Science & Engineering at Oregon Health & Science University.

Van der Merwe, R. and E. A. Wan (2001). The square-root unscented Kalman filter for state and parameter-estimation. In: *Proceedings of the 2001 IEEE International Conference on Acoustics, Speech, and Signal Processing. (Cat. No. 01CH37221)*. Vol. 6, pp. 3461–3464.

Varde, K., D. Popa, and L. Varde (1984). Spray Angle and Atomization in Diesel Sprays. In: *SAE Technical Paper* (No. 841055), pp. 1–9.

VDI-Wärmeatlas, ed. (2013). Wärmeatlas, VDI. 11., bearbeitete und erweiterte Auflage. Berlin Heidelberg: Springer Vieweg Verlag.

Vibe, I. (1970). Brennverlauf und Kreisprozess von Verbrennungsmotoren. VEB Verlag Technik, Berlin.

Vogt, M., N. Müller, and R. Isermann (2004). On-line Adaptation of Grid-based Look-up Tables using a Fast Linear Regression Technique. In: *Journal of Dynamic Systems, Measurement and Control* 126 (4), pp. 732–739.

Wan, E. A. and A. T. Nelson (1997). Neural dual extended Kalman filtering: applications in speech enhancement and monaural blind signal separation. In: *Neural Networks for Signal Processing VII. Proceedings of the 1997 IEEE Signal Processing Society Workshop*. Portland, Oregon, USA, pp. 466–475.

Wan, E. A. and R. Van der Merwe (2000). The unscented Kalman filter for nonlinear estimation. In: *Proceedings of the IEEE 2000 Adaptive Systems for Signal Processing, Communications, and Control Symposium (Cat. No. 00EX373)*. IEEEE, pp. 153–158.

Wan, E. A., R. Van der Merwe, and A. T. Nelson (2000). Dual Estimation and the Unscented Transformation. In: *Advances in Neural Information Processing Systems*. Vol. 12. MIT Press, Cambridge, MA, USA, pp. 666–672.

Warnatz, J., U. Maas, and R. Dibble (2007). Combustion - Physical and Chemical Fundamentals, Modeling and Simulation, Experiments, Pollutant Formation. 4th Edition. Springer Verlag, Berlin.

Welch, G. and G. Bishop (2006). An Introduction to the Kalman Filter. Tech. rep. University of North Carolina at Chapel Hill, NC, USA.

Wimmer, A., R. Pivec, and T. Sams (2000). Heat Transfer to the Combustion Chamber and Port Walls of IC Engines - Measurement and Prediction. In: *SAE Transactions - Journal of engines* 109, pp. 675–689.

Wintrich, T., M. Krüger, and D. Naber (2017). Bosch common rail for passenger car light duty – the first 20 years. In: *17th International Stuttgarter Symposium Automotive and Engine Technology*. Vol. 1, pp. 177–191.

Wolfer, H. (1938). Der Zündverzug im Dieselmotor. VDI-Forschungsheft 392, VDI-Verlag, Berlin.

Woschni, G. (1970). Die Berechnung der Wandverluste und der thermischen Belastung der Bauteile von Dieselmotoren. In: *MTZ - Motorentechnische Zeitschrift* 31 (12), pp. 491–499.

Zacharias, F. (1966). Analytische Darstellung der thermischen Eigenschaften von Verbrennungsgasen. Dissertation, TU Berlin.

Zahn, S. (2012). Arbeitsspielaufgelöste Modellbildung und Hardware-in-the-Loop-Simulation von Pkw-Dieselmotoren mit Abgasturboaufladung. Dissertation. TU Darmstadt.

Zapf, H. (1969). Beitrag zur Untersuchung des Wärmeübergangs während des Ladungswechsels im Viertakt-Dieselmotor. In: *MTZ - Motorentechnische Zeitschrift* 30 (12), pp. 461–465.

Zimmerschied, R. (2008). Identifikation nichtlinearer Prozesse mit dynamischen lokal-affinen Modellen. Dissertation. TU Darmstadt.

Zydek, S. (2018). Optimale Regelung des Dieselmotors zur Minimierung von Realfahrtemissionen und -verbrauch. Dissertation. TU Darmstadt.

Publications by the Author

Weber, A. (2019a). Semi-Physical Real-Time Models for Combustion and Emissions with Online Parameter Estimation. In: *FVV Information Sessions Engines 2019*. Vol. 587. FVV Research Association for Combustion Engines e.V., Frankfurt am Main, pp. 129–163.

Weber, A. (2019b). Semi-physikalische Echtzeitmodelle für Verbrennung und Emissionen mit Online-Parameterschätzung. Abschlussbericht 1231. FVV Research Association for Combustion Engines e.V., Frankfurt am Main.

Weber, A. and R. Isermann (2017). Crank Angle Resolved Semi-Physical Combustion Model with Parameter Estimation for Real-Time Applications. In: *Symposium for Combustion Control 2017*. Aachen, pp. 245–254.

Weber, A. and R. Isermann (2018). Model-Based Combustion Analysis for the Development of Control Functions at the EiL-Test Bench. In: *18th Stuttgart International Symposium Automotive and Engine Technology*. Vol. 2. Stuttgart, pp. 345–359.

Weber, A. and R. Isermann (2019). Semi-Physical State and Parameter Estimation of Diesel Combustion Phases. In: *Symposium for Combustion Control 2019*. Aachen, pp. 73–81.

Weber, A. and R. Isermann (2020). Semi-physical state and parameter estimation of diesel combustion phases for real-time applications. In: *International Journal of Engine Research*. Vol. 21. 10, pp. 1800–1818.

Zydek, S., D. Casper, R. Isermann, and A. Weber (2016). Determining the Initial In-Cylinder Gas State Based on Semi-Physical Models. In: *8th IFAC Symposium on Advances in Automotive*. Kolmården Wildlife Resort, Sweden, pp. 464–470.

Supervised student work

Abresch, P. (2017). Simulationsbasierte Entwicklung zur Einhaltung zukünftiger Emissionsgesetzgebung. Proseminar - Institut für Automatisierungstechnik und Mechatronik, TU Darmstadt.

Abresch, P. (2018). Inbetriebnahme eines Hardware-in-the-Loop-Simulators für die Entwicklung von Motorsteuerungen. Bachelorarbeit - Institut für Automatisierungstechnik und Mechatronik, TU Darmstadt.

Berger, J.-N., J. Boehm, and H. Li (2018). Untersuchung von Methoden zur Identifikation von Totzeit behafteten Systemen. Projektseminar Mechatronik im Automobil - Institut für Automatisierungstechnik und Mechatronik, TU Darmstadt.

Böhm, C. (2016). Entwicklung einer Simulationsumgebung zur Untersuchung des Fahrer- und Fahrzeugeinflusses beim Realfahrtversuch. Masterarbeit - Institut für Automatisierungstechnik und Mechatronik, TU Darmstadt.

Böhm, C., J. Kunkel, and P. Stenger (2015). Recherche und Vergleich physikalischer Grundmodelle für das Luftsystem. Projektseminar Regelungstechnik im Automobil - Institut für Automatisierungstechnik und Mechatronik, TU Darmstadt.

Böhm, C., J. Kunkel, and P. Stenger (2016). Modellierung des Einspritzsystems eines Common-Rail-Dieselmotors. Projektseminar Mechatronik im Automobil - Institut für Automatisierungstechnik und Mechatronik, TU Darmstadt.

Böhmert, N. (2018). Entwicklung eines simulationsbasierten Prozesses für die virtuelle Validierung von Emissionskalibrierungen von Motorsteuergeräten. Masterarbeit - Institut für Automatisierungstechnik und Mechatronik, TU Darmstadt.

Didion, M., S. Günzel, and Y. N. Ferreira (2016). Implementierung eines arbeitsspielaufgelösten Verbrennungsmodells auf einer Echtzeithardware. Projektseminar Regelungstechnik im Automobil - Institut für Automatisierungstechnik und Mechatronik, TU Darmstadt.

Gottschalg, G., O. Schön, and C. Wolz (2016). Systemanalyse und Identifikation dynamischer Modelle der Reaktionskinetik selbstzündender Verbrennungsmotoren. Projektseminar Mechatronik im Automobil - Institut für Automatisierungstechnik und Mechatronik, TU Darmstadt.

Hamroun, I., A. Kassebi, C. Ludwig, and I. Tayeche (2019). Entwurf und Umsetzung einer Motorreglung am HiL-Motorsimulationsprüfstand. Projektseminar Mechatronik im Automobil - Institut für Automatisierungstechnik und Mechatronik, TU Darmstadt.

Knerr, J., V. Lizenberg, and A. K. Sacakli (2016). Entwurf und Analyse von Verfahren zur Brennverlaufsrechnung für die zylinderdruckbasierte Verbrennungsregelung eines Dieselmotors. Pro-

jektseminar Mechatronik im Automobil - Institut für Automatisierungstechnik und Mechatronik, TU Darmstadt.

Konrad, M. and M. Voß (2019). Untersuchung des dynamischen Motorverhaltens hinsichtlich Verbrauch und Emission unter Realfahrtbedingungen. Projektseminar Mechatronik im Automobil - Institut für Automatisierungstechnik und Mechatronik, TU Darmstadt.

Mende, H. and T. Schenkel (2017). Inbetriebnahme eines Hardware-in-the-Loop-Simulators. Projektseminar Mechatronik im Automobil - Institut für Automatisierungstechnik und Mechatronik, TU Darmstadt.

Pasic, K. (2019). Kombinierte Zustands- und Parameterschätzung des Zylindergaszustands in einem Verbrennungsmotor mithilfe eines Extended Kalman Filter. Masterarbeit - Institut für Automatisierungstechnik und Mechatronik, TU Darmstadt.

Protasiewicz, W. (2016). Entwicklung und Implementierung eines zylinderdruckbasierten Verbrennungs- und Emissionsmodells für einen Dieselmotor. Diplomarbeit - Institut für Automatisierungstechnik und Mechatronik, TU Darmstadt.

Seilberger, D. (2017). Konzepte für die hochpräzise Regelung von Stellaktoren im Automobil. Proseminar - Institut für Automatisierungstechnik und Mechatronik, TU Darmstadt.

Seilberger, D. (2018). Implementierung und Inbetriebnahme einer Positionsregelung für einen General-Purpose Actuator an einem Hardware-in-the-Loop Prüfstand. Bachelorarbeit - Institut für Automatisierungstechnik und Mechatronik, TU Darmstadt.

Stein, F. (2018). Zylinderdruckbasierte Schätzung des Zylindergaszustands bei einem Verbrennungsmotor mithilfe eines Extended Kalman Filter. Masterarbeit - Institut für Automatisierungstechnik und Mechatronik, TU Darmstadt.

Wang, J. (2017). Cycle-resolved Estimation of the Initial In-Cylinder Gas State of a Combustion Engine. Masterarbeit - Institut für Automatisierungstechnik und Mechatronik, TU Darmstadt.

Wang, Q., Y. An, and F. Miao (2016). Korrelations- und Sensitivitätsanalyse von Sensorsignalen des Dieselmotors zur Erkennung von Zustandszusammenhängen. Projektseminar Mechatronik im Automobil - Institut für Automatisierungstechnik und Mechatronik, TU Darmstadt.

Zhu, B. (2017). Modellierung der dynamischen Emissionen eines Verbrennungsmotors mithilfe von lokal-linearen Neuro-Fuzzy-Modellen. Masterarbeit - Institut für Automatisierungstechnik und Mechatronik, TU Darmstadt.